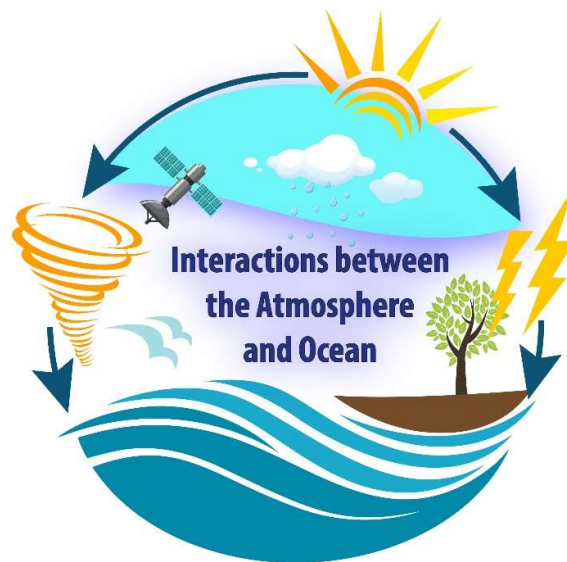


**34<sup>th</sup> Annual Conference of  
SOUTH AFRICAN SOCIETY FOR  
ATMOSPHERIC SCIENCES**

**20 - 21 September 2018**

**DURBAN, South Africa**



**SASAS 2018**

**Conference Proceedings**

# SPONSORS



[www.ukzn.ac.za](http://www.ukzn.ac.za)



[atmres.ukzn.ac.za](http://atmres.ukzn.ac.za)

**Journal of Neutral Atmosphere**

[www.jnatm.org](http://www.jnatm.org)

## **PREFACE**

The 34<sup>th</sup> Annual Conference of South African Society for Atmospheric Sciences (SASAS) has been hosted in KwaZulu Natal province, just after 5 years from our last time host by 2013. The theme for the SASAS 2018 conference is “**Interactions between the atmosphere and oceans**”. The major aim of the conference is to discuss, understand and share our knowledge on the complex dynamics of the Earth’s atmosphere and oceans. In general, studies of the Earth’s atmosphere is governed by various in-situ/ground-based and space borne measurements, models and simulations and its interaction with land and oceans.

We have made available an online version of conference communication process, which includes a dedicated webpage for the conference, contributed by the University of KwaZulu-Natal (UKZN). We believe that most of the participants have benefited the online registration (expression of interest), short abstract submission and access to all useful information.

Based on several requests, we have allowed authors a maximum of 4 pages for their research contributions. The review process for the conference proceedings were led by one of the conference organizing committee members, Professor Willem Landman (University of Pretoria). He has ensured that the challenging job of the review process was conducted successfully, and the **quality** of all conference proceedings was improved through peer review process. In total, 42 conference proceedings were peer reviewed and published with ISBN. The conference proceedings will be available for download through SASAS and SASAS 2018 webpage.

In addition to the conference, we have organized 4<sup>th</sup> student training workshop, held on 16-19 September 2018 and which focused on “Mathematical tools and software applied on Atmospheric Science” ([atmres.ukzn.ac.za/workshop4.html](http://atmres.ukzn.ac.za/workshop4.html)), where approximately 28 students participated. The workshop was sponsored through the Africa Laser Centre (ALC), for a limited financial support to South African students and workshop registration fee for all the students were waived.

On behalf of the SASAS 2018 organizing committee, we would like to thank everyone for their enthusiasm and contribution to the 34<sup>th</sup> Annual SASAS Conference. We are also grateful to our sponsors from University of KwaZulu Natal (UKZN), Atmospheric Research Group (ATM-RES) and Journal of Neutral Atmosphere (J-N-ATM). We sincerely acknowledge and appreciate their contribution and support.

**Prof. Sivakumar Venkataraman**  
Conference Chair

## **MESSAGE FROM THE PRESIDENT**

Dear Delegates

I warmly welcome you to the 34<sup>th</sup> South African Society for Atmospheric Sciences (SASAS) Conference. After a successful 33<sup>rd</sup> annual conference held at Polokwane, the University of KwaZulu-Natal's Atmospheric Science Research Group is delighted to be hosting SASAS 2018 in Ballito, Durban.

I would like to extend my special appreciation to all the participants and to international delegates from Europe, United Kingdom, United States of America and Australia. We believe that delegates will benefit from a wealth of knowledge being shared from the distinguished key note addresses, invited lectures and the various talks by academics and postgraduate students.

The goal of SASAS as a society is to promote and develop atmospheric sciences in a broader context over South Africa. It includes, but not confined to, all major topics related to atmospheric structure and dynamics, meteorology, agro-meteorology, climatology, air quality and information, hydrology, various levels of atmospheric interactions, remote sensing instruments, numerical modelling and oceanography.

We believe that the introduction of peer reviewed conference proceedings over the past 7 years have improved the quality of the research produced by the South African atmospheric science community.

SASAS 2018 has about 75 conference delegates and pleased to note that many are students or young researchers who may play major role in the future of atmospheric science research and to our society. We believe that the delegates are from various higher educational institutions and research organizations across the country, and will come together to share their scientific knowledge on a common platform. Furthermore, we hope that students take this opportunity to initiate stimulating discussions with their peers as they strive to enhance their knowledge.

Although we have tried our best to enhance the value of the society, I personally would like all the members to actively participate one or the other way, and aim to lighten the SASAS star into a brighter sky. Lastly, SASAS encourages members to share their opinions/ideas, concerns and valuable comments to continuously improve the society. I encourage everybody to join SASAS by completing the membership form that you will find in on the website. Let's work together and make SASAS grow.

**Prof. Sivakumar Venkataraman**

(Atmospheric Research Group – UKZN : atmres.ukzn.ac.za)

SASAS President

## **COMMITTEES**

### **LOCAL ORGANIZING COMMITTEE**

**Prof. Sivakumar Venkataraman - Chair**

**Dr. Sangeetha Sivakumar**

**Dr. Paulene Govender**

**Mrs. Leena Rajpal**

**Miss. Chuene Shiela Seanego (UKZN / NRF)**

**Miss. Zanele Pretty Mtshali (UKZN / NRF)**

**Mr. Anthony Govender (UKZN / NRF)**

**Mr. Asokaran Rajah**

### **CONFERENCE PROCEEDING PEER REVIEW COMMITTEE**

**Prof Willem Landman (Chair)**

Dr Warren Tennant

Prof Mathieu Rouault

Dr Liesl Dyson

Dr Christien Engelbrecht

Mr Mavhungu Muthige

Prof Sivakumar Venkataraman

Mrs Anzel de Lange

Dr Asmerom Beraki

Dr Johan Malherbe

Dr Thando Ndarana

Dr Chris Lennard

Miss Lerato Mpheshea

Mr Steven Phakula

Mr Robert Maisha

Dr Olivier Crespo

Dr Christo Rautenbach

Prof Chris Reason

Dr Rebecca Garland

Mrs Anika de Beer

Mrs Stephanie Landman

Dr Andries Kruger

Dr Mary-Jane Bopape

Dr Hector Chikoore

Dr Gregor Feig

Dr Caradee Wright

Mrs Patience Mulovhedzi

Dr Mark Tadross

Miss Seneca Naidoo

Dr Mogesh Naidoo

### **STANLEY JACKSON AWARD REVIEWERS**

Prof Mike Harrison, Climate Change Risk Management (CCRM), UK

Prof Babatunde Abiodun, University of Cape Town, South Africa

Dr Roelof Burger, North-West University, South Africa

All rights reserved. No part of this publication may be reproduced or copied in any form – graphic, electronic, or mechanical, including photocopying, taping, or information storage and retrieval systems – without the prior written permission of the publisher. Contact SASAS for permission pertaining to the overall collection. Authors retain their individual rights and should be contacted directly for permission to use their material separately. The manuscripts reproduced herein are a collection of refereed papers presented at the 34<sup>th</sup> Annual Conference of the South African Society for Atmospheric Science. The peer reviewed conference proceeding in this collection constitute formal publication.

ISBN for peer reviewed conference proceedings: **978-0-620-80825-5**

## **REVIEW PROCESS**

The South African Society for Atmospheric Sciences annual meeting provides the opportunity for scientists to publish their work in the conference proceedings. All the papers in the proceedings underwent a blind review process to improve quality, performance and provide credibility to the research. Each paper was independently reviewed by two reviewers on the review panel. The reviewers were tasked to categorize the paper into; accept as is; accept with minor/major revisions; or reject. Based on the reviewers' comments, the convenor made the final decision on acceptance. The reviewers' comments and decision on acceptance were sent to lead authors. Following this, corrections were made by authors for final acceptance. A total of 41 conference proceedings were submitted.

*Conference proceedings edited by Prof. Sivakumar Venkataraman*

## Table of contents

<b>1<sup>st</sup> Author</b>	<b>Title of the presentation</b>	<b>Pg No</b>
<b>ATMOSPHERE-OCEAN Interaction</b>		
Mary-Jane Bopape	Weather and Climate Numerical Models Development Programme in South Africa	01
Serge Tomety	Coastal variability and change in the Benguela Upwelling System: Decadal trend analysis.	05
Arielle Stela Nkwinkwa Njouodo	Impact of the Agulhas Current on coastal South African precipitation	09
Georges-Noel T. Longandjo	Central Africa Low: identification, annual cycle and its influence on regional climate and water vapor transport over Central Africa	13
<b>Atmospheric Dynamics</b>		
Marie-Lou Bach�elery	How low-frequency Equatorial Kelvin Wave activity and local coastal winds modulate the south-eastern interannual Atlantic variability?	18
Thando Ndarana	The energetics of ridging South Atlantic Ocean anticyclones over South Africa	22
Tania Williams	Space and time varying wind-wave interaction in False Bay, South Africa.	26
<b>Weather Extreme and Forecasts</b>		
Nosipho Zwane	Verification of Site-Specific Processing System using the data generated from the South African Weather Service radiometric stations	30
Christina M Botai	Dependency characteristics of extreme precipitation indices in flood-prone areas of Gauteng	33
Markus Geldenhuys	Poor-man's experimental design: Measuring wind and turbulence in a complex environment	36
Surprise Mhlongo	Improving ENSO forecasts through statistical intervention	40
<b>Aerosols and Air Pollution</b>		
Lerato Shikwambana	Black carbon and carbon monoxide over South Africa using satellite observation: Preliminary results	43
Yegeshni Moodley	Trends and variability of PM2.5 in the Vaal Triangle area (Three Rivers, S26°4 E27°6): A pilot study	47
Anzel de Lange	Finding a relationship between meteorological Air Dispersion Potential and Particulate Matter for six sites in South Africa	50
Mzimkhulu Msimanga	A comparison of CALPUFF and AERMOD for simulating PM10 and SO2 concentration in the North West Province	55
<b>Aerosol, Ozone and Solar Radiation</b>		
David Jean du Preez	An exploratory analysis on low-ozone events during spring and summer months over Cape Point, South Africa	59
Paulene Govender	Investigating the effect of aerosols on diffuse solar irradiance	63

	in Durban, South Africa	
Zimbini Faniso	Contrast of Inland aerosol optical thickness behavior	67
<b>Weather, Climate and model</b>		
Johan Malherbe	The Bidecadal climate cycle : Alive and well	70
Thato Masithela	Present and future variability of heat units for Mpumalanga Province	74
Liesl Dyson	An Era-Interim hail climatology for South Africa	77
Henno Havenga	The trends thermodynamic indices over Irene, Gauteng	80
Thabo Makgoale	The sensitivity of simulated temperatures in climate models to aerosols over southern Africa	87
<b>CLIMATE and RAINFALL</b>		
Stephanie Landman	Analysis of the atmospheric conditions during 2014 – 2017 for the winter rainfall season of South Africa	92
Jan H. Vermeulen	Five Minute to Yearly Record Rainfalls for South Africa (excluding Lesotho) from 1860 to 2017	96
Willard Zvarevashe	Annual and Seasonal Spatial Analysis of Rainfall variability in Western Cape, South Africa	101
<b>Climate and Environment/Social Impacts</b>		
Marc de Vos	Coastal Marine Weather and Safety: Towards an integrated understanding for Marine Weather Services	105
Siphamandla Daniel	Climate Change Impacts on Accumulated Winter Chill for the Western Cape	109
Nisa Ayob	Perceived benefits of hail nowcasts over the Gauteng Highveld	112
Rakhee Lakhraj-Govender	Temperature anomalies over South Africa during El Niño Modoki and Conventional El Niño events.	117
Thulebona Mbhamali	Statistical prediction of sugarcane yields over southeastern Africa	121
<b>Poster Sessions</b>		
Aimee Serafini	Exploring the predictability of lightning-caused wildfires in the Western Cape	125
Tshidi Machinini	Inter-comparison of total column ozone from ozonesonde with the Dobson spectrophotometer measurements from Irene, South Africa: 2012 - 2017.	129
Paulene Govender	Assessment of cloud types over Durban, South Africa, using day time cloud cover observations : an initial study	133
Christo Rautenbach	Interannual variability correlation between the Cape Point wave record and large-scale climate modes	137
Christien J. Engelbrecht	Seasonal rainfall anomalies over the all-year and winter rainfall regions of South Africa	142
Lehlohonolo Thobela	The influence of thermal and vorticity advection on the development of continental tropical low-pressure systems over southern Africa	146
Katlego Ncongwane	A Decade of heat stress conditions over Gauteng Province, South Africa	154

Samkelisiwe Thwala	An evaluation of a ten-year lightning variability over the Western Cape Province, South Africa using weather circulation classification	158
Rene T LOUA	Climatological analysis of temperature and pluviometry in Guinea 1960-2016	162
Michael G. Hart-Davis	An assessment of the importance of combining wind, ocean currents and stochastic motions in a particle trajectory model for search and rescue applications	166

## ***Weather and Climate Numerical Models Development Programme in South Africa***

Mary-Jane Bopape<sup>1</sup>, Francois Engelbrecht<sup>2</sup>, Babatunde Abiodun<sup>3</sup>, Asmerom Beraki<sup>2</sup>, John McGregor<sup>4</sup>, Thando Ndarana<sup>5</sup>, Lucky Ntsangwane<sup>1</sup>, Robert Plant<sup>6</sup>, David Randall<sup>7</sup>, Hannes Rautenbach<sup>1</sup>, Happy Sithole<sup>8</sup>, Mthetho Sovara<sup>8</sup>, Jongikhaya Witi<sup>1</sup>

<sup>1</sup>South African Weather Service, Pretoria, South Africa

<sup>2</sup>Council for Scientific and Industrial Research, Pretoria, South Africa

<sup>3</sup>University of Cape Town, Cape Town, South Africa

<sup>4</sup>Commonwealth Scientific and Industrial Research Organisation, Melbourne, Australia

<sup>5</sup>University of Pretoria, Pretoria, South Africa

<sup>6</sup>University of Reading, Reading, United Kingdom

<sup>7</sup>Colorado State University, Fort Collins, United States

<sup>8</sup>Centre for High Performance Computing, Cape Town, South Africa

### ***Abstract***

In this document we propose that institutions that are already embarking on model development activities work together and support each other, as well as new entrants to accelerate model development activities in the country and increase the critical mass with an advanced understanding of models faster. The ultimate purpose of this initiative is that South Africa becomes an independent user of models, and develops one or more home-grown models that can be used for operational and research purposes. Each participating institution can make contributions on any model of interest, and these contributions can include work with consortia on international models. These initial steps will help build capacity, which can contribute towards the development of one or more home grown models. The development of a critical mass of researchers that can develop models will require investment in human resource capital development. This programme will enhance collaboration between organisations with modelling capabilities towards jointly informing policy developments and implementation of frameworks in the country. Close collaboration between the South African Weather Service (SAWS) which is a mandated meteorological service organisation, and other research organisations will ensure that all modelling research taking place nationally, that can improve weather and climate early warning systems, is incorporated into the SAWS operations, for the benefit of the society and public in general. Moreover, the Council for Scientific and Industrial Research (CSIR) Earth System Model development programme and related generation of climate change projections for Africa will be furthered by this enhanced collaboration.

**Keywords:** *numerical modelling, model development, human capital development, collaboration*

### ***Introduction***

South African scientists started participating in the development or improvement of weather and climate numerical models in 2002, after being inactive in the area for over a decade. The regeneration of model development activities started at the University of Pretoria (UP) through a Water Research Commission (WRC) funded project where a dynamical core of a nonhydrostatic sigma- coordinate model (NSM) was developed from scratch (Engelbrecht, 2006; Engelbrecht et al., 2007). These activities served to encourage others in the country to also contribute in the model development space. The NSM was later extended to include moisture and microphysics schemes at the CSIR in collaboration with UP (Bopape et al., 2014a; 2014b). This model is currently only available for use in research mode and is written in serial, however, the underlying dynamics are similar to those used in the Conformal Cubic Atmospheric Model (CCAM).

Most other model development activities in the country built on existing modelling systems from first world countries. For example Abiodun et al (2008a and b) improved the dynamical core of CAM to use stretched grid with higher resolution over an area or process of interest while at Iowa State University and continued the development while in the

employ of University of Cape Town (UCT). Model development activities in the country also include the coupling of different components of the earth system together. At SAWS, Beraki et al (2015) coupled the ECHAM4.5 model to MOM3.

A recent development is the configuration of the first African-based Earth System Model at the CSIR, through a collaboration with the Commonwealth Scientific and Industrial Research Organisation (CSIRO) (Engelbrecht et al., 2012, 2018). The Variable-resolution Earth System Model (VrESM) became the first African-based model to register for CMIP6 in 2017. It uses as atmospheric and land-surface components the CCAM and CABLE models of the CSIRO, whilst the ocean component VCOM (Variable-cubic Ocean Model) was developed at the CSIR. Development activities are focused on different aspects of the earth system, including the carbon cycle, and the project will allow Africa to contribute global simulations towards the generation of Assessment Report Six (AR6) of the Intergovernmental Panel on Climate Change (IPCC).

### ***Background to Programme***

Despite model development activities having started over a decade ago, the progress in model development activities in the country has been slow, and the number of people who truly understand models and can contribute to the model

development exercise remains low. Discussions on possible collaboration efforts and information sharing amongst those working on model development started in 2017. The intention is that when model developers in the country work together, model development activities will be accelerated. Although the different organisations use different models, similar issues such as a lack of solutions for certain resolutions apply to all models. Some sub-grid schemes are used in a number of models, and so an understanding of the performance of such schemes when linked to different dynamics can be of mutual benefit to all organisations involved. Together, the different organisations can identify common training needs and training workshops that can be co-organised to deal with known shortcomings in the country. Furthermore, through working together the country can become an independent developer of weather and climate models (whilst strengthening collaboration in this field with international model development centres). Randall (1996) suggested that model development should continue at universities to train model developers at a rate matched to the community's demand for developers. This implies that model development can take place at both universities and research institutions.

A workshop on model development was held at SAWS on the 28<sup>th</sup> October 2017 where researchers that have contributed to the space from SAWS, CSIR, UP and UCT met to discuss ideas on how the country can accelerate model development activities. Prof David Randall from Colorado State University in the United States of America (USA), Prof. Robert Plant from the University of Reading in the UK, as well as Dr John McGregor from the CSIRO in Australia were invited to contribute through an online platform and provide advice to the workshop delegates. These three colleagues were invited to the workshop because they are considered as some of the world renowned scientists in model development, and existing close relationships with them are already in place with scientists in the country. Modelling activities taking place in the participating organisations were discussed, as well as future plans to inform the development of a programme that aligns with strategic objectives of each of the participating organisations/institutions. The sections below are informed by resolutions of the workshop.

#### *Goals and Objectives of the Programme*

*The purpose of the programme is to establish an environment that will make it possible for weather and climate operational obligations of South Africa to be met using home grown models in ten years. The home grown models will also be used for research purposes and to meet policy requirements such as the National Communications on Climate Change and National Adaptation Strategy.*

The main goal of the framework is to ensure that there is a coordinated weather and climate numerical model development effort in South Africa which can lead to the following outcomes:

- South Africa becomes an independent developer of numerical weather and climate models;
- South Africa is a part of a new trend in model development instead of waiting for others to develop schemes suitable for Africa;
- Local domain expertise on different systems such as African thunderstorms, aerosols and the southern ocean is incorporated into the models;
- A closer relation is forged between model developers at Universities, and SAWS to ensure

that research conducted outside of SAWS benefits operational activities of the SAWS, and Earth System Modelling at the CSIR

- Expertise is developed not only to identify biases and weaknesses in models, but to also improve models;
- Strengthen synergies between the institutions involved in model development and the Centre for High Performance Computing (CHPC), towards also strengthening high-performance computing skills in South Africa;
- There is increased support for postgraduate students working on model development activities at universities and some of the students can be hosted in research organisations;
- Model development activities support policy making and national initiatives;
- Improved understanding of local processes and hence improvement in models.
- Increased collaboration with model developers internationally; and
- Increased opportunities for programming training necessary for model development.

#### *Implementation Mechanism*

The implementation of this framework takes account of the fact that model development is a slow process. In order to develop a robust system, a minimum period of five years is required, and this minimum period can also take up to ten years. The plan also recognises that model development activities can result in very few publications. This means that researchers working on model development may not be able to grow smoothly on their research career ladder if they can't use other models. The planned activities also consider the past and ongoing efforts in the country, which will provide a good launch pad to enhanced model development. Contributions to the plan are therefore not model specific and the expectation is that the participating organisations will work on this project, in parallel to other modelling activities where any models of choice can be used. It is also noted that model development activities do not have to be started from scratch but contributions can be made by building on existing models.

Work will be conducted across timescales so that activities are able to benefit weather forecasting as well as climate predictions and projections. When diagnosing sources of errors, different components of models will be considered including sub-grid models as well as the dynamical cores. The plan also considers institutional arrangements to ensure that the contributions are relevant and also contribute to the mandates and strategic objectives of the participating organisations. The coordinated project can lead to publications which are necessary in an academic career, but at the same time can contribute to the operational activities at SAWS and the CSIR. This means that the research conducted across South Africa will be able to contribute to SAWS early warning systems and can therefore inform decision making to save lives and property. This programme should provide an environment wherein SAWS can be in a position to compare local and international models in the recent future for a decision on its main operational model. This will only happen if local models perform at a level that is on par with international models. In the case of the CSIR, the intention of this programme is to involve a larger pool of post-graduate students and university researchers in the continued

development and application of the African-based Earth System Model.

The following activities will be undertaken:

**Model contributions:** Contributions will be made in two ways: 1) Creation of models that are fully developed in South Africa. These may include atmospheric, ocean, land-surface and sea-ice models. This contribution includes model development that builds on existing models with a significant contribution from South Africa to the extent that South Africa can be considered as a lead in the development process. 2) Participate in open/partnership model development activities internationally. This contribution will include model development activities in open models such as CCAM, WRF and CAM, as well as somewhat closed models where a formalised relationship is required before model contributions can be made.

**Steering Committee:** The implementation of the programme will be led by a steering committee which will be identified as soon as the programme is approved. The committee will be comprised of at least five individuals from participating local organisations. The steering committee will also include at least two international experts (i.e. not based in South Africa) who will serve as advisors to the committee. The committee will also include at least one PhD student to ensure that views and needs of students are represented.

**Local experts and active international collaborators data:** A list will be compiled with South African based scientists who have worked on model development, with details of contributions made. The list will also include international experts that have or are working closely with the South African scientists.

**Intercomparison study:** The first five years of the project will focus on two topics identified in a way that allows all participating institutions to contribute to at least one of the topics. The two topics to be considered are 1) Thunderstorms, while the second topic will focus on 2) seasonal rainfall predictability. A list of variables, number of levels, and required format of the model output data which will be submitted for the intercomparison study will be identified, discussed and finalised by the steering committee. The experimental design which will include amongst others, the minimum domain size, the grid spacing, the simulation period as well as a testing framework which will be finalised during the second implementation quarter of the framework. The simulations and observations will be compared against each other as informed by a testing framework that will be developed when the configuration is decided on. Results from the comparison study will be discussed and submitted to an accredited journals.

**Sensitivity studies and model improvements:** In diagnosing sources of errors identified in the inter-comparison study, sensitivity studies will consider different aspects of the model. The sensitivity studies will consider both the dynamics and the physics in the model.

**Working group meetings:** Two working groups, one focusing on the thunderstorms and another will focus on the seasonal rainfall predictability. Each working group will include at least one individual from the organisations that are contributing simulations to the topic. The working groups will meet at least once a quarter to report on progress on an online platform, and in person at least once a year. Meetings can be arranged to take advantage of events such as the CHPC National Meeting, the South African Society for Atmospheric Sciences (SASAS) annual conference and other symposia. The working groups are not organised as informed by different components of the models because the community is still currently spread thinly. Furthermore the

diagnoses of the causes of errors will not make pre-determined decisions on where the models go wrong.

**Postgraduate studies:** Increasing the critical mass that will ensure that South Africa is an independent model developer, requires investment, and postgraduates working in the space. Both the CSIR and SAWS have a research institution status which means they can host PhD students. At Masters level and below, students will not be expected to contribute towards model development by modifying any of the codes that are in use. Students who majored in physics, meteorology, atmospheric science, and applied mathematics have and will be increasingly recruited to address different aspects of model development.

**Postdoctoral fellows:** Postdoctoral fellows will be recruited by the institutions of higher learning and research institutions to work on different aspects of the models, on work that needs to be done on the project. Attention will also be given to the recruitment of internationals who can contribute to the project for a period of two to three years. Such recruits will bring a different perspective and experience from other countries that have experience in the development of models.

**Tutorials and Workshops:** Tutorials and workshops will be organised such that a minimum of one takes place per year. These workshops will be organised as side events as well as independent of national or international conferences. Different institutions will lead the organisation of the workshops in different years, and co-hosting will also be possible depending on what is convenient. SAWS and the Universities have computer labs that can be used for such training, and therefore the majority of the events will be hosted by project partners. At SAWS the training will be conducted in cooperation with World Meteorological Organization (WMO) Regional Training Centre (RTC).

**International Meetings held in South Africa:** The South African model development community will work with the international modelling community to propose to host some international meetings. These include WCRP in general or specific working groups such as WGENE and Pan GASS.

**International Meetings outside South Africa:** The South African scientists will be encouraged to attend international meetings. An email list with South Africans interested in model development will be set-up where international modelling conferences, seasonal schools, or tutorials will be advertised. Where international funding is provided, early career scientists will be encouraged to apply. Where international funding is not provided, national resources will be mobilised. It may be noted that some workshops are streamed to allow remote participation, information on such meetings will be distributed.

### *Conclusions*

Any institution interested in participating in the programme can get in touch with the corresponding author. The programme document is dynamic, other contributions are welcomed.

### *References*

- Abiodun BJ, JM Prusa and WJ Gutowski Jr, 2008a: Implementation of a nonhydrostatic, adaptive-grid dynamics core in CAM3. Part I: Comparison of dynamics cores in aqua-planet simulations. *Climate Dynamics* . **31** ,795-810.
- Beraki AF, DG DeWitt, WA Landman and C Olivier, 2014: Dynamical Seasonal Climate Prediction Using an Ocean-Atmosphere Coupled Climate Model Developed in

Partnership between South Africa and the IRI. *Journal of Climate*, **27**, 1719-1741.

Abiodun BJ, WJ Gutowski Jr and JM Prusa and 2008b: Implementation of a nonhydrostatic, adaptation, adaptive-grid dynamics core in CAM3. Part II: Dynamical Influences on ITCZ behaviour and tropical precipitation. *Climate Dynamics*. **31**, 811-822.

Bopape MM, FA Engelbrecht, DA Randall and WA Landman, 2014: Advances towards the development of a Cloud Resolving Model in South Africa. *South African Journal of Science*, **110**, 9/10, 61-62. <http://dx.doi.org/10.1590/sajs.2014/20130133>

Bopape MM, FA Engelbrecht, DA Randall and WA Landman, 2014: Simulations of an isolated two-dimensional thunderstorm: sensitivity to cloud droplet size and the presence of graupel. *Asia Pacific Journal of Atmospheric Science*, **50(2)**; 139-151, DOI:10.1007/s13143-014-0003-z .

Engelbrecht FA, 2006: Theory and application of quasi-elastic-equations in terrain following coordinates based on the full pressure field. Doctoral thesis. University of Pretoria. Published online. 208 pp.

Engelbrecht FA, JL McGregor and CJdeW Rautenbach, 2007: On the development of a new nonhydrostatic atmospheric model in South Africa. *South African Journal of Science* , **103** , 127-134.

Engelbrecht FA, M Tsugawa and JL Engelbrecht, 2012: Development of a new coupled climate model in South Africa. Recent development and future plans. SASAS 2012: Bridging the Gap. Protea Breakwater Lodge, Water Front, Cape Town, South Africa. 26-27 September. ISBM: 978-0-620-53375-1.

Engelbrecht F.A., Chang N. and Sovara M. (2018). VrESM ocean-atmosphere coupler. CSIR Technology Demonstrator, Level 6.

Landman S, FA Engelbrecht, CJ Engelbrecht, LL Dyson and WA Landman: A short-range weather prediction system for South Africa based on a multi-model approach. *Water SA*, **38**, 5, 765-774.

Randall DA, 1996: A University Perspective on Global Climate Modelling. *Bulletin American Meteorological Society*, **77**, 2685-2690.

Reason CJC, F Engelbrecht, WA Landman, JRE Lutjeharms, S Pickett, H Rautenbach and BC Hewitson, 2006: A review of South African research in atmospheric science and physical oceanography during 2000-2005. *South African Journal of Science*, **102**, 35-45.

## Coastal variability and change in the Benguela Upwelling System: Decadal trend analysis

F. S. Tomety<sup>1,2</sup> M. Rouault<sup>1,2</sup> and S. Illig<sup>1,3</sup>

<sup>1</sup>Department of Oceanography, Ma-Re Institute, University of Cape Town, South Africa.

<sup>2</sup>Nansen-Tutu Center for Marine Environmental Research, University of Cape Town, South Africa

<sup>3</sup>Laboratoire d'Etudes en Géophysique et Océanographie Spatiales; ICMASA; OMP/LEGOS, Toulouse, France

### Abstract

A rigorous analysis of sea surface temperature and surface wind of various datasets over 36 years is used to examine sea surface temperature and wind speed linear trends and decadal variability in the Angola, Benguela and Agulhas currents. Statistically significant warming trends in SST are found off the Angolan coast ( $> 0.35^{\circ}\text{C}$  per decade) and in the Agulhas retroreflection region ( $\sim 0.5^{\circ}\text{C}$  per decade). In Angola, the warming trend is concurrent with a negative trend in local wind speed. Cooling trends in SST are found in the Southern Benguela in most of the SST dataset. Cooling SST trend in the Southern Benguela is more pronounced in the late austral autumn and winter. However, the trend in reanalysed surface wind speed is negative which contradict the SST trends in the Southern Benguela. In summer, the cooling trend in SST is weak in Southern Benguela concurrent with an increase of surface wind speed. In addition, there is a decadal pattern in wind data highly correlated with a decadal pattern in the SST in NCEP2 wind speed and OISST  $1^{\circ}\times 1^{\circ}$  but absent in the other reanalysis.

### Introduction

Sea Surface Temperature is a good indicator of upwelling strength in Eastern Boundary Currents such as the Benguela Current. South-easterly wind lead to upwelling of cold water along the west coast of Southern Africa. The upwelling in the Benguela system is controlled by the anticyclonic wind of the South Atlantic Anticyclone (Veitch et al., 2010). Satellite remote sensing provides estimation of sea surface temperature for most of the ocean since the 1980's and allows to quantify the decadal and interannual variabilities. An apparent paradox associated with global warming is that it might lead to intensified upwelling favorable wind leading to cooling of coastal upwelling such as the Benguela Upwelling System (BUS). Rouault et al. (2010) and Blamey et al. (2015) found that trend in SST for the period 1982-2009 in the Benguela upwelling system using a  $1^{\circ}\times 1^{\circ}$  Optimum Interpolation (OI) Reynolds has a distinct seasonality but there were discrepancies in trends between various SST dataset. They found that some regions have warmed up (North Benguela), some regions have cooled down (South Benguela). Vizy and Cook (2016) explain the warming off Angola and Northern Benguela by a decrease in wind speed due a poleward shift of the south Atlantic anticyclone. Such shift is already mentioned by Jarre et al. (2015). Detecting trend in coastal upwelling remains a challenge due to the proximity of the coast, cloud cover and the unavailability of long enough, homogenous time series of measured data.

### Data and Method

For this study, we calculate the linear trends from 1982 to 2017 of SST and wind speed from various reanalyzed climate and SST datasets and test the statistical significance at the 95% confidence level using Spearman's rank correlation test. For the oceanic dataset, we used monthly Optimum Interpolation SST (OISST), gridded at a  $1^{\circ}\times 1^{\circ}$  resolution (Reynolds et al., 2002); OISST  $1/4^{\circ}\times 1/4^{\circ}$  resolution (Reynolds et al., 2007);  $1^{\circ}\times 1^{\circ}$  Hadley SST (HadISST1 Rayner et al., 2003),  $4\text{km} \times 4\text{km}$  resolution AVHRR

Pathfinder version 5.3. OISST and HadISST1 are blended products combining in-situ and satellites data. Due to the lack of long enough and homogenous time-series of historical wind data from observational measurements, we analyse and compare four global atmospheric reanalysis datasets (winds data at 1000 hpa pressure level) generated by different institutions:  $2.5^{\circ}\times 2.5^{\circ}$  horizontal resolution National Centre for Environmental Prediction Department of Energy Reanalysis 2 (NCEP2) (Kanamitsu et al., 2002),  $0.75^{\circ}\times 0.75^{\circ}$  horizontal resolution Era-Interim (ERA-I)(Dee et al., 2011),  $0.625^{\circ}\times 0.5^{\circ}$  horizontal

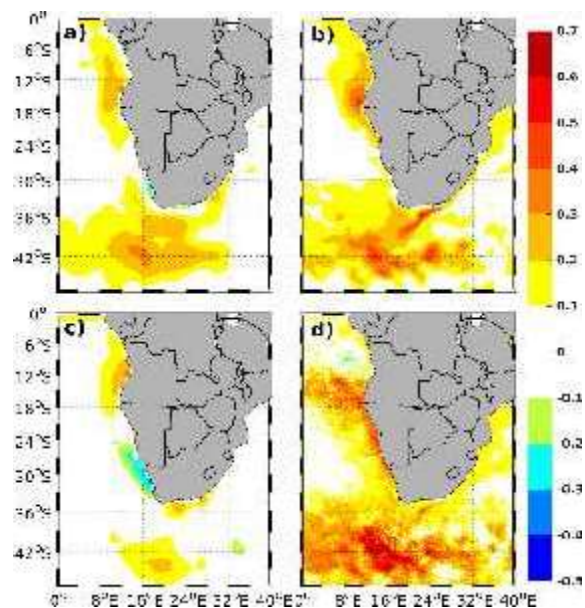


Figure 1: Linear trend in annual mean SST ( $^{\circ}\text{C}$  per decade) for the a) OISST  $1^{\circ}\times 1^{\circ}$ , b) OISST  $1/4^{\circ}\times 1/4^{\circ}$ , c) HadISST and d) AVHRR Pathfinder during the period 1982-2017

resolution Modern Era Retrospective Analysis for Research and Application-2 (MERRA-2) (Molod et al., 2015) and 1.25°x1.25° horizontal resolution Japanese 55-year Reanalysis (JRA-55)(Kobayashi et al., 2015) (Kobayashi et al., 2015). All the wind reanalysis data are monthly and are from 1982 to 2017. The second step of this study is to analyse the correlation between meridional wind and SST at low frequency. For that purpose, we calculate the monthly detrended interannual anomalies and apply a moving average over a 10-year windows. The monthly normalized anomalies are estimated by subtracting the monthly mean climatology for the period 1982 to 2017 from the monthly value and then by divided the result by the standard deviation of that month

*SST trend function of the season*

First, we look at the linear trend in annual mean (Figure 1) and seasonal mean SST (not shown) using the different SST dataset previously cited. Figure 1 shows a statistical-significant warming trend centered on the Angola Benguela front (10°S-24°S) and in the Agulhas Current and Agulhas retroflection region in all dataset. A statistical-significant cooling trend is observed in the south Benguela in most of dataset. Differences in SST trends occur among the dataset especially along the coast. A cooling trend is observed in the entire Benguela upwelling system using Hadley SST dataset while a warming trend is observed with Pathfinder AVHRR dataset (Figure 1c and 1d). The cooling trend is only observed in the south of the Benguela with OISST 1°x1° and OISST 1/4°x 1/4°. Cooling or warming trends and their magnitude are seasonally dependent. The cooling trend is more pronounced mainly in the late austral autumn and winter (not shown). Weak trends exist in austral summer which is the upwelling season. The datasets have all a warming trend over the Angola Benguela Front and the Agulhas retroflection region. Discrepancies among the datasets mainly occur in the South African region. By constructing a time series of annual means of SSTs for the four datasets at different location in the BUS, St Helena Bay (~32°S, 18°E), we find that the HadISST1 and OISST 1° x 1° start with a warmer state than the other which could explain the difference in cooling trend observed in BUS between datasets.

*Wind speed trends as a function of season*

Because the upwelling in the Benguela system is controlled by the south-easterly wind (Veitch et al., 2010), cooling or warming trend should be triggered by increase or decrease of the south-easterly wind respectively. We thus analyze and compare the linear annual and seasonal wind speed trend of the four-reanalysis atmospheric dataset previously cited. Figure 2 illustrates the wind speed trends over the period 1982-2017 of NCEP2. The results estimated for the Era-Interim, JRA-55 and MERRA-2 lead to similar conclusion to those described by NCEP2 (not shown). However, the magnitude in trend in the Era-Interim is less than the other datasets. There are also slight differences among the datasets along the coast. Generally, the wind speed trends in all datasets show a strong seasonal variability. Positive trends, up to 0.7 m/s per decade, are observed in the open ocean and along the Namibian and South African west coast. These positive trends along the coasts are more pronounced in austral summer (November - January) when the center of South Atlantic Anticyclone High is farthest

poleward and in the center of the basins (Sun et al., 2017). This enhances the intensity of south easterly winds. The trend is weak and not significant in winter (May - July) while the trend in SST shows a pronounced cooling in that area, which is an inconsistency according to Ekman dynamics. Therefore, it is difficult to conclude that the intensification of south-easterly wind due to the shift of South Atlantic Anticyclone High enhances the upwelling in the Benguela system as suggested in some previous studies (Narayan et al., 2010; Santos et al., 2012). In the open ocean the positive trends are more pronounced in austral winter and earlier spring. A Negative trend in wind speed, up to -0.6 m/s per decade, is observed in the Agulhas region (36°S - 46°S) and along the Angolan coast. The negative trends observed along the Angola coast is more pronounced at the end of winter and early spring in most of datasets when the centre of South Atlantic Anticyclone High is either close to the equator and on the western side of the South Atlantic basin (Sun et al., 2017). As consequence, the decreasing in wind speed off the Angolan coast would reduce evaporation (latent heat flux) in the area. That could explain the warming trend observed in SST along the Angola coast.

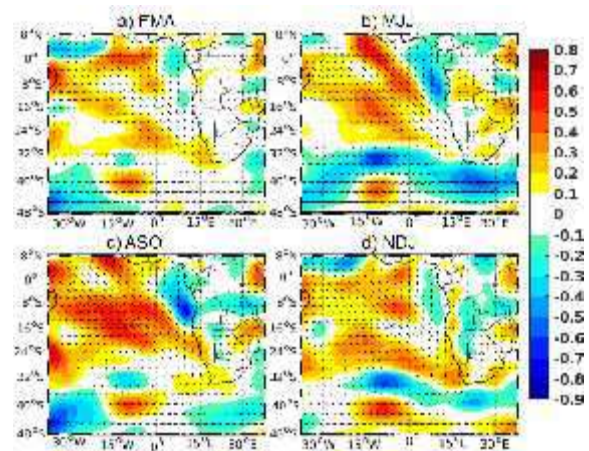


Figure 2: Seasonal linear trend of NCEP2 at 1000hpa wind speed (m/s per decade) over the period 1982-2017 superimposed with the climatological mean direction

*Correlation in meridional wind and SST at low frequency*

To improve our understanding of the link between local wind and SST at the decadal scale in the Benguela system, we present in Figure 3 the monthly normalized detrended interannual anomalies (blue and red line) and moving average over a ten year windows (black and green dotted line) in the meridional wind and SST in four domains: Angola Benguela front, North Benguela, Centre Benguela and South Benguela using monthly OI SST 1° x 1° and NCEP2 wind data. From 1982 to 1988 and from 2009 to 2017, weaker than normal southerly wind occurred in Angola Benguela Front, north Benguela and Centre Benguela whereas from 1989 to 2008, stronger than average southerly wind is observed (Figure 3 blue line). In that respect NCEP2 meridional wind appear to present decadal pattern in the Benguela system except in the south Benguela. The SST, primarily, doesn't show this

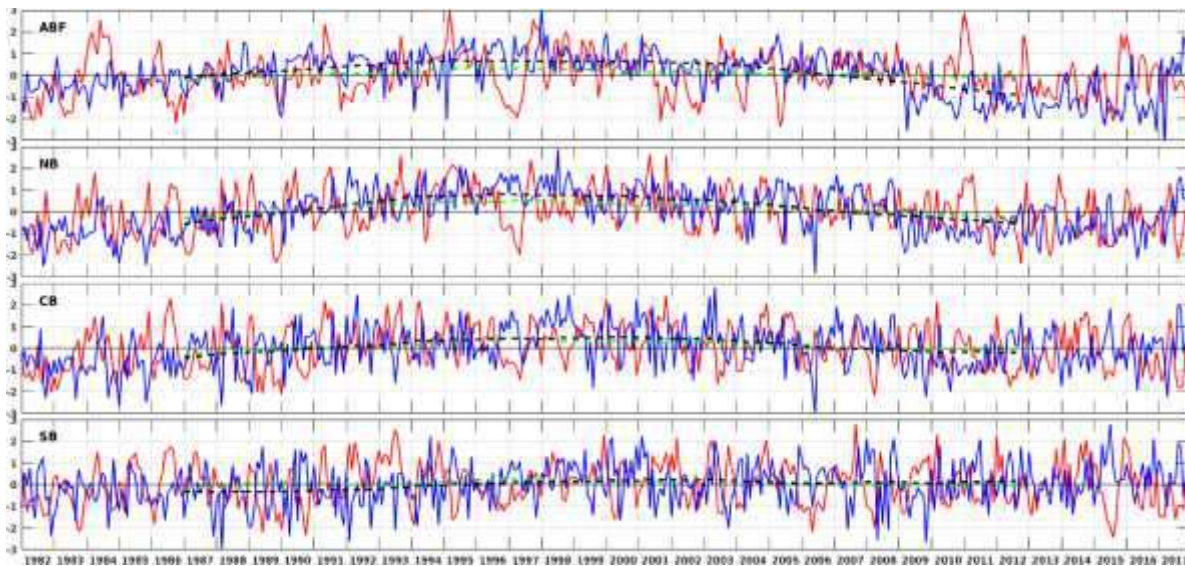


Figure 3. Time-series of detrended normalized interannual anomalies of meridional wind (blue line), of the SST (red line); moving average over 10 year windows SST green dot line and meridional wind black dot line From top to bottom Angola Benguela Front (ABF), North Benguela(NB), Centre Benguela(CB) and South Benguela(SB); each domain is a box of 4° latitude by 1° off the coast in longitudinal direction for SST and 4° latitude by 2.5° off the coast in longitudinal direction except centre Benguela which is box of 2° latitude. Each domain is centred at 16.5°S, 22.5°S, 27.5°S and 32.5°S respectively for ABF, NB, SB decadal pattern by observing the normalized detrended SST anomalies at monthly scale (Figure 3 red line) but observing the moving average over the 10-year windows (Figure 3 green dotted line), the SST data appear also to present a decadal pattern highly correlated by a decadal pattern in meridional wind. Correlations between SST and meridional wind detrend normalized anomaly at decadal scale (10 year moving average) exceeds 0.8 and with statistically significant at 99% in all domain except the South Benguela where the correlation is 0.7 but still statistically significant at 99%.

### Conclusion

The trends observed both in SST and wind speed show a strong spatial and seasonal variability. The weakening of wind speed along the Angola would reduce evaporation (latent heat flux) and weaken the Ekman transport in the area, which in turn could explain the increase in SST in coastal fringe. Our results presented here suggested that the SST in South Benguela is influenced by the variability of the wind, but the seasonal cooling trend observed in SST is not explain by the positive trend depicted in wind speed. Finally, we highlighted in our study a decadal pattern in wind data highly correlated with a decadal pattern in the SST using NCEP2 and OISST 1°x1° products.

### Acknowledgments

The authors acknowledge funding support from Chair-, and Nansen-Tutu center. We also gratefully acknowledge the Climate Prediction from NOAA, the Japan Meteorological Agency and the GES DISC for the dissemination of respectively NCEP2, JRA-55 and MERRA-2. Era -interim data used in this study have been obtained from the ECMWF data server

### Reference

Blamey, L.K., et al., 2015. Ecosystem change in the southern Benguela and the underlying processes. *Journal of Marine Systems* 144, 9-29.  
 Dee, D.P., et al., 2011. The ERA-Interim reanalysis: configuration and performance of the data assimilation system. *Quarterly Journal of the Royal Meteorological Society* 137, 553-597.  
 Jarre, A., et al., 2015. Synthesis: climate effects on biodiversity,

abundance and distribution of marine organisms in the Benguela. *Fisheries Oceanography* 24, 122-149.  
 Kanamitsu, M., et al., 2002. NCEP-DOE AMIP-II Reanalysis (R-2). *Bulletin of the American Meteorological Society* 83, 1631-1644.  
 Kobayashi, S., et al., 2015. The JRA-55 reanalysis: General specifications and basic characteristics. *Journal of the Meteorological Society of Japan. Ser. II* 93, 5-48.  
 Molod, A., et al., 2015. Development of the GEOS-5 atmospheric general circulation model: evolution from MERRA to MERRA2. *Geoscientific Model Development* 8, 1339-1356.  
 Narayan, N., et al., 2010. Trends in coastal upwelling intensity during the late 20th century. *Ocean Science* 6, 815-823.  
 Rayner, N., et al., 2003. Global analyses of sea surface temperature, sea ice, and night marine air temperature since the late nineteenth century. *Journal of Geophysical Research: Atmospheres* 108, 4407.  
 Reynolds, R.W., et al., 2002. An improved in situ and satellite SST analysis for climate. *Journal of climate* 15, 1609-1625.  
 Reynolds, R.W., et al., 2007. Daily high-resolution-blended analyses for sea surface temperature. *Journal of Climate* 20, 5473-5496.  
 Rouault, M., et al., 2010. Coastal oceanic climate change and variability from 1982 to 2009 around South Africa. *African Journal of Marine Science* 32, 237-246.  
 Santos, F., et al., 2012. Differences in coastal and oceanic SST trends due to the strengthening of coastal upwelling along the Benguela current system. *Continental Shelf Research* 34, 79-86.  
 Sun, X., et al., 2017. The South Atlantic subtropical high: climatology and interannual variability. *Journal of Climate* 30, 3279-3296.

- Veitch, J., et al., 2010. Modeling equilibrium dynamics of the Benguela Current System. *Journal of Physical Oceanography* 40, 1942-1964.
- Vizy, E.K., Cook, K.H., 2016. Understanding long-term (1982–2013) multi-decadal change in the equatorial and subtropical South Atlantic climate. *Climate Dynamics* 46, 2087-2113.

## Impact of the Agulhas Current on coastal South African precipitation

Arielle Stela Nkwinkwa Njouodo<sup>1,2</sup>, Shunya Koseki<sup>3</sup>, Noel Keenlyside<sup>3,4</sup>, Mathieu Rouault<sup>1,2</sup>

<sup>1</sup>Department of Oceanography, MARE Institute, University of Cape Town, South Africa

<sup>2</sup>Nansen-Tutu Centre for Marine Environmental Research, University of Cape Town, South Africa

<sup>3</sup>Geophysical Institute, University of Bergen/Bjerknes Centre for Climate Research, Norway

<sup>4</sup>Nansen Environmental and Remote Sensing Center, Bjerknes Centre for Climate Research, Norway

**Corresponding author:** Arielle Stela Nkwinkwa Njouodo ([a.nkwinkwa@yahoo.fr](mailto:a.nkwinkwa@yahoo.fr))

### Abstract

The influence of the Agulhas Current on the weather and climate of South Africa is not well known. Here, using state of the art datasets, and a regional atmospheric model, we show that the Agulhas Current is a driver of a band of rainfall along the east coast and above it. The Agulhas current's warm core causes sharp gradients in sea surface temperature and sea level pressure, that drive a convergence of low-level winds, resulting in a co-located narrow band of precipitation. These features are similar to those in the Gulf Stream. Moreover, model experiments indicate that the Agulhas Current mostly impacts convective rainfall. This study is a contribution that enhances our understanding of the effect the Agulhas current has on South African rainfall.

**Keywords:** Agulhas Current, Rainfall, Wind convergence, SLP, South Africa

### Introduction

The Agulhas Current is the strongest western boundary current of the Southern Hemisphere. As the Gulf Stream and the Kuroshio, the Agulhas Current is warmer than the surrounding ocean, leading to high sensible and latent heat fluxes (Rouault *et al.* 2003). Several mechanisms explaining the role of the Gulf Stream and the Kuroshio on precipitation are proposed (Minobe *et al.* 2008; Parfitt *et al.* 2016; Sasaki *et al.* 2012). However, the influence of the Agulhas Current on Southern Africa weather and climate is not well known. Radiosonde and heat fluxes measurements above the Agulhas Current show that the vigorous exchange of moisture and energy above the current penetrates into the troposphere to at least 1500 m (Rouault *et al.* 2000). This phenomenon causes distinct cloud lines above the Agulhas Current during fair weather high-pressure synoptic conditions (Rouault *et al.* 2000). The diurnal cycle of rainfall (Rouault *et al.*, 2013) along the eastern coast of South Africa was related to the proximity of the Agulhas Current. Regional impacts of the Agulhas Current on climate have not been thoroughly investigated using numerical models, although the climatic impact of the greater Agulhas Current system was studied using a coarse resolution model (Reason, 2001). The purpose of this study is to understand using observations, reanalysis, and a regional atmospheric model how the warm SST associated with the Agulhas Current affects the low-level atmosphere and rainfall off and over the east coast of South Africa.

### Data

We use the monthly outputs of the Climate Forecast System Reanalysis (CFSR, Saha *et al.* 2012) provided by NCEP (National Centers for Environmental Prediction),

from 2001 to 2005. CFSR is a global coupled atmosphere–ocean–land–sea-ice system, on a horizontal grid of 0.5° x 0.5°. We also use the 0.25° x 0.25° resolution GlobCurrent surface geostrophic current (Johanessen *et al.* 2015), derived from altimetry for the representation of the Agulhas Current. We use the 0.05° by 0.05° climatology of Tropical Rainfall Measuring Mission Precipitation Radar (TRMM PR, Biasutti *et al.* 2012) for precipitation from 1998 to 2007. The regional atmospheric model we use is the Weather Research and Forecasting model (WRF, Skamarock and Kepler 2008). This model is applied to investigate the impact of the core of the Agulhas Current on the atmosphere. We did 2 sensitivity runs: the control experiment (CTL) and the experiment where the SST had been smoothed, with the same settings as CTL. The SST is smoothed by a spatial filter based on 9-neighbour grid method. The result at each grid point is a weighted average of the grid point plus the 8 surrounding points. The model domain is 17–43°S and 8–52°E, and the spatial resolution is 25 km x 25 km with 56 vertical eta-coordinate levels. The simulations extend from 2001 to 2005.

### Diagnostic analysis of pressure adjustment mechanism

With the objective of understanding how rainfall is formed above the Agulhas Current, the relationship between the near surface wind convergence and SLP Laplacian is investigated by using a simple Marine Atmospheric Boundary Layer (MABL) model (Minobe *et al.* 2008),

$$\begin{cases} \varepsilon u - f v = -p_x / \rho_0 \\ \varepsilon v + f u = -p_y / \rho_0 \end{cases}$$

where  $x$  and  $y$  are the zonal and meridional coordinates,  $u$  and  $v$  are the surface wind velocities, frictional stress from above the MABL are neglected here.  $\rho_0$  is the MABL density and  $p$  is the pressure in the MABL.  $\varepsilon$  denotes the constant damping coefficient, and  $f$  represents the Coriolis parameter. Surface wind convergence is linked to SLP Laplacian by a linear relationship,

$-\rho_0(u_x + v_y) = (p_{xx} + p_{yy})\varepsilon/(\varepsilon^2 + f^2)$ , SLP and underlying SST are also connected linearly according to  $\varepsilon p + H(u_x + v_y) = -\gamma T$ , where  $T$  is the SST,  $\gamma$  is a constant, and  $H$  is the equivalent depth of the MABL. As seen by applying two quantities to isolate the strength of this relation at the finer scale of the Agulhas warm core.

Results

The analysis of the annual climatology of CFSR and WRF model reveal a clear relation between the Agulhas Current and precipitation (Fig. 1). The Agulhas Current is around 100 km wide and runs south-westward along the eastern coast of South Africa, following roughly the continental shelf until it retroflects and flows westward (Fig. 1a). Here, we focus on the core of the current, which is a few degrees warmer than the surrounding ocean (contours Fig. 1), and its coastal part (where the current hugs the coast). TRMM PR and CFSR reanalysis show a narrow band of precipitation along the eastern coast of South Africa, just over the core of the Agulhas Current (Fig. 1c, d). In the Agulhas region, annual precipitation average varies from 3 to 4 mm/day for TRMM PR, while a few degrees to the east it is about 1 mm/day less. CFSR has a good representation of the rain band, especially near the coast to the east, although it differs from TRMM PR by 1 to 2 mm/day. The local evaporation exceeds rainfall by between 2 to 5 mm/day over the entire region, with the greatest excess over the Agulhas Current (Fig. 1b). Thus, local moisture supply is consistent with the broad scale rainfall over the region, as well as the enhanced rainfall over the Agulhas. However, moisture alone does not lead to rainfall. Air masses must be lifted to saturation by low-level wind convergence, atmospheric convective processes, or by frontal processes. This mechanism may explain rainfall patterns over the Agulhas Return Current, where the current and the southern hemisphere storm track align. Recent studies suggest that the low-level convergence and associated rainband over the Gulf Stream is the result of the interaction of synoptic-scale atmospheric variability with the sharp SST front (O'Neill et al. 2017; Parfitt et al. 2016; Sheldon et al. 2017).

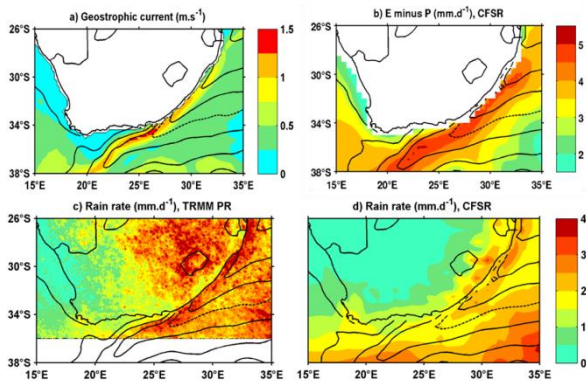


Fig. 1: Annual climatology of: a) GlobCurrent surface geostrophic current, b) CFSR evaporation minus precipitation (E-P), and rain rate of c) TRMM PR, d) CFSR. Solid contours represent annual climatology of OI SST and CFSR SST respectively for a),c) and b),d) with 1° interval, the dash line is 22°C SST.

Fourier decomposition, the last equation implies surface pressure is proportional to surface temperature. Here, we compare the Laplacian of these

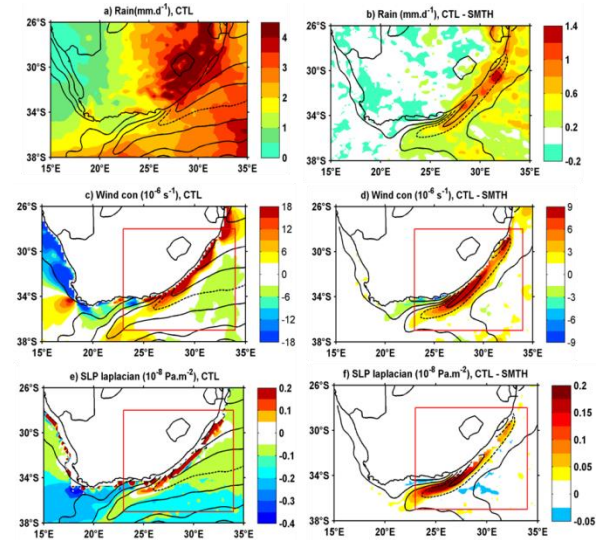
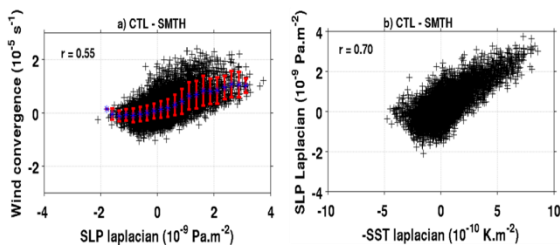


Fig. 2: Annual climatology of: a) rainfall, c) wind convergence, e) SLP Laplacian simulated by CTL with the SST contours of CTL overlaid, differences between CTL and SMTH of the corresponding variables in the right panels (b,d,f); the contours show the SST difference between CTL and SMTH (0.5°C interval and dashed line for 1°C).

We compare the annual climatology of SST Laplacian, wind convergence and SLP Laplacian for CFSR (not shown), and the difference between our 2 WRF experiments. A tight relation among these quantities indicates that warmer (colder) SST drives lower (higher) SLP, and in turn enhances surface wind convergence (divergence). The Laplacian acts as a spatial high-pass filter that highlights sharp gradient.

We perform the regional model experiments to isolate the role of the Agulhas warm core on the atmosphere. The regional model driven with observed SST (CTL) reproduces the rain band along the Agulhas Current realistically (Fig. 2a). In CTL, the Agulhas Current precipitation rate varies between 2 and 4 mm/day and is similar to the TRMM PR observations (Fig. 1c), but is 2 mm/day more than CFSR (Fig. 1d). Over land the simulated annual precipitation is stronger than the observations and reanalysis. This may be due to a strong sensitivity of cumulus convection schemes to the topography, a common issue with this regional model (Pohl et al. 2014).

The rain band along the South Africa coast adjacent to the Agulhas Current is strongly reduced in the experiment with smoothed SST (SMTH) compared to CTL (Fig. 2b). The difference is up to 1.4 mm/day with a maximum offshore Kwazulu-Natal (around 30.5°S; 31.5°E). The coastal rainfall in SMTH is around 40% less than in CTL. The coastal rain band is mostly due to convective precipitation: rainfall due to large-scale circulation is almost identical between the two simulations (Not shown), while the coastal convective precipitation is highly diminished in SMTH. Thus, the experiments show that the warmer Agulhas Current SST enhances precipitation along the eastern coast of South Africa.



**Fig. 3:** a) Relationship between wind convergence and SLP Laplacian and b) between SLP Laplacian and sign reversed SST Laplacian for monthly climatology differences between CTL and SMTH from 23 to 34°S, and from 28 to 37°E (red boxes of Fig. 2).

The wind convergence and the positive SLP Laplacian over the Agulhas Current are well simulated (Fig 2c, e). The difference of wind convergence between CTL and SMTH shows a well-defined maximum over the Agulhas Current (Fig. 2d) collocated with the corresponding difference of SLP Laplacian (Fig. 2f). The spatial correlation between the SLP Laplacian and wind convergence from the difference of the experiments is 0.55 (Fig. 3a), which is similar to the value from CFSR reanalysis (not shown). The spatial correlation between SLP Laplacian and the negative SST Laplacian from the difference of the experiments is 0.70 (Fig. 3b) (also similar to that from CFSR). These results provide strong support for the pressure adjustment in anchoring the rain band over the Agulhas. Moreover, the regional model experiments show that the Agulhas Current drives the local overturning circulation. In CTL, the vertical motion at lower levels (up to 800 hPa) occurs closer to the coast than in the reanalysis, and there is a broader band of subsidence to the east of the upward motion (Not shown). Around the same levels, patterns of the horizontal divergence are present. There is hardly any indication of upward motion at 650 hPa. The difference between CTL and SMTH confirms that SST associated with the Agulhas Current drives this vertical circulation, which is associated with the rain band along the southern African coast (Fig. 4a,b).

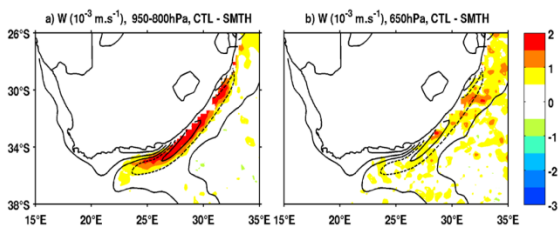


**Fig. 4:** Difference between CTL and SMTH of the annual mean vertical velocity a) vertically averaged between 950 and 800 hPa, b) at 650 hPa, with the SST contours overlaid.

#### Discussion and conclusions

We have shown that the warm core of the Agulhas Current drives a band of coastal precipitation off the east coast of South Africa. We found that spatially smoothing the SST leads to a decrease of 50% for wind convergence, of 100% for SLP Laplacian, and a 40% reduction in coastal convective precipitation close to the core of the Agulhas Current. Correlations among wind convergence, SLP and SST indicate that these features show high degree of similarity to those in the Gulf Stream. Model experiments further indicate that the Agulhas Current mostly impacts convective rainfall. Finally, it is important to resolve the fine structure of ocean temperature for simulating the climate of the region. This has

implications for the prediction of South African weather and climate, and for understanding past and present climate.

#### Acknowledgments

This work has been performed with the support of the SCAMPI project (234205/H30) funded by the Research Council of Norway under the SANCOOP program. Computing resources were provided by NoTur (nn9039k and ns9039k). The authors thank the NRF SARCHI chair of Ocean Land Atmosphere modeling, ACCESS, NRF, DST, DAAD-AIMS, and the Nansen Tutu Center for their support. The data on which this study is based are publicly available at the following links: <https://rda.ucar.edu/>, <http://www.globcurrent.org> and <http://kage.ldeo.columbia.edu:81/>,

#### Reference

1. Biasutti, M., Yuter, S. E., Burleyson, C. D., & Sobel, A. H. Very high resolution rainfall patterns measured by TRMM precipitation radar: seasonal and diurnal cycles. *Climate dynamics*, 39(1-2), 239-258 (2012).
2. Johannessen, J. A., B. Chapron, F. Collard, M. H. Rio, J. F. Piollé, G. Quartly, J. Shutler, R. Escola, C. Donlon, R. Danielson, A. Korosov, R. P. Raj, V. Kudryavtsev, M. Roca, J. Tournadre, G. Larnicol, S. Labroue, P. Miller, F. Nencioli, M. Warren and M. Hansen GlobCurrent: Sentinel-3 Synergy in Action. In ESA Special Publication (Vol. 734, p. 2) (2015).
3. Jury, M. R., Valentine, H. R., & Lutjeharms, J. R. Influence of the Agulhas Current on summer rainfall along the southeast coast of South Africa. *Journal of Applied Meteorology*, 32(7), 1282-1287 (1993).
4. Minobe, S., Kuwano-Yoshida, A., Komori, N., Xie, S. P., & Small, R. J. Influence of the Gulf Stream on the troposphere. *Nature*, 452(7184), 206-209 (2008).
5. Parfitt, R., & Czaja, A. (2016). On the contribution of synoptic transients to the mean atmospheric state in the Gulf Stream region. *Quarterly Journal of the Royal Meteorological Society*, 142(696), 1554–1561. <https://doi.org/10.1002/qj.2689>
6. Pohl, B., Rouault, M., & Roy, S. S. (2014). Simulation of the annual and diurnal cycles of rainfall over South Africa by a regional climate model. *Climate Dynamics*, 43(7–8), 2207–2226. <https://doi.org/10.1007/s00382-013-2046-8>
7. Reason, C. J. C. Evidence for the influence of the Agulhas Current on regional atmospheric circulation patterns. *Journal of Climate*, 14(12), 2769-2778 (2001).
8. Rouault, M., Lee-Thorp, A. M., & Lutjeharms, J. R. E. The atmospheric boundary layer above the Agulhas Current during alongcurrent winds. *Journal of physical oceanography*, 30(1), 40-50 (2000).
9. Rouault, M., & Lutjeharms, J. R. E. Air–sea exchange over an Agulhas eddy at the subtropical convergence. *Global Atmos. Ocean Syst*, 7, 125-150 (2000).
10. Rouault, M., Roy, S. S., & Balling, R. C. The diurnal cycle of rainfall in South Africa in the austral summer. *International Journal of Climatology*, 33(3), 770-777 (2013).
11. Rouault, M., White, S. A., Reason, C. J. C., Lutjeharms, J. R. E., & Jobard, I. Ocean–atmosphere interaction in the Agulhas Current region and a South African extreme weather event. *Weather and Forecasting*, 17(4), 655-669 (2002).

12. Rouault, M., Reason, C. J. C., Lutjeharms, J. R. E., & Beljaars, A. C. M. Underestimation of latent and sensible heat fluxes above the Agulhas Current in NCEP and ECMWF analyses. *Journal of Climate*, 16(4), 776-782 (2003).
13. Saha, S., Moorthi, S., Pan, H. L., Wu, X., Wang, J., Nadiga, S., et al. (2010). The NCEP Climate Forecast System Reanalysis. *Bulletin of the American Meteorological Society*, 91(8), 1015–1058. <https://doi.org/10.1175/2010BAMS3001.1>
14. Sasaki, Y. N., Minobe, S., Asai, T., & Inatsu, M. (2012). Influence of the Kuroshio in the East China Sea on the early summer (baiu) rain. *Journal of Climate*, 25(19), 6627–6645. <https://doi.org/10.1175/JCLI-D-11-00727.1>
15. Skamarock, W. C., and Klemp, J. B. (2008). A time-split nonhydrostatic atmospheric model for Weather Research and Forecasting applications. *Journal of Computational Physics*, 227(7), 3465–3485. <https://doi.org/10.1016/j.jcp.2007.01.037>

## ***Central Africa Low: identification, annual cycle and its influence on regional climate and water vapor transport over Central Africa***

Georges-Noel T. Longandjo<sup>1,2</sup> and Mathieu Rouault<sup>1,2</sup>

<sup>1</sup>Oceanography Department, University of Cape Town;

<sup>2</sup>Nansen Tutu Center for Environmental Marine Research, University of Cape Town, Rondebosch 7701, South Africa

### ***Abstract***

This study aims to characterize the low-pressure system over central Africa and to explore what is its possible impact on the regional climate and the water vapor transport over central Africa. The results highlight, over the central African landmass, the existence in the mid-lower troposphere, between 1000 and 500 hPa, of a dominant cyclonic and quasi-permanent circulation pattern that drives the atmospheric large-scale circulation and its associated water vapor transports, namely the Central Africa Low from October to April. The Central Africa Low variation is strongly modulated by El Niño Southern Oscillation (ENSO) so that its influence on regional climate is reminiscent of the impact of La Nina-like atmospheric conditions, with high rainfall over Southern Africa and West Africa and drought conditions over East Africa. Nevertheless, when the Central Africa Low prevails, Central Africa is a sink of water vapor, with the Indian Ocean as the main supplier. In May to September, the weakening of the Central Africa Low is associated with the reversal of the water vapour transport at the northern boundary channel, leading central Africa to become a source of moisture. During this season, both surrounding oceans are suppliers of moisture, with some additional contribution from the Congo basin rainforest.

Keywords: Central Africa; Central Africa Low; ENSO; Southern Africa; Water vapour transport

### ***Introduction***

Few papers (Dezfuli et al. 2015 and Dezfuli 2017) highlighted some characteristics of a low-pressure system over equatorial region of central Africa from December to March. But the seasonal evolution and variability of the low-pressure system over central Africa ( $07^{\circ}$ - $33^{\circ}$ E;  $10^{\circ}$ N- $15^{\circ}$ S) as well as its influence on the neighboring regions of central Africa are not well documented yet. The main motivation of this study is limited to assess these two-fold issues:

- (a) How to characterize the Central Africa low-pressure, to determine its seasonal evolution, location and intensity
- (b) To diagnose how the central Africa Low modulates rainfall, adjoining SST and their associated moisture transports

### ***Data***

We use atmospheric variables from the European Centre for Medium-Range Weather Forecasts (ECMWF) ERA-Interim reanalysis ( $0.75^{\circ}$  grid, Dee et al., 2011) spanning the 37-year period from 1979 to 2015 to characterize the Central Africa

Low. The geopotential height, specific humidity, zonal and meridional wind components at monthly time steps are selected. For rainfall and sea surface temperature (SST), we use the average of the satellite/rain-gauge estimates of the Global Precipitation Climatology Project (GPCP) monthly precipitation data set (Adler et al., 2003), the Climate Prediction Center Merged Analysis of Precipitation (CMAP, Xie and Arkin, 1997), the NOAA optimum interpolated (OI) SST version 2.2 (Reynolds et al., 2002) and Extended Reconstructed Sea Surface Temperature version 3b (ERSST, Smith et al. 2008).

### ***Results***

#### **1. Identification and seasonal evolution of the Central Africa Low**

We first analyze the seasonal evolution of the vertically mean (between 1000- and 500- hPa) of the geopotential height area-averaged over the large Central Africa domain ( $20^{\circ}$ W –  $60^{\circ}$ E;  $25^{\circ}$ S –  $20^{\circ}$ N) to highlight the formation and development of the Central Africa Low. The low-pressure

system over central Africa that is less than the 2580- (geopotential) thickness (gpm) value will be referred as Central Africa Low. Fig. 1 shows the seasonal evolution of Central Africa Low 2580- gpm isoline (red contour) over central Africa and its surrounding regions. We find out that the Central Africa Low 2580- gpm isoline encompasses the entire central Africa region from October to April (ONDJFMA) and defines a prominent cyclonic system over central Africa (Fig. 1). During this season, the rainfall associated with this low-pressure system represents around 70% of total rainfall over Central Africa (Fig. 1). Nevertheless, from October to April, the Central Africa Low 2580- gpm isoline is surrounded by regions that experience relatively high tropospheric pressure (Fig. 1). This means that the atmospheric circulation, over the central African troposphere (above 850- hPa), is essentially north-easterly in the northern Hemisphere and south-easterly in southern Hemisphere (Fig.

1), indicative of barotropic circulation, except over Atlantic coast (07-15°E) at low levels (from surface up to 850- hPa), where the Central Africa Low is associated with weak wind (Fig. 1). In May to September (MJJAS), the Central Africa Low 2580- gpm isoline jumps further to the northeast and emerges over the Arabian Sea (Fig. 1). This leads to the surge of a relative high geopotential thickness over central Africa, suggestive of a relative higher pressure system (subsidence) than during the previous season (from October to April). This northward displacement of the 2580-gpm isoline is associated with the meridional displacement of rainfall and the reversal of the circulation at lower and middle troposphere over East Africa and the Horn of Africa (Fig. 1). This subsidence over Central Africa due to the weakening of Central Africa Low is likely to suppress local convection and lead to less rainfall.

2. Central Africa Low interannual variability: influence on regional climate and water vapour transport over Central Africa

### 2.1. Water vapor transport channels over central Africa

To understand any potential role the Central Africa Low might play to influence the progression of water vapour transport, an insight of the inflows and outflows of water vapour over central Africa and the Congo basin (black and red boxes, in Fig. 2) are plotted in Fig. 2. The water vapour transport defined as the vertically integrated moisture transport (flux,  $Q$ ) is computed as in Trenberth et al. (2005):

$$Q_u = - \langle qu \rangle \quad (1)$$

$$Q_v = - \langle qv \rangle \quad (2)$$

with  $u$  and  $v$ , the zonal and meridional component of the horizontal wind;  $q$  the specific humidity; and the angle bracket  $\langle \rangle$  is the mass-weighted vertically integration.

In October to April, owed by the presence of the Central Africa Low, the spatial pattern of water vapour transport into Central Africa is largely carried by the dominant mid-lower easterly wind, namely African Easterly jets (AEJs, Fig. 2g). The visual analysis of water vapour transports over central Africa lead us to determine three incoming channels: the southern, eastern and northern boundaries and one export channel: the western boundary (Fig. 2g). The characteristics of moisture transport over central Africa demonstrate two dominant channels at the eastern and northern boundaries, and a weaker incoming channel at the southern boundary (Fig.2j) whereas over Congo basin region (red box), there are two incoming channels at its northern and eastern boundaries and two outgoing channels at its western and southern boundaries. The total moisture transport shows that Central Africa is a sink of water vapour, originating predominantly from the Indian Ocean (Figs. 2g; j). Nonetheless, the reduction in total water vapour flux values of about 22% over Congo basin (Fig. 2j) is indicative of increased rainfall over this region (Fig. 2d). At low levels, despite central Africa being a sinking region of water vapour, the Congo basin seems to be a small source of water vapour due probably to the weakness of the horizontal wind components over the Congo basin rainforest, owed by the quasi-permanent presence of Central Africa Low. This

suggests that the water vapour provided by Congo basin rainforest play a local role via recirculation (Pokam et al. 2012).

In May – September, the weakening of Central Africa Low – associated with the jump of the 2580- gpm isoline over Arabian Sea – reverses the water vapour flow at the northern water vapour transport channel of central Africa (Figs. 2b; h). Hence, Central Africa has two incoming channels, the eastern channel and the southern channel and two outgoing channels, the northern channel and the western channel (Fig. 2h). The reversal of the northern water vapour transport channel is associated with northward migration of high rainfall over central Africa (Fig. 1), with a strong increase of the low-level water vapour flux at the northern branch of the Congo basin area. Nevertheless, the low-level moisture flux contribution to the total tropospheric moisture flux values over central Africa ranges from ~50% for the eastern water vapour transport channel to 75.1% for the northern water vapour transport channel. At the same time, over the Congo basin, the low-level moisture transport contributions to the total moisture transport are lower than 45% on all moisture transport channels, except on the northern channel. This substantiate why the outgoing flow turn the Congo basin into a source of moisture transporting it out towards East Africa and Great Horn of Africa. This finding suggests a crucial role played by this low-level moisture transport at the northern channel to modulate the total moisture flux variability and to affect its associated rainfall in this season. Total tropospheric moisture flux over central Africa indicates that central Africa is a source of moisture (Fig. 2k), even though at low levels, central Africa is a sink of moisture (Fig. 2e). This result provides an interesting insight on how the water vapour is likely to be advected out of central Africa towards East Africa and Great Horn of Africa, consistent with Anyah and Semazzi (2006). However, the weakness of low-level water vapour inflow from Atlantic Ocean is likely to lead to water vapour being rained out over Central Africa rather than to be transported to Sudan and

Ethiopia, inconsistent with Viste et al. (2013). So, we infer that it is the Congo basin rainforest water vapour that is transported out of central Africa. Thus, during this season (MJJAS), both Atlantic and Indians Oceans are the main contributors of water vapour over Central Africa, with Congo basin rainforest as an additional source.

## 2.2. Rainfall and sea surface temperature

In this section, we use the normalized mid-lower thickness index as a metric to describe the intensity of the interannual variability of the Central Africa Low to examine the change on regional climate associated with the Central Africa Low. To do so, we consider rainfall and SST variables as the main representative of the climate. The Central Africa Low index is extracted at the core of Central Africa Low ( $15^{\circ}$ - $30^{\circ}$ E;  $5^{\circ}$ N- $5^{\circ}$ S, red box in Fig. 2) and detrended as we are only interested by the interannual variability. We selected all years with a value greater than 0.5 standard deviation or less than -0.5 standard deviation. The Central Africa Low is positive (CAL > 0.5) during 13 years (1983, 1987, 1988, 1990, 1991, 1992, 1995, 1998, 2002, 2003, 2007, 2010 and 2015) and Central Africa Low experienced negative phase (CAL < -0.5) for 12 years (1982, 1984, 1985, 1986, 1989, 1996, 2000, 2006, 2008, 2009, 2011 and 2012). The composite of the Central Africa Low as identified by the 2580- gpm isoline during the positive (passive) and the negative (active) phases of rainfall and SST is not shown. However, during the active phase (CAL < -0.5), the Central Africa Low 2580-gpm isoline is well developed over all the tropical Africa area and its adjoining Oceans, indicative of deep convection (not shown). Meanwhile, the Central Africa Low climatology indicates that strong convection is mainly located over central Africa landmass. On the other hand, during passive phase, the Central Africa Low 2580- gpm isoline shrinks further so that deep convection is essentially confined at its core, suggestive of a strong local influence (not shown). The composite difference of rainfall during active and passive phases of the Central Africa Low indicates no substantial change of rainfall over

central Africa. This finding suggests that despite high rainfall mean over central Africa, the change of Central Africa Low area induces an anomalous subsidence over central Africa that have a stabilizing effect to limit the interannual variability of local rainfall. Nevertheless, rainfall surplus is found over southern Africa and west Africa, while rainfall deficit occurred in east Africa and western Indian Ocean, reminiscent of the impacts of La Nina-like conditions, consistent with McHughes (2006). Furthermore, the strong correlation between ENSO (Nino 3.4) and Central Africa Low indices of 0.72 ( $p < 0.01$ ), highlights that the Central Africa Low variance is primarily controlled by ENSO.

#### *Conclusion*

In this study, we outlined the existence of a dominant cyclonic and quasi-permanent circulation pattern in the mid-lower troposphere that drives the atmospheric large-scale circulation and its associated water vapor transports from October to April, namely the Central Africa Low. When the Central Africa Low prevails, central Africa is a sink of water vapor, with the Indian Ocean as the main supplier and AEJs, as the key carriers of water vapour into Central Africa. In May to September, the weakening of the Central Africa Low is associated with the reversal of the water vapor transport at the northern boundary channel, that shift the Central Africa to become a source of moisture. During this season, both surrounding oceans are suppliers of moisture, with some additional contribution from the Congo basin rainforest. The Central Africa Low variation is strongly driven by ENSO so that its influence on regional climate is reminiscent of the impact of La Nina-like conditions.

#### *Acknowledgement*

The first author research is supported by a Postdoctoral Fellowship under the National Research Foundation SARChI Chair in Ocean–Atmosphere–Land modelling.

#### *Reference*

1. Adler, R. F., G. J. Huffman, A. Chang, R. Ferraro, P.-P. Xie, J. Janowiak, B. Rudolf, U. Schneider, S. Curtis, D. Bolvin, A. Gruber, J. Susskind, P. Arkin, and E. Nelkin (2003). The Version-2 Global Precipitation Climatology

Project (GPCP) Monthly Precipitation Analysis

(1979–Present), *J. Hydrometeorol.*, 4 (6), 1147–1167.

2. Anyah R. and Semazzi F. (2006) Climate variability over the Greater Horn of Africa based on NCAR AGCM ensemble. *Theor. Appl. Clim.* 86(1):39-62
3. Dee D P et al. (2011). The ERA-Interim reanalysis: configuration and performance of the data assimilation system *Q. J. R. Meteorol. Soc.* 137 553–97
4. Dezfūli, A. K., Zaitchik, B. F. and Gnanadesikan, A. (2015). Regional atmospheric circulation and rainfall variability in south equatorial Africa. *Journal of Climate*, 28(2), 809–818.
5. Dezfūli, A.K., (2017): Climate of western and central equatorial Africa. Oxford Research Encyclopedia of Climate Science, Invited Contribution.
6. McHugh MJ. (2006). Impact of South Pacific circulation variability on east African rainfall. *Int. J. Climatol.* 26: 505–521.
7. Pokam WM, Djiotang LAT, Mkankam FK. (2012) Atmospheric water vapor transport and recycling in equatorial Central Africa through NCEP/NCAR reanalysis data. *Clim. Dyn.*38, 1715–1729.
8. Reynolds RW, Rayner NA, Smith TM, Stokes DC, Wang W. (2002). An improved in situ and satellite SST analysis for climate. *Journal of Climate* 15: 1609–1625.
9. Smith, T. M., and R.W. Reynolds, T. C. Peterson, and J. Lawrimore, (2008). Improvements to NOAA’s historical merged land–ocean surface temperature analysis (1880–2006). *J. Climate*, 21, 2283–2296.
10. Trenberth, K, J. Fasullo, and L. Smith, (2005). Trends and variability in column integrated atmospheric water vapor. *Clim. Dyn.*, 24, 741–758
11. Viste, E., D. Korecha, and A. Sorteberg, (2013). Recent drought and precipitation tendencies in Ethiopia. *Theor. Appl. Climatol.*, 112, 535–551
12. Xie P, Arkin PA (1997). Global precipitation: a 17-year monthly analysis based on gauge observations, satellite estimates and numerical model outputs. *Bull Am Meteorol Soc* 78:2539– 2558.

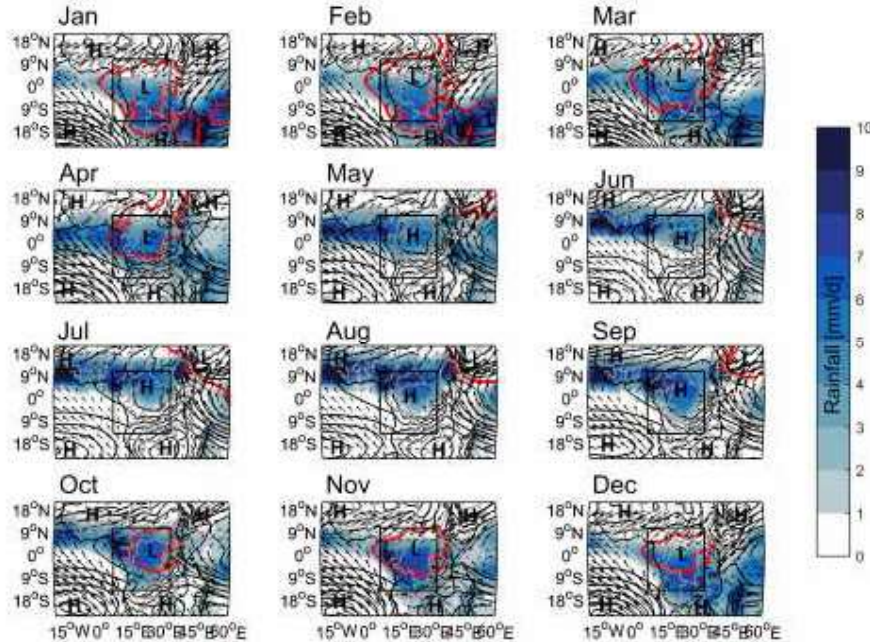


Fig 1. Annual cycle of the mid-lower thickness (geopotential height vertically averaged between 1000- to 500- hPa, contours, gpm), horizontal wind at low-levels (vertically average between 1000 and 850- hPa, arrows, m/s) and rainfall (shading, mm/d). Wind speed with less than 1m/s is not represented. The red contour indicates the 2580- gpm isoline, indicative of Central Africa Low. H and L represent the High and Low pressure systems respectively. All variables are from ERA-Interim. More details in the text.

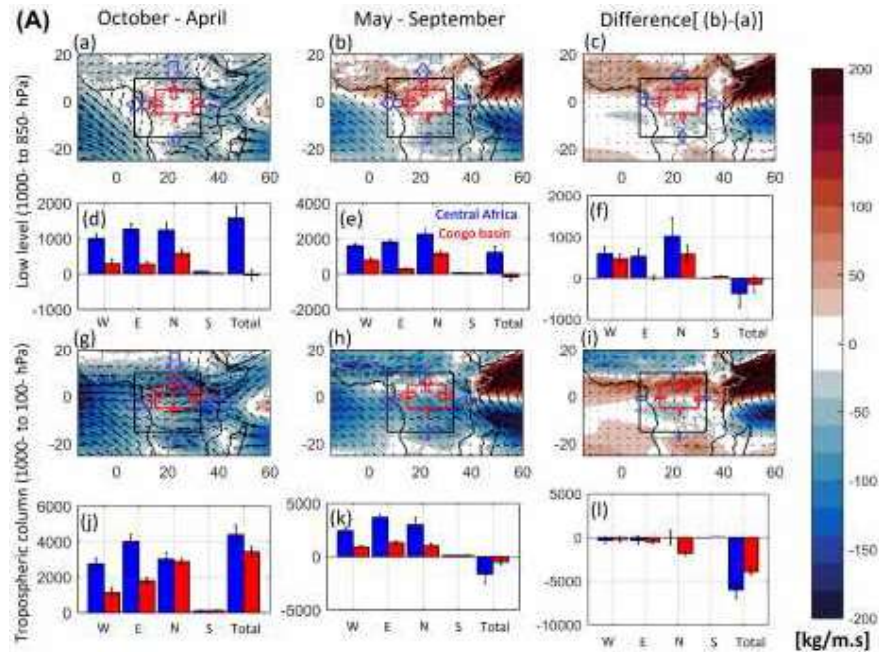


Fig 2. ERA-Interim vertically integrated water vapour transport throughout all the tropospheric column (surface to 100- hPa, arrows, (a-c) and the intensities of each moisture transport channel at each boundary of Central Africa and Congo basin (d-f, blue and red bars) and at low-levels (surface to 850- hPa, arrows (g-i) and the intensities of each moisture transport channel at each boundary of Central Africa and Congo basin bars (j-l, blue bars)). In each panel, the zonal water vapour transport is overlaid (shading, kg/m. s).

## How low-frequency Equatorial Kelvin Wave activity and local coastal winds modulate the south-eastern interannual Atlantic variability?

M-L. Bachèlery<sup>1,2</sup>, S. Illig<sup>3,1</sup> and M. Rouault<sup>1,2</sup>

<sup>1</sup>Department of Oceanography, Mare Institute, University of Cape Town, South Africa.

<sup>2</sup>Nansen-Tutu Center for Marine Environmental Research, University of Cape Town, South Africa

<sup>3</sup>Laboratoire d'Etudes en Géophysique et Océanographie Spatiale (LEGOS), CNRS/IRD/ UPS/ CNES/ICEMASA Toulouse, France

The objective of this study is to describe the low-frequency modulation of the Equatorial Kelvin Wave (EKW) activity in the tropical Atlantic as well as the local coastal winds along the coast of south-western Africa. We aim at investigating the role of each forcing in modulating the oceanic interannual variability off the coasts of Angola/Namibia. The evaluation of the equatorial forcing reveals a low-frequency modulation (5-10 years) of the EKW activity. Variations are associated with changes in EKW baroclinic mode contribution to interannual sea level anomalies: from 1958 the second baroclinic mode dominates and is then balanced by the third baroclinic mode after the late 1990's. Our results suggest that the change in the amplitude of the remote equatorial forcing plays an important role in modulating the interannual variability off the coasts of south-west Africa. In the Southern Benguela, the coastal interannual variability is dominated by the influence of the local alongshore winds. However, periods during which the equatorial forcing is intensified, EKW propagate and imprint the oceanic variability off the coast of Namibia.

### 1 Introduction

Dominated by coastal upwelling dynamics, the Southeastern Atlantic Ocean, from the equator to the Benguela Upwelling System (BUS), hosts very diversified and productive ecosystems. However, the regional climate and fish-stock availability are subject to a large variability with regular occurrences of extreme warm/cold interannual events called Benguela Niños/Niñas. Interestingly, recent analyses have documented low-frequency changes of physical ocean properties and ecosystems off the south-western African coasts with, in particular, the increase of the upwelling, chlorophyll and temperature interannual variability since the early 1990s (Blamey et al., 2012; Jarre et al., 2015). As an illustration, **Figure 1** shows the modulation of the amplitude of the interannual variability at low-frequency of the coastal temperature and Sea Level Anomalies (SLA) off the Angolan coast. Up to now, few studies have addressed the mechanisms associated with these changes owing observations limitation. Two main mechanisms have been identified to be responsible for the interannual variability. 1) At a regional scale, wind events trigger significant variations of the upwelling intensity and force poleward propagating Coastal Trapped Wave (CTW). Jarre et al., (2015) suggested that the increase of interannual oceanic variability off South Africa coincides with a shift in the position of the Saint Helena high pressure system and the fluctuation of the coastal winds. 2) The southeastern African coastal ocean variability is connected to the equatorial dynamics. Part of the energy of eastward propagating Equatorial Kelvin Waves (EKW) is transmitted poleward and propagate along the South African coasts as CTW. During their propagation CTW imprint the ocean SLA and temperature variability. A modification of the intensity of the southern Atlantic anticyclone might also affects the wind forcing at the equator which might impact the interannual EKW characteristics. This paper aims at documenting the low-frequency changes of the equatorial and coastal atmospheric forcing as well as their contribution in modulating the interannual coastal variability in the southeastern Atlantic Ocean.

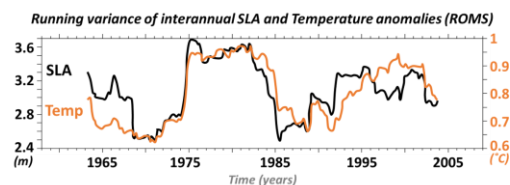


Figure 1: 10-year running variance of interannual coastal (0.5°-width band) SLA and temperature (averaged over the first 150m) from a regional ocean simulation (see section 2 for more details about the model).

### 2 Method

We based our methodology on the development of a long interannual oceanic simulation using the AGRIF (Penven et al., 2005) version of the Regional Ocean Modeling System ROMS v3.1 (Shchepetkin & McWilliams, 2005). Our configuration of the South-eastern Atlantic Ocean is similar to the one of Bachelery et al. (2016). The domain extends from 7°N to 34°S and from 10°W to the African continent with a horizontal resolution of 1/12° and 37 sigma vertical levels stretch in the surface layer. Model initial conditions and open lateral boundary conditions (West and South) are derived from Simple Ocean Data Assimilation (SODA) v2.1.6 (Carton & Giese, 2008). Surface atmospheric forcings come from the 3h 10m winds and daily heat/water fluxes of Drakkar Forcing Set v5.2 (DFS; Dussin et al., 2016). The simulation was performed over the 1958-2008 period, during which 5day averages of model state variables were stored. Performances of the model simulation have been evaluated against in-situ and satellite images. The simulation fairly reproduces the temperature mean state and the coastal interannual and decadal variability in the southeastern Atlantic sector. SODA outputs are also used to quantify the equatorial forcing over the 1958-2008 period. As most of the energy projects on the gravest baroclinic modes (Illig et al., 2004), contributions of the first three EKW modes in the Atlantic Oceans are computed following the methodology described in Illig et al. (2004). EKW modes are expressed in terms of the contribution to equatorial SLA.

3 Results and discussions

First, the modulation of the coastal ocean properties might be linked to changes in the amplitude of the equatorial forcing. **Figure 2.a** shows the running variance of the sum of the first three EKW modes averaged in the Gulf of Guinea. Low-frequency modulation of the EKW energy are observed over the 1958-2008 period. The interannual EKW activity peaks in 1965, 1982 and 2000, almost in phase with the peaks of energy of coastal interannual temperature and SLA (**Fig 1**). Also, we observed an increase in the interannual EKW activity in the early 1990s. This is consistent with the increase of the temperature and the upwelling variability off the coast of Angola (Blamey et al., 2012 and **Fig. 1**) and support the possible control of the equatorial forcing on the oceanic southeastern coastal properties.

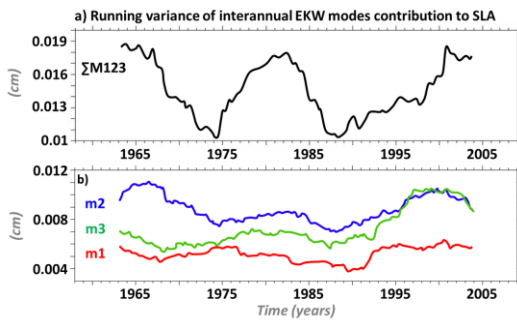


Figure 2: 10-year running variance of EKW mode contribution to interannual SLA (m) in the Guinea Gulf (averaged within  $[5^{\circ}\text{W}-5^{\circ}\text{E};1^{\circ}\text{S}-1^{\circ}\text{N}]$ . (a) Summed-up contribution of the three gravest baroclinic modes. (b) Modulation of the first (red), second (blue) and third (green) EKW mode contributions.

To further analyze the low-frequency modulation of the equatorial forcing we then look at the low-frequency modulation of each baroclinic mode individually (**Figure 2.b**). In agreement with Illig et al. (2004), the second and the third baroclinic modes are the most energetic in the eastern part of the basin. Interestingly, the modulation of each mode is different. The amplitude of the second baroclinic mode gradually decrease and is then compensated in the late 1990s by the increase of the slower and more dissipative third baroclinic mode. EKW modes are triggered by equatorial zonal wind stress fluctuations, which are stronger in the western part of the basin. EKW amplitudes results from the summation of the wind-forcing contributions accumulated retrospectively along the wave propagation/reflection path. In agreement with the wave decay-scale and the value of the Wind-Projection Coefficient (WPC), each EKW mode is forced in different regions along the equatorial waveguide. In the tropical Atlantic, the second baroclinic mode is mostly triggered in the western part of the basin ( $[20^{\circ}\text{W}-10^{\circ}\text{W}]$ ), while the third baroclinic mode in mainly forced in the Gulf of Guinea ( $[5^{\circ}\text{W}-5^{\circ}\text{E}]$ , not shown). To understand the mechanisms responsible of the low-frequency modulation of each EKW baroclinic modes, **Figure 3.a-b** show the running variance of the zonal wind stress and the WPC associated with each EKW mode, both averaged where each mode has been forced. Results show that the reduction of the second baroclinic mode is mainly due to the reduction of the amplitude of the interannual zonal winds from 1958 to 2008 (**Fig 3a; blue curve**) in the western part of the basin. Conversely, the increase in the third EKW mode energy is associated with the increase of the WPC in the eastern Equatorial Atlantic (**Fig 3.b; green curve**). The latter is due to the intensification of the mean vertical stratification and to the

shallowing thermocline (**Fig. 3.c**). In conclusion, the interannual equatorial forcing shows substantial fluctuations at low-frequency with modification in the contribution of each mode. Since each mode is characterized by different phase speeds and dissipation rates, change in the amplitude of the dominant mode might modify the characteristics of remotely forced CTW and then, the maximum latitude at which they can propagate and imprint the coastal oceanic variability.

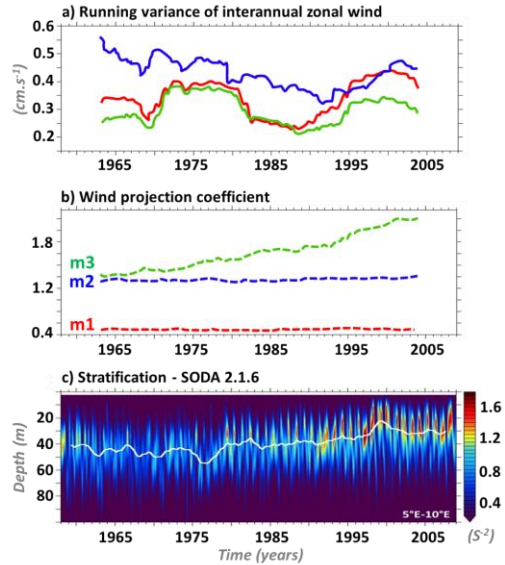


Figure 3: (a) 10-year running variance of the DFS zonal winds ( $\text{cm.s}^{-1}$ ) (b) Low-frequency evolution of the three first modes WPC. Wind and WPC have been averaged between  $[1^{\circ}\text{S}-1^{\circ}\text{N}]$  and at the location where the EKW modes are forced:  $[10^{\circ}\text{W}-0^{\circ}\text{E}]$  for the first (red line),  $[20^{\circ}\text{W}-10^{\circ}\text{W}]$  for the second (blue line) and  $[5^{\circ}\text{W}-5^{\circ}\text{W}]$  for the third mode (c). SODA vertical stratification ( $\text{S}^{-2}$ ) averaged within  $[5^{\circ}\text{W}-5^{\circ}\text{E};1^{\circ}\text{S}-1^{\circ}\text{N}]$  in function of depth (m) and time. The white line denotes the (smoothed) position of the maximum values.

The modulation of the coastal ocean properties might also be linked to changes in the amplitude of the coastal winds. The evaluation of the variance in function of latitude of the interannual alongshore winds shows that the interannual wind activity is much more energetic south of  $15^{\circ}\text{S}$  (not shown). Off the Angolan coast, one peak of energy is observed between 1976 and 1988 while the variance over the other period remains low and constant. Further south, in the BUS, the evolution over time of alongshore winds amplitude is similar than in **figure 1**, with peaks of variance in 1970, 1985 and 1992 and a slight increase of the variability starting in the early 90s. In the following, we will investigate the role of the low-frequency modulation of the EKW activity and coastal local winds on the coastal ocean interannual variability in the southeastern Atlantic sector.

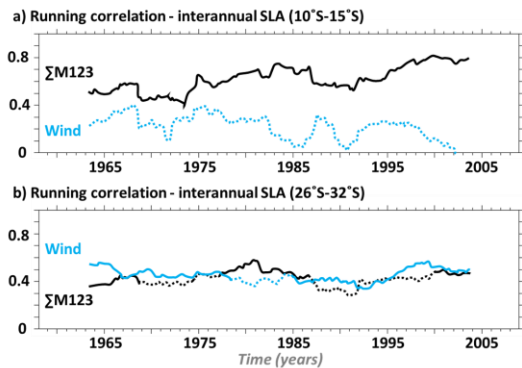


Figure 4: 10-year running correlation between interannual coastal ROMS SLA and EKW mode amplitude (summed-up contribution of the three first baroclinic modes; black line) or ROMS alongshore wind (blue line). EKW have been averaged in the Guinea Gulf ( $5^{\circ}\text{W}$ - $5^{\circ}\text{E}$ / $1^{\circ}\text{S}$ - $1^{\circ}\text{N}$ ) while SLA and alongshore wind stress have been averaged between  $10^{\circ}\text{S}$ - $15^{\circ}\text{S}$  (Fig 3.a) and  $26^{\circ}\text{S}$ - $32^{\circ}\text{S}$  (Fig 3.b). Dashed lines indicate correlation with a level of significance lower than 95% (Sciremammano, 1979).

**Figure 4.a-b** (black line) show the long-term coherence between interannual EKW activity of the summed-up contribution of the three first gravest baroclinic modes and the interannual coastal SLA variability off Angola ( $10^{\circ}\text{S}$ - $15^{\circ}\text{S}$ ; **Fig2.a**) and in the southern BUS ( $26^{\circ}\text{S}$ - $32^{\circ}\text{S}$ ; **Fig2.b**). Along the Angolan coast, statistically significant correlation coefficient (at 95% level of confidence; Sciremammano, 1979) are found for the whole period (1958-2008). Note that similar results were obtained for temperature (not shown). Interestingly, we observe a slight increase of the coherence with the equatorial variability in mirror with the progressive reduction over time of the correlation with the coastal alongshore wind stress (**Fig. 4.a**). Quasi-similar results are found down to  $20^{\circ}\text{S}$  in the northern BUS (not shown). Further south, in the southern BUS, the coherence between the EKW activity and the coastal dynamic decreases. Off the Namibian coast statistically significant correlations appear only during three periods: before 1970, between 1977 and 1986 and after 2000 (**Fig 4.b**) which correspond to the periods where the remote equatorial forcing is more energetic. Furthermore, the interannual alongshore wind stress significantly contributes to the coastal interannual SLA during the full period except during the 1979-1985 period (**Fig. 4.b**). The lack of coherence with the equatorial forcing is attributed to the reduction of the EKW amplitude during some periods and to the stronger contribution of the local forcing which competes or sometimes controls the coastal ocean dynamic.

#### 4 Conclusions

In this paper, we have investigated the role of the remote equatorial and local atmospheric forcings in the low-frequency modulation of the oceanic coastal interannual variability along the southwestern coast of Africa. Analyzing the EKW characteristics and a long-term (51 years) model simulation, we first document the modulation of the EKW interannual activity in the equatorial band. Results show a significant modulation of EKW amplitude associated with changes in the contribution of the dominant EKW modes to the interannual SLA. We reported the dominance of the second EKW mode up to the early 90's which is then compensated by the increase of the amplitude of the third EKW mode. Changes are associated with the modulation of the zonal wind and the increase and shallowing

of the equatorial stratification in the Guinea Gulf. Finally, this study emphasizes the contrast between the coastal ocean dynamics north and south of the Angola-Benguela front ( $\sim 20^{\circ}\text{S}$ ) which are controlled and modulated by different forcings. From the equator to the northern Benguela ( $20^{\circ}\text{S}$ ), the interannual variability is mainly driven and modulated by the equatorial Kelvin waves activity, while in the southern Benguela the strong coherence with the alongshore winds suggests a more important contribution of the local forcing. However, periods where the equatorial forcing is intensified, EKW can imprint the oceanic variability off the coast of Namibia. In future works, we will investigate the stressors controlling the modulation of the zonal equatorial and coastal alongshore winds in the southern Benguela, in particular regarding the shift in the position of the Saint-Helena high-pressure system.

#### Acknowledgements

Marie-Lou Bachelery received funding from the NRF SARCHI chair on modeling ocean atmosphere land-interactions NRF Sarchi Chair and the Nansen-Tutu Center. Computations were performed using facilities of the University of Cape Town's ICTS High-Performance Computing team (<http://hpc.uct.ac.za>).

#### References

- Bachelery, M.-L., Illig, S., & Dadou, I. (2016). Interannual variability in the South-East Atlantic Ocean, focusing on the Benguela Upwelling System: Remote versus local forcing. *Journal of Geophysical Research: Oceans*, 121, 284–310. <https://doi.org/10.1002/2015JC01116>
- Blamey, L.K., Howard, J.A.E., Agenbag, J. and Jarre, A. (2012) Regime-shifts in the southern Benguela shelf and inshore region. *Prog. Oceanogr.* 106:80–95.
- Carton, J. A., & Giese, B. S. (2008). A reanalysis of ocean climate using simple ocean data assimilation (SODA). *Monthly Weather Review*, 136, 2999–3017. <https://doi.org/10.1175/2007MWR1978>.
- Dussin, R., B. Barnier and L. Brodeau (2016), The making of Drakkar forcing set DFS5, DRAKKAR/MyOcean Rep. 01–04–16, Laboratoire de Glaciologie et Geophysique de l'Environnement, Grenoble, France.
- Illig, S., Dewitte, B., Ayoub, N., Du Penhoat, Y., Reverdin, G., De Mey, P., et al. (2004). Interannual long equatorial waves in the tropical Atlantic from a high-resolution ocean general circulation model experiment in 1981–2000. *Journal of Geophysical Research*, 109, C02022. <https://doi.org/10.1029/2003JC001771>
- Jarre, A., Hutchings, L., Kirkman, S.P., Kreiner, A., Tchikalanga, P., Kainge, P., Loeng, H., (2015). Synthesis: climate effects on biodiversity, abundance and distribution of marine organisms in the Benguela. *Fish. Oceanogr.* 24 (S1), 122–149.
- Penven, P., Echevin, V., Pasapera, J., Colas, F., & Tam, J. (2005). Average circulation, seasonal cycle, and mesoscale dynamics of the Peru Current System: A modeling approach. *Journal of Geophysical Research*, 110, C10021. <https://doi.org/10.1029/2005JC00294>

Sciremammano, F. (1979). A suggestion for the presentation of

correlations and their significance levels. *Journal of Physical Oceanography*, 9, 1273–1276

Shchepetkin, A. F., & McWilliams, J. C. (2005). The Regional Oceanic Modeling System: A split-explicit, free-surface, topography following coordinate ocean model. *Ocean Modelling*, 9, 347–404. <https://doi.org/10.1016/j.ocemod.2004>.

## ***The energetics of ridging South Atlantic Ocean anticyclones over South Africa***

Thando Ndarana

Department of Geography, Geoinformatics and Meteorology

University of Pretoria

### **Abstract**

The energetics associated with ridging Atlantic Ocean cyclones are examined using ECMWF reanalysis data from 1980 to 2016. Simple composite analysis that considers only the duration of the ridging events as a basis for averaging is used. When the ridging portion of the events breaks off from the parent structure, the energy centre that originates south of the high pressure system propagates in the north easterly direction. Ageostrophic geopotential flux convergence is more important for the development of the energy centres than baroclinic conversion, while energy fluxes by the total flow are responsible for propagating the energy eastward.

### **Introduction**

The clearest and most concise framework of presenting energy conservation in the atmosphere is the Lorenz energy cycle (see Fig 1; Lorenz, 1995). The atmosphere generates mean available potential energy (MAPE) by means of meridional differential heating. This MAPE constitutes only about half a percent of the total potential energy (Holton and Hakim, 2014). Baroclinic eddies then convert the MAPE to eddy available potential energy (EAPE), whilst at the same time convert the latter to eddy kinetic energy (EKE), as they develop and grow. These conversions are facilitated by meridional and vertical heat fluxes, respectively, and the former is only possible when the basic state atmosphere is baroclinically unstable. Poleward eddy momentum fluxes, in the presence of anticyclonic barotropic shear (i.e. baroclinic processes) then convert EKE into mean kinetic energy (MKE), thus accelerating the basic flow, and in particular the eddy driven jet in the middle latitudes. The Lorenz energy cycle is entirely consistent with the conservation of atmospheric angular momentum, which is transported poleward via the meridional drift and the eddies taking over and depositing it into the jet (Holton and Hakim, 2014).

The diagnostics discussed above assume a zonally averaged basic state flow, and so the eddy flux representations that result are also zonally symmetric and therefore cannot be used to analyze local dynamical processes. Assuming a time symmetric basic state flow, Murakami (2011) developed local energetics and showed that additional processes to the conversions between the various types of energy are present in the atmosphere. These are interactions between the various energy reservoirs depicted in Figure 1.

Based on this approach, Tennant and Reason (2005) demonstrated that wet summers are associated with an increase in subtropical energy exchange, a poleward displacement of the subtropical jet and stronger ridging of the South Atlantic ocean anticyclone. This suggests that the energy conversions in the South African domain might be playing a role during ridging anticyclones. Precisely how the energy structures of ridging anticyclones develop and evolve is still an open question.

4. Atlantic Ocean and across the 25E meridian.

Various studies in other parts of the world such as South America (e.g. Piva et. al. 2010) and North America (e.g. Decker and Martin 2005) have shown that the energetics of weather systems can be disintegrated and their stages of development may be understood from the point of view of the

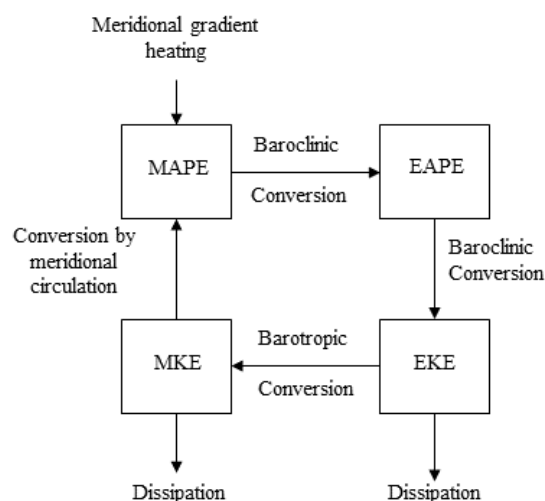


Figure 1: The Lorenz energy cycle.

### **Data**

We use six hourly European (ECMWF) data from 1980 to 2016. The data is on a 2.5 x 2.5 resolution. This is deemed sufficient because ridging anticyclones are synoptic scale processes. The variables used to calculate the diagnostics are temperature, zonal and meridional wind fields and mean sea level pressure (MSLP).

### **Methods**

To objectively identify ridging events a three step method is employed (see Ndarana et al. 2018).

1. Closed contours in MSLP in the domain bounded by 40W, 60E, the Equator and 50S are identified;
2. All concentric contours are then grouped together and are considered to belong to the same anticyclone at any given six hourly time step;
3. Anticyclones are then considered to ridge if at least the outermost contour extends eastward from the South

evolution of their energy structures. These were based on the Orlandy and Katzfey (1991)'s EKE equation

$$\frac{\partial K}{\partial t} = -\nabla \cdot (\mathbf{v}_a \phi) - \omega \alpha - \nabla_3 \cdot (\mathbf{V}_3 K) - \mathbf{v} \cdot (\mathbf{v}_3 \cdot \nabla_3) \mathbf{V}_m + \mathbf{v} \cdot \overline{(\mathbf{v}_3 \cdot \nabla_3) \mathbf{v}} + R \quad (1)$$

where the capital letters with subscript  $m$  represent the basic flow and the capital (small) letter, either with subscript 3 or no subscript represent the total (perturbation) variables, such that

$$A = A_m + a$$

The terms on the right side of Equation (1) are the ageostrophic geopotential flux convergence (AGFC), the baroclinic generation / conversion (BARC), the energy flux convergence (EFC), the barotropic generation/conversion (BART), the time mean stress (TMS) and residual (RES) terms, respectively.  $\mathbf{v}_a$  is the irrotational component of the flow. The EKE is defined as

$$K \equiv \frac{u^2 + v^2}{2}$$

Decker and Martin (2005) and Piva et al. (2010) and other similar studies integrate all the terms in the vertical. In this study, we opted not to follow that approach but to calculate the various terms of Equation 1 at the 1000 and 250 hPa levels. The rationale for our approach is informed by Ndarana et al. (2018). It was shown in that study that ridging anticyclones are linked to lower stratospheric Rossby wave breaking mechanisms and so the evolution at the surface would significantly differ from that which occurs aloft.

Composites of ridging and the different terms were generated using the duration (see Figure 2) on of the ridging process as the basis for the calculation of the composite means.

**Preliminary results**

A total of 4,923 ridging events were identified from 1980 to 2016. These vary significantly in duration with the shortest lived events (less than 1 day) occurring most frequently and the longer lived events more rare. The frequency of ridging events decreases exponentially as a function of duration, as shown in Figure 2.

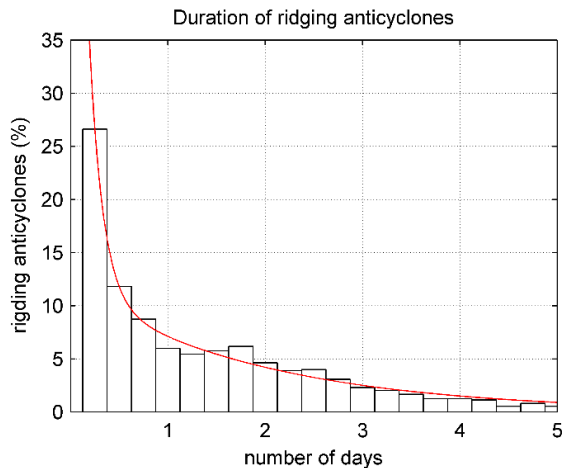


Figure 2: Histogram showing the frequency of occurrence of Atlantic ridging anticyclones (y axis) as a function of duration in days. The red curve is a fitted exponential function.

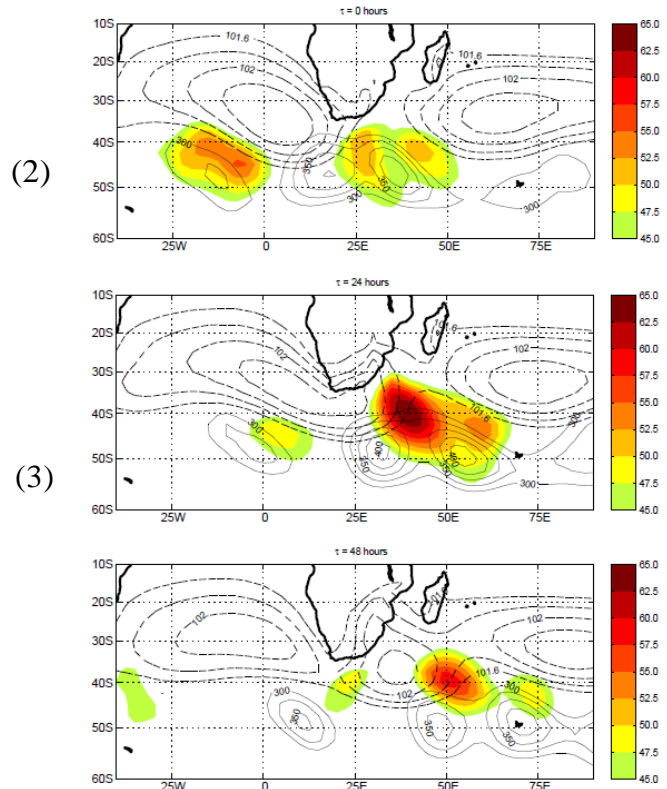


Figure 3: Composite mean evolution of mean level pressure (dashed contours) in kPa with EKE at the 1000 hPa (shaded) and 250 hPa (solid contours) levels at 0 hours (top panel), 24 hours (middle panel) and 48 hours (bottom panel). A total of 191 events were involved in the calculation of the composites.

The ridging highs exhibit very little seasonal variability. This is contrary to expectations (Tyson and Preston-Whyte, 2000). For this reason, the composites were formed using all the events for a particular duration, without taking the seasonal changes into consideration. We present results for events that have a 54 hour duration and show only the  $\tau = 0, 24$  and 48 hours composites, both at the 1000 hPa and the 250 hPa,

It is evident from Figure 3 that the evolution of EKE at the surface is significantly different from the one aloft. There exists two EKE centres that appear to be associated with ridging at the surface (shaded areas in the top panel of Figure 3) together with a pre-existing centre located just behind the Indian Ocean high. The leading centre, which is located at the front of the ridging high, intensifies as the ridging matures, whilst the trailing centre weakens. The latter propagates in a south-easterly direction and then changes direction toward the region where the ridging high pressure system breaks off from the parent South Atlantic system. The structure at 250 hPa is consistent with the presence of Rossby wave breaking processes ( Ndarana et al. 2018) that are associated with ridging highs in that part of the atmosphere. The two processes are vertically coupled by potential vorticity anomalies. As was the case at the surface, the energy centres associated with ridging at this level, intensify at the same as those found at the surface.

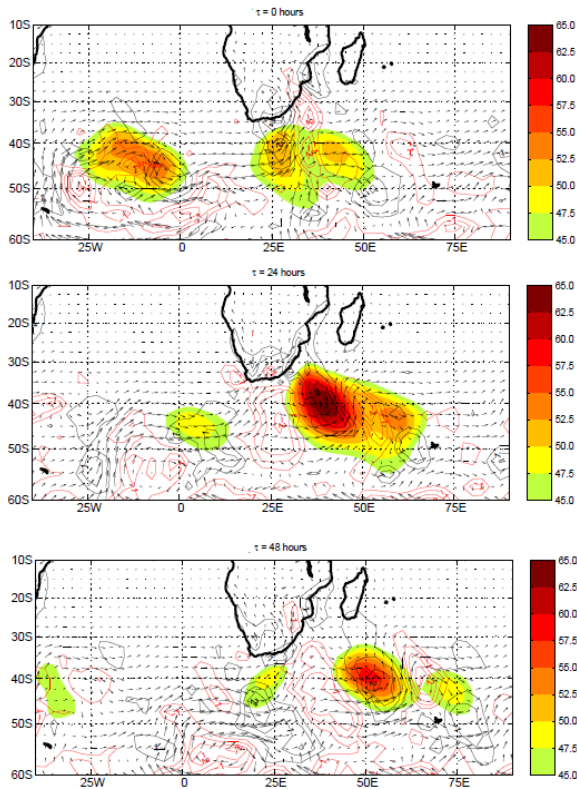


Figure 4: Composite mean evolution of EKE (shaded) at 1000 hPa with contours representing the contribution of AGFC to the tendency of EKE. The black (red) represent positive (negative) values of AGFC plotted at  $0.5 \times 10^3 \text{ m}^2 \text{ s}^{-3}$ . The vectors represent the ageostrophic geopotential fluxes.

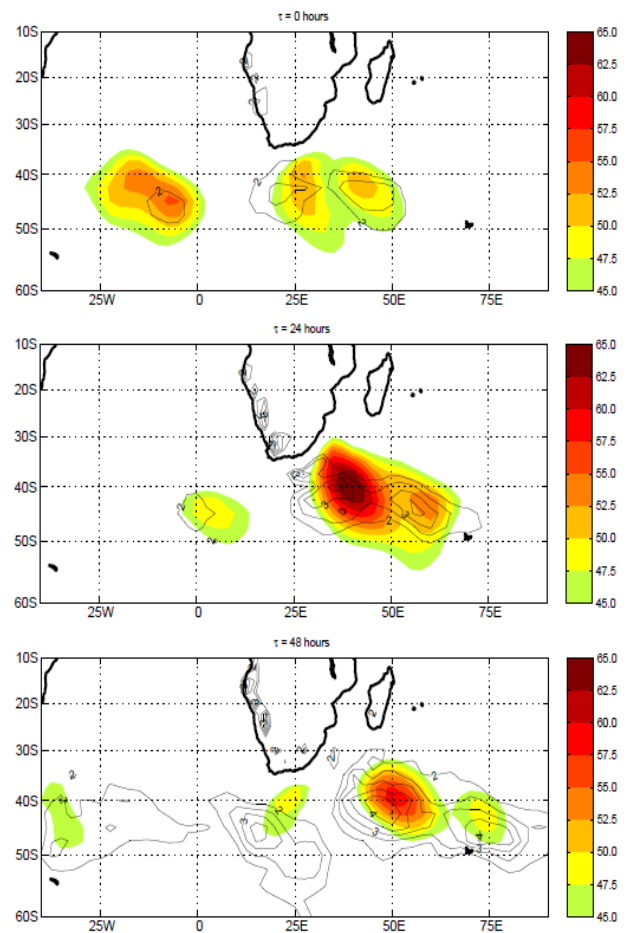


Figure 5: Same as Figure 4 but the contours represent BARC plotted in intervals of  $2 \times 10^4 \text{ m}^2 \text{ s}^{-3}$ .

Figures 4 and 5 show the composite evolution of AGFC (and the fluxes) and the BARC terms. Firstly, the AGFC is an order of magnitude larger than the BARC. This suggests that the former plays a more significant role in contributing to the evolution of EKE. Furthermore, the AGFC appears to coincide much more accurately with the leading EKE centre than does the BARC. Both points suggest that AGFC plays a more important role in influencing the increase in EKE kinetic energy at the leading edge of the ridging anticyclone. A similar picture is observed at the 250 hPa (not shown). In fact at this level, the BARC centres appear to be spatially uncorrelated with the EKE centres.

The BARC zone that is associated with the leading EKE centre appears to be receiving ageostrophic flux of EKE from a southeasterly direction, as the ridging process begins (top panel in Figure 4). It intensifies, as the AGFC does the same. Some of the energy is lost east of it by downstream radiation, which is deposited just east of 50E to help the pre-existing EKE centre to increase in magnitude. This is consistent with previous studies that have cyclone waves (Orlanski and Katzfey, 1991, Decker and Martin, 2005), surface cyclolysis (McLay and Martin, 2002), and moving troughs (Piva et al., 2010).

The eastward propagation of energy in ridging high pressure systems is largely influenced by advective processes. This is suggested by the structure of EFC. This term appears not to be contributing to the intensity of EKE, but rather to its eastward advection by the total flow. This is

clearly indicated by the strength of the energy flux at the centre of EKE and the sources and sinks of energy that astride the EKE centre. At the 250 hPa the EFC follow the EKE centres, which propagate eastward. This is consistent with the picture painted by Orlanski and Sheldon (2003).

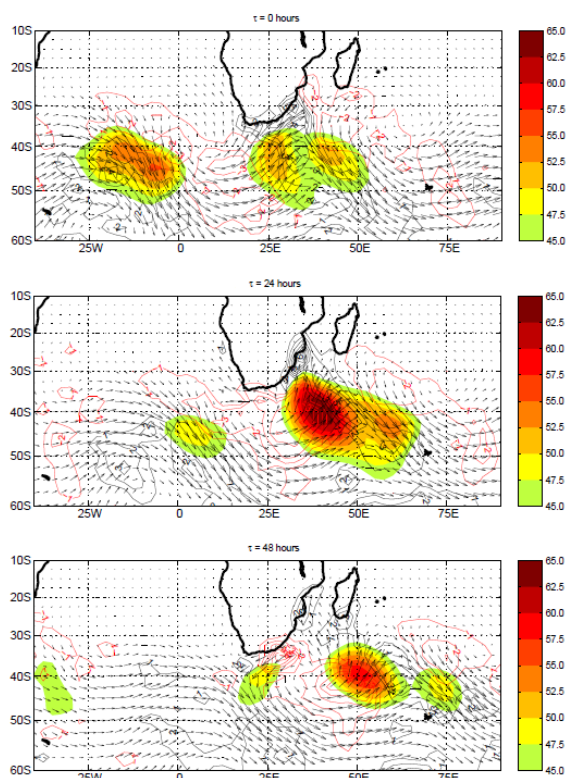


Figure 6: Same as in Figure 4 but for EFC.

**Discussion and conclusion**

In this study, it was shown that downstream development that is associated with ageostrophic geopotential flux might be important for ridging high pressure systems. This downstream development is also important at higher levels as these ridging events are associated with breaking waves near the dynamical tropopause. There is some contribution of baroclinic conversion of eddy available potential energy to eddy kinetic energy but it is overwhelmed by the convergence of ageostrophic geopotential flux. The eastward propagation of the energy centres is largely associated with advective fluxes. The direction of propagation in the upper troposphere is eastward, while it is north-easterly at the surface.

**References**

Decker, S.G. and Martin, J.E. (2005). A local energetics analysis of the life cycle differences between consecutive, explosively deepening, continental cyclones. *Monthly Weather Review*: **133**, 295 – 316.

Lorenz, E.N. (1955). Available potential energy and the maintenance of the general circulation. *Tellus*: **7**, 157 – 167.

McLay, J.G. and Martin J.E. (2002). Surface cyclosis in the North Pacific Ocean Part III: Composite local energetics of tropospheric deep cyclone decay associated with surface cyclosis. *Monthly Weather Review*: **130**, 2507 – 2529.

Ndarama, T. Bopape, M. Waugh, D. and Dyson L. (2018): The influence of the lower stratosphere on ridging Atlantic

Ocean anticyclones over South Africa. *Journal of Climate*: **31**, 6175 - 6187.

Orlanski, I. and Katzfey, J. (1991). The life cycle wave in the Southern Hemisphere. Part i: Eddy energy budget. *Journal of the Atmospheric Sciences*: **48**, 1972 – 1998.

Orlanski, I. and Sheldon, J.P. (1995). Stages in the energetics of baroclinic. *Tellus* **47A**, 605 – 628.

Piva, E.D., Gan, M.A. and Rao V.B. Energetics of winter troughs entering South America. *Monthly Weather Review*. **138**: 1084 - 1103

Tennant, W.J. and Reason, C.J.C. Associations between the global energy cycle and regional rainfall in South Africa and Southwest Australia. *Journal of Climate*: **18**, 3032 - 3047

Tyson, P.D. and Preston-Whyte, R.A. (2000). The weather and climate of southern Africa. Oxford University Press.

## ***Space and time varying wind-wave interaction in False Bay, South Africa***

Tania Williams<sup>1,2</sup> Ana Vilaplana-Domingo, Giles G. Fearon<sup>2,3</sup> and Christo Rautenbach<sup>1,2,3</sup>

<sup>1</sup>South African Weather Service, Marine Unit, Cape Town, South Africa

<sup>2</sup>Oceanography department and Marine Research Institute, University of Cape Town, South Africa

<sup>3</sup>Advisian, Worley Parsons Group, Cape Town, South Africa

### ***Abstract***

The wind circulation over False Bay largely influence the hydrodynamic characteristics of the bay. This study investigates the performance of a spatial varying wind product over False Bay. The spatial varying winds reproduces the wind over the bay fairly well, particularly over the western side of the bay. The comparison leads to the implementation of the spatial varying WASA product into a wave model in the bay. The wave model shown to perform better in the western side of the bay. Further studies will focus on the different influences of wind and swell wave components in False Bay.

### ***Introduction***

False Bay is located at the southwestern tip of South Africa. It is considered the largest true bay in the region and spans over 1000 km<sup>2</sup>. The bay is surrounded by two main mountain ranges, the Cape Peninsula mountain range to the West and the Hottentots Holland mountain chain to the North (Jury, 1991). The study of False Bay is not only fascinating for its oceanographic complexity, but also for its imperative relevance for its social and economic components (Taljaard et al. 2000).

The circulation in False Bay is mainly driven by the winds in the region (Atkins 1970; Wainman et al. 1987; Taljaard et al. 2000). False Bay is dominated by four wind regimes, as describe by Jury (1991). During summer the winds follow a South-East regime, thus initiating upwelling in the region of Hangklip and Gordon's Bay (Jury, 1991). The winter regime in the region is dominated by the North-West wind regime, creating a well-mixed layer throughout the bay (Jury 1991; Dufois & Rouault 2012).

These wind regimes play an important role in wave generation. While observed wind data sets with high spatial and temporal resolution are limited in South Africa, simpler assumptions are often used to generate models in the region. Several wind products are available to evaluate global and regional winds. Each data set is distinguished by differences in the methodology, spatial resolution and temporal resolution. This study investigates the performance of a high resolution wind product over False Bay during summer. The high resolution (space-varying) wind product with a horizontal resolution of 3 km is the output from the Wind Atlas of South Africa (WASA) project as described in Lennard et al. (2015). This space-varying wind is validated against observed wind and a global wind product. The global dataset is low resolution reanalysis product, ERA interim. ERA-Interim is a global atmospheric reanalysis which starts from 1979 and is continuously updated in real time. The ERA interim data has a spatial resolution of ~80 km and provides 6 hourly data for wind speed and direction (Dee et al., 2011). The second part of this study investigates how the high resolution wind product from WASA performs as an input into a wave model for False Bay. Due to the limited data availability the study focuses on short time periods.

### ***Wind data Comparison***

Two locations within False Bay are used to validate the two model products. The first station, Strand, is located on the eastern side of False Bay. The Roman Rock station is located

on the western side of False Bay (34.18°S, 18.46°E). Roman Rock measurements were provided by the Institute for Maritime Technology (IMT). The wind measurements at Strand (34.14°S, 18.84°E) were provided by the South African Weather Service (SAWS).

Fig. 1 and 2 provide time-series comparisons of the modelled and measured data at Roman Rock and Strand stations. All measured wind speeds were adjusted to the reference level of 10 m above ground using standard empirical formulae. Roman Rock is a small rocky outcrop, wind measurements from this location are considered to be largely representative of the winds over the adjacent ocean, making it an ideal candidate for validating the products over False Bay. The comparison in Fig. 1 indicate that the winds compare favourably with the Roman Rock measurements. The event scale is well captured with only minor discrepancies in wind speed and direction. The comparison also indicated that the ERA interim data underestimates the wind speed and roman rock, missing some of the events at the location. The wind direction is well captured by the ERA interim data.

Fig. 2 indicate that while wind directions are well resolved at the Strand measurement location, wind speeds are over-predicted by the WASA model when compared with the measurements, particularly when the south-easterly winds are strongest. Potential reasons for the discrepancy include local features near the land-based measurement station. ERA-interim winds compare favourably with the Strand measurements. The event scale is well captured with only minor discrepancies in the wind direction and speed. Given the spatial and temporal coverage of the WASA wind product, as well as the reasonable comparison with the measurements, particularly Roman Rock, the WASA winds are the most appropriate wind data source to carry on with the present study.

The wind roses in Fig. 3 show the dominant wind direction as being south-easterly in False Bay. The ERA-interim and WASA models are able to reproduce the dominant south-easterly wind direction.

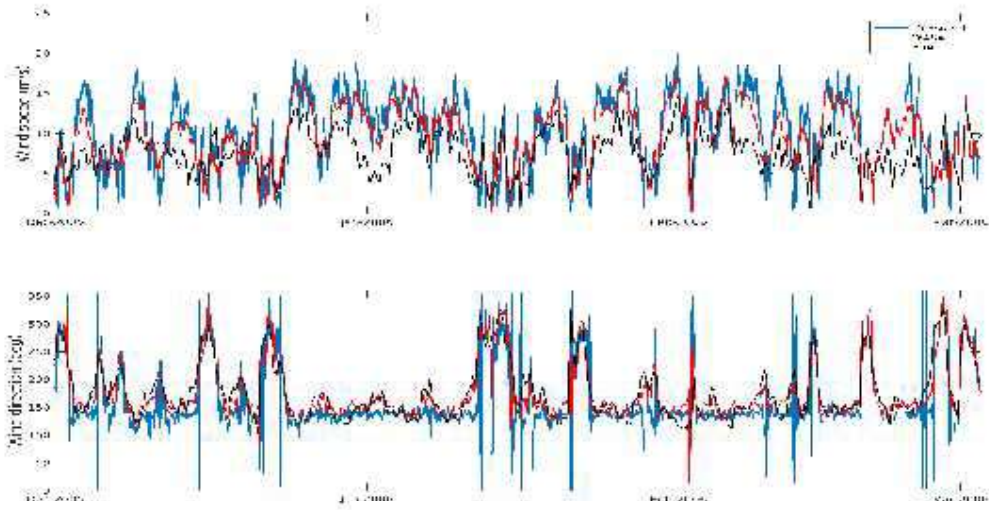


Figure 1: Time-series of measured vs ERA interim and WASA wind speed and direction at Roman Rock over a summer period

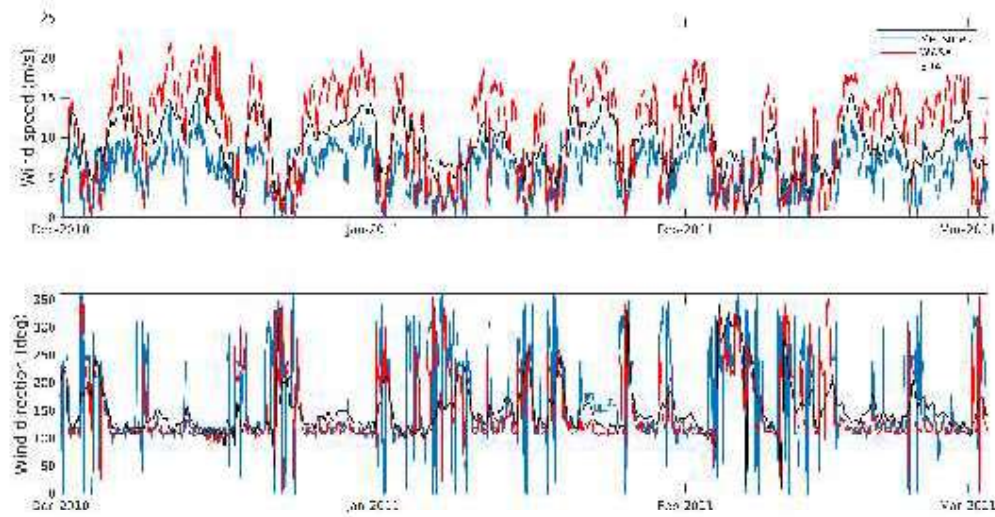


Figure 2: Time-series of measured vs ERA interim and WASA wind speed and direction at Strand over a summer period.

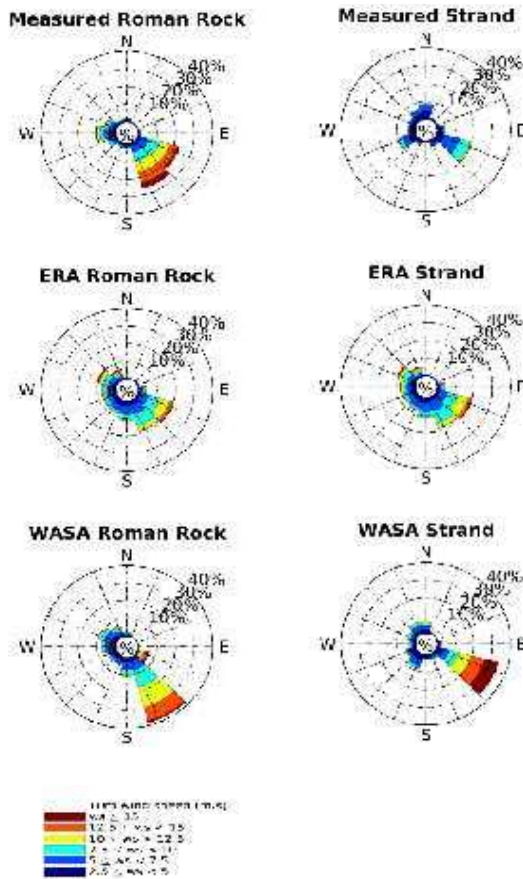


Figure 3 Annual wind roses for roman rock and strand for observed, ERA and WASA winds.

Wave Simulation

The WASA wind data was used to force the wave model. The relevant parameters of interest for this study are space and time-varying wind speed components ( $u$  and  $v$ ) at 10 m height above the ground at hourly intervals and at a spatial resolution of  $0.03^\circ$  ( $\sim 3$  km). The Simulating WAVes in the Nearshore (SWAN) model was used to resolve the directional wave spectrum propagation into False Bay. Fully spectral offshore boundary conditions were used as well as swell boundaries based on the National Centers for Environmental Prediction (NCEP) global model outputs. NCEP provides offshore model outputs (<http://www.nco.ncep.noaa.gov/pmb/products/wave/>). The spectra wave model was then forced with the WASA atmospheric model described above.

Wave Model Results

This section focuses on the validation of model wave parameters which was forced using the space varying WASA winds. Two stations are used to validate the wave parameters in False Bay. Station 1 is Acoustic Doppler Current Profiler (ADCP) measurements near Gordons Bay, East side of False Bay at a mooring depth of  $\sim 12$  m while station 2 is ADCP measurements near Simons Town, West side of False Bay at a mooring depth of  $\sim 12$  m. Bulk wave parameters are used in the comparison. The ADCP data was provided by the Council for Scientific and Industrial Research. Fig. 4 and 5 provide time-series comparisons of the modelled and measured wave parameter data.

The comparisons in Fig. 4 and indicate that the model behaves favourably in the western side of False Bay. The model overestimates the significant wave height ( $H_{m0}$ ) at both stations. The model captured both peak period ( $T_p$ ) and peak direction (Peak dir) at the Gordons bay station. The Simons Town comparison shows slight discrepancies of the peak period ( $T_p$ ) and peak direction (Peak dir).

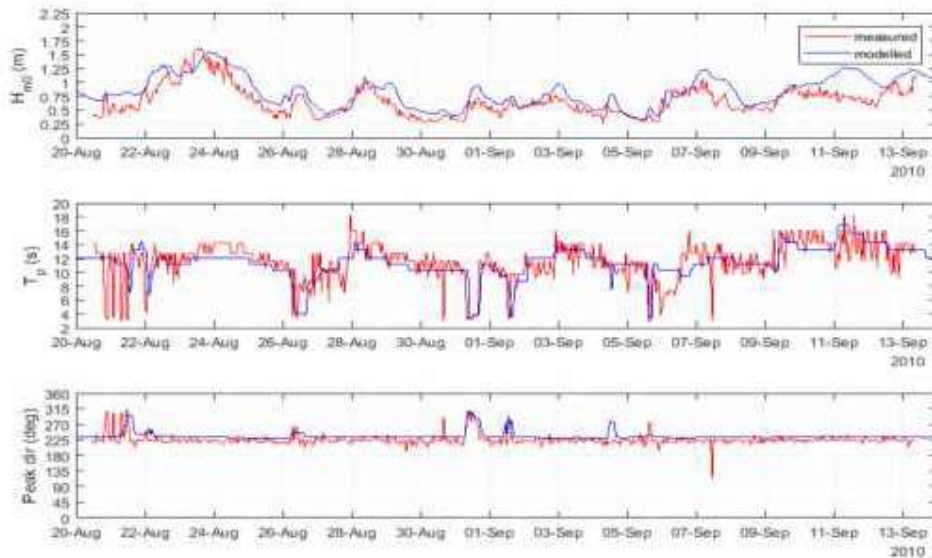


Figure 4. Time-series of measured vs modelled wave parameters at Simons Town.

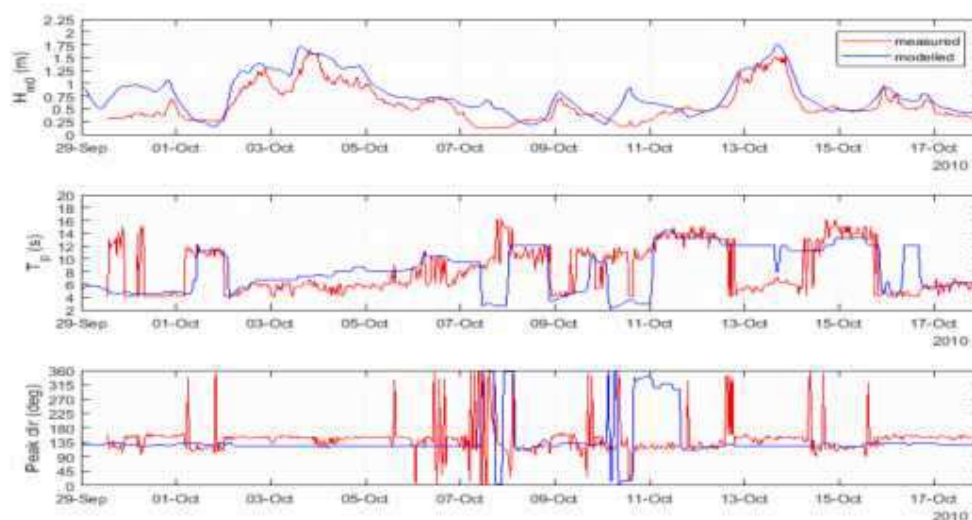


Figure 5. Time-series of measured vs modelled wave parameters at Gordons Bay

### Conclusion

It has been shown that False Bay wave dynamics depend critically on the wind direction and its spatial distribution over the Bay (Van Foreest and Jury, 1985). The spatial varying winds reproduces the wind over the bay fairly well, particularly over the western side of the bay as seen in Fig. 1.

The model in the present study performed well in reproducing the waves in False Bay. The wave model in this study produces more realistic wave period and peak in the western side of the bay, while the eastern side peak period and peak direction shows more discrepancies with measurements. It is important to note that deep ocean swells generate waves with different periods and size than local wind generated waves. Waves will still be present in False Bay without local wind forcing. The influence of the wind generated and swell generated waves need to be investigated to show the influence and importance of space-varying winds on wave generation in False Bay. The differences between wind and swell wave generation in False Bay will be investigated in future work.

### References

Atkins, G. 1970. Winds and current patterns in False Bay. *Transactions of the Royal Society of South Africa*. 39(2): 139-148.

Dee, D.P., Uppala, S.M., Simmons, A.J., Berrisford, P., Poli, P., Kobayashi, S., Andrae, U., Balmaseda, M.A., Balsamo, G., Bauer, D.P. and Bechtold, P., 2011. The ERA-Interim reanalysis: Configuration and performance of the data assimilation system. *Quarterly Journal of the royal meteorological society*, 137(656), pp.553-597.

Dufois, F. & Rouault, M. 2012. Sea surface temperature in False Bay (South Africa): Towards a better understanding of its seasonal and inter-annual variability. *Continental Shelf Research*. 4324-35.

Jury, M. 1991. The weather of False Bay. *Royal Society of South Africa. Transactions* 47(4/5).

Lennard, C., Hahmann, A.N., Badger, J., Mortensen, N.G. and Argent, B., 2015. Development of a numerical wind atlas for South Africa. *Energy procedia*, 76, pp.128-137.

Taljaard, S., Van Ballegooyen, R.C. & Morant, P.D. 2000. False Bay Water Quality Review. Volume 1: Executive Summary. Report to the False Bay Water Quality Advisory Committee. CSIR Report. ENV-S-C 2000-086/1.

Van Ballegooyen, R.C. 1991. The dynamics relevant to the modelling of synoptic scale circulations within False Bay. *Transactions of the Royal Society of South Africa*. 47(4): 419-432.

Van Foreest, D. & Jury, M.R. 1985. A numerical model of the wind-driven circulation in False Bay. *South African Journal of Science*. 81(6): 312-317.

Wainman, C., Polito, A. & Nelson, G. 1987. Winds and subsurface currents in the False Bay region, South Africa. *South African Journal of Marine Science*. 5(1): 337-346.

## Verification of Site-Specific Processing System using the data generated from the South African Weather Service radiometric stations

Nosipho Zwane<sup>1\*</sup>, Brighton Mabasa<sup>1</sup>, Katlego Ncongwane<sup>1</sup>, Joel Botai<sup>1</sup>

<sup>1</sup>South African Weather Service, Eco Glades block 1b, Eco Park, Cnr Olievenhoutbosch and Ribbon Grass Streets, Centurion, 0157, South Africa

### Abstract

Solar radiation is one of the inexhaustible, promising renewable energy resources for power generation. South Africa is among the top three countries in the world with 2 500 hours of sunshine per year and direct solar radiation range between 4.5-6.5 kWh/m<sup>2</sup> per day. The present work investigated the performance of Site-Specific Processing System (SSPS) using four South African Weather Service (SAWS) ground-based solar radiometric stations. The non-parametric Wilcoxon Rank Sum test was used to rank and categorize the stations into: top performing stations and least performing stations during September to November in 2017. For the three solar parameters investigated, the model was able to capture observations with small biases. Therefore, the SSPS can be used for more solar application such as solar mapping and forecasting solar power.

Keywords: Verification, Observed data, Model data, Radiometric stations, Solar energy

### Introduction

The main electricity supply utility in South Africa is Eskom, responsible for approximately 90% electricity demand. The other 10% electricity demand is fulfilled by Independent Power Producers (IPPs) and municipalities (Singh et al., 2017). The recent load shedding (Steenkamp et al., 2016) experienced across the country has proven that an energy crisis is looming and that Eskom is facing challenges to meet the country's energy demand. The South African government has put forth plans and policies such as the IPPs to deal with the energy crises while also reducing the emissions of greenhouse gases. The government has made a commitment to reduce greenhouse gas emissions by 34% by 2020 and further by 42% by 2025 (Herbst and Rautenbach, 2005).

South Africa aims to generate 40% of its energy from renewable technology by 2030. The South African Department of Energy (DoE) in its renewable energy independent power produce program, has prioritized Concentrating Solar Power (CSP), Solar Photovoltaic (PV) and biomass as the main renewable energy technologies (Craig et al., 2017).

As it stands, the most dominant renewable energy sources are wind (53%) and solar PV (35%). These renewable resources are clean and abundant. All that is necessary for us is to use our scientific and technical skills to fully utilize these resources.

With efforts to accelerate the adoption and deployment of solar resource in South Africa, the South African Weather Service (SAWS) established a solar radiation ground-based observation network of 13 stations (Figure 1) across the

country (See Table 1 for installation of the four stations). The SAWS radiometric station measures the Direct Normal Irradiance (DNI), Diffuse Horizontal Irradiance (DIF) and Global Horizontal Irradiance (GHI). Only one station is under the Baseline Surface Radiation Network (BSRN) (<https://dataportals.pangaea.de/bsrn/?q=LR0100>). The stations are installed in six climatic zones and therefore ensure national availability of high quality accurate data to assist in measuring the country's potential to harness solar energy. Furthermore, SAWS uses the forecasts from the Unified Model to run the Site Specific Processing System (SSPS) to investigate variable renewable energy (VRE) resources under climate change in order to provide accurate VRE forecasts and products in South Africa.

The objective of this study is to verify the performance of SSPS forecast data with the SAWS solar ground observation data in order to have confidence in developing solar energy maps, application and forecast such as the solar power, installation of CSP and solar PV.

Station Name	Short Name	Climate Zone	Installation Date
De Aar	DAA	Cold interior	2014-04-10
Upington	UPN	Arid Interior	2014-01-23
Polokwane	PLK	Temperate interior	2015-02-27
Bethlehem	BTH	Cold interior	2014-12-05

Data and Methodology

Observation data

Solar radiation data from four of the thirteen stations, indicated in red and green in Figure 1 for the period September to November 2017 were considered due to the availability of model data. The data have been subjected to the BSRN Quality Control (QC) tests by Long and Dutton (2000), observing three QC checks, namely 1) Physical possible limits, 2) Extremely rare limits and 3) Comparison. The observation data are recorded every minute and a median over 60 minutes on 15 minute interval is calculated to convert the minute data to hourly. The non-parametric Wilcoxon Rank Sum test (Wild, 1997) was used to rank and group the stations according to the top two performing stations and bottom two least performing stations. The top two performing stations were Uppington and De Aar (green circles in Fig. 1) and the bottom two least performing stations were Bethlehem and Polokwane (red circles in Fig 1). In order to verify the model data, Eq. (1) was applied to the observation data to convert DNI to Diffuse Horizontal Irradiance (DHI) because the model output DHI where  $sza$  is the solar zenith.

$$GHI = DNI \cdot \cos(sza) + DHI \quad eqn(1)$$

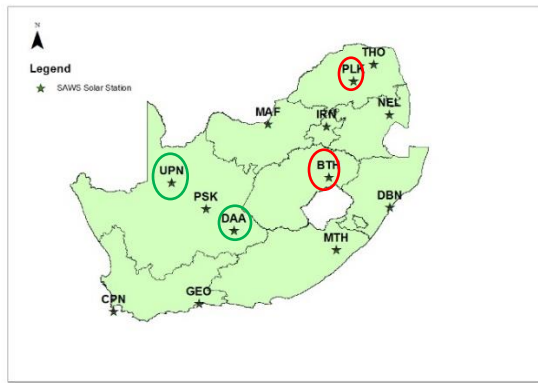


Figure 1: SAWS Solar Radiometric Network

SS PS model data verification

The main atmospheric model is the Unified Model (UM) which was configured to run in-house at SAWS at 4 km and 1.5 km resolution for four cycles (0000Z, 0600Z, 1200Z and 1800Z) in 2017. The specific sites created are in the longitude and latitude of the SAWS solar radiometric stations. Only SA4 was considered due to the completeness of the data set.

Results and Discussion

Figure 2 shows solar radiation per hour of the day for both the observation and the forecast for three solar parameters: GHI, DIF and DHI. Clearly demonstrated is that the three

parameters behave differently from each other and that the model captures observations very well with small biases across the parameters (shown in Table 2 and Table 3). Overall, the influence of time of the day on the bias is variable (Figure 3).

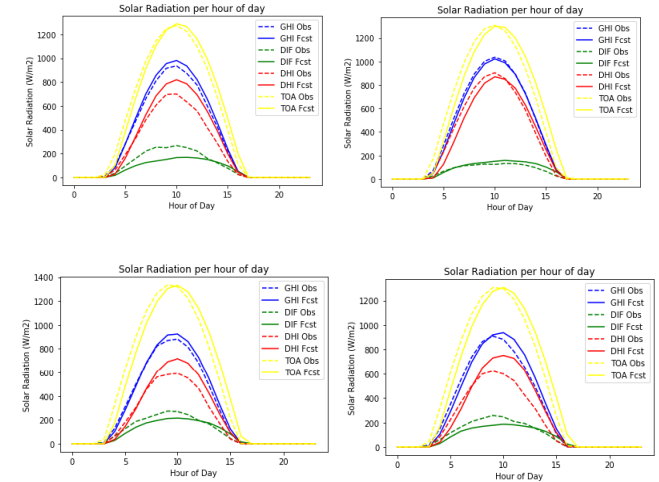


Figure 2: Solar Radiation per hour of day for top two performing stations (above) two least performing stations (below)

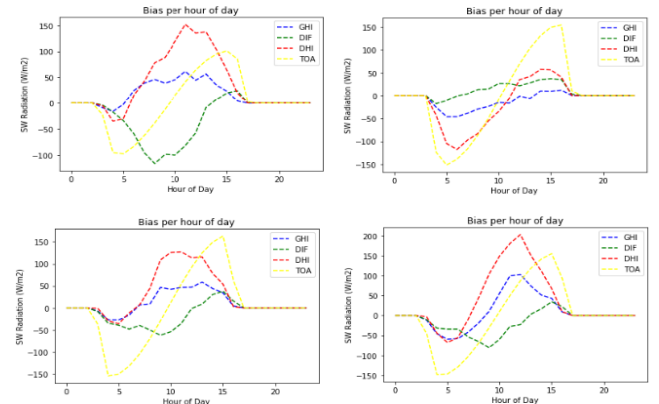


Figure 3: Bias per hour of the day for top two performing stations (above) two least performing stations (below)

Table 2: Statistics for top two performing stations

UPN			DAA		
GHI	Mean Bias	-8.89	GHI	Mean Bias	16.37
	MAE	29.02		MAE	56.35
	RMSE	68.24		RMSE	129.44

DIF	Mean Bias	9.10	DIF	Mean Bias	-25.48
	MAE	29.14		MAE	52.30
	RMSE	57.09		RMSE	119.23
DHI	Mean Bias	-12.69	DHI	Mean Bias	36.96
	MAE	56.91		MAE	90.22
	RMSE	112.74		RMSE	186.74
TOA	Mean Bias	-0.61	TOA	Mean Bias	3.35
	MAE	55.28		MAE	38.67
	RMSE	82.85		RMSE	62.23

Table 3: Statistics for least two performing stations

BTH			PLK		
GHI	Mean Bias	8.79	GHI	Mean Bias	10.89
	MAE	59.71		MAE	53.37
	RMSE	135.13		RMSE	120.34
DIF	Mean Bias	-14.38	DIF	Mean Bias	-11.76
	MAE	43.14		MAE	38.14
	RMSE	84.71		RMSE	75.79
DHI	Mean Bias	35.07	DHI	Mean Bias	29.25
	MAE	86.64		MAE	73.16
	RMSE	181.88		RMSE	161.65
TOA	Mean Bias	-0.40	TOA	Mean Bias	-0.58
	MAE	55.46		MAE	55.82
	RMSE	82.14		RMSE	83.43

### Conclusions

This study demonstrates that the SSPS can be used to forecast the three solar parameters GHI, DIF and DHI for any sites in South Africa with important solar energy applications. Results illustrated that the solar radiometric parameters derived from the UM model compared very well with the SAWS observation data. It is therefore expected that the model output could be used for mapping/forecasting solar energy potential across South Africa.

### Acknowledgments

The authors acknowledge South African Weather Service, Pretoria for support during the entire work.

### References

- Craig, O.O., Brent, A.C., Dinter, F. (2017). Concentrated Solar Power (CSP) Innovation Analysis in South Africa. *South African Journal of Industrial Engineering* 28(2) 14-27
- Herbst, L., Rautenbach, H. (2015). Climate Change Impacts on Mean Wind Speeds in South Africa. *The Clean Air Journal*, 25(2): 17-25.
- Singh, J., Kruger, A. (2017). Is the summer season losing potential for solar energy applications in South Africa? *Journal Energy Southern Africa* 22(2) 52-60.
- Singh, J., Tyagi, B., Ntsangwane, L. and Botai, J. (2017) Analysis of Aggregated Solar PV Output in South Africa. *Journal of Clean Energy Technologies* 5(5) 378-382
- Steenkamp, H., February, A., September, J., Taylor, A., Hollis-Turner, S., Bruwer, J. (2016). The influence of load shedding on the productivity of hotel staff in Cape Town, South Africa. *Expert Journal of Business and Management* 4(2) 69-77
- Wild, C., (1997). The Wilxon Rank Sum Test. University of Auckland, Department of Statistics

## ***Dependency characteristics of extreme precipitation indices in flood-prone areas of Gauteng***

Christina M. Botai<sup>1</sup>, Joel O. Botai<sup>1</sup>, Jaco P. de Wit<sup>1</sup>  
<sup>1</sup>South African Weather Service, Private Bag X097, Pretoria 0001

### ***Abstract***

Analysis of the frequency of occurrence of flood and the inherent relationship with temperature and precipitation extremes are essential for flood impact mitigation. In this paper, a bivariate copula model was used to assess the dependence of extreme precipitation indices namely the annual maximum one-day (hereafter RX1D) and five-day consecutive maximum precipitation (RX5D) across flood prone areas of Gauteng Province. The aim of this analysis is to demonstrate that extreme precipitation events not only exhibit dependence structures due to proximity in time but also in space and common covariates. The results indicate that the Survival Joe (16) is the best copula model for the maximum one-day precipitation, whereas the Survival BBS (20) and Survival Gumbel (14) are the most appropriate copula family model to describe the dependence of RX5D. Overall, based on the Spearman rho analysis, there exists a high probability of flood occurrences from one region to another. This implies that when flood mitigation measures are being put in-place for one region, similar plans ought to be placed on the other region to mitigate potential flood impacts.

Keywords: Climate, Precipitation intensity, SDII, Flash floods, Gauteng

### ***Introduction***

Rainfall-derived floods are considered as one of the most costly and dangerous natural and environmental hazards across the world (Hallegatte et al. 2013). The impacts of such floods are felt by various sectors, including water, agriculture, environmental and health. South Africa experiences various forms of floods that impair crops, settlement, roads and infrastructure. Devastating floods and flash floods that resulted in human fatalities as well as infrastructure and property loss have been reported across the country (e.g. Simpson and Dyson, 2018, CLS-CAELUM-1991-2017).

Precipitation data play a significant role in assessing extreme rainfall events that often lead to (flash) floods at national as well as global time-scales (Dyson, 2009). Such data can be as inputs to assessments of flood risk (Min et al. 2011; IPCC, 2012). The derived information can be used in flood mitigation measures as well as provide support towards the development and sustainability of effective operational policies as well as decision-making in relation to flood protection infrastructure.

Numerous studies have suggested a multivariate analysis on flood variables, particularly in flood-prone areas (Cameron et al., 1999; Blazkova and Beven, 2004; Requena et al. 2013). Although multivariate analysis can be computationally demanding, it provides valuable information, particularly regarding the natural probability of flood occurrences as well as the return period in terms of risk of reservoir overtopping. Alternatively, copula models can be used due to their flexibility on hydrological data requirements (Nelsen, 1999; Requena et al. 2013). For more information on copulas the reader is referred to Joe (1997), Nelsen (1999) and Salvadori et al. (2007). In this paper, the copulas methodology is adopted and utilized to investigate the probability of flood occurrence from a given area to another, with the focus being the flood-prone areas in Gauteng Province. For the purpose of this paper,

precipitation data from the South African Weather Service (SAWS) Automated Weather Stations (AWS), spanning 2002 – 2017 was analysed. These datasets were then used to derive the RX1D and RX5D indices which are considered here as proxies for extreme precipitation events associated with severe flooding.

### ***Study Area***

The study area considered in this contribution is the flood-prone areas of Gauteng Province. The areas were identified based on the South African Weather Service's (SAWS) publication – CAELUM. This publication documents weather-related events dated from the 1600's, and the document edition used is the CLS-CAELUM-1991-2017. Based on CAELUM publication, the flood-prone areas in Gauteng province include Alexandra along the Jukskei River, Soweto (e.g. Dobsonville, Orlando West, Klipspruit Valley Road and Dube), and most of the eastern parts of Johannesburg (e.g., Bedfordview, Benoni, Edenvale, Fourways, Kempton Park). However, due to data availability limitations, only four areas were considered. These areas were represented by four AWS, namely Irene, OR Tambo (ORT) International, Leeukop and Zuurbekom.

### ***Data***

The daily precipitation data (from 2002 – 2017) were obtained from four SAWS AWS stations located in flood-prone areas around Gauteng. Most of the stations initially selected were discarded due to the large number of missing data. The remaining four stations contained continuous data sets (~ 98%) for the selected study period. Details (including the Mean Annual Total Precipitation: MAP) of the selected stations are summarized in Table 1.

Table 1. List of the selected stations and their mean annual precipitation

Station [Station number]	Latitude	Longitude	MAP (mm)
Irene [1]	-25.91	28.21	636.21
ORT International [2]	-26.14	28.23	708.23
Leeukop [3]	-26.00	28.05	641.50
Zuurbekom [4]	-26.30	27.81	593.83

Methodology

The spatial-temporal characteristics of the RX1D and RX5D indices (definition given in Table 2) were described using the following statistical parameters, the median, standard deviation (STD), coefficient of variation (CV), skewness as well as kurtosis coefficients. The Copula model (Joe, 1997; Requena et al., 2013) was used to assess the dependence relationship of the RX1D and RX5D between the selected AWS stations. Generally, the copula model structure can be formulated as given in Equation 1

$$C_{\phi}(u, v) = \phi^{-1}(\phi(u) + \phi(v)), \text{ for } u, v \in [0, 1] \quad (1)$$

where  $\phi$  denotes the copula generator with domain  $[0, 1]$  and range  $[0, \infty]$ ,  $\phi^{-1}$  is the inverse copula generator, and  $u$  and  $v$  correspond to marginal distributions of the variables X and Y, here considered as  $RXnD_a$  and  $RXnD_b$ , where  $n = 1$  day or 5 day, and  $a$  and  $b$  denote the AWS stations (e.g.  $RX1D_{(station 1)}$  versus  $RX1D_{(station 2)}$ ). For each AWS paired stations, ten sets of copula families (see Table 3) were fitted to the RX1D and RX5D series to model the dependence relation as well as to assess the best copula that describes the dependence relation between the pair stations. In addition, the dependence relationship was assessed based on estimates of copula parameters as well as Kendall's tau and Spearman rho correlation (Genest and Favre, 2007).

Table 2. Extreme precipitation indices

Index	Description
RX1D	Annual maximum 1 day precipitation
RX5D	Annual maximum consecutive 5 day precipitation

Table 3. Bivariate elliptical copula families used and their rotation degrees as well as copula class

No.	Copula	Degrees rotation & class
13	Clayton	180 degrees, survival Clayton
14	Gumbel	180 degrees, survival Gumbel
5	Frank	
16	Joe	180 degrees, survival Joe
17	BB1	180 degrees, survival BB1
18	BB6	180 degrees, survival BB6
19	BB7	180 degrees, survival BB7
20	BB8	180 degrees, survival BB8
214	Tawn type 2	180 degrees,

Results and discussion

Time series characteristics of RX1D and RX5D

As given in Table 4, the median and STD statistical moments of the RX1D range from 14 to 17 and 16 to 18, respectively. These values are less compared to those derived from the RX5D index. The CV for RX1D ranges from 87% to 98%

whereas for RX5D the CV ranges from 93% to 103%. The kurtosis coefficient is positive across the indices and stations. In addition, all the stations across the indices exhibit positive skewness that range from 0.8 to 1.3 for RX1D and 0.7 to 1.6 for RX5D.

Table 4. Statistical characteristics of the RX1D and RX5D climate indices in terms of the median, STD, CV, kurtosis and skewness statistical parameters

Climate Index: RX1D					
Statistical moment	Median (mm)	STD	CV (%)	Kurtosis	Skewness.
Irene	13.8	16.3	93	2.87	0.77
ORT International	16.9	17.1	87	3.36	0.80
Leeukop	14.0	17.9	98	3.76	1.07
Zuurbekom	14.0	17.6	96	4.88	1.29
Climate Index: RX5D					
Irene	25.9	30.1	97	3.77	1.06
ORT International	27.3	28.8	88	2.51	0.68
Leeukop	27.1	32.9	103	7.32	1.63
Zuurbekom	25.5	29.0	93	3.77	1.06

Spatial dependence characteristics between RX1D and RX5D climate indices

The dependence analysis is aimed at assessing the probability of flood occurrences from one flood-prone area to another (Chebana and Ouarda, 2011). The results are summarized in Table 5. In the table, station 1 corresponds to Irene, 2 to ORT International, 3 to Leeukop and 4 to Zuurbekom. The Survival Joe (16) copula family is the most suitable for RX1D between stations 1 and 2, 1 and 4, 2 and 4 and 3 and 4. On the other hand, the Survival Gumbel (14) and Tawn type 2 (214) are the most appropriate copula families For RX1D between stations 1 and 3 as well as 2 and 3.

When considering RX5D climate index, the Survival BB8 (20) copula family is found to be the most suitable for stations 1 and 2 as well as 2 and 4 whereas Frank (5) copula family is the most appropriate for stations 1 and 3 as well as 2 and 3. In addition, the Survival Gumbel (14) copula family is found to be the most suitable for stations 1 and 4 as well as 3 and 4.

The Spearman rho correlation estimates for both RX1D and RX5D climate indices depicts a strong correlation across the different pairs of stations. This suggests that there exists a high probability of flood occurrence from one area to another. Thus, for instance, if Irene area experiences floods, there is a high probability that the ORT International will also experience flood during the same period. The  $p$ -values estimated from Kendall's tau are statistically insignificant across the climate indices and stations pairs.

Generally, the results demonstrate a strong spatial dependence of the copula families. In addition, the present study illustrate that the set of feasible copula models capable of representing the dependence structure of the precipitation extremes that could be associated to flooding are those from higher dimensional copulae. Our results illustrate that, that extreme precipitation events not only exhibit dependence structures due to proximity in time but also in space and common covariates.

This implies that flooding risks have inherent localized spatial-temporal dependence. This information is vital for flood risk preparedness, planning and management.

Table 5. Spatial dependency characteristics of climate indices between stations

Climate Index: RX1D			
Station	Copula family (Number)	Spearman rho correlation	Kendall's tau
1 - 2	Survival Joe (16)	0.78	0.6
1 - 3	Survival Gumbel (14)	0.80	0.64
1 - 4	Survival Joe (16)	0.70	0.54
2 - 3	Tawn type 2 (214)	0.84	0.64
2 - 4	Survival Joe (16)	0.704	0.55
3 - 4	Survival Joe (16)	0.703	0.54
Climate Index: RX5D			
1 - 2	Survival BB8 (20)	0.85	0.64
1 - 3	Frank (5)	0.841	0.67
1 - 4	Survival Gumbel (14)	0.75	0.55
2 - 3	Frank (5)	0.86	0.70
2 - 4	Survival BB8 (20)	0.78	0.60
3 - 4	Survival Gumbel (14)	0.72	0.54

Conclusion

This contribution analysed the probability of flood occurrences from one region to another using copula model. A range of copulas family models were fit to the RX1D and RX5D climate indices for different station pairs to obtain the most appropriate model that best describes the dependence relationship between the considered stations. For RX1D, the Survival Joe (16) was found to be the most appropriate copula model to describe the dependence relation in three station pairs. On the other hand, the Survival BBS (20) and Survival Gumbel (14) were found to be the best copula families to describe the dependence of RX5D. There exist a strong correlation of dependence structure between the paired stations. This suggests that when one station area experiences flood there is a high probability that the other areal station will also experience flood simultaneously.

References

Blazkova, S., Beven, K. (2004). Flood frequency estimation by continuous simulation of subcatchment rainfalls and discharges with the aim of improving dam safety assessment in a large basin in the Czech Republic, *J. Hydrol.*, 292, 153–172, 2004.

Cameron, D. S., Beven, K. J., Tawn, J., Blazkova, S., Naden, P. (1999). Flood frequency estimation by continuous simulation for a gauged upland catchment (with uncertainty), *J. Hydrol.*, 219, 169-187.

Chebana, F. and Ouarda, T. (2011). Multivariate quantiles in hydrological frequency analysis, *Environmetrics*, 22, 63-78.

Dyson, L (2009). Heavy daily-rainfall characteristics over Gauteng Province. *Water SA* 35 (5) 627-638.

Genest, C. and Favre, A.-C (2007). Everything you always wanted to know about copula modeling but were afraid to ask, *J. Hydrol. Eng.-ASCE*, 12, 347-368.

Hallegatte, S., Green, C., Nicholls, R.J., Corfee-Morlot, J. (2013). Future floods losses in major coastal cities. *Nat. Clim. Change*, 3: 802-806.

Joe, H. (1997). *Multivariate model and dependence concepts*, Chapman and Hall. London.

Nelsen, R. B. (1999). *An introduction to copulas*, Springer, New York.

Min, S.K., Zhang, F.W., Friederichs, P. and Hense, A. (2011). Signal detectability in extreme precipitation changes assessed from twentieth century climate simulations. *Climate Dynamics*, 32: 95-111.

Requena, A.I., Mediero, L., Garrote, L. (2013). A bivariate return period based on copulas for hydrologic dam design: accounting for reservoir routing in risk estimation. *Hydrol. Earth. Syst. Sci.*, 17: 3023-3038.

Salvadori, G., De Michele, C., Kottegoda, N. T., Rosso, R. (2007). *Extremes in nature, an approach using copulas*. Springer, Dordrecht, the Netherlands.

Simpson L., Dyson L. L. (2018). Severe weather over the Highveld of South Africa during November 2016. *Water SA*, 44: 75-85.

IPCC, (2012). *Managing the risks of extreme events and disasters to advance climate change adaptation. A special Report of Working Groups I and II of the Intergovernmental Panel on Climate Change* [Field, C.B., Barros, V., Stocker, T.F., Qin, D., Dokken, D.J., et al. (eds.)]. Cambridge University Press, Cambridge, UK, and New York, NY, USA, 582 pp.

## Poor-man's experimental design: Measuring wind and turbulence in a complex environment

Markus Geldenhuys<sup>1 a,b</sup>, Deon van der Mescht<sup>a</sup> and Liesl L. Dyson<sup>b</sup>

<sup>a</sup>South African Weather Service, Port Elizabeth Forecasting Office, Port Elizabeth Airport, Port Elizabeth

<sup>b</sup>University of Pretoria, Natural and Agricultural Sciences, Department of Geography, Geoinformatics and Meteorology, Lynwood Road, Pretoria

### Abstract

Studies of turbulence in complex terrain often involve expensive experiments. Following a fatal aircraft crash in the Kareedouw-Tsitsikamma Mountains, an experiment was designed cheaply following the 6 W's of design: *Why?*, *What?*, *Where?*, *When?*, *Who?* and *Whereby?*. Experiments within these mountains were conducted to measure blocking, gap flow and mountain waves. Initial experiments consisted of dropsondes and tethered sondes, while plans to create a dronesonde flying a pre-determined grid, or simultaneous soundings, was hampered by logistics. Ultimately, mountain waves, blocking and gap flow were successfully measured with instrumentation confined to; Automatic Weather Stations, party balloons and pilot balloons with radiosondes. This study makes recommendations on how to achieve this during any type of field study.

Keywords: Observations, Automatic Weather Station, Radiosonde, Dronesonde, Small-scale terrain, funding limitation

### 1. Introduction

The complexities of wind flow in complex terrain often result in features individually analyzed or simplified for research on numerical models. There is no doubt that meteorological features are complex and interact with one another, which makes observational studies so important. A fatal light aircraft crash, within the Kareedouw mountains, highlighted the need to equip forecasters with the knowledge of the turbulence produced when wind flow encounters complex small-scale terrain near a cold front (Van der Mescht and Geldenhuys, 2018). This study's aim was to design an experiment to measure blocking, gap flow and mountain wave interaction.

The scope of this article is to use case studies of windflow in complex terrain as an example experiment and provide notes and guidance on the lessons learnt in design. Sections 2 - 5 deal with the experiment and the article is concluded by a brief discussion and conclusion.

### 2. Prior to Experiment Design

The experiment was designed according to the 6 W's of design; *Why?* *Who?* *What?* *Where?* *When?* and *Whereby?*

- *Why?* – Why is this important? Why study this? Will the results warrant the financials and time required?
- *Who?* – Who can assist with this study? Who will benefit? Who are the relevant role-players? Who needs to provide permission to do the experiment? Who did similar work, and what can you learn from them?
- *What?* – What will be measured? What features and processes are expected? What is required to characterise these features? What are the initial conditions, and do this need to be measured? What instruments are at your disposal? What is the instrumentation bias?

- *When?* – When will this take place? How long will the experiment/event last? How frequent is this observed? When will you have optimal results? Is a preliminary study required in order to understand when and where the phenomena are expected?
- *Where?* – Where is the optimal location? What are the limiting factors (such as accessibility)? Where does what instruments need to be placed?
- *Whereby?* – By which methods and means will this be achieved? How will this project be completed?

*Who?*: Previously blocking was observed by radiosondes, LIDAR, satellite altimetry and a RADAR equipped aircraft (Neiman *et al.*, 2010 & Overland and Bond, 1995). Early gap flow studies (Reed, 1931) comprised of weather stations and radiosondes. Recent studies included the use of conventional weather stations combined with modern aircraft tail Doppler RADAR (Colle and Mass, 2000), satellite-borne synthetic aperture RADAR (Pan and Smith, 1999), LIDAR and dropsondes (Marić and Durran, 2009). Van der Mescht (2012) already defined a South African mountain wave experiment using upwind and downwind radiosondes.

*What?*: To design a successful experiment, one needs to fully understand the processes and the parameters that characterize and quantify the processes. Wind flow in a mountainous terrain can take different patterns, three of these are; mountain waves, gap flow and blocking. As wind approaches a barrier, firstly, the barrier blocks the wind, secondly, the wind flows around the barrier (gap flow) and lastly, a mountain wave form as the wind overshoots the barrier. Momentum, thermal forcing or pressure-gradient drives gap flow (Gaberšek and Durran, 2004).

Literature suggests parameters (all successfully applied by the experiment described here) characterizing blocking, gap flow and mountain waves include; Burger number, Rossby Radius-, thermal wind-, Bernoulli-equations, Froude-, Scorer-parameter and trapped wave criteria (Durran, 2003; Gaberšek and Durran, 2004 & Overland and Bond, 1995).

### 3. The Main Experiment

In this experiment the *When?*, *Where?* and *Whereby?* can be discussed in combination. The aircraft crash occurred in close vicinity to a passing cold front; this dictated a large portion of the *When?*. The *Where?* was similarly dictated and the study site was selected within the same mountain range as the crash; simply in a more accessible gap. Preceding the event phase, a six-month forecasting study was launched testing NWP forecasts on satellite images to confirm the *When?*. This saved costs by limiting the unsuccessful campaigns. A nowcasting approach in the field also saved costs during events. Clouds were studied in the vicinity and on satellite images; if mountain waves existed to the west (the system approached from the west) the experiment was continued. If a stationary mountain wave started drifting, the experiment was put on hold (as this means the changing of incident conditions). The *Whereby?* was severely limited by funding.

In these cases, exceptional planning is required to allow for optimal results with limited instrumentation and supplies. Another factor to consider is what instruments literature suggests, and what instruments are at hand. To design a successful experiment, it is required to understand the strengths and weaknesses of the instruments. In this study, small-scale features were measured using radiosondes, but would have been beneficial employ an area measurement (like Doppler RADAR, SODAR, etc.). A problem with the instrumentation was that some data fell within the instrumentation bias rendering the results questionable.

Selection of the study site can commence, following the understanding of the strengths and weaknesses of the instrumentation. An in-depth meteorological and topographical study preceded the selection of each automatic weather station (AWS) and radiosonde release site. Careful inspection with multiple study site visits (four in this study) is required to optimise the experiment. Site visits are to occur during meteorological conditions similar to the events that one would like to measure. During these site visits, careful consideration was given to the environment (spotting wind eddies in the Fynbos); looking at the clouds (Fig. 1(a) & (c)), the vegetation (Fig. 1(b)) the gliding birds, etc. Another fruitful exercise was the deployment of multiple smoke grenades and party balloons to provide visual indications of turbulence and wind flow.



Figure 1: (a) The Lenticular cloud over study site is an indication of where you want your balloon to drift. (b) As the tree in the study gap has no branches pointing southward, this is an excellent position to put an AWS to measure gap flow from the south. (c) The lee-side rotor cloud is an indication of where to ‘aim’ your balloon.

Following the selection of the study site, one should consider if there are any other complementary data sources in the vicinity? Data from satellite measurements can greatly enhance any study and if possible, events should be correlated with these passovers. Before designing this study’s surface AWS network, a review of the instrumentation surrounding the study site revealed four upwind AWSs. Field inspections of these rendered one station not usable; however, the remaining three completed the upwind AWS design, turning attention to the lee side.

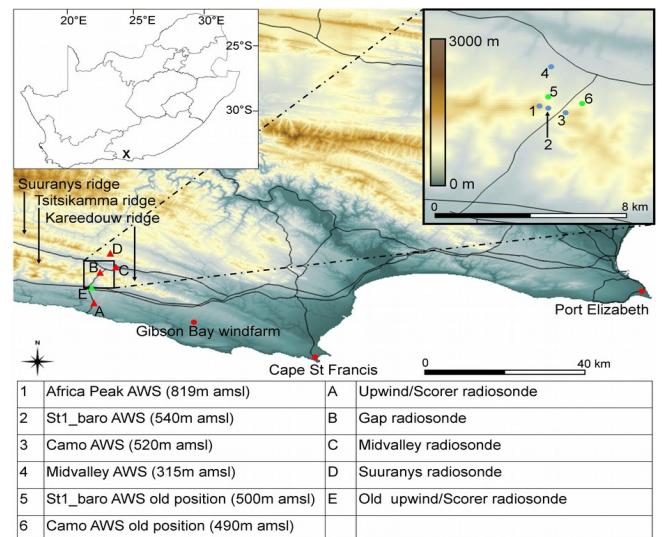


Figure 2: Topography of the study site and surrounding terrain. Radiosonde release locations include letters A through to E. The permanent AWS network consists of CSIR Gibson Bay windfarm, and the South African Weather Service owned Cape St Francis, and Port Elizabeth stations (top right). In the smaller window, the semi-permanent stations numbered and named in the table.

Instrumentation constraints left four temporary stations for field deployment. To represent a continuous look at incident conditions at peak height, Africa Peak was the first AWS site (1 on Fig. 2). However, the winds at this station were greatly accelerated by the compressional effect caused by the mountain; rendering measurements not representable of

upwind conditions. The strong winds also damaged the station rendering 11 months of wind speed data incorrigible, as regular inspections were not possible. The lesson learnt here was; accessibility is more important than the optimal location for the station. Potential temperature from this station provided key input in the analysis to infer wind flow (Overland and Bond, 1995 & Van der Mescht, 2012).

The purpose of stations 5 and 6 (Fig. 2) was to measure the divergence at the gap exit. Data analysis a month after deployment revealed these stations with below average wind speeds and frequently, odd directions. The conclusion was that these stations were located in eddies and the stations were moved to location 2 and 3. To determine the pressure and temperature gradients across the barrier, the lee valley was the position of the last available station. These gradients linked to the winds of station 2 and 3, yielded good results. A valuable lesson learnt was to control the experiment, but also at times let the data from the experiment dictate the next step.

The advantage of radiosondes is that they measure in the vertical and are cheap (in relation to RADAR). However, one needs to understand them in order to optimize their output. Firstly, release locations close to topography is troublesome; the radiosonde signal works through line-of-sight and is easily lost in close vicinity to high mountainous areas. Secondly, some radiosondes calculate pressure through the hypsometric equation, which requires an accurate surface pressure (or at the very least a good ballpark). Keeping any experiment consistent is crucial. A fixed ascent rate achieves this but requires some planning. A low ascent rate will result in a long ascent time and can result in a half-measured event. On the contrary, if the ascent rate is too fast, the number of data points are lower and there is a lower likelihood of riding the mountain wave into a downdraft. In this study, a fixed weight (0.5kg – same as Van der Mescht (2012)) upon inflation achieved a constant ascent rate; if the balloon lifted the weight, the supply of hydrogen was cut.

If the experiment demands multiple radiosondes, from different release locations, good access roads are required. In this study, radiosonde release locations were dictated by the processes; firstly, blocking required an upwind sounding to provide data for the parameters to characterize the feature. This radiosonde doubled to test the parameters calculated by measuring the physical blocking jet and tripled as an upwind (Scorer) sounding for mountain waves. Initially, this was released at location E (Fig. 2), however, this was not representative of upwind conditions as the radiosonde passed over the barrier too rapidly. To avoid this, the ascent location was moved further upwind of the barrier (Fig. 2 A). The

second radiosonde, released in the gap centerline (Fig. 2 B), doubled to measure the gap ‘jet’ and the gap exit conditions as it drifted downwind. This radiosonde obtained good results as it followed the gap flow in a downdraft into a hydraulic jump like feature; simulating an expansion fan. Here a low buoyancy balloon (balloon with a much-reduced ascent rate) was especially good at following the gap flow downwind. Radiosondes C (middle of the valley) and D (on top of the downwind ridge) both provided good results in the party balloon experiment and was included in the final experiment.

#### *4. Experiments leading up to the main experiment*

Testing of multiple experiments occurred for inclusion in the main experiment. The experiments and the reason for not including them in the main experiment were;

- *A tethersonde* is a radiosonde fixed to the surface by a line. If the upward force of the gas is weaker than the wind force on the balloon, the balloon will slowly drift to the surface in a semi-circle.
- *Dropsondes* have been successful in other studies, however, here many difficulties were encountered. To have the radiosonde wind (calculated from the GPS position) comparable to the normal soundings, the parachute and the ascending balloon needs an equal cross-sectional area. However, the wind exerts a strong horizontal force on large parachutes, closing them and drops the instruments to the surface. To keep the parachute open, a smaller parachute or stilts are recommended. An aeroplane, drone or a balloon can drop dropsondes. To use a balloon the setup was as follows; the radiosonde is attached to the parachute (which remained closed in ascent), attached to the balloon via a string. A special timer cuts the string on reaching its end.
- Research has employed *smoke* to visualize wind flow from as early as 1969 (Federal Aviation Administration, n.d). In this study, the value of smoke was again emphasized when it highlighted a rotor with an unexpected orientation – which otherwise would have remained undetected. Smoke is good for visualizing and plays a major role in designing an experiment; however, it cannot be quantified scientifically.
- *Party balloons* – already discussed

On paper designed experiments, never employed in the experiment, included;

- *A dronesonde* is a weather station attached to a drone and has massive potential. It is cheap, reusable and one can design a textbook experiment by controlling the drone flight path. Wind measurements were most challenging and it is recommended to place a 3-D sonic wind sensor  $\pm 30\text{cm}$  above the propellor; correcting the wind speed and direction with drone speed and tilt. The drone company was unable to assist further and the experiment halted.

- A *parasail* is a specialised parachute, pulled along by a moving vehicle, keeping it in the air. Parasail's exhibited potential, however, it was logistically pointless to have a car driving up and down to keep the parasail in the air.
- *Simultaneous ascents* from different locations (similar ascent rates) or from the same location (different ascent rates), will yield a 3-D look at a narrow band in the atmosphere – penetrating features at different positions.

## 5. Discussion & Conclusion

In today's day and age, many studies chose the cheaper option of a numerical study. This is useful, however, observational studies still have its place in validating models, while shedding light on unknown features. This project proved that careful consideration and exceptional planning according to the 6W's of design could optimally design an experiment. An in-depth study of literature and the environment needs to precede the design phase. Theory can aid the process, however, at times outside-of-the-box thinking and improvisation are required (in experiment design and especially while conducting the experiment). Smoke grenades and other simple experiments (e.g. party balloons) should test the first draft of the experiment (made from topographical maps and Google Earth). Observing and analyzing the data of at least one event is the only way of determining the feasibility of the final experiment. It remains important to control the experiment, but also let the data from the experiment dictate the next step. To facilitate any successful study, it is important to keep close to your aims and objectives. In this study, the greatest limiting factors were financial constraints, accessibility and arguably instrumentation bias.

This study proved that experiments can be conducted with basic instruments and cheaply. Data pooled together can save costs and maximize data as well as the results. To complete any observational project, an area observation is always beneficial (to study small-scale features and the time evolution of a feature) but not a prerequisite. Such instrumentation is not always in the budget, but if required, the meagre observations (by AWS and radiosonde) should then be input and compared to an adequate model run; to fill in the gaps and draw final conclusions.

This study produced an overload of data. To save costs during similar experiments, the recommendation is to analyze the data after every experiment (to ascertain whether another experiment is required). Much of the data produced during this study can be applied to other fields of research (e.g. renewable energy, agriculture, plant biology, etc.). Observations of gap flow and blocking were evident in both radiosonde and AWS data, but mountain waves were only

evident in radiosonde data. Data from AWSs successfully captured and explained gap flow, concerning across-barrier temperature and pressure gradients. Radiosonde data were useful, however, was insufficient to effectively measure and resolve fine-scale features such as expansion fans.

## Acknowledgements

I (M Geldenhuys) would like to express my gratitude to the late Prof. J van Heerden, for teaching me everything I know concerning experiment design. Mr E Engelbrecht, for the field campaigns. Ms E Geldenhuys for her support and proofreading. Mr H van Niekerk and the SAWS Eastern Cape forecasting team, without your support, this project would not have been possible. I would like to thank **InterMet Africa Systems** for radiosondes, **Air Liquide** for hydrogen gas and the **SAWS** for the study bursary.

## References

- Colle, B. A. and Mass, C. F., 2000. High-Resolution Observations and Numerical Simulations of Easterly Gap Flow through the Strait of Juan de Fuca on 9-10 December 1995. *Monthly Weather Review*, Vol 128, pp. 2398-2422.
- Durran, D., 2003. Lee Waves and Mountain Waves. In: J. Holton, J. Pyle and J. Curry, eds. *Encyclopedia of Atmospheric Sciences*. s.l.:Elsevier Science Ltd, pp. 1161-1169.
- Federal Aviation Administration, n.d. Wake Turbulence Training Aid, s.l.: Federal Aviation Administration.
- Gaberšek, S. and Durran, D., 2004. Gap Flows through Idealized Topography. Part I: Forcing by Large-Scale Winds in the Non-Rotating Limit. *J of the Atmospheric Sciences*, Vol 61, pp. 2846-2862.
- Marić, T. and Durran, D., 2009. Observations of Gap Flow in the Wipp Valley on 20 October 1999: Evidence of Subsidence. *J of Atmospheric Sciences*, Vol 66, pp. 984-1000.
- Neiman, P., Sukovich, E., Ralph, F. and Hughes, M., 2010. A Seven-Year Wind Profiler-Based Climatology of the Windward Barrier Jet along California's Northern Sierra Nevada. *Monthly Weather Review*, 138(April 2010), pp. 1206-1232.
- Overland, J. and Bond, N., 1995. Observations and Scale Analysis of Coastal Wind Jets. *Monthly Weather Review*, Vol 123, pp. 2934-2941.
- Pan, F. and Smith, R., 1999. Gap Winds and Wakes: SAR Observations and Numerical Simulations. *J of the Atmospheric Sciences*, Vol 56, pp. 905-922.
- Reed, T. R., 1931. Gap winds of the Strait of Juan de Fuca. *Monthly Weather Review*, Vol 59, p. 373-376.
- Van der Mescht, D., 2012. Mountain wave turbulence in the lee of the Hex River Mountains, Stellenbosch: MSc Dissertation, Stellenbosch University, Department of Geography and Environmental Studies.
- Van der Mescht, D. and Geldenhuys, M, 2018: *In Press* Meteorological applications.

## Improving ENSO forecasts through statistical intervention

Surprise Mhlongo and Willem A. Landman

Department of Geography, Geoinformatics and Meteorology, University of Pretoria

### Abstract

This paper is about statistically improving skill of global sea-surface temperature (SST) forecasts using the multivariate, Canonical Correlation Analysis (CCA) approach. The prediction skill levels of monthly global sea-surface temperature forecasts from coupled models has generally improved over the years. However, these levels may be further improved by applying statistical techniques to global model forecasts. Application of CCA to equatorial Pacific Ocean SST forecasts from two coupled ocean-atmosphere models is performed over several decades in order to improve the forecasts. It is demonstrated through standard verification procedures that the statistically post-processed multi-model SST forecasts have indeed been further improved. Moreover, this improvement outcores the improvement from correcting forecasts of individual models. Significantly, statistical post-processing has been found to improve the skill for El Niño-Southern Oscillation (ENSO)-neutral conditions so that its skill levels become comparable with the skill found when predicting ENSO states.

Keywords: Niño3.4. Model. Lead-times. Canonical correlation analysis. Cross-validation

### Introduction

Sea-surface temperatures (SSTs) influence atmospheric circulations significantly, especially over the tropics. In atmospheric modelling SSTs are used as a boundary condition of the atmosphere (Graham et al., 2000). SSTs therefore have the most noticeable influence on atmospheric circulations during ENSO events. There is a strong relationship between SSTs and climate trends over some regions in the world, including Africa (Landman and Mason, 2001). Previous studies show that SSTs are predictable for about 6 months through the use of statistical models (Landman and Mason, 2001). Here we focus on forecast lead times not exceeding this period.

Dynamical models that are used to produce SST forecasts always have systematic errors, which is a result from forecasts having low skill (Dewitt et al., 2011). However, skill in SST forecasts can be improved through the use of statistical corrections on the forecasts. These statistical corrections improve the forecasts without compromising the properties of the dynamical models. Moreover, statistical corrections have an additional benefit of calibrating models' outputs more closely to match observations (Tippett et al., 2005).

Notwithstanding local efforts to predict global SST anomalies (e.g. Landman and Mason 2001), here we focus on the equatorial Pacific Ocean where forecast skill is already high at several months lead-time.

### Data and Methods

#### A. Sea-Surface Temperature Data

Archived monthly sea-surface temperature forecasts for the period 1982 until 2017 are obtained from the data library of the International Research Institute for Climate and Society (IRI). SST forecasts from the Center For Ocean-Land-Atmosphere Studies (COLA) coupled climate model and Geophysical Fluid Dynamics Laboratory (GFDL) coupled climate model (COLA-RSMAS-CCSM4 and GFDLp5-FLOR-B01) are obtained. These archived SST forecasts are from the month of April 1982 to present. January SST forecasts are known to be highly predictive, in this study we therefore focus more on improving further the forecasts skill of this month. The data was initialized from 0-month up to 11-months

lead times for each calendar month, but here we considered only forecasts up to 3-months lead time. Global observed Optimum Interpolation (OI) SST data are obtained for the same period, also from the data library of the IRI.

#### B. Sea-Surface Temperature models and software

Climate Predictability Tool (CPT) software is used to combine the two data sets of archived monthly SST forecasts. The two sets of data are combined in order to form a multi-model forecast, consisting of COLA and GFDL models. This combination is done through merging the two data sets in CPT. A Canonical Correlation Analysis (CCA) is subsequently applied on multi-model forecasts and the individual models forecasts using OI SST data as predictand, in order to perform pattern correction on the forecasts. Further considerations are given to mean and bias correction of raw forecasts, in order to correct biases and the variances of forecasts. The performance of these methods is compared. All these statistical post-processing and correction methods are applied only over the Niño3.4 region (5°S to 5°N and 120°W to 170°W), in the equatorial Pacific Ocean (Barnston et al., 1997). The Niño3.4 region is shown in Fig. 1.

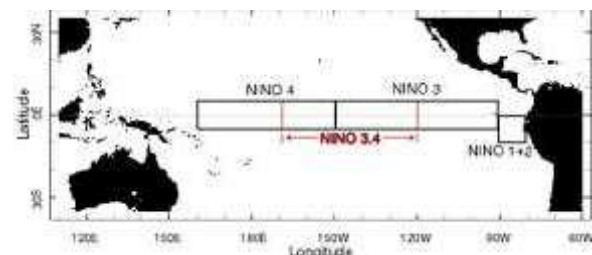


Figure 1: The study area of SST forecasts over the equatorial Pacific Ocean, Niño regions.

#### C. Forecasts lead times and Significant Tests

In improving SST forecasts for each month from April 1982 until October 2017, four lead times are considered. Forecasts produced at the beginning of the month of the forecast (zero-month lead time) until those produced three months before the month of the forecast (three-months lead time) are improved. Cross-validation of all the forecasts is performed in order to evaluate how much of corrections are made by the statistical methods on the archived

forecasts. The maximum number of modes are used for all variables and for the CCA is nine.

Retro-Active forecasts are made by all post-processing models. The first 18 years forecasts data are used as training period to make retro-Active forecasts for the remaining years of the forecasts data. Attributes diagrams and ROC area maps are subsequently produced for reliability (whether the confidence communicated in the forecasts is appropriate) and discrimination (whether the forecasts are discernibly different given different outcomes) of the forecasts.

Results and Discussion

The skill of a CCA statistically post-processed SST forecasts is compared with the skill of the SST forecasts without any statistical correction. Spearman’s correlation skill maps in Figs. 2 and 3 show a correlation between SST forecasts and their matching observations. There is an improvement in skill of the statistically corrected forecasts made by the COLA model as can be seen in Fig. 3(a) from the statistically uncorrected forecasts made by the same model in Fig. 2(a). The skill has increased notably over the northeastern part of the equatorial Pacific Ocean. The statistically corrected forecasts made by the GFDL model in Fig. 3(b) shows no significant improvement in skill from the forecasts without statistical correction as shown in Fig. 2(b). Multi-model statistically forecasts skill shown in Fig. 3(c) is higher than those of the statistically corrected and statistically uncorrected individual models. The skill has increased notably over the central part of the equatorial Pacific Ocean.

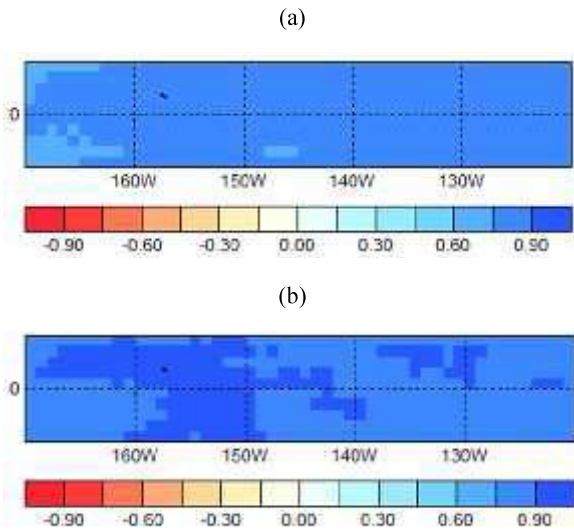


Figure 2 Spearman’s correlation skill maps of (a) COLA and (b) GFDL model forecasts of January SSTs at 3-month lead time over Niño3.4 region made with GCM Validation.

In account of the ability to discriminate forecasts, Figs. 4(a), (b) and (c) show that statistical post-processing improves the skill for ENSO-neutral condition so that its skill levels become comparable with the skill found when predicting ENSO states. The improvement of this skill is supported by the comparable level of reliability of the ENSO-neutral condition in Fig. 5(a), (b) and (c).

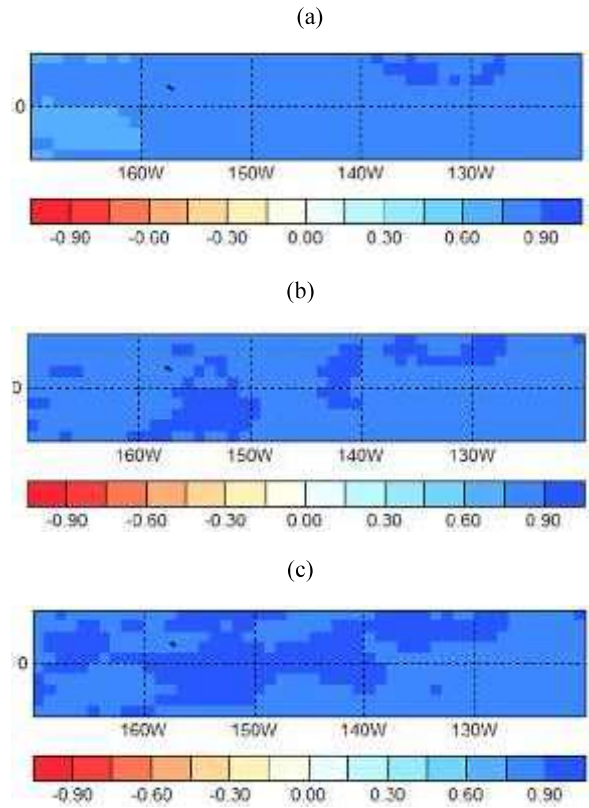


Figure 3. Spearman’s correlation skill maps of (a) COLA model and (b) GFDL model and (c) Multi-model statistically post-processed forecasts of January SSTs at 3-months lead time over Niño3.4 region.

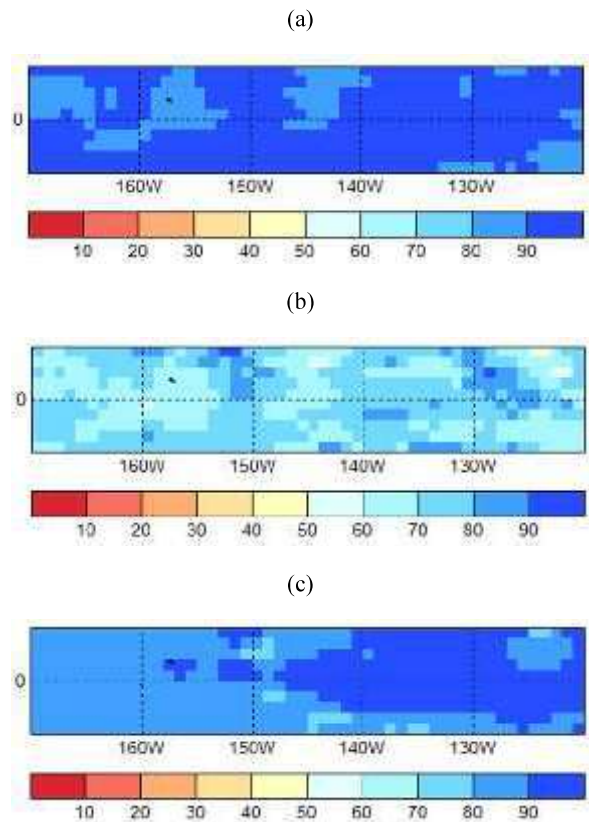


Figure 4. ROC area maps of (a) Above-normal, (b) Neutral and (c) Below-normal categories statistically post-processed SST forecasts of January at 3-months lead time from multi-model.

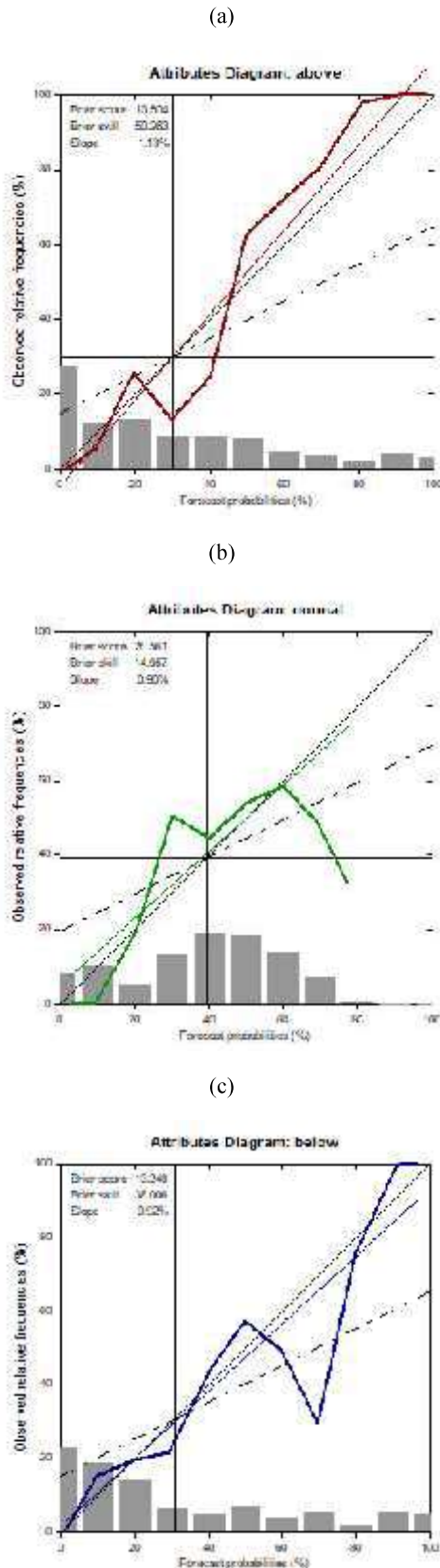


Figure 5. Attributes diagrams of (a) Above-normal, (b) Normal and (c) Below-normal categories statistically post-processed SST multi-model forecasts of January at 3-months lead time.

Conclusions

Statistical post-processing of SST forecasts over the central equatorial Pacific Ocean improves the deterministic (correlation) and probabilistic (reliability of forecast probabilities) skill of the forecasts. Multi-model statistically post-processed forecasts shows an improvement in the skill of the forecasts of the individual models. In addition to general improvement on the skill, statistical post-processing improves the skill of ENSO-neutral condition forecasts, which makes its skill levels become comparable with the skill found when predicting ENSO states. The general improvement of the Niño3.4 SST forecasts across all categories, including the near-normal category (ENSO-neutral states), can help to improve the use of rainfall seasonal forecasts over the Southern Africa region.

Acknowledgements

Comments and suggestions from Dr. E. Klopper and Dr. L. Dyson improved the quality of this paper. We thank Cobus Olivier from the South African Weather Service for assistance in script writing.

References

Barnston, A.G., Chelliah, M. and Goldenberg, S.B. (1997). Documentation of a highly ENSO-related sst region in the equatorial pacific: Research note. *Atmosphere-Ocean*. 35: 367-383.

Dewitt, D., Lee, D., Beraki, A. and Lotter D. (2011). Seasonal Rainfall Prediction Skill Over South Africa: One-versus Two-tiered Forecasting Systems. 27: 489-501.

Graham, R.J., Evans, A.D.L., Milne, K.R., Harrison, M.S.J. and Robertson K.B. (2000): An assessment of seasonal predictability using atmospheric general circulation models. *Q. J. R. Meteorol. Soc.* 126: 2211–2240.

Landman, W.A. and Mason, S.J. (2001). Forecasts of Near-Global Sea Surface Temperature Using Canonical Correction Analysis. *American Meteorological Society*. 14: 3819-3833.

Tippett, M.K, Barnston, A.G., Dewitt, D.G. and Zhang, R. (2005). Statistical Correction of Tropical Pacific Sea Surface Temperature Forecasts. *American Meteorological Society*. 18: 5141-5162.

## Black carbon and carbon monoxide over South Africa using satellite observation: Preliminary results

Lerato Shikwambana<sup>1,2\*</sup> and Venkataraman Sivakumar<sup>2</sup>

<sup>1</sup>Space Science Division, South African National Space Agency, Hermanus 7200, South Africa

<sup>2</sup>School of Chemistry and Physics, University of KwaZulu-Natal, Durban 4000, South Africa

### Abstract

Black carbon (BC) and carbon monoxide (CO) are byproducts of incomplete combustion from similar sources. BC is especially dangerous to human health because of its tiny size. BC affects visibility, harms ecosystems and exacerbates global warming. The two main methods used for this study was the Modern-Era Retrospective analysis for Research and Applications, Version 2 (MERRA-2) model which was used to determine the CO emission, BC concentration and the total surface precipitation. The Moderate Resolution Imaging Spectroradiometer (MODIS) was used to determine the Normalized Difference Vegetation Index (NDVI). In this study we observed that Gauteng, KwaZulu Natal, Mpumalanga and the Western Cape provinces were the major contributors of BC and CO in South Africa. Agricultural burning, industrial processing plants, power stations, diesel usage in agriculture and cars on the road could be the major activities for the production of BC and CO.

Keywords: Biomass burning, emissions, NDVI, veld fires

### Introduction

Human activities are responsible for most of the world's air pollution. The burning of fossil fuels such as coal and gasoline is the single largest source of air pollutants (Wuebbles and Sanyal, 2015). Fossil fuels continue to be used widely for heating, transportation, in generating electricity, in manufacturing and other industrial processes. Burning these fuels causes smog, acid rain and greenhouse gas emissions. Burning fossil fuels also increases some heavy metal contaminants and the amount of soot in the air. Too much of these air pollutants have harmful effects on human health (Kampa and Castanas, 2008; Coker and Kizito, 2018).

Fires are also associated with atmospheric pollution largely because of the release of carbon monoxide (CO), black carbon (BC) and ozone during biomass burning (Duncan et al., 2009). For example, farmers tend to burn crop residues after harvest as a means to control pests and weeds, improve soil fertility through ash and to facilitate planting of new crops (Vadrevu et al., 2011; Kharol et al., 2012). On the other hand, lightning strikes may serve as a source of natural ignition to wild fire, particularly in areas with predominantly dry vegetation biomass (Ruffener and Abrams, 1998; Müller et al., 2013). The vegetation fires result in large amounts of biomass burning (BB) aerosols being injected into the atmosphere.

Since there are predominately three main sources of CO and BC, industrial processes, residential fuel combustion and vegetation fires, we would like to investigate distribution of these constituents and how they are produced in South Africa.

### Data and Method

A veld fire risk map of South Africa is shown in Fig. 1. According to the map the eastern parts of South Africa are susceptible to veld fires whereas the interior and western parts of South Africa have a lower risk of veld fires. However, there are some areas in the western parts of South Africa that have a high risk of veld fires.

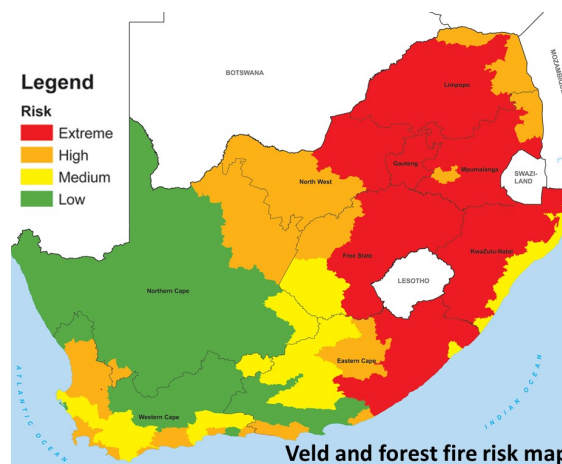


Figure 1. South African veld and forest fire risk map (Image from the Department of Agriculture forestry and fisheries, South Africa).

The Modern-Era Retrospective analysis for Research and Applications, Version 2 (MERRA-2) provides data from 1980 to the present. MERRA-2 was introduced to replace and extend the original MERRA dataset (Rienecker et al. 2011), which ended in February 2016. It is produced using version 5.12.4 of the GEOS DAS. Gridded data are released at a 0.625° longitude x 0.5° latitude resolution on 72 sigma–pressure hybrid layers between the surface and 0.01 hPa. The bottom 32 layers are terrain following, while remaining model layers from 164 to 0.01 hPa are constant pressure surfaces (Wargan et al. 2017). More details on MERRA can be found in Rienecker et al (2011). The data used in this study are the CO emissions, BC concentrations and the total surface precipitation. The spatial distributions of these parameters were determined in South Africa.

The Moderate Resolution Imaging Spectroradiometer (MODIS) has 36 channels spanning the spectral range from 410 to 14400 nm representing three spatial resolutions: 250 m (2 channels), 500 m (5 channels), and 1 km (29 channels). MODIS is currently flying on the NASA Terra and Aqua platforms. MODIS imagers on the Terra and Aqua Earth Observing System (EOS) platforms provide the capability for globally retrieving cloud and aerosol properties using passive solar reflectance and infrared techniques. A detailed description and operation of the Terra MODIS has been described by several authors such as Kaskaoutis et al. (2008), El-Metwally et al. (2010) and Baddock et al. (2009). The data used in this study is Normalized Difference Vegetation Index (NDVI). NDVI was used to measure healthy vegetation. High NDVI values indicate healthier vegetation whereas low NDVI values indicate less or no vegetation.

### Results

Seasonal distribution of BC concentrations over South Africa are shown in Fig. 2. In all the seasons it is observed that BC is dominant in the Gauteng Province (GP), eastern parts of the North West Province, western parts of the Mpumalanga Province, and lower and interior parts of the KwaZulu Natal (KZN) Province. However, the concentration of BC varies seasonally. For both GP and KZN the highest BC concentration was observed in the winter (JJA) and spring (SON) seasons, whereas the lowest BC concentration was

observed in the summer (DJF) season. In GP and KZN the highest BC concentrations were approximately  $1 \times 10^{-9} \text{ kg.m}^{-3}$  and  $0.9 \times 10^{-9} \text{ kg.m}^{-3}$  and the lowest BC concentrations were  $0.5 \times 10^{-9} \text{ kg.m}^{-3}$  and  $0.4 \times 10^{-9} \text{ kg.m}^{-3}$  respectively. The high BC concentration in GP and KZN in the winter season could be due to human induced fires that are used for bush control, weed and residue burning and harvesting practices.

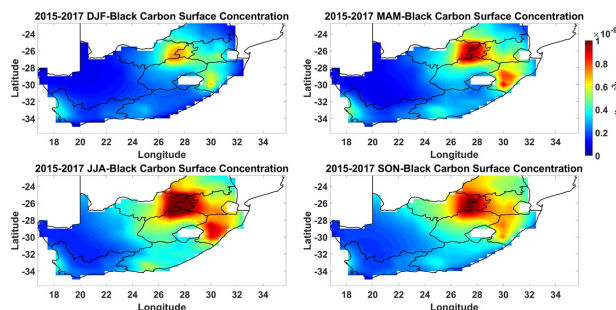


Figure 2. Seasonal spatial distribution of surface black carbon concentration over South Africa from 2015-2017.

The seasonal distribution of CO emissions over South Africa is shown in Fig.3. GP is the region with the most CO emissions seasonally, followed by the east of Mpumalanga and the south of KZN. The highest CO emission of  $2 \times 10^{-9} \text{ kg.m}^{-2}\text{s}^{-1}$  was observed in all the seasons in GP. Vehicle emission is one of the contributors of regional CO, however, engines and vehicle emissions-control equipment operate less efficiently when cold: Air-to-fuel ratios are lower, combustion is less complete, and catalysts take longer to become fully operational. This results in the higher concentrations of CO, amongst other products. In the eastern parts of Mpumalanga high CO emissions were observed in the spring and summer seasons. The south western parts of the Western Cape Province observed the highest CO emission in the summer season while the other seasons had lower CO emissions. Mpumalanga and the Western Cape experience the most severe fire seasons largely because of their native vegetation, topography and climate (Strydom and Savage, 2016).

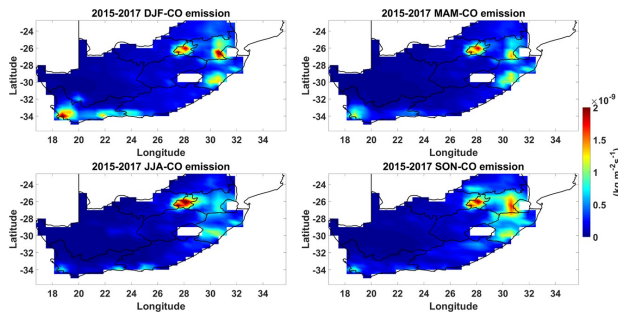


Figure 3. Seasonal spatial distribution of carbon monoxide emissions over South Africa from 2015-2017.

The Normalized Difference Vegetation Index (NDVI) is one of the most commonly used vegetation indexes for monitoring vegetation phenology. In this study we show the correlation between BC, OC and NDVI. Fig 4 shows the seasonal MODIS NDVI over South Africa. Seasonally we observed that the Northern Cape had the lowest average NDVI value  $\sim 0.15$  compared to the rest of South Africa. The highest NDVI value of 0.8 was observed in the summer season in KZN and the Mpumalanga province. These are the typical planting seasons of sugar cane. However, the NDVI values are lower in these provinces in the winter and spring seasons. Biomass burning could be one contributor to the decrease in the NDVI values in these provinces. The burning of sugar cane happens because (1) the burning process makes it easier to harvest the sugar cane, (2) the flames drive away cane rats and snakes that can pose a threat to workers and (3) burning reduces the weight of the harvested crop which means transport costs are lower and it improves the quality of the sucrose within the sugar cane stalk.

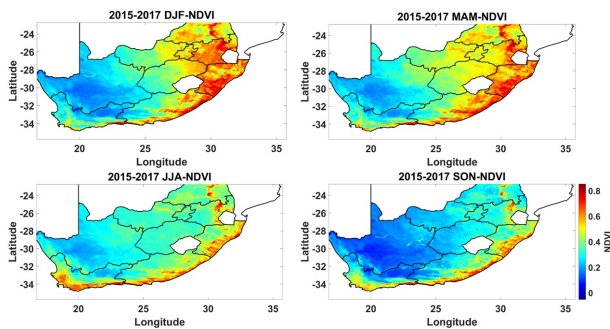


Figure 4. Seasonal distribution of NDVI over South Africa from 2015-2017.

In the southern parts of the Western Cape, where grapes are mostly grown for the production of wine, a high NDVI value of 0.8 is observed in the winter season. The grapes are grown in the winter season and harvested in the summer season hence a low NDVI value. Unlike sugar cane plantations in KZN and the Mpumalanga provinces, the vineyards are not

burnt hence low values of BC and CO. Therefore, a high CO emission (Fig. 3) in the Cape Town region in the summer season is from veld fires. In general, we observe that biomass burning, which releases BC and OC leads to low NDVI values.

Seasonal averaged precipitation distribution over South Africa is shown in Fig. 5. Precipitation is prevalent in the interior and the eastern parts of South Africa. The highest precipitation of 200 mm/month is observed in the summer season in the KZN and Mpumalanga provinces. It is interesting to observe that the areas with high precipitation correlate to areas with high NDVI (Fig. 4). For example, in the summer season, observations suggest that a heavy precipitation helps the vegetation to grow rapidly hence the high NDVI values in the KZN and Mpumalanga regions. The opposite is also true, areas with a low precipitation results in a low NDVI value. A low precipitation ( $>50$  mm/month) is observed in the winter season which implies dry conditions. These conditions favour the start and spread of fires. A high black carbon concentration (Fig. 2) in the winter season confirms this hypothesis.

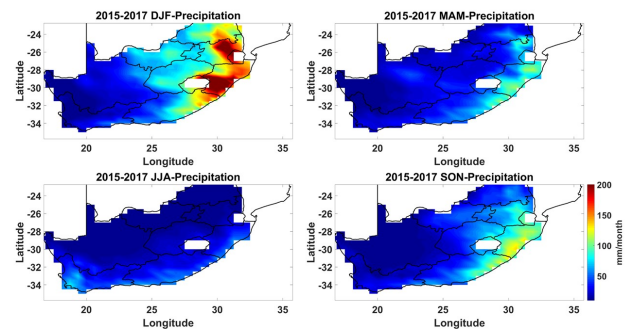


Figure 5. Seasonal distribution of precipitation over South Africa from 2015-2017.

#### Discussion and Conclusions

Biomass burning is a major contributor to BC and CO emissions. GP, KZN and the Mpumalanga provinces have shown to be the major sources of BC and CO seasonally. The activities that are responsible for the emission of BC and CO include agricultural burning, industrial processing plants, power stations, diesel usage in agriculture and cars on the road to name a few. The south western parts of the Western Cape Province showed that the major source of CO is in the summer season. This was mostly as a result of veld fires. The NDVI indicated that most of the vegetation was lost in the winter and spring seasons in GP, KZN and the Mpumalanga province from agricultural burning. In the Western Cape we suspect that the large vegetation could be from the growing of grapes in the winter season. And the less vegetation was as a result of harvesting and planting in the summer and autumn season respectively. Precipitation helps control the growth of

the vegetation and can clean air pollutants such as BC and CO in the atmosphere.

#### *Acknowledgements*

We acknowledge the GES-DISC Interactive Online Visualization and Analysis Infrastructure (Giovanni) for providing us with MERRA-2 and MODIS data. Analysis in this work was done using Matlab.

#### *References*

- Baddock, M.C., Bullard, J.E. and Bryant, R.G. (2009). Dust source identification using MODIS: A comparison of techniques applied to the Lake Eyre Basin, Australia. *Remote Sensing of Environment*. 113: 1511–1528.
- Coker, E. and Kizito, S. (2018). A Narrative Review on the Human Health Effects of Ambient Air Pollution in Sub-Saharan Africa: An Urgent Need for Health Effects Studies. *International Journal of Environmental Research and Public Health*. 15: 427.
- Department of Agriculture forestry and fisheries, South Africa. <http://www.daff.gov.za/daffweb3/Branches/Forestry-Natural-Resources-Management/Forestry-Regulation-Oversight/Forests/Urban-Forests/Forestry-Maps>. Last accessed 11/04/2018.
- Duncan, B., Kangmann, B., Textor, C., Trentmann J. and Van der Werf, G.R. (2009). Vegetation fire emissions and their impact on air pollution and climate. *Atmospheric Environment*. 43:107–116.
- El-Metwally, M., Alfaro, S.C., Abdel Wahab, M.M., Zakey, A.S. and Chatenet, B. (2010). Seasonal and inter-annual variability of the aerosol content in Cairo (Egypt) as deduced from the comparison of MODIS aerosol retrievals with direct AERONET measurements. *Atmospheric Research*. 97: 14–25.
- Kampa, M. and Castanas, E. (2008). Human health effects of air pollution. *Environmental Pollution*. 151: 362-367.
- Kaskaoutis, D.G., Kambezidis, H.D., Nastos, P.T. and Kosmopoulos, P.G. (2008). Study on an intense dust storm over Greece. *Atmospheric Environment*. 42: 6884–6896.
- Kharol, S.K., Badarinath, K.V.S., Sharma, A.R., Mahalakshmia, D.V., Singh, D. and Prasad, V.K. (2012). Black carbon aerosol variations over Patiala city, Punjab, India -A study during agriculture crop residue burning period using ground measurements and satellite data. *Journal of Atmospheric and Solar-Terrestrial Physics*. 84: 45–51.
- Müller, M.M., Vacik, H., Diendorfer, G., Arpaci, A., Formayer, H. and Gossow, H. (2013). Analysis of lightning-induced forest fires in Austria. *Theoretical and Applied Climatology*. 111: 183–193.
- Rienecker, M.M., Suarez, M.J., Gelaro, R., Todling, R., Bacmeister, J., Liu, E., Bosilovich, M., Schubert, S., Takacs, L., Kim, G.K., et al. (2011). MERRA: NASA’s Modern-Era Retrospective Analysis for Research and Applications. *Journal of Climate*. 24: 3624 – 3648.
- Ruffner, C.M. and Abrams, M.D. (1998). Lightning strikes and resultant fires from archival (1912-1917) and current (1960-1997) information in Pennsylvania. *Journal of the Torrey Botanical Society*. 125: 249-252.
- Strydom, S. and Savage, M.J. (2016). A spatio-temporal analysis of fires in South Africa. *South African Journal of Science*. 2016: 112.
- Vadrevu, K.P., Ellicott, E., Badarinath, K.V.S. and Vermote, E. (2011). MODIS derived fire characteristics and aerosol optical depth variations during the agricultural residue burning season, north India. *Environmental Pollution*. 159: 1560–1569.
- Wargan, K., Labow, G., Frith, S., Pawson, S., Livesey, N. and Partyka, G. (2017). Evaluation of the Ozone Fields in NASA’s MERRA-2 Reanalysis. *Journal of Climate*. 30: 2961-2987.
- Wuebbles, D.J. and Sanyal, S. (2015). Air Quality in a Cleaner Energy World. *Current Pollution Reports*. 1:117–129.

## Trends and variability of PM<sub>2.5</sub> in the Vaal Triangle area (Three Rivers, S26°4 E27°6): A pilot study

Yegeshni Moodley<sup>1</sup> and Venkataraman Sivakumar<sup>1</sup>

<sup>1</sup> University of KwaZulu-Natal, Westville campus

PM<sub>2.5</sub> for the Three Rivers monitoring station in the Vaal Triangle Airshed Priority Area was examined for 2010. The highest recorded PM<sub>2.5</sub> concentration of 99.1 µg/m<sup>3</sup> was in June, the lowest concentration of 7.4 µg/m<sup>3</sup> in August, with an annual mean of 34.0 µg/m<sup>3</sup>. January to July showed a closer correspondence between PM<sub>10</sub> and PM<sub>2.5</sub>, than August to December. Five exceedances were recorded; four in June and one in November. Future work includes examining a historical record of PM<sub>2.5</sub> in the VTAPA, for the period from 2007 to 2016.

Keywords: fine particulate matter, air quality, priority area

### Introduction

Fine particulate matter, or PM<sub>2.5</sub>, is becoming a pollutant of increasing interest in the air quality and health communities, and for regulatory authorities. PM<sub>2.5</sub> requires further investigation to quantify ambient concentrations in the South African context (Wright and Oosthuizen, 2010). The costs of morbidity and mortality associated with air pollution, including particulate matter, are high. A recent World Health Organisation (WHO) study estimated the costs at over US\$3 trillion for the European region only (WHO Regional Office for Europe OECD, 2015). Particulate matter can enter the respiratory system and the different size fractions deposit on tissue at varying levels within the body. PM<sub>2.5</sub> can travel as far as the lower respiratory tract, with the constituents < 1 µm depositing on alveoli and entering the bloodstream (Guarnieri and Balmes, 2014).

Particulate matter in the atmosphere has both natural and anthropogenic origins (WHO, 2013). Naturally occurring particulate matter is the result of windblown dust, volcanoes, biomass fires, and other naturally-occurring phenomena. Anthropogenic sources of particulate matter include industrial combustion processes, vehicle tailpipe emissions, waste incineration, domestic fuel burning, and mining. The composition of particulates is variable, to include possible components as heavy metals, and chemically-reactive compounds, such as diluted acids.

National ambient air quality standards were published in South Africa in 2009, and updated to include PM<sub>2.5</sub> in 2012 (Table 1) (Department of Environmental Affairs, 2012). Daily and annual standards are applied to address the acute and chronic impacts of PM<sub>2.5</sub>, respectively. A more stringent standard will also be effected in January 2030, which is intended to promote continuous emission reduction measures in the control of PM<sub>2.5</sub>.

**Table 1: National ambient air quality standards for PM<sub>2.5</sub>** (Department of Environmental Affairs, 2012)

Pollutant	Averaging period	Limit value (µg/m <sup>3</sup> )	Number of permissible exceedances per annum
PM <sub>2.5</sub>	24-hour	40 (25) <sup>1</sup>	0
	Calendar year	20 (15) <sup>1</sup>	0

<sup>1</sup>: Implementation date 1 January 2030

### Instrumentation and Method

Monitoring of ambient concentrations of atmospheric constituents provides useful localised measurements that can be used to derive information on impacts and management. Monitoring data are limited to the location where measurements are taken, and the radius of influence of the monitoring point on surrounding areas. Monitoring techniques for fine particulate matter are largely ground-based, and in South Africa, networks and sampling technology have progressed significantly in recent years.

The South African Air Quality Information System (Saaqis) is a web-based repository for air quality monitoring data collected from ground-based stations across South Africa. The South African Weather Services (SAWS) is the custodian of the system, however, data is validated by station owners and uploaded onto the system.

PM<sub>2.5</sub> data for the study was requested from Saaqis. A 1-year dataset from 2010 was used for the pilot study of the area. The area of interest was the Vaal Triangle Airshed Priority Area (VTAPA). The Department of Environmental Affairs has an established monitoring network in the area, as part of priority area management initiatives. The Three Rivers monitoring station is the

subject of this article. It is located in Vereeniging in the Sedibeng district of Gauteng (Fig. 1, Table 2). Activities influencing the emission profile include commercial, industrial and vehicular traffic from the city centre, Lethabo power station, and the Sasolburg industrial complex.

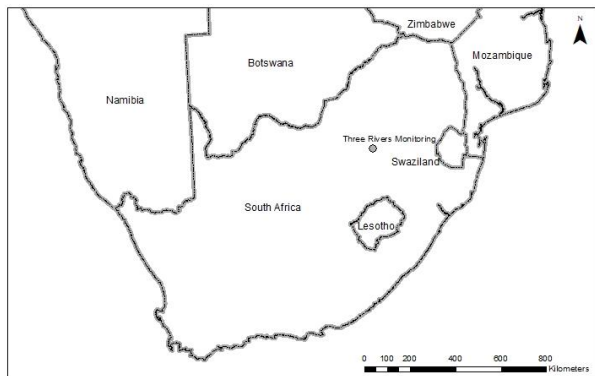


Figure 1: Monitoring station location

Table 2: Monitoring location and record history

Site	Latitude	Longitude
Three Rivers	S26°39'25,26"	E27°59'58,06"

### Results and Discussion

The daily average of PM<sub>2.5</sub> for the annual dataset shows variation across the year, with higher concentrations observed in July to August (Fig. 2). The monitoring record is relatively complete, with a large set of missing data noted in November and December. The highest recorded concentration of 99.1 µg/m<sup>3</sup> is in June, and the lowest recorded concentration of 7.4 µg/m<sup>3</sup> is in August. The annual mean is 34.0 µg/m<sup>3</sup>.

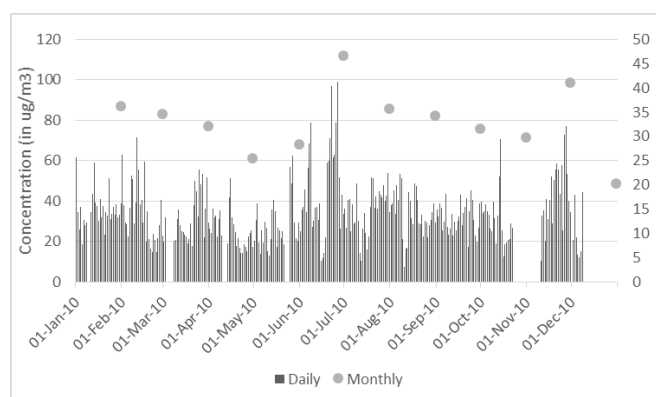


Figure 2: Daily and monthly monitored PM<sub>2.5</sub> for 2010 (in µg/m<sup>3</sup>)

Monthly averages display a decreasing trend from January to May, thereafter increasing to peak in July,

decreasing again to December. The peak value in November is possibly an anomaly or error due to limited data collection in the month. The highest monthly average of 46.6 µg/m<sup>3</sup> is in June, and the lowest monthly average of 20.4 µg/m<sup>3</sup> is in December.

PM<sub>10</sub> is also plotted with PM<sub>2.5</sub> for 2010 to determine the relationship between coarse and fine fraction particulate matter (Fig 3). Daily averages display an inter-relationship between coarse and fine particles at the site. PM<sub>2.5</sub> is generally lower than PM<sub>10</sub>, which is expected. The period January to July shows a closer correspondence between PM<sub>10</sub> and PM<sub>2.5</sub>, than the period August to December. Monthly averages also display a similar trend (Fig. 3b). This may indicate that PM<sub>2.5</sub> forms a larger fraction of PM<sub>10</sub> during drier months, and more coarse particles are present during wet months.

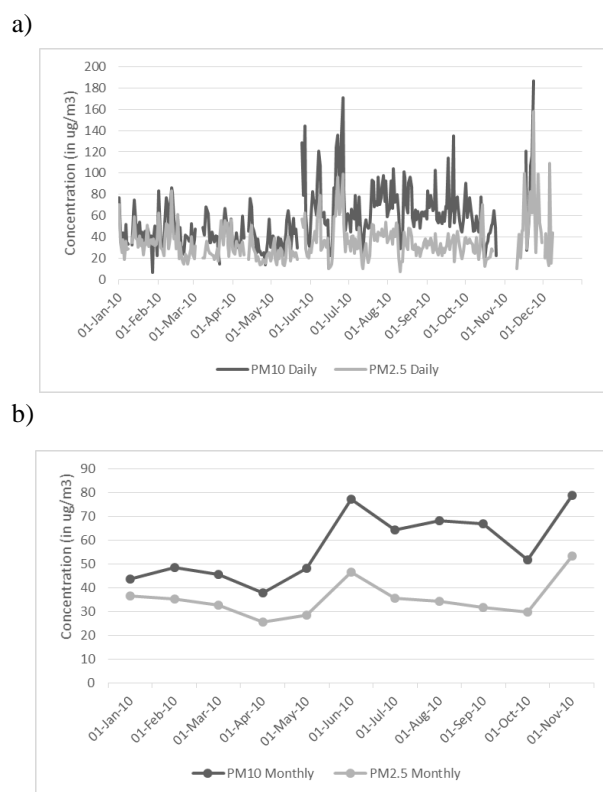


Figure 3: PM<sub>10</sub> and PM<sub>2.5</sub> a) daily, and b) monthly average for 2010 (in µg/m<sup>3</sup>)

Limited exceedances of PM<sub>2.5</sub> were recorded at the station (Table 3), of which four were recorded in June. One exceedances was recorded in November as well. The exceedances in June correspond to dry, mid-winter conditions, with reduced dispersion capability of the atmosphere (Tyson and Preston-Whyte, 2000).

**Table 3: Exceedances of daily PM<sub>2.5</sub> standard**

Date of exceedance	Concentration value (in µg/m <sup>3</sup> )
08 June 2010	78.9
22 June 2010	96.7
25 June 2010	79.0
26 June 2010	99.1
27 November 2010	77.3

emerging priority pollutant in South Africa - Impacts on Human Health', pp. 1–16.

Future work includes examining a historical record of PM<sub>2.5</sub> in the VTAPA, for the period 2007 – 2016. This will incorporate other monitoring stations in the network area. PM<sub>2.5</sub> concentrations and satellite remote sensing data will also be examined during the volcanic eruption that occurred in Culpaco, Chile in 2015.

### Summary

PM<sub>2.5</sub> data for the study was requested from Saaqis for the Three Rivers monitoring station as part of the VTAPA. A 1-year dataset from 2010 was used for the pilot study of the area. The highest recorded PM<sub>2.5</sub> concentration of 99.1 µg/m<sup>3</sup> is in June, and the lowest recorded concentration of 7.4 µg/m<sup>3</sup> is in August. The annual mean is 34.0 µg/m<sup>3</sup>. The period January to July shows a closer correspondence between PM<sub>10</sub> and PM<sub>2.5</sub>, than the period August to December. Limited exceedances of PM<sub>2.5</sub> were recorded at the station, of which four were recorded in June and one in November. Future work includes examining a historical record of PM<sub>2.5</sub> in the VTAPA, for the period 2007 – 2016.

### Acknowledgements

Dr Sangeetha is gratefully acknowledged for her assistance with pre-processing the dataset using Matlab.

### References

- Department of Environmental Affairs (2012) *National ambient air quality standard for particulate matter (PM2.5)*.
- Guarnieri, M. and Balmes, J. R. (2014) 'Outdoor air pollution and asthma', *The Lancet*. Elsevier Ltd, 383(9928), pp. 1581–1592. doi: 10.1016/S0140-6736(14)60617-6.
- Tyson, P. and Preston-Whyte, R. (2000) *The Weather and Climate of Southern Africa*. 2nd edn. Oxford University Press Southern Africa, Cape Town.
- WHO (2013) 'Review of Evidence on Health Aspects of Air Pollution—REVIHAAP Project; First Results', p. 29p.
- WHO Regional Office for Europe OECD (2015) 'Economic cost of the health impact of air pollution in Europe: Clean air, health and wealth.', *European Environment and Health Processes*, pp. 1–54.
- Wright, C. and Oosthuizen, R. (2010) 'PM<sub>2.5</sub> as an

## ***Finding a relationship between meteorological Air Dispersion Potential and Particulate Matter for six sites in South Africa***

Anzel de Lange<sup>\*1</sup>, Liesl Dyson<sup>1</sup>, Rebecca M Garland<sup>1,2</sup>

<sup>1</sup> Department of Geography, Geoinformatics and Meteorology, University of Pretoria

<sup>2</sup> Council for Scientific and Industrial Research (CSIR)

Measured hourly PM concentrations from air quality monitoring stations situated in Gauteng, Mpumalanga and Limpopo has been collected and analyzed. Meteorological parameters, which have an influence on the dispersion of pollutants in the atmosphere were modelled and used to calculate Air Dispersion Potential (ADP). ADP is an index developed here to describe the meteorological potential for pollution dispersion in the atmosphere. PM<sub>10</sub> and PM<sub>2.5</sub> concentrations at six stations were compared with calculated ADP values. It was found that for all scenarios, there exists a weak relationship between the ADP index and PM classes. Summer and winter seasons were considered separately in order to establish when, where and for which PM concentrations classes, the ADP forecast performs best. Two qualifying sites, with highest accuracy, were studied further. For the cases considered, it was shown that the most successful class predicted was for high, and consequently dangerous, PM concentrations. The performance of the ADP forecast in different classes should be investigated further at well-maintained background stations.

Keywords: Air pollution, Particulate Matter, Pollution dispersion, Air Dispersion Potential

### *Introduction*

Particulate Matter (PM) pollution, being possibly the most complex type of pollution, has recently become a global issue due to its effects on health and the environment. Owing to the negative impacts of coarse and fine particulates, it is necessary for countries to set standards for, and attempt to lower, PM pollutant concentrations. Dangerously high concentrations of PM are problematic for many developing and industrialized countries throughout the world. South Africa is also affected by the particulate pollutant problem; this becomes especially clear when considering the WHO Global Urban Ambient Air Pollution Database (WHO, 2016).

Meteorological science is an important tool in the field of air pollution research, especially in countries where measured air pollutant concentration and emission data are scarce (Fajersztajn et al., 2014). The combined characterization of the ability of the atmosphere to adequately dilute and disperse any admixture is often referred as Air Pollution Potential (APP) and was proposed by Niemeyer in 1960. APP is based on two meteorological parameters, mixing height and wind speed and has been investigated over the United States by Holzworth (1962 & 1967). The possibility of using single meteorological parameters to find relationships with pollutant concentrations has been investigated in many studies internationally (Zhang et al., 2015, Kim et al., 2005, Li et al., 2017, Grundström et al., 2015, Olvera Alvarez et al., 2018). Using a combination of meteorological information, as in the index used here, to describe the dispersion potential of the atmosphere, may be an improvement.

The meteorological potential of a region to disperse pollution should play a major role in decision-making with regards to the addition and expansion of air pollution producing industries. This is especially true in developing and industrialized countries where dangerously high concentrations of PM are a significant problem. Theoretical and modelling results can be utilized for assessing the background climatic and air quality conditions needed for planning.

Finding a meaningful relationship between meteorological parameter/s and PM concentrations in South African could lead to the possibility of using these parameters as a proxy for pollutant concentrations. Pollutant concentration forecasts based on meteorological parameters can be vital in health and early warning for high-risk groups of people.

### *Air Dispersion Potential*

In this paper we present Air Dispersion Potential (ADP) which is a comprehensive and contemporary representation of the characteristics of air pollution. The ADP calculation is used to determine the potential for air to disperse pollutants based on three meteorological parameters: (i) horizontal wind velocity ( $\text{ms}^{-1}$ ), (ii) mixing height (m), and (iii) atmospheric stability, which is described by Monin-Obukhov Length (MOL), measured in meters (m) (Swart, 2016). The ADP index is based on the conditional probability distribution of these parameters, which allows for constructing the relevant probability tree. Probability of the comprehensive ADP index (Equation 1) is the multiple of probabilities for wind speed  $P(|\vec{V}|)$ , height of the PBL  $P(H)$ , and stability  $P(L)$ .

Therefore, the probability tree for individual realization of ADP will be:

$$P(\text{ADP})=P(|\vec{V}|)P(H)P(L) \quad (1)$$

The dimension of the ADP is  $\text{m}^3\text{s}^{-1}$  multiplied by the stability factor  $P(L)$ . Therefore, ADP index gives how many cubic metres per second (ventilation rate) are passing through a certain point and what the conditions are for the pollutants to diffuse. The thresholds for the meteorological parameters are based on a combination existing classifications. Wind speeds were classed according to the Beaufort Wind Scale, mixing height (MH) classes for ADP calculation were adapted from definitions of stable and unstable atmospheric boundary layer conditions as defined in Seibert et al. (2000) and MOL was classed as in Gryning et al. (2007), Sathe et al. (2011) and Peña et al. (2010).

Table 1. Wind speed, mixing height and MOL intervals, resulting ADP value and ADP classification.

Meteorological parameter	Very unfavourable	Unfavourable	Moderate	Favourable	Very Favourable
Wind speed	0 to 0.2 ms <sup>-1</sup>	0.3 to 1.5 ms <sup>-1</sup>	1.6 to 3.3 ms <sup>-1</sup>	3.4 to 5.4 ms <sup>-1</sup>	>5.5 ms <sup>-1</sup>
Mixing Height	0 to 150 m	150 to 300 m	300 to 500 m	500 to 800 m	>800 m
MOL	10 to 200 m	200 to 500 m	> 500 or < -500 m	-200 to -500 m	-50 to -200 m
ADP (Result)	20	> 20 to 40	> 40 to 60	> 60 to < 80	>= 80
ADP class	1	2	3	4	5

The intervals for the wind speed, mixing height, and MOL are quantified by proxy for very unfavourable, unfavourable, moderate, favourable, and very favourable for pollution dispersion. Table 1 provides the classification of the resultant ADP parameter. The coefficients for the ADP index are chosen in such a way that the ADP value can be in the range 20 to 100.

Methodology & Data

a. Study region and PM data

Six sites across South Africa (Fig. 1) were chosen for this study based on their location and availability of data. Marapong and Lephalale are located 10 km from one another. Marapong is a low-income residential area (both informal and formal dwellings) and Lephalale is a residential area (mostly formal dwellings), both located close to a mine and two power stations. Zamdela, a residential site, with industries to the north, mines to the west and is surrounded by residential dwellings. Xanadu is residential site with objective to monitor background air concentrations. Camden is located less than 2km from a power station and in close proximity to a couple of mines. The site in Witbank is influenced by urban, industrial and rural pollution sources.

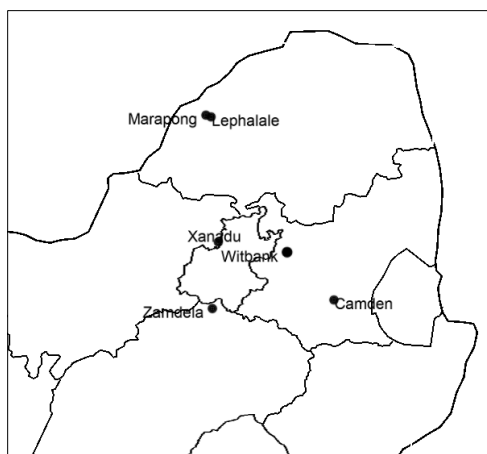


Figure 1. The locations of 6 sites chosen for this study.

Hourly measured PM concentration data from the South African Air Quality Information System (SAAQIS) was obtained for each of the chosen sites for 2013 to 2016.

b. The Air Pollution Model (TAPM)

The Air Pollution Model (TAPM), developed by Australian

CSIRO Atmospheric Research Division, is a prognostic air-pollution model which simulates meteorology and air chemistry. TAPM predicts the flows important to local-scale air pollution transport against a background of larger-scale meteorology provided by synoptic analyses (Hurley, 2008). The meteorological component of TAPM was used to produce the modelled meteorological data needed for the calculation of ADP.

c. Evaluating ADP performance

In order to statistically investigate the relationship between PM concentrations and ADP, both variables are classed according to pre-determined intervals. Categories for PM are site specific and based on 20th percentiles of the actual measured pollutant concentration data after quality correction. Very favourable ADP and very low PM concentrations were allocated classifications of 5 while very unfavourable ADP and very high concentrations of PM were classed as 1. This process simplified the data assisted in determining a relationship between the two variables.

Table 2. Description, equation and ranges for the chosen categorical statistics used to evaluate forecast performance (Adapted from CAWCR, 2018).

Score	Description	Equation	Range	Perfect score
A	A gives the fraction of correct forecasts in each category.	$A=(H+CN)/Total$	0 to 1	1
POD	POD measures the hit rate of the forecast. POD does not take into account false alarms.	$POD=H/(H + M)$	0 to 1	1
SR	SR gives an indication of the observed classes that were correctly forecasted. SR does not consider misses.	$SR=H/(H+FA)$	0 to 1	1
FAR	FAR is an indication of the predicted events that did not occur.	$FAR=FA/(FA+C N)$	0 to 1	0

While evaluating the model performance, we considered the following statistics in Table 2. The statistical scores and ratios described in Table 2, Accuracy (A), Probability of Detection (POD), Success Ratio (SR) and False Alarm Ratio (FAR) can be calculated from the information contained in a multi-category contingency table. To calculate statistics from contingency tables, all the data in the table needs to be classified as: Hits (H) (event forecasted and observed), Misses (M) (event not forecasted but observed), False Alarms (FA) (event forecasted but not observed), and Correct Negatives (CN) (event forecasted not to occur and was not observed).

Results and Discussion

Considering the diurnal variation of ADP and PM (Fig. 2), it is clear that ADP values peak during the day, between 07:00 and 18:00, and stays mostly constant during the night with values varying between 20 and 40. Because the ADP calculation is based on parameters which are influenced by solar radiation, like MOL and mixing height, it is expected that ADP values are more favourable during the day when solar radiation is peaking.

While ADP peaks for a few hours during the day, PM pollution concentrations peak in the morning and again in the evening. A similar pattern is present for most sites (Xanadu, Lephallale, Zamdela, Witbank) in Fig. 2. These particulate pollution peaks, in the morning and afternoon, can be attributed to traffic and residential sources, like domestic burning. PM<sub>2.5</sub> concentrations at Marapong are lower than at any of the other monitoring stations considered and stay relatively constant throughout the day. PM concentrations at Camden also differ from this pattern, only showing a slight peak at night. This monitoring station is also located near various mining and power generation activities and close to a power station, similar to Marapong.

a. Identifying a relationship

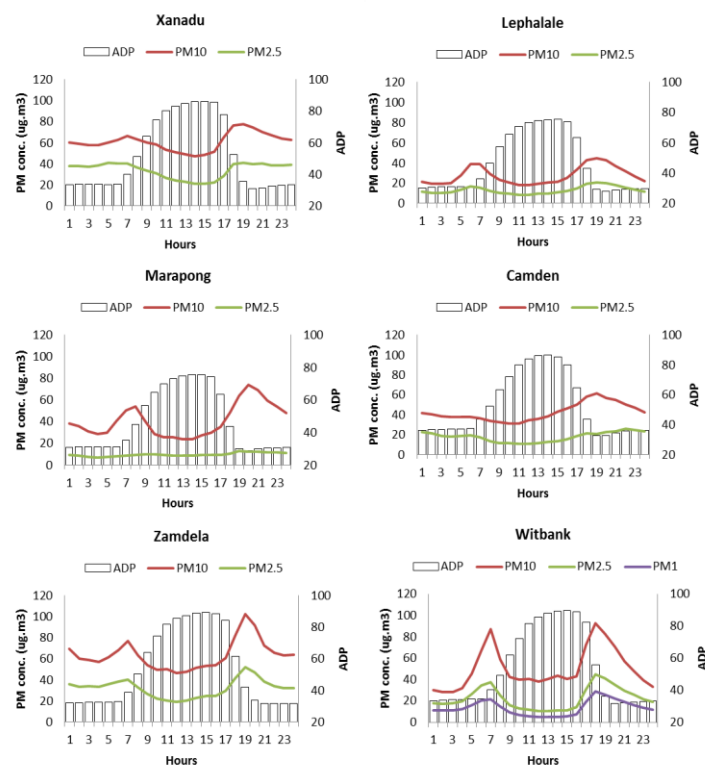
Scatterplots for each site and type of PM (figures not shown) were investigated and all cases showed similar patterns. The dominant ADP class for all observations is class 2. This means that most of the hours with observations experienced unfavourable conditions for pollution dispersion. The most frequent class combination is PM<sub>10</sub> class 1 (high pollutant concentration) and ADP class 2 (unfavourable conditions). The ADP class that occurs the least is class 1 which indicates very unfavourable ADP.

In order to investigate the strength of the relationship between ADP and PM classes, it is useful to calculate the correlation between the two datasets. All calculated correlation coefficients ADP and PM concentration classes vary from weak to medium strength and are positive. This means that higher classes (more favourable) ADP are related to higher classes (lower concentrations) of PM.

Xanadu and Lephallale, have relatively good correlations in the winter for both PM<sub>10</sub> and PM<sub>2.5</sub> and very weak correlations in the summer. For all stations, except Camden (for PM<sub>10</sub>) and Marapong, the correlation between ADP and PM concentration is stronger for the winter case. In most of the cases considered (Xanadu, Camden, Zamdela, Witbank) coarse particulates show a weaker relationship between its concentration classes and ADP and fine particulates show more promising results with medium

strength relationships.

Figure 2. Average hourly PM concentrations and ADP values for all sites throughout the entire period (2013 to 2016).



b. Forecast performance

Using the information produced from multi-category contingency tables, accuracy for winter and summer for each station was calculated. Accuracy, for the cases considered, was never higher than 0.30. This means that the fraction of forecasts in the correct category is less than 30% for all cases.

Overall, the best scoring sites in terms of accuracy are Zamdela in summer and Lephallale during the winter. These two sites are investigated further using POD, SR and FAR scores. The POD gives an indication of how well the PM classes were forecasted by the predictor (ADP). POD and SR are used together with the FAR in order to get a clear picture of the performance of the forecasting tool.

Lephallale (Fig. 3) produces very similar results for PM<sub>10</sub> and PM<sub>2.5</sub> when considering SR, POD and FAR. High SR scores and low POD scores and relatively low FAR in class 1. Class 2 has a high POD score, lower SR and an increase in FAR from class 1. Zamdela in the summer (figure not shown) has no events in class 1. Class 5 shows relatively high FAR for PM<sub>10</sub> and a lower score (0.6) for class 5 of PM<sub>2.5</sub>. POD and SR scores show similar patterns for PM<sub>10</sub> and PM<sub>2.5</sub>. Class 2 scores well with respect to POD (as for Lephallale).

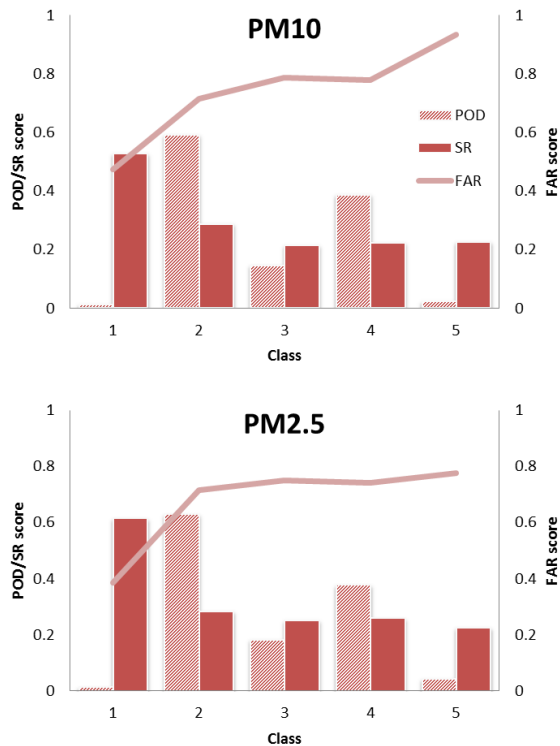


Figure 3. Visual representations of POD, SR and FAR for Lephallale in the winter.

This means, for Lephallale, a relatively large fraction of class 1 forecasted events were observed even though only a few events in this class actually occurred. Class 2 performs the best with respect to hit rate for both Lephallale and Zamdela, this means that class 2 was relatively well-forecasted by the predictor (ADP).

### Conclusions

From the results, it can be concluded that ADP as a forecasting tool performs best in class 2 as indicated in Fig. 3. Class 2 for ADP is for unfavourable conditions while class 2 for PM concentrations is high. In the study of particulate pollutants, this is a significant result, ADP classes work best when used to forecast high concentration events of PM which are dangerous to human health.

The results for correlation and covariance between ADP and PM classes are weak and accuracy scores for predicting PM classes from ADP are low. The locations of the monitoring stations must be considered when interpreting the results obtained. The chosen sites are classified as residential, industrial, rural and urban. Most of these monitoring stations are located in or close to residential areas with industries, mines and roads in the vicinity. For the sites considered, pollution dispersion is heavily affected by factors that are not meteorological. The performance of the ADP forecast in different classes should be investigated further at well-maintained background stations.

### Acknowledgements

We would like to acknowledge The South African Weather Service (SAWS) for providing 2013 to 2016 pollutant concentration data for all investigated sites through SAAQIS. We also extend appreciation to the Laboratory for Atmospheric Studies (LAS) at the University of Pretoria and Professor George Djolov.

### References

- Collaboration for Australian Weather and Climate Research (CAWCR). (2018). [Online] Available at: <http://www.cawcr.gov.au/projects/verification/>
- Fajersztajn, L., Veras, M., Barrozo, L. and Saldiva, P. (2014). Air monitoring coverage in low-income countries: an observational study. *The Lancet*, 384, pp. S14.
- Grundström, M., Hak, C., Chen, D., Hallquist, M., & Pleijel, H. (2015). Variation and co-variation of PM10, particle number concentration, NOx and NO2 in the urban air - Relationships with wind speed, vertical temperature gradient and weather type. *Atmospheric Environment*.
- Gryning SE, Batchvarova E, Brummer B, Jørgensen H, Larsen S. (2007). On the extension of the wind profile over homogeneous terrain beyond the surface layer. *Boundary-Layer Meteorology* 2007; 124(2):251–268, doi: 10.1007/s10546-007-9166-9.
- Hurley, P. (2008). TAPM V4. User Manual. CSIRO Marine and Atmospheric Research Internal Report No. 5.
- Holzworth, G. (1962). A Study of Air Pollution Potential for the Western United States. *Journal of Applied Meteorology*, 1(3), pp.366-382.
- Holzworth, G. (1967). Mixing Depths, Wind Speeds and Air Pollution Potential for Selected Locations in the United States. *Journal of Applied Meteorology*, 6(6), pp.1039-1044.
- Kim, K., Kim, M., Hong, S., Youn, Y., & Hwang, S. (2005). The effects of wind speed on the relative relationships between different sized-fractions of airborne particles. *Chemosphere*.
- Li, X., Ma, Y., Wang, Y., Liu, N., & Hong, Y. (2017). Temporal and spatial analyses of particulate matter (PM10 and PM2.5) and its relationship with meteorological parameters over an urban city in northeast China. *Atmospheric Research*.
- Niemeyer, L. E., (1960). Forecasting Air Pollution Potential, *Monthly Weather Review (Mon. Wes. Rev.)*, 88(3), 88-96.
- Olvera Alvarez, H., Myers, O., Weigel, M., & Armijos, R. (2018). The value of using seasonality and meteorological variables to model intra-urban PM 2.5 variation. *Atmospheric Environment*.
- Peña, A., Gryning, S. and Mann, J. (2010). On the length-scale of the wind profile. *Quarterly Journal of the Royal Meteorological Society*, 136(653), pp.2119-2131.
- Sathe, A., Mann, J., Barlas, T., Bierbooms, W. and van Bussel, G. (2012). Influence of atmospheric stability on wind turbine loads. *Wind Energy*, 16(7), pp.1013-1032.
- Seibert P, Beyrich F, Gryning SE, Joffre S, Rasmussen A, Tercier P. (2000). Review and intercomparison of operational methods for the determination of the mixing height. *Atmospheric Environment* 2000; 34(7):1001–1027.
- South African Air Quality Information System (SAAQIS). (2018). [Online] Available at: <http://www.saaqis.org.za/Default.aspx>
- Swart, A. (2016). Assessment of the Baseline Meteorological and Air Quality Conditions over Uubvlei, Oranjemund, Namibia. [Online] Available at: [https://repository.up.ac.za/bitstream/handle/2263/60862/Swart\\_Assessment\\_2017.pdf?sequence=1](https://repository.up.ac.za/bitstream/handle/2263/60862/Swart_Assessment_2017.pdf?sequence=1)
- World Health Organization (WHO). (2016). WHO Global Urban Ambient Air Pollution Database (update 2016). [Online] Available at:

[http://www.who.int/phe/health\\_topics/outdoorair/databases/cities/en](http://www.who.int/phe/health_topics/outdoorair/databases/cities/en)

Zhang, H., Wang, Y., Hu, J., Ying, Q., & Hu, X. (2015). Relationships between meteorological parameters and criteria air pollutants in three megacities in China. *Environmental Research*.

## A comparison of CALPUFF and AERMOD for simulating PM<sub>10</sub> and SO<sub>2</sub> concentration in the North West Province

Bafana Mzimkhulu Msimanga, Anzel de Lange

Department of Geography, Geoinformatics and Meteorology, University of Pretoria.

PM<sub>10</sub> and SO<sub>2</sub> from 60 emission point sources were modelled for a period of one year over a 50×50 km area in the Northwest Province. Two pollution dispersion models, AERMOD and CALPUFF are used as tools to predict the PM<sub>10</sub> and SO<sub>2</sub> concentrations. The modelled pollutant concentrations from both models are compared against each other. Although there are minor differences, the models indicate a high agreement in prediction of the pollutant concentrations. Graphs and statistical measures used show that the prediction of concentration by both models can be considered acceptable.

**Keywords:** AERMOD, CALPUFF, PM<sub>10</sub>, SO<sub>2</sub>, Point sources.

### Introduction

Air pollution is a global problem that affects everyone from all walks of life. It affects the population on a small scale where emission sources create an environment which is unfavourable for habitation. On a large scale, we see how air pollution impacts climate change. The main contributors to air pollution are anthropogenic and natural activities. Anthropogenic activities include all pollution causing activities performed by human beings which includes activities like domestic burning and the burning of fossil fuels, etc. Natural activity is when for example, a volcano erupts, and the volcanic ash is transported into the atmosphere hence polluting it (Hansell and Oppenheimer, 2004).

In South Africa (SA) most of the air pollution comes from industrial activity. Industrial pollution includes sources from many industries (mining, poultry farming, power plants, etc.) in SA. The steel industry, for example, employs more than 8 million people (Pillay, 2015). An example of a stationary source is a point source. Harmful by-products are emitted from industrial point sources (industrial stacks) and into the atmosphere. Some of the harmful pollutants emitted from these industrial plants are Sulphur Dioxide (SO<sub>2</sub>) and Particulate Matter of 10 Micrometres in aerodynamic diameter or smaller (PM<sub>10</sub>). SO<sub>2</sub> is a pungent, colourless, toxic gas which is created when sulphur burns in the atmosphere. The gas stays suspended in the air for a long period (approximately one day) and when it rains, it evolves into sulphuric acid and falls to the earth as acid rain. Acid rain greatly affects crop yields (Henmi and Reiter, 1977). PM<sub>10</sub> is harmful to human beings in that if it is inhaled the particles invade the respiratory system's defences and gets lodged deep in the lungs, respiratory problems like bronchitis may result (Moore *et al.*, 2010).

The pollutants are modelled to see the impact they have on the atmosphere and the health of people. Knowing how they can be predicted effectively using models will help greatly in seeing how they disperse into the atmosphere and how far they travel. Predicting the pollutant concentration is vital in knowing the exact impacts these have on the air quality (Brunelli *et al.*, 2015). A comprehensive system or method of transport and dispersion of the pollutants into the atmosphere needs to be understood well in order for a viable solution to be proposed. As a tool of investigation and a measure of severity of the emissions, air dispersion modelling is one way of managing and improving any control that is in place or control that will be in place in the future.

Atmospheric dispersion modelling is a mathematical simulation of how pollutants are dispersed into the atmosphere. This simulation is comprehensive in its

transportation dynamics of the pollutants when emitted. A computer programme is used to solve equations and algorithms that have been used to simulate the dispersion of the pollutants (Neshuku, 2012). The modelling is primarily developed for the prediction of concentrations of pollutants in the atmosphere. Within different pollution dispersion models, there are many differences, including differences in assumptions and the algorithms that are used in each model. The models to be compared in this research are the AMS/EPA Regulatory Model (AERMOD) and the California Puff Model (CALPUFF) (DEA, 2011). Because of the differences in equations of the models, it would be interesting to find out what the output results will be for each model. For this reason, we expect the concentrations to differ. The outcome of this paper will further facilitate an understanding of how the models perform in a South African context.

The aim of this paper is to apply the two air dispersion models for predicting SO<sub>2</sub> and PM<sub>10</sub> for comparison of model results against each other.

### Instrumentation and Method

#### Study area description

The comparison and air quality assessment was performed for a study area in the North West Province. The area of study that is chosen is an area with dimensions of 50 × 50 km. The emission data collected for the mentioned area is for the year 2012.

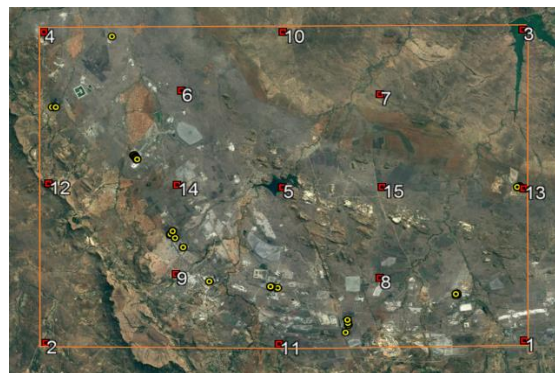


Figure 1: Study area in the North West Province. Industrial point sources are indicated in yellow circles and the red squares indicate receptors (Adapted from Google 2016).

The study area in Figure 1 was chosen based on availability of emission source information and the limitations of the pollution dispersion models with respect to the domain size. The study region has high industrial activity and hence suitable to simulate the pollutant concentrations so that the

models can be compared. The provided SO<sub>2</sub> and PM<sub>10</sub> emissions in the study are at ground level and are from 60 point emission sources. This emission data was used as input into the two dispersion models.

Meteorological data

Meteorological data is important for running dispersion models. The Air Pollution Model (TAPM) was run for the year 2012. From the run five types of meteorological files were produced. AERMOD requires upper level wind profile data (PFL file) and surface data (SFC file) as meteorological input. For CALPUFF the input files are the GEO.DAT file, UP.DAT file and a SUR file (Cimorelli et al., 2004). The TAPM model output was not verified as the emphasis is to compare the output of different dispersion models using the same meteorological input.

AERMOD and CALPUFF data input.

To run the AERMOD and CALPUFF models two sets of data are needed, the two categories of data that are needed are (1) the emission data and (2) the meteorological data. The AERMOD model was run using the Windows Command Prompt and the CALPUFF model was run using the FORTRAN program. The source codes and the appropriate executable files for both models were downloaded from the Support Centre for Regulatory Atmospheric modelling (SCRAM) website. A standard setup was used for the runs.

The models were then used to assess the pollutant concentrations of SO<sub>2</sub> and PM<sub>10</sub> from the 60-point sources indicated on Figure 1. A gridded receptor network was drawn up into both model script input files. A total of 15 receptors were chosen within the study domain. The receptors collected simulated pollutant concentration amounts for analysis and to be used for the model comparison.

Results and Discussion

A comparison of AERMOD and CALPUFF for 1-hour, 24-hour and annual average concentrations was done. The dispersion model results are compared with each other to identify agreement between their concentrations. The median and mean of the results of each model is compared to each other to get an understanding of how the data is distributed. Figure 2 to 7 shows simulated pollutant concentration for the specified domain in the North West Province. The figures show pollutant average concentrations for 2012 at 15 receptors for AERMOD and CALPUFF.

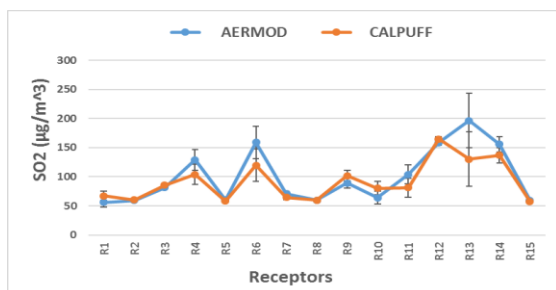


Figure 2: First Highest 1-Hour SO<sub>2</sub> concentration for 2012.

For the first highest 1- hour averages (Figure 2) SO<sub>2</sub> results from AERMOD (blue) and CALPUFF (orange) show a similar pattern from receptors 1 to 3, 5, 7 to 10 and 14 to 15. At receptor 4, 6 and 13 there are significant differences predicted by AERMOD. There concentrations for receptor 4, 6 and 13 are predicted by AERMOD to be 19%, 25% and 22%, respectively, higher than the predictions made by CALPUFF. The figure also shows standard deviation (SD)

error bars to highlight the uncertainty in the reported concentrations.

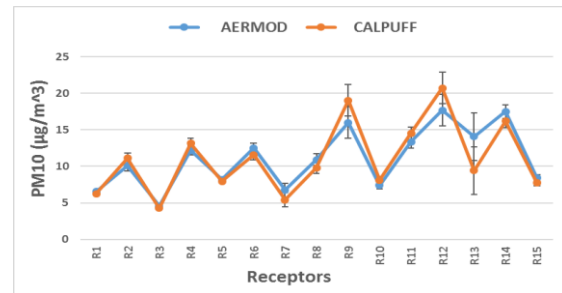


Figure 3: First highest 1-Hour PM<sub>10</sub> concentrations for 2012.

For the first highest 1-hour averages (Figure 3) PM<sub>10</sub> results from AERMOD and CALPUFF look similar for Receptors 1 to 10 and 14 to 15, however, concentrations at receptor 9 and 12 are predicted by CALPUFF to be 16% and 15% (respectively) higher than the concentrations predicted by the AERMOD model. Receptor 13 is predicted by AERMOD to be 33% higher than for CALPUFF. The SD bars on the line graph gives a general idea of the preciseness of the concentration outputs.

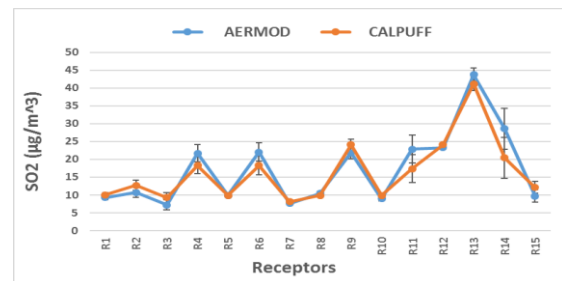


Figure 4: First highest 24-Hour SO<sub>2</sub> concentration for 2012.

Figure 4 (first highest 24-hour averages) shows results of AERMOD and CALPUFF concentrations. Receptors 1 to 10, 12 to 13 and 15 looks similar, concentrations at receptors 11 and 14 are predicted by AERMOD to be 24% and 29% higher (respectively) than CALPUFF. The highest concentration is predicted by AERMOD, this value is 6% higher than predicted by CALPUFF. For Figure 4 the SD error bars show a large spread at receptors 11 and 14. For these receptors the variability from the mean is large.

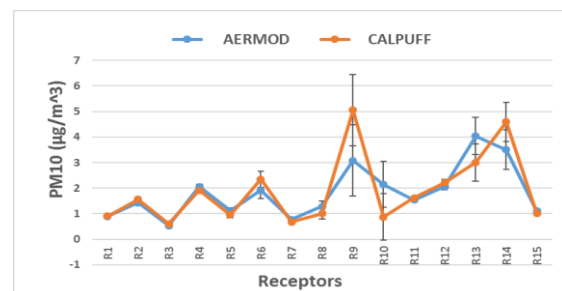


Figure 5: First highest 24-Hour PM<sub>10</sub> concentration for 2012.

For the first highest 24-Hour averages (Figure 5) PM<sub>10</sub> results from the two dispersion models look similar for receptors 1 to 8, 11 to 12 and 15. There is a significant difference for receptors 9, 10, 13 and 14. Pollutant concentration at receptor 9 is predicted by CALPUFF to be 39% higher than AERMOD. At receptor 10 AERMOD predicted a value 59% higher. Receptor 13 predicted by AERMOD is 26% higher and receptor 14 predicted by CALPUFF is 24% higher in comparison. The SD bars on the

line graph show a relatively larger spread from receptor 9 and 10, here there is a large variability from the mean.

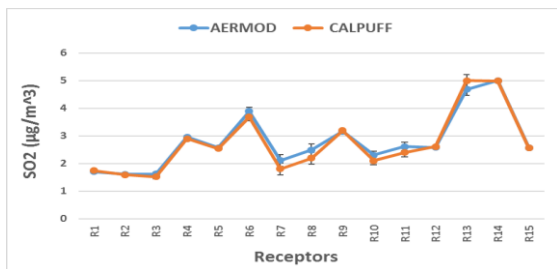


Figure 6: Annual SO<sub>2</sub> concentration for 2012.

For annual averages (Figure 6) SO<sub>2</sub> results from AERMOD and CALPUFF look similar for receptors 1 to 5, 12 and 14 to 15. Receptors 6, 7, 8, 10, 11 and 13 have minor differences. Concentrations predicted by AERMOD are higher at receptor 6 (5%), 7 (14%), 8 (12%), 10 (9%) and 11 (9%). These values are higher than those predicted by CALPUFF. Receptor 13 predicted by CALPUFF is 7% higher than AERMOD. The SD bars are small indicating a low spread in the predicted concentrations.

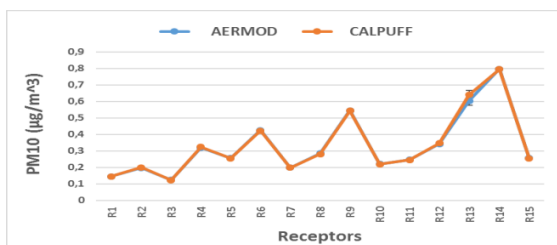


Figure 7: Annual PM<sub>10</sub> concentration for 2012

Figure 7 shows annual averages PM<sub>10</sub> results from AERMOD and CALPUFF look similar for receptor 1 to 15 except for receptor 13. The concentration at receptor 13 is predicted by CALPUFF to be 6% higher than CALPUFF. All other predictions differ by 1 to 2 percent in being higher than the other. The receptors are in high agreement. The SD error bars in this figure show very small bars indicating low spread from the predicted concentrations by the model.

A preliminary assessment of all figures shows a similar pattern of predicted concentrations from the two dispersion models. The median values are similar indicating a high agreement from both models for the simulated concentration values of the pollutants. There is no overlapping in the SD error bars in all figures indicating that the differences are not statistically significant. However, a statistical test needs to be done for confirmation. (Jafarigol *et al.*, 2016). Peak concentrations of the modelled pollutants lie between receptors 12 and 15. These receptors are closer to the emission sources. Similar meteorological condition are seen as reason for this similarity. These conditions do not vary much across the domain of study. (Vieira de Melo *et al.*, 2012). Overall, AERMOD and CALPUFF predictions are similar but AERMOD predicts higher pollutant concentration values than CALPUFF.

Table 1. Median, Mean and Standard deviation values of the models.

		AERMOD			CALPUFF		
		Median	Mean	Stdev	Median	Mean	Stdev
1-Hour	SO <sub>2</sub>	81.15	100.22	47.19	81.17	91.48	33.58
	PM <sub>10</sub>	10.91	11.08	4.12	9.79	11.03	4.89
24-Hour	SO <sub>2</sub>	10.70	17.20	10.31	12.72	16.38	8.76
	PM <sub>10</sub>	1.54	1.83	1.03	1.56	1.89	1.38
Annual	SO <sub>2</sub>	2.55	2.79	1.03	2.58	2.72	1.10
	PM <sub>10</sub>	0.26	0.33	0.18	0.25	0.33	0.19

Table 1 shows that the results have skewed datasets. The medians of all predicted pollutant concentration in the models are less than the mean. This indicates that a majority of outliers are at the high end of the distribution. The standard deviation highlights the dispersion of a set of the data values. Both models are in agreement as represented by the calculated mean and median comparison. The comparison shows that the datasets are skewed to the right.

Since both models shown a high degree of agreement when it comes to the predicted pollutant concentrations (in the study area) it can be concluded that either model would be of sufficient use in simulating pollutant concentrations.

### Conclusion

The results of the comparison of the AERMOD and CALPUFF models have shown that either model can be used for pollutant concentration for the study area. The receptors of both models are consistently in agreement with each other. This can be viewed as a good indication of acceptable estimation of pollutant concentration. Sound decision making in view of air quality management can be as a result.

If the same approach for predicting pollutant concentrations was to be implemented on a larger scale, there would be a concern regarding the availability of emission data and the fact that one of the models works best for a 50 × 50 km area.

### References

Brunelli, U., Piazza, V., Pignato, L., Sorbello, F., and Vitabile, S. (2007). "Two-days Ahead Prediction of Daily Maximum Concentrations of SO<sub>2</sub>, O<sub>3</sub>, PM<sub>10</sub>, NO<sub>2</sub>, CO in the Urban Area of Palermo, Italy." Atmospheric Environment. 11 September, Vol 41, pp 41-55.

Cimorelli, A. J., S.G. Perry, A. Venkatram, J. C. Weil, R. J. Paine, R. B. Wilson, R. F. Lee, W. D. Peters, R. W. Brode, and J. O. Paumier, (2004). AERMOD: Description of Model Formulation, U.S. Environmental Protection Agency, Research Triangle Park, NC.

Department of Environmental Affairs and Tourism (DEA), (2011). Environmental Outlook: Air Quality. NATIONAL ENVIRONMENTAL MANAGEMET: AIR QUALITY ACT, 1989 (Act No. 73 of 1989).

Google earth. 2013. "North West Province." 25°25'12.00" S and 27° 9'36.00" E. December 12, (2016). May 13, 2018

Jafarigol, F., Atabi, F. Moatar, F., Nouri, J., (2016). The Survey of NOX Distribution Using Dispersion Models AERMOD and CALPUFF at a Gas Refinery. Journal of Environmental Health Engineering, 3(3), pp.193-205. Available at: <http://dx.doi.org/10.18869/acadpub.jehe.3.3.193>

Katharine F. Moore, Vishal Verma, María Cruz Minguillón, Constantinos Sioutas. (2010). Inter- and Intra-Community Variability in Continuous Coarse Particulate Matter (PM<sub>10-2.5</sub>) Concentrations in the Los Angeles Area. Aerosol Science and Technology 44:7, pages 526-540.

Neshuku, M. (2012). Comparison of the performance of two atmospheric dispersion models (AERMOD and ADMS) for open pit mining sources of air pollution. Master of Science. University of Pretoria, Pretoria.

South Africa.

Pillay, V. "The hard reality about SA steel industry." September (2015), <business.report.co.za> [Accessed 28 March 2018].

Vieira de Melo, A.M., Santo, J. M., Mavroidis, I., Reis Junior, N. C., (2012). Modelling of odour dispersion around a pig farm building complex using AERMOD and CALPUFF. Comparison with wind tunnel results. Building and Environment, 56, pp.8-20. Available at: <http://dx.doi.org/10.1016/j.buildenv.2012.02.017>.

Anna Hansell & Clive Oppenheimer (2004) Health Hazards from Volcanic Gases: A Systematic Literature Review, Archives of Environmental Health: An International Journal, 59:12, 628-639.

Teizi Henmi & Elma Reiter (1977). Regional residence time of sulfur dioxide over the eastern United States, Atmospheric Environment (1967), Volume 12, Issues 6–7, 1978, Pages 1489-1495

## An exploratory analysis of low-ozone events during spring and summer months over Cape Point, South Africa

David Jean du Preez<sup>1,2\*</sup>, Nelson Bègue<sup>3</sup>, Hassan Bencherif<sup>3</sup> and Caradee Yael Wright<sup>4,1</sup>

<sup>1</sup>Department of Geography, Geoinformatics and Meteorology, University of Pretoria

<sup>2</sup>South African Weather Service

<sup>3</sup>Université de La Réunion, Laboratoire de l'Atmosphère et des Cyclones

<sup>4</sup>Environmental and Health Research Unit, South African Medical Research Council

Decreased stratospheric ozone levels contribute towards increased ultraviolet (UV) radiation at the Earth's surface with potential negative impacts on public health. This study sought to determine whether or not the break-up of the polar vortex has an effect on stratospheric ozone levels and the resulting UV-B radiation at Cape Point. Using a dynamical model, it was shown that the polar vortex has a limited effect on ozone levels at Cape Point in September and that tropical air-masses had a larger impact on ozone levels during summer months. Decreased levels of stratospheric ozone resulted in increased UV radiation at the surface.

*Keywords: stratospheric-ozone, clear-sky, UV radiation*

### Introduction

Ozone gas occurs naturally throughout the atmosphere with approximately 90% of all ozone found in the stratosphere. Ozone in the stratosphere absorbs ultraviolet (UV) radiation with a wavelength of 280 – 310 nm (UV-B) (Hegglin et al., 2014). Ozone levels in the atmosphere vary due to natural and anthropogenic factors. Ozone Depleting Substance (ODS's) have caused a decrease in ozone levels around the world (Hegglin et al., 2014). This has resulted in increased levels of UV-B radiation at the surface of the Earth (Herman et al., 1996).

The Antarctic ozone hole forms during the Southern Hemisphere winter due to the unique conditions in the Antarctic atmosphere. The Antarctic ozone hole has a direct impact on ozone levels in the Southern hemisphere (Ajtic' et al., 2004; de Laat et al., 2010) and atmospheric phenomena such as the Southern Annular Mode (SAM) (Bandoro et al., 2014). Decreases in atmospheric ozone due to the Antarctic ozone hole have led to increased levels of UV-B radiation in Australia, New Zealand and Chile (McKenzie et al., 1999; Gies et al., 2013; Abarca and Casiccia, 2002).

The occurrence of a low-ozone event over Irene, South Africa can be attributed to the transport of both tropical and polar air-masses (Semane et al., 2006). Over South Africa, the Total Ozone Column (TOC) is affected by the seasonal variability of synoptic scale weather systems (Barsby and Diab, 1995).

This paper presents a portion of the analyses and results from a larger study. Presented here, are the outcomes based on the following objectives: 1) to identify specific low Stratospheric Column Ozone (SCO) and TOC events over Cape Point during spring and summer seasons; 2) to determine the origin of ozone-poor air-masses during low-ozone events using a dynamical transport model; 3) to determine the subsequent effect of low-ozone events on surface UV-B radiation.

### Data and Methods

Daily satellite TOC and SCO data in Dobson Units (DU) for 2007-2016 were obtained for the following grid-area (West: 16.5 °E, South: 36.35 °S, East: 20.6 °E, North: 31.98 °S) over the Cape Peninsula in the Western Cape, South Africa. The Cape Peninsula is affected by a south-easterly wind which transport maritime air from the South Atlantic Ocean (Kruger, et al., 2010). TOC data from the Ozone Monitoring Instrument (OMI) a 0.25° spatial resolution (Levelt, et al., 2006). SCO data from the Microwave Limb Sounder (MLS) provided SCO levels up to the thermal tropopause (Livesey et al., 2017). Both the OMI and MLS are on National Aeronautics and Space Administration (NASA's) Aura satellite (NASA Goddard Space Flight Center, 2006).

The origin of ozone-poor air was determined using the Mesoscale Isentropic Transport Model of Stratospheric Ozone by Advection and Chemistry (Modèle Isentropique du transport Méso-échelle de l'ozone stratosphérique par advection avec CHIMIE or MIMOSA-CHIM). The dynamical component of the model is forced by meteorological variables from the European Centre for Medium-Range Weather Forecasts (ECMWF) daily analyses. The model has a 1° x 1° resolution and isentropic levels from 350 – 950 K (Hauchecorne et al., 2002).

Hourly solar UV-B radiation from the South African Weather Service (SAWS) Cape Point (34.35°S, 18.5°E) weather station given in Minimal Erythemal Dose (MED) units was converted to Standard Erythemal Dose (SED) using Eq. (1). The UV-B radiation was recorded with a Solar Light 501 UV-B Biometer. The biometer has an analog voltage output which is proportional to the amount of radiation received (Solarlight, 2014).

$$SED = MED \times 2.1 \quad (1)$$

where: MED is 210 J.m<sup>-2</sup> and SED is 100 J.m<sup>-2</sup>

Low-ozone events were only identified on clear-sky days during the spring and summer seasons. Clear-sky days were determined using the method defined by du Preez and Wright (2018). Low-ozone days were determined as days when TOC or SCO levels were one and a half standard deviations (1.5 STD) below the climatological mean

\*corresponding author: jean.dupreez@weathersa.co.za

(Schuch, et al., 2015). The TOC and SCO climatological means as referred to in du Preez and Wright, 2018, were used to determine the low-ozone events.

The MIMOSA-CHIM model was initialised 14-days before each low-ozone event to account for model spin-up and Potential Vorticity (PV) maps were analysed at isentropic levels that correspond to 18 km, 20 km and 24 km above ground level. The lower part of the ozone layer is covered by these heights (Sivakumar and Ogunniyi, 2017). PV can be used to trace ozone-poor air when diabatic and frictional terms are small and PV is conserved on isentropic levels over short time periods (Holton and Hakim, 2013).

The UV-B radiation levels at solar noon on low-ozone days were compared to the UV-B climatology for Cape Point as described by du Preez and Wright, 2018.

*Results and Discussion*

The summer seasons of 2009/2010 and 2015/2016 are classified as El Niño seasons during which period higher TOC levels are expected over the midlatitude region (Kalicharran et al., 1993). From the identified low-ozone events (Table 1), only one event occurred during an El Niño season.

**Table 1. Low-ozone events on clear-sky days at Cape Point during spring and summer months.**

<i>Date</i>	<i>Decrease TOC (%)</i>	<i>Decrease SCO (%)</i>	<i>Increase SED (%)</i>
30 Jan 2009	6.1*	10.1*	29.9
6 Feb 2009	5.0*	4.5*	35.0
15 Feb 2009	4.7*	1.9	33.4
28 Feb 2011	4.3*	4.1*	6.4
16 Jan 2012	0.6	5.1*	20.9
8 Feb 2012	3.8*	2.2	29.8
13 Nov 2012	13.3*	13.3	43.8
14 Nov 2012	11.7*	11.1	39.8
6 Sep 2013	12.7*	11.6*	22.5
9 Nov 2013	4.6	13.3*	21.4
1 Sep 2014	9.5*	18.0*	-1.7
2 Sep 2014	14.9*	15.3*	-2.1
9 Sep 2014	6.4*	14.9*	-4.8
11 Jan 2016	-0.3	5.1*	-8.0

Note: \* -Indicates if TOC or SCO was low during event.

Stratospheric ozone reductions are dominant when TOC and SCO decreases are similar. Tropospheric ozone reductions are dominant when the TOC percentage decrease is high and the SCO percentage decrease low. 1 September 2014 had the largest SCO reduction (18% decrease) (Table 2) with low-ozone events in September mainly due to SCO reductions. Low-ozone events in February months were characterised by dominant decreases in tropospheric ozone.

The low-zone events that occurred during November months resulted in the largest increases in SED levels (~35%) this resulted from a dominant reduction in stratospheric ozone. In a previous study decreases in SCO over southern Australia have resulted in increases in UV-B radiation of 40% (Gies et al., 2013).

The origin of ozone-poor air-masses over Cape Point during low-ozone events was determined using MIMIOSA-CHIM. A low-ozone event during September is used to demonstrate the limited effect of the Antarctic polar vortex on SCO over Cape Point. The low-ozone event of 2 September 2014 (Fig. 1) shows the general pattern for September months.

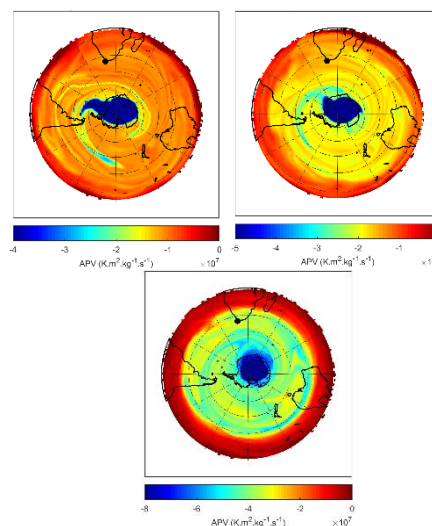


**Figure 1. PV maps from MIMOSA-CHIM at 435 K (top left), 485 K (top right) and 600 K (bottom) on 2 September 2014.**

Considering the origin of air-masses during other low-ozone events it was found that Cape Point was affected by air-masses from tropical and polar regions through the distortion of the polar vortex. The effect of tropical air-masses on atmospheric ozone over South Africa has been demonstrated with the isentropic transport across the subtropical barrier (Semane et al., 2006).

*Conclusions*

This study investigated if the 15 largest low-ozone events (2007-2016) over Cape Point were as a result of the break-up of the Antarctic ozone hole during spring and summer.

SCO levels during September were slightly influenced by the Antarctic polar vortex. During September months, air-masses did not move between latitude regions (tropical, midlatitude and polar). Increased UV radiation due to low-ozone resulted in an average increase ~14% over September months.

#### *Acknowledgements*

The authors would like to thank the South African Weather Service for providing solar UV-B radiation data and acknowledge the use of Total Ozone Column data from the Ozone Monitoring Instrument (OMI) and Stratospheric Column Ozone data from the Microwave Limb Sounder (MLS). The author wishes to thank the University of Reunion Island for the provision of the MIMOSA-CHIM model. This study was funded in part by the South African Medical Research Council as well as the National Research Foundation of South Africa to grant-holder CY Wright.

#### *References*

- Abarca, J. F. and Casiccia, C. C. (2002). Skin Cancer and ultraviolet-B radiation under the Antarctic ozone hole: southern Chile, 1987-2000. *Photodermatol Photoimmunology Photomed.* 18: 294-302.
- Ajtic', J.V., Connor, B. J., Lawrence, B. N., Bodeker, G. E., Hoppel, K. W., Rosenfield, J. E. and Heuff, D. N. (2004). Dilution of the Antarctic ozone hole into the southern midlatitudes. *Journal of Geophysical Research.* 109: 1-9. doi:10.1029/2003JD004500.
- Bandoro, J., Solomon, S., Donohoe, A., Thompson, D. W. and Santer, B. D. (2014). Influences of the Antarctic Ozone Hole on Southern Hemispheric Summer Climate Change. *Journal of Climate.* 27: 6245-6264. doi: 10.1175/JCLI-D-13-00698.1.
- Barsby, J. and Diab, R. D. (1995). Total ozone and synoptic weather relationships over southern Africa and surrounding oceans. *Journal of Geophysical Research.* 100: 3023-3032. doi:10.1029/94JD01987.
- de Laat, A., van der A, R. J., Allaart, M. F., van Weele, M., Benitez, G. C., Casiccia, C., Paes Leme, N.M., Quel, E., Salvador, J. and Wolfram, E. (2010). Extreme sunbathing: Three weeks of small total O<sub>3</sub> columns and high UV radiation over the southern tip of South America during the 2009 Antarctica O<sub>3</sub> hole season. *Geophysical Research Letters.* 37: doi:10.1029/2010GL043699.
- du Preez, D.J. and Wright, C.Y. (2018). Spring-time ozone and solar ultraviolet radiation variations over the Western Cape, South Africa. *Masters dissertation, University of Pretoria.*
- Gies, P., Klekociuk, A., Tully, M., Henderson, S., Javorniczky, J., King, K., Lemus-Deschamps, L. and Makin, J. (2013). Low ozone over southern Australia in August 2011 and its impact on solar ultraviolet radiation levels. *Photochemistry and Photobiology.* 89: 984-994. doi:10.1111/php.12076.
- Hauchecorne, A., Godin, S., Marchand, M., Hesse, B. and Souprayen, C. (2002). Quantification of the transport of chemical constituents from the polar vortex to midlatitudes in the lower stratosphere using the high-resolution advection model MIMOSA and effective diffusivity. *Journal of Geophysical Research.* 107: doi:10.1029/2001JD000491.
- Hegglin, M. L., Fahey, D. W., McFarland, M. and Montzka, S. A. (2014). Twenty Questions and Answers About the Ozone Layer: 2014 update. In *Scientific Assessment of Ozone Depletion* (p. 84). Geneva: World Meteorological Organisation.
- Herman, J. R., Bhartia, P. K., Ziemke, J., Ahmad, Z. and Larko, D. (1996). UV-B increases (1979-1992) from decreases in total ozone. *Geophysical Research Letter.*, 23: 2117-2120. doi:10.1029/96GL01958
- Holton, J. R. and Hakim, G. J. (2013). Circulation, Vorticity and potential vorticity. In *An Introduction to dynamic meteorology* (Fifth ed., p. 121). Oxford: Academic Press.
- Kalicharran, S., Diab, R. D. and Sokolic, F. (1993). Trends in total ozone over southern African stations between 1979 and 1991. *Geophysical Research letters.* 20: 2877-2880. doi:10.1029/93GL03427.
- Kruger, A.C., Goliger, A.M., Retief, J.V., and Sekele, S. (2010). Strong wind climatic zones in South Africa. *Wind and Structures* 13, pp37-55.
- Levelt, P. F., van den Oord, G. H., Dobber, M. R., Mälkki, A., Visser, H., de Vries, J., Stammes, P., Lundell, J.O.V. and Saari, H. (2006). The Ozone Monitoring Instrument. *Transactions on Geoscience and remote sensing.* 44: doi:10.1109/TGRS.2006.872333.
- Livesey, N. J., Read, W. G., Wagner, P. A., Froidevaux, L., Lambert, A., Manney, G. L., Valle, L.F.M., Pumphrey, H.C., Santee, M.L., Schwartz, M.J., Wang, S., Fuller, R.A., Jarnot, R.F., Knosp, B.W. and Martinez, E. (2017). *The earth observing system (EOS) Aura microwave limb sounder (MLS) Version 4.2xlevel 2 data quality and description document.* Retrieved April 25, 2017, from [https://mls.jpl.nasa.gov/data/v4-2\\_data\\_quality\\_document.pdf](https://mls.jpl.nasa.gov/data/v4-2_data_quality_document.pdf)
- McKenzie, R., Connor, B. and Bodeker, G. (1999). Increased Summer time UV radiation in New Zealand in response to ozone loss. *Science.* 285: 1709-1711.
- NASA Goddard Space Flight Center. (2006). *Earth Science Reference Handbook : A guide to NASA's Earth science program and Earth observing satellite missions* (Annual ed.). Washington, D.C.: National Aeronautics and Space Administration.
- Schuch, A. P., dos Santos, M. B., Lipinski, V. M., Vaz Peres, L., dos Santos, C. P., Cechin, S. Z., Schuch, N.j., Pinheiro, D.K. and da Silva Loreto, E. L. (2015). Identification of influential events concerning the Antarctic ozone hole over southern Brazil and the biological effects induced by UVB and UVA radiation in an endemic treefrog species. *Ecotoxicology and Environmental Safety.* 118: 190-198. <http://dx.doi.org/10.1016/j.ecoenv.2015.04.029>.
- Semane, N., Bencherif, H., Morel, B., Hauchecorne, A. and Diab, R. D. (2006). An unusual stratospheric ozone decrease in the southern hemisphere subtropics linked to isentropic air-mass transport as observed over Irene (25.5°S, 28.1°E) in mid-May 2002. *Atmos. Chem. Phys.* 6: 1927-1936.
- Sivakumar, V. and Ogunniyi, J. (2017). Ozone climatology and variability over Irene, South Africa determined by ground based and

satellite observations. Part 1: Vertical variations in the troposphere and stratopshere. *Atmosfera*. 30: 337-353.

Solarlight. (2014). *Solar Light*. Retrieved January 23, 2017, from [http://solarlight.com/wp-content/uploads/2015/01/Meters\\_Model-501-.pdf](http://solarlight.com/wp-content/uploads/2015/01/Meters_Model-501-.pdf)

## Investigating the effect of aerosols on diffuse solar irradiance in Durban, South Africa

P. Govender<sup>1</sup>, V. Sivakumar<sup>1</sup> and A. C. Govender<sup>1</sup>

<sup>1</sup>School of Chemistry and Physics, University of KwaZulu-Natal, Durban, 4041.

### Abstract

This study investigates the effect of Aerosol optical depth (AOD) on diffuse ( $D_H$ ) solar irradiance in Durban (29.87° S; 30.98° E), located on the east coast of South Africa. Simultaneous measurements of AOD and diffuse irradiance obtained from ground-based sensors were used to compare daily averages of the two quantities. In most cases when AOD levels were high, there was a corresponding increase in diffuse irradiance due to an increase in scattering of incoming radiation. In addition, some days had high  $D_H$  radiation despite the low AOD levels, suggesting that in these cases clouds have a more significant contribution to the scattering of  $D_H$  radiation as compared to aerosols.

Keywords: Aerosol optical depth, diffuse irradiance, pyranometer, sun photometer

### Introduction

Aerosols are a key component of the Earth's radiative system, where they can affect the Earth's radiation budget by absorption or scattering of the incoming solar radiation (Mishra *et al.* 2015). Origination of aerosols emitted into the atmosphere are through either natural or anthropogenic processes (Adesina *et al.* 2015). Examples of the former include volcanic eruptions, forest fires, sea spray and desert dust, while the latter includes burning of coal and other fossil fuels and biomass burning for energy consumption.

Aerosols can be classified in terms of their chemical composition and according to their physical characteristics such as size, shape, density and mass. Depending on the type of particle, aerosols have differing properties that determine their role in atmospheric processes (Lohman *et al.* 2016). As explained by Adesina (2016), AOD is the measure of transparency of aerosol to solar radiation and the degree to which it prevents the solar radiation from scattering and absorption.

As the solar radiation passes through the Earth's atmosphere, it undergoes scattering and absorption, where the scattered component of the radiation is referred to as diffuse radiation. Diffuse radiation that arrives at the surface of the Earth first encounters several atmospheric constituents such as water vapor, carbon dioxide (CO<sub>2</sub>), dust, aerosols, clouds, etc., and thereafter released as scattered radiation in several directions (Sen, 2008).

For the present study, it is the interaction of aerosols with diffuse radiation that will be investigated. Although there have been previous studies that have investigated aerosol optical depth (AOD) either over some parts or the entire of South Africa (SA) using both ground-based instruments (Kumar *et al.*, 2013; Adesina *et al.*, 2014; Adesina *et al.*, 2015; Hersey *et al.*, 2015) and satellite-based instruments (Kumar *et al.*, 2014), there are limited studies that focused on the effect of

aerosols on diffuse irradiance in Durban. Durban is a coastal location with sub-tropical humid climate. Winter is characterized as having clear cloud-free sky conditions, while summer experiences significant cloud variation (Govender, 2017). It is therefore expected that the

AOD levels are low and high in winter and summer, respectively. The present study investigates the effect of aerosols on diffuse radiation by comparing daily averages of AOD and diffuse irradiance recorded by ground-based instruments in Durban.

### Instrumentation and Method

Aerosol and irradiance data used for this study were recorded in Durban (29.87° S; 30.98° E), South Africa. The instruments are located on a roof platform 200 m above mean sea level. Measurements of diffuse horizontal irradiance ( $D_H$ ) data were obtained using a Kipp and Zonen CMP11 pyranometer (see Fig. 1). Pyranometers measure the radiation that is incident on them within the solid angle  $2\pi$ . The pyranometer uses a shading device covering the sensing element so that direct sun rays will be blocked. The pyranometer is mounted on a Solys2 sun tracker that faces in the North direction. A CIMEL Sunphotometer (see Fig. 2) which is part of the Aerosol Robotic Network (AERONET), was used to obtain measurements of AOD at 500 nm. Daily averages of  $D_H$  and AOD were used for this analysis. Measurements were used for total of 200 days that span across March-November 2015, January-June, August, September, November-December 2016 and January 2017. These data sets were chosen since these were the periods during which there were simultaneous measurements from both instruments.



Figure 1: A Kipp and Zonen (CMP11) pyranometer used for diffuse irradiance measurements, and which is mounted on a Solys2 sun tracker. A shading device is used to block out the direct sun rays.



Figure 2: CIMEL Sunphotometer used for AOD measurements is shown facing north.

### Results and Discussion

Relationship between daily AOD and  $D_H$  averages for Durban is shown in Fig. 3. It can be seen that majority of the days cluster in a region close to zero, where AOD and  $D_H$  are low. Since these are daily averages, these points correspond to days that have low AOD and as a result there is less scattering of  $D_H$  irradiance. These types of days will have clear sky conditions, i.e. no clouds present, and a low concentration of aerosol particles. Some days were found have high AOD ( $> 0.4$ ) and relatively low  $D_H$  ( $100 < D_H < 200$ ) averages. These points correspond to days that have a high aerosol concentration which causes a moderate degree of scattering in the diffuse irradiance. Days that correspond to points with low AOD ( $< 0.2$ ) and high  $D_H$  ( $200 < D_H < 400$ ) averages suggest that scattering of the diffuse irradiance is not just due aerosols but may be due to the presence of clouds. As presented in Govender (2017), diffuse irradiance levels may be doubled in the presence of clouds, which seems to be a reasonable assumption for such data points.

Values with  $D_H > 400$  suggest extreme situations which correspond to days where the  $D_H$  component undergoes significant scattering, and which may be influenced largely by the presence of clouds,

rather than only AOD. The degree of scattering will depend on the type of cloud and its physical and optical properties.

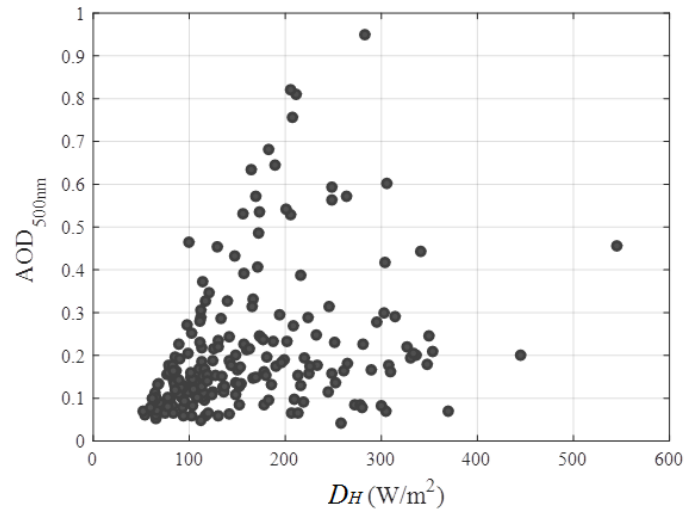


Figure 3: Comparison between daily averages of AOD<sub>500 nm</sub> and  $D_H$  for all 200 days in Durban. A significant number of days have low AOD and  $D_H$  averages.

Fig. 4 shows the relationship between AOD and  $D_H$  and the variation according to the season. Spring shows a large variation in the values. The high AOD in spring has been found to be a direct result of the large number and high frequency of agricultural activities and fire hotspots due to biomass burning that takes place in the dry season (Adesina *et al.*, 2015; Adesina *et al.*, 2016). Summer has significantly lower AOD than spring, but similar values for  $D_H$ , where  $D_H$  is fairly high. This indicates that the scattering in  $D_H$  may be due to clouds rather than AOD, which is consistent with Durban having a high percentage of cloud cover during summer (Govender, 2017). Autumn has several days that are sunny ( $D_H < 150$ ) with low AOD ( $< 0.2$ ). Winter, similar to Autumn has days with low  $D_H$  and AOD, but also shows days with significantly high AOD (AOD  $> 0.4$ ) although  $D_H$  remains fairly low. The occurrence of low  $D_H$  in winter is consistent with Durban experiencing mostly sunny days during June and July (Govender, 2017). However, the presence of days with high AOD values during these months may be due to an increase in biomass burning for heating in areas with no electrification.

Shown in Fig 5, 6 and 7 are profiles of the AOD and  $D_H$  for three randomly chosen days in the data set. In Fig. 5, the AOD and  $D_H$  values are characteristic of a day with sunny conditions before midday and with low aerosol concentration. Towards the early afternoon, the AOD level shows a very slight increase and the  $D_H$  also increases, however not as smoothly but in rather sharp spikes specifically at two instances. This may suggest that the  $D_H$  is not responding to AOD but rather to the presence of clouds where

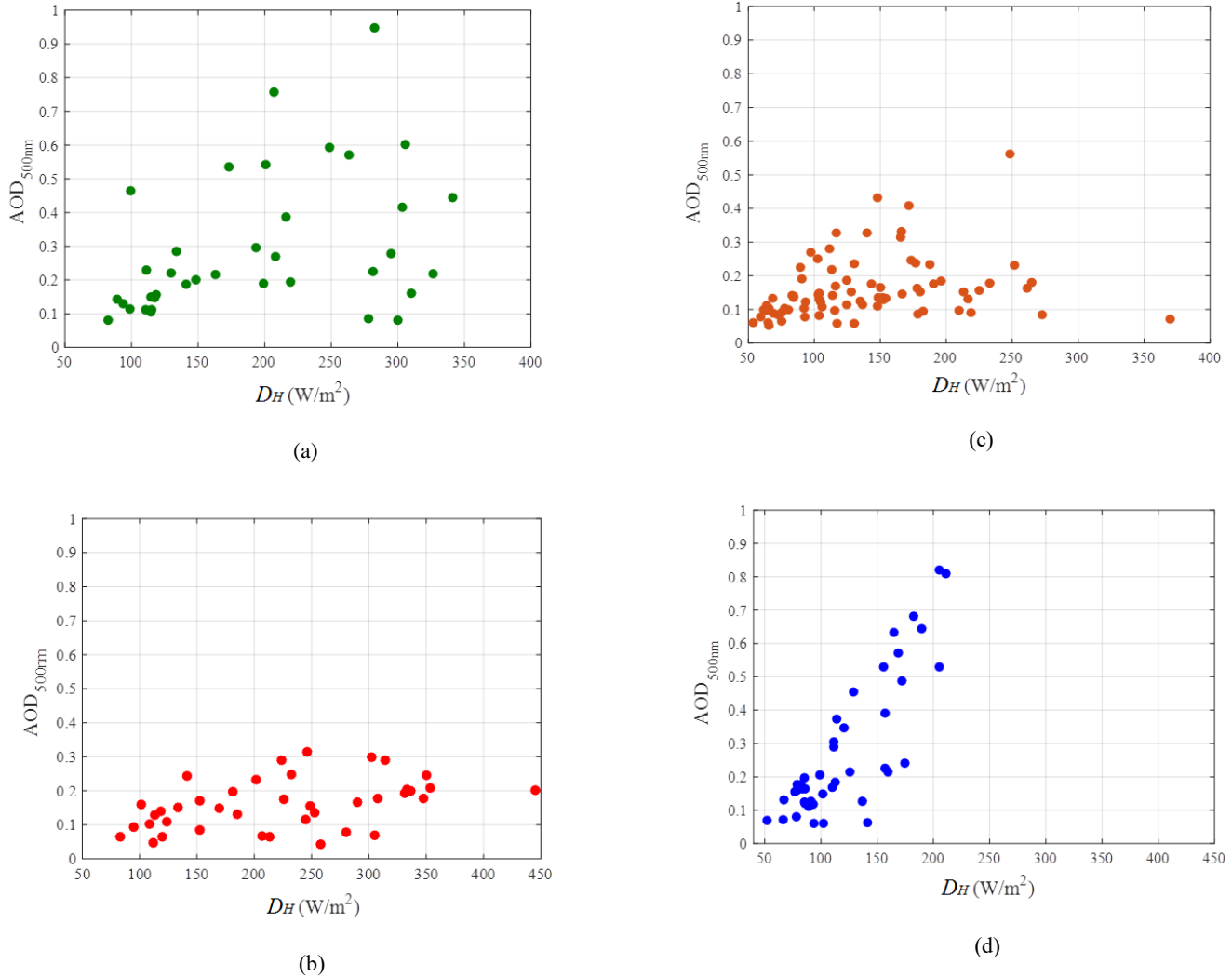


Figure 4: Comparison between AOD and  $D_H$  for (a) spring (b) summer (c) autumn and (d) winter in Durban.

irradiance may be reflected off the edge of a cloud, thus causing  $D_H$  to spike at those times. Fig. 6 shows the AOD and  $D_H$  profiles for a typical clear day in Durban, where the AOD remains low through most of the day, and  $D_H$  remains fairly constant with an average of approximately  $93 \text{ W/m}^2$ . In Fig. 7 the AOD has an average of approximately 0.3 indicating the presence of aerosols, and  $D_H$  shows a significant increase as it deviates from clear sky conditions during the early morning.

In general, when AOD levels are high,  $D_H$  shows a corresponding increase. However, there were some cases where  $D_H$  was high despite AOD levels being low. This suggests that in these cases clouds contribute more significantly to the scattering of  $D_H$ , as compared to aerosols. This can also be observed in the sharp spikes in  $D_H$  when AOD remained fairly constant below 0.2 (i.e. Fig.5).

### Conclusion

This study investigated the effect of AOD on diffuse irradiance in Durban. It was found that in most cases when AOD levels were

high, there was a corresponding increase in diffuse irradiance. This was expected since aerosols result in scattering of the incoming solar radiation. However, it was found that some days had high  $D_H$  despite the low AOD levels. These cases suggest that clouds have a more significant contribution to the scattering of  $D_H$  as compared to aerosols. Further work will include quantifying the scattering of  $D_H$  due to aerosols.

### Acknowledgements

The authors wish to acknowledge the AERONET program for the establishment and maintenance of the network, and for the availability of AOD data for the station in Durban, South Africa.

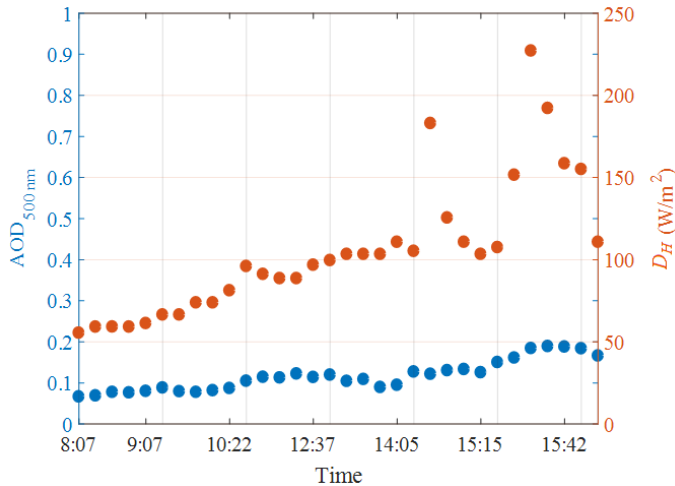


Figure 5: AOD and  $D_H$  for a typical day with sunny conditions before midday and low aerosol concentration. Towards the later part of the day, the  $D_H$  also increases sharply at two separate instances. These profiles were for 19 January 2017.

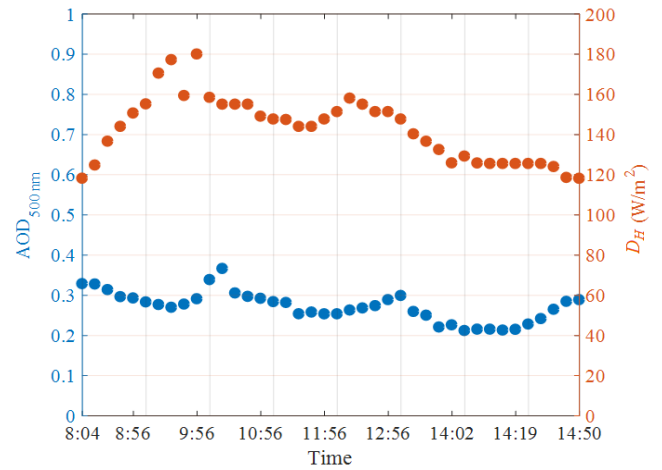


Figure 7: AOD and  $D_H$  for a day with some aerosol concentration and increased diffuse irradiance during some parts of the day. These profiles were for 19 April 2016.

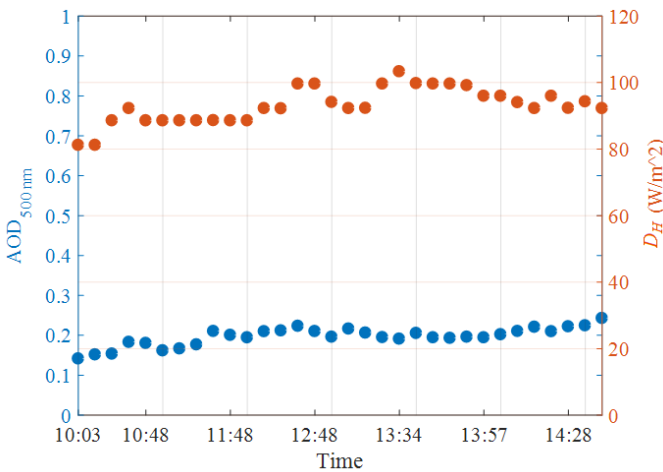


Figure 6: AOD and  $D_H$  for typical sunny conditions with low aerosol concentration and low diffuse irradiance throughout most of the day. These profiles were for 28 July 2015.

### References

Adesina, A.J., Kumar, K.R., Sivakumar, V., Griffith, D. (2014). Direct radiative forcing of urban aerosols over Pretoria (25.75° S, 28.28° E) using AERONET sunphotometer data: first scientific results and environmental impact. *Journal of Environmental Sciences*. 26: 2459-2474.

Adesina J. A. (2015). Aerosol characteristics over different regions of Southern Africa using sunphotometer and satellite measurements. PhD Thesis. University of KwaZulu-Natal.

Adesina, A. J., Kumar, K. R., Sivakumar, V. (2016). Aerosol-cloud-precipitation interactions over major cities in South Africa: impact on regional environment and climate change. *Aerosol and Air Quality Research* 16, 195-211.

Govender, P. (2017). Cluster analysis for classification and forecasting of solar irradiance in Durban, South Africa. PhD Thesis. University of KwaZulu-Natal.

Hersey, S., Garland, R., Crosbie, E., Shingler, T., Sorooshian, A., Piketh, S., Burger, R. (2015). An overview of regional and local characteristics of aerosols in South Africa using satellite, ground, and modeling data. *Atmospheric Chemistry and Physics* 15, 4259-4278.

Kumar, K. R., Sivakumar, V., Reddy, R. R., Gopal, K. R. Adesina, A. J. (2013). Inferring wavelength dependence of AOD and Ångström exponent over a sub-tropical station in South Africa using AERONET data: influence of meteorology, long-range transport and curvature effect. *Science of the Total Environment* 461, 397-408.

Kumar, K. R., Sivakumar, V., Yin, Y., Reddy, R., Kang, N., Diao, Y., Adesina A. J., Yu, X. (2014). Long-term (2003-2013) Climatological trends and variations in aerosol optical Parameters retrieved from MODIS over three stations in South Africa. *Atmospheric Environment* 95, 400-408.

Lohmann, U., Luond, F. and Mahrt, F. (2016). An introduction to clouds: from the microscale to climate. Cambridge University Press, UK.

Mishra, A.K., Koren, I, Rudich, Y. (2015). Effect of aerosol vertical distribution on aerosol-radiation interaction: a theoretical prospect. *Heliyon* Article No-e00036, 1-25.

Sen, Z. (2008). Solar energy fundamentals and modeling techniques. Springer, London.

## Contrast of Inland Aerosol Optical Thickness behaviour

Z Faniso, Email: ZFaniso@csir.co.za, CSIR, DPSS, OSS

DJ Griffith, Email: DGriffith@csir.co.za CSIR, DPSS, OSS

Corresponding Author Email: ZFaniso@csir.co.za

### Abstract

Atmospheric observation is becoming important nowadays. Numerous instruments are installed around the world that detects and record atmospheric behaviour and conditions, to better understand the impact of aerosol on climate change. It is crucial to investigate aerosol distribution in the atmosphere. Hence the study has conducted surveillance of Aerosol Optical Thickness (AOT) behaviour of inland areas. The study observed AOT behaviour over Aeronet instruments in Pretoria (CSIR). The instrument record AOT over different selected wavelengths daily. They show distinct aerosols over different weather conditions. Aerosol Optical Thickness over different selected spectral channels (wavelengths) and water vapour has been observed for both areas. It has been observed that radiative forcing has an influence on the aerosol behaviour.

**Keywords:** Aerosol, Technology systems, Aeronet, Aerosol Optical Thickness, Radiative forcing.

### Introduction

Aerosol optical thickness identification plays a very important role in the atmospheric modelling study. Processes like climate change, air quality damage, radiative forcing have a need to be investigated. The spatial and temporally resolved information on the atmospheric load and optical radiative properties of aerosol is needed especially for the estimation of radiative forcing Antonio J *et al.*, (2003). The studies outline that without proper assessment of the current aerosol concentrations and optical properties, it is impossible to measure change in the aerosol radiative forcing and thus the impact on the climate change Antonio J *et al.*, (2003). The performance of field experiments of aerosol properties is crucial as it provides comprehensive analysis of aerosol properties. The optical Thickness obtained from direct solar radiation, aerosol size distribution and the single scattering albedo are the key attributes that address the optical state of the atmosphere King *et al.*, (1997). The difference in each environment provides different types of aerosols influenced by various mechanisms Palve *et al.* (2018).

Sun photometer measurements of aerosol optical thickness from the Aerosol Robotic Network (AERONET) instruments Holben *et al.*, (1998) have been installed in different countries in Africa and South Africa is one of the countries that own stations of the AERONET.

In this paper results of aerosol optical thickness data collected at CSIR in Pretoria for winter and summer season are presented. Comparison of the Aerosol optical thickness over daily hours is presented.

### Instrumentation and Methods

Aerosol optical thickness measurements were obtained in Pretoria-CSIR-DPSS station (25.757 S, 28.280E) on the Inland of South Africa. The measurements selected are on two months, June and December 2017 in order to observe winter and summer behaviour of aerosol optical thickness. The instrument directly points towards sun direction all throughout the day and when it encounters a cloud or rain it points down and stops recording measurements until the sun appears once again.

Sun radiances are made in eight spectral channels (340, 380, 440, 500, 675, 870, 1020 and 1640nm) from visible to near

infrared range of the Electromagnetic spectrum. The instruments measures water vapour throughout the day

According to Antonio J *et al.*, (2003) the angstrom exponent  $\alpha$ , an indirect measure of aerosol is calculated as follows

$$\alpha = - \frac{\ln \left( \frac{\tau_{870}^a}{\tau_{440}^a} \right)}{\ln(870/440)}, \quad (1)$$

Aeronets are Ground based remote sensing instruments that record aerosol loading Yael Etzion (2012). The performance of ground remote sensing of aerosols is always in vertical or oblique columns, providing the Aerosol Optical Thickness (AOT) at different visible-NIR wavelengths from 400nm-2200nm Yael Etzion (2012).. When rain or heavy cloud covers the area the instruments has algorithms that shutter the instrument then it continues to record data when the sun appears. The study extracted data of the 4<sup>th</sup> June and 13<sup>th</sup> December in Pretoria and 4<sup>th</sup> June.

### Results and Discussion

Magnitude of the Aerosol Optical Thickness in Pretoria – DPSS

Fig. 1 presents the Aerosol Optical thickness on the 4<sup>th</sup> of June 2017. The magnitude of the aerosol optical thickness was high on the visible range, it ranges from 0.17 to 0.60 from 340nm, 0.10 to 0.30 during the day and 0.30 towards the afternoon from 440nm and for 380nm the size starts from 0.11 to 0.44 during the day and 0.40 on the afternoon. The aerosol optical thickness increases in the morning and becomes higher in the midday and cools down by small rate towards the afternoon and this is due to human activities.

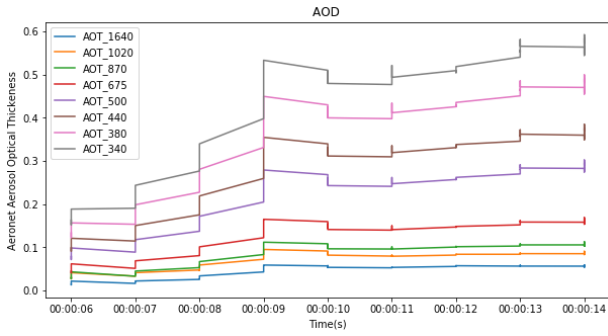


Figure 1: Aerosol optical thickness on the 4<sup>th</sup> of June 2017

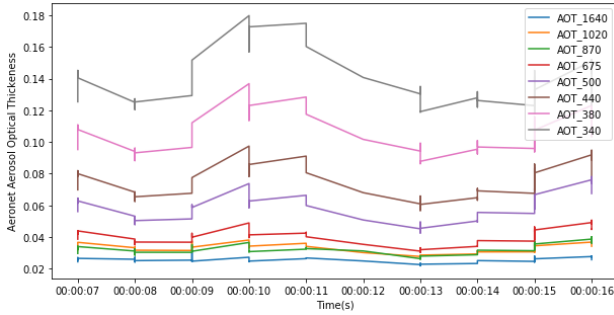


Figure 2: Aerosol optical thickness on the 13<sup>th</sup> of December 2017

Fig. 2 shows summer season data, the aerosol optical thickness size is small it ranges from 0.02 to 0.018 and it increases from near infrared to visible range of the electromagnetic selected wavelengths. It shows high reflections in the midday and decrease in the afternoon this is due to unstable summer weather conditions resulting to low albedo.

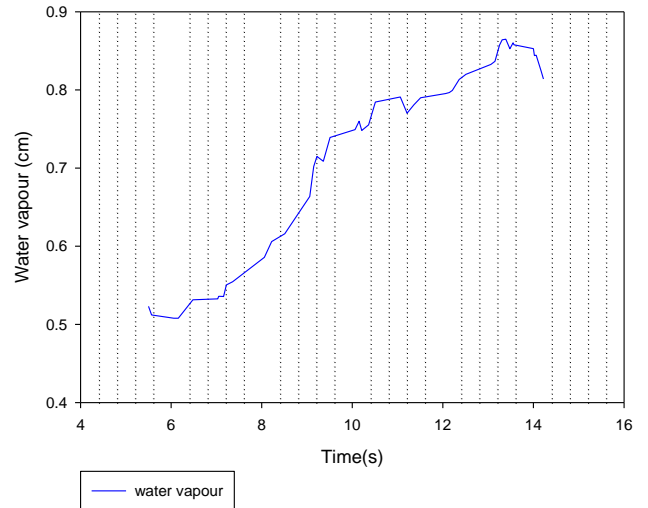


Figure 3: Inland winter water vapour

Fig . 3 presents winter water vapour, winter has high rate of water vapour, it increases from 0.5cm to 0.8 cm, and winter seasons have constant sun radiations illuminated over the Earth surface with clear sky.

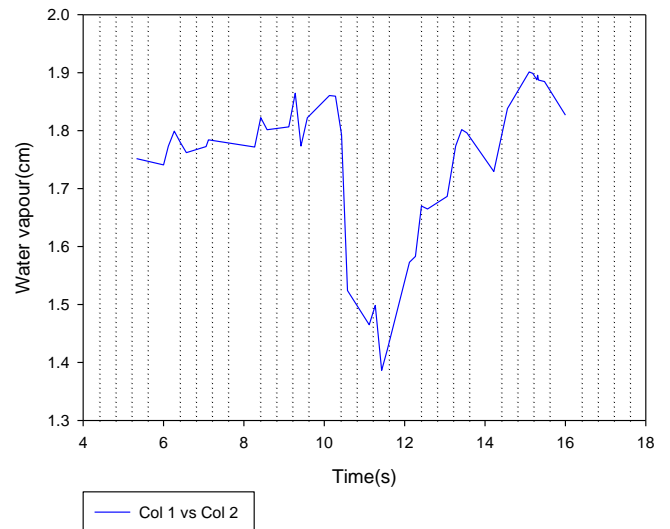


Figure 4: Inland summer water vapour

Summer water vapour starts at a high rate in the morning decreases in the midday but increases towards the afternoon, due to fluctuations in the summer weather conditions in Pretoria water vapour increases with increase in temperature and decreases with decrease in temperature.

Table 1: Comparison of the wavelength aerosol optical in winter and summer.

Time	$\tau_a$ 1040	$\tau_a$ 1020	$\tau_a$ 870	$\tau_a$ 675	$\tau_a$ 500	$\tau_a$ 440	$\tau_a$ 380	$\tau_a$ 340
<b>winter</b>								
Morning	0.58	1.02	1.14	1.71	2.91	3.70	4.78	5.77
Midday	0.78	1.16	1.41	2.06	3.60	4.63	5.97	7.13
Afternoon	0.74	1.12	4.58	2.07	3.71	4.72	6.14	7.33
<b>summer</b>								
Morning	0.36	0.48	0.45	0.57	0.81	1.05	1.47	1.96
Midday	0.18	0.23	0.22	0.27	0.40	0.54	0.79	1.09
Afternoon	0.55	0.70	0.73	0.89	1.35	1.04	2.24	2.80

Table 1 shows aerosol optical thickness size behaviour in a day of winter and summer. The aerosol differs for each selected wavelength from far near infrared and visible range. The day time (morning, midday and afternoon) winter the aerosol optical size increases from near infrared to visible range. Pretoria is normally covered by haze in the winter morning seasons, towards midday the human activities begin until afternoon. Winter has higher aerosol optical size

### **Conclusions**

Measurements of aerosol optical thickness were made using AERONET data in Pretoria in South Africa on 4<sup>th</sup> June and 13<sup>th</sup> December 2017 to characterise the behaviour of atmospheric aerosol optical thickness over this area.

The measurements have shown clear behaviour of aerosol sizes within two different seasons of the year. The levels of aerosol optical thickness observed between these two seasons differ in average size winter has 3.07 and summer has 0.85 average size for all morning, midday and afternoon size over the selected wavelengths.

Aerosols size distribution does not only affect cities environments it has a huge impact on climate change of the whole world. Understanding influences on the atmospheric visibility is important because low visibilities can have disastrous impacts Baumer et al, (2007)..

List of figures

Figure 1: Figure 1: Aerosol optical thickness on the 4<sup>th</sup> of June 2017

Figure 2: Aerosol optical thickness on the 13<sup>th</sup> of December 2017

Figure 3: Inland winter water vapour

Figure 4: Inland summer water vapour

### **Acknowledgements**

1. I would to extend my gratitude to Derek Griffith for helping on the data interpretation.

### **References**

1. Antonio J. Queface, Stuart J. Piketh, Harold J. Annegarn, Brent N. Holben and Rogerio J. Uthui (2003), Retrieval of aerosol optical thickness and size distribution from the CIMEL Sun photometer over Inhaca Island, Mozambique.
2. S.N Palve, P.D Nemade, S.D. Ghude. (2018) Effect of Aerosols on Ocean Parameters in India by Using Satellite Data.
3. Qi-Xiang Chen, Yuan Yuan, Xing Huang, Yan-Qiu Jiang, He-Ping Tan, (2017) Estimation of surface-level PM<sub>2.5</sub> concentration using aerosol optical thickness through aerosol type analysis method.
4. Paul-Etienne Mallet, Olivier Pujol, Jerome Brioude, Stephanie Evan, Andrew Jensen, (2018). Marine aerosol distribution and variability over the pristine Southern Indian Ocean.
5. Holben, B.N., Tanre, D., Smirnov, A., Eck, T.F., Slutsker, I., Abuhassan, N., Newcomb, W.W., Schafer,

compared to summer this is because winter has high albedo and there are high climate forcing's causing high reflections. In the summer season the aerosol optical size increases from near infrared to visible range of the electromagnetic spectrum channels selected. But the summer has lower sizes of the aerosol optical thickness this is because summer has low albedo there is high rate of precipitation cloud covering the atmosphere obstructing the sun from transmitting sun-radiation

J.S., Chatenet, B., Lavenu, F., et al., 2001. An emerging ground-based aerosol climatology: aerosol optical depth from AERONET. *J. Geophys. Res.: Atmos.* 106, 12067–12097.

7. Yael Etzion, Thomas Jarmer, Tsafir Kolatt, Maxim Shoshany & David M. Broday, (2012) Night-Time Ground Hyperspectral Imaging for Urban-Scale Remote Sensing of Ambient PM. I. Aerosol Optical Thickness Acquisition.

8. Ming Zhang, Yingying Ma, Wei Gong, Boming Liu, Yifan Shi, Zhongyong Chen, (2018). Aerosol optical properties and radiative effects: assessment of urban aerosols in central china using 10 year observations.

9. D. Baumer, B. Vogel, S. Versick, R. Rinke, O. Mohler, M. Schnaiter (2007). Relationship of visibility, aerosol optical thickness and aerosol size distribution in an ageing air mass over South-West Germany.

## ***THE BIDECADEAL CLIMATE CYCLE: ALIVE AND WELL***

Johan Malherbe<sup>1</sup>, Izak Smit<sup>2</sup>

<sup>1</sup> CSIR – Natural Resources and the Environment

<sup>2</sup> SANParks

e-mail:jmalherbe@csir.co.za

We consider rainfall variability over the Lowveld in northeastern South Africa during the last 8 decades and demonstrate the persistence of a bi-decadal rainfall cycle in the region. We also note associations with the Southern Annular Mode and with the Southern Oscillation Index together with temporal changes in the association between these two indices, related to the global patterns associated with cycle.

---

**KEYWORDS:** Decadal variability, Southern Annular Mode, Antarctic Oscillation, Southern Oscillation, El Niño

---

### *Introduction*

The bidecadal cycle is characteristic to the rainfall signal over northeastern South Africa and indeed much of subtropical southern Africa (Tyson 1980, Tyson et al. 2002). More recently, the cycle has been confirmed in the rainfall over northeastern South Africa into the 21<sup>st</sup> century (Malherbe et al. 2012). Furthermore, an association was noted with the direct impact of tropical cyclones over the Limpopo River Basin, associated with changes in the zonal steering flow at this time scale (Malherbe et al. 2012; 2014) and associated at a hemispheric scale with changes in the zonal pressure anomalies as reflected by the Southern Annular mode (SAM) during late summer (JFM), explaining certain teleconnections noted earlier by Tyson et al. (2002). The cycle was also demonstrated to be present over the period 1920 – 2015 in the extent of drought over South Africa, together with, at this time scale, the negative association with the SAM (Malherbe et al. 2016). Within the rainfall sequence, and despite being remarkably stable for multiple decades during the 20<sup>th</sup> century, the cycle displays a phase shift in the early part of the 20<sup>th</sup> century (Tyson 1975, Tyson et al. 2002). Nevertheless, the persistence of the 16-20-year cycle over the last few millennia has been deemed a striking feature of southern African climate variability (Tyson et al. 2002).

The recent strong El Niño in 2015/16 resulted in widespread drought over large parts of Southern Africa. The early summer was affected more negatively than the late summer during this event (Archer et al. 2017). Furthermore, the late-summer circulation patterns were characterized in the Southern Hemisphere by a strong positive SAM. While the association between ENSO and SAM is by no means linear, earlier studies suggested a negative relationship at inter-annual time scales (Pohl et al. 2009). However, the variation of the SAM with the

bidecadal cycle during late summer despite the ENSO signal were demonstrated also (Malherbe et al. 2014).

Here we consider rainfall data together with circulation patterns to indicate the persistence of the bi-decadal climate cycle

### *Data and Methodology*

Rainfall data from the South African National Parks for the Kruger Park were obtained, for a number of stations located in the park, starting as early as 1910 and continuing until 2018. Data were also obtained from SAEON (The South African Earth Observation Network) for one location, namely Phalaborwa, located just outside the western border of the park. Data were screened and where the record was incomplete, data were substituted with that of the nearest available station. Complete datasets were created for the period 1941 – 2017 for 4 stations located in and around the Kruger Park: Punda Maria (north), Phalaborwa (central-west), Satara (central-east) and Skukuza (southwest). The rainfall values for these stations were normalized and averaged to obtain an index for the rainfall, on a yearly time scale, for the summer rainy season (July – June).

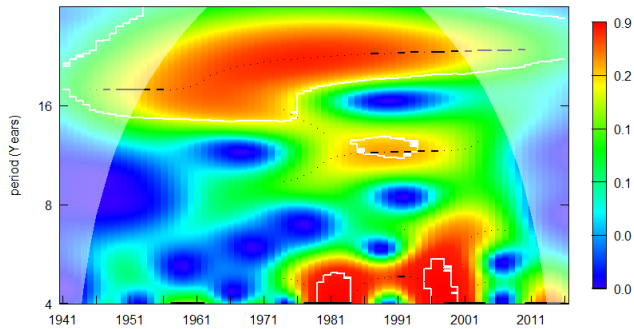
Other datasets used for the paper are: NCEP Reanalysis data for wind and geopotential height at various pressure levels (Kalnay et al. 1996), the monthly SAM (calculated by subtracting the normalized 850 hPa height at 65°S from that at 40°S - Gong and Wang 1999) using NCEP Reanalysis I. The monthly Southern Oscillation Index values were obtained from the Australian Bureau of Meteorology (BOM – [www.bom.gov.au](http://www.bom.gov.au)).

The impact of tropical cyclones over the region was quantified by the association of rainfall figures at the various stations with observed dates following landfall of systems, as identified by Malherbe et al. 2012 for the period 1948 – 2011, with a similar

approach to identify systems (and associated rainfall) after 2011.

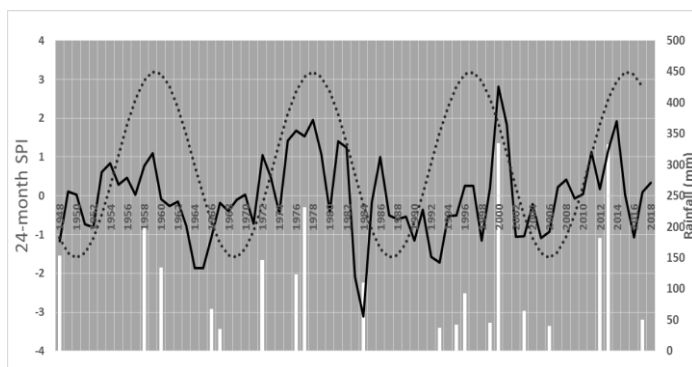
**Results and Discussion**

Figure 1 shows a wavelet analysis result based on the rainfall index derived from the annual July-June rainfall of all 4 stations considered for the period 1941 - 2018.



**Figure 1** Wavelet power spectrum of the annual (July-June) total rainfall index at 4 stations in the Kruger National Park. The greyed out outer regions delineate the area under which power can be underestimated as a result of edge effects, wrap-around effects and zero padding. White contour lines show the 90 % confidence limits based on 5000 Monte Carlo simulations of the red noise background spectrum.

The significant oscillation at bidecadal scale is clearly visible in the wavelet power spectrum, throughout the time series. Figure 2 shows, for the same period the association between summer rainfall, the rainfall contributed directly by tropical systems from the Southwest Indian Ocean (see Malherbe et al. 2012) and the 18.6-year rainfall cycle.



**Figure 2** 24-month Standardized Precipitation Index at Punda Maria in the north of the Kruger National Park (solid black line, primary y-axis), rainfall contributed

directly by tropical systems from the Southwest Indian Ocean (white bars, secondary y-axis) and idealized 18.6-year rainfall cycle (broken black line).

Figure 2 shows the persistence of the rainfall signal together with the direct influence of tropical systems from the Southwest Indian Ocean continuing until the present, following similar results in 2012 (Malherbe et al. 2012). During the most recent positive phase of the cycle, Tropical Storm Dando (2012) and a tropical depression in 2013 brought heavy rain to the region while Tropical Cyclone Dineo (2017) brought further widespread rain albeit lighter than the totals seen with the systems earlier in the wet epoch.

The association of rain from tropical systems moving inland from the Southwest Indian Ocean with the cycle remains one of the most striking elements and is associated with a stronger zonal easterly flow during late summer (Malherbe et al. 2014).

The lower rainfall associated with the 2015/16 El Niño is visible, similar to that of 1997/98 (during the previous wet epoch), but weaker so than during the strong El Niños outside the wet epochs (1991/92, 1982/83) indicated by the broken line in Figure 1. Both the 1997/98 and 2015/16 El Niños were associated with a positive late-summer SAM. This may suggest that global patterns during the high phase of the bidecadal cycle, associated with or forcing El Niño events, differ from that during the low phase. To demonstrate this possibility, Figure 3 shows the rainfall-SAM association during the wet and dry epochs, according to the bidecadal cycle, respectively.

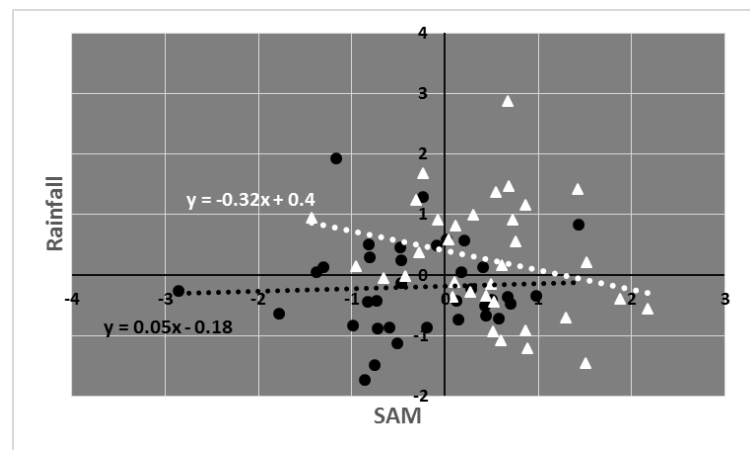


**Figure 3** Scatterplot showing the association between rainfall, as represented by the rainfall index for 4 stations in the Kruger National Park (y-axis) with the JFM SAM (x-axis). The 2 series are for the wet phase of the cycle (as per Malherbe et al. 2014) (white triangles and white trend line) and dry phase of the cycle (black circles and black trend line).

Figure 3 shows that summer rainfall tends to increase (weak positive association –  $R^2 < 0.01$ ) with increasing values of the

SAM during the dry phase of the bidecadal cycle while the association becomes negative ( $R^2 = 0.12$ ) during the wet phase of the cycle. This change in rainfall-SAM association between wet and dry phases of the cycle is significant at the 90% confidence level as determined by identical treatment of 1000 randomized time series based on the original data. Figure 4 shows an example from the most recent high phase of the cycle as represented by the SAM and local circulation anomalies. It shows the existence of a cyclonic anomaly to the east of South Africa during JFM 2016, to the north of the subtropical high-pressure belt contracted very far south, while easterly anomalies over the subtropical latitudes around  $15^\circ\text{S}$  is very much weakened. In fact, weak anticyclonic centres are visible around  $10 - 17.5^\circ\text{S}$ , over the subcontinent and the Indian Ocean to the east. With a weakly negative SAM in JFM 2017, the high-pressure anomalies contributing to the SAM was somewhat further to the north, with anticyclonic centres from  $30 - 20^\circ\text{S}$ , and enhanced subtropical easterlies around  $15^\circ\text{S}$ . The anomalies juxtaposed here contribute to the enhanced negative correlation between rainfall over the Lowveld and the SAM during the high phase of the bidecadal cycle.

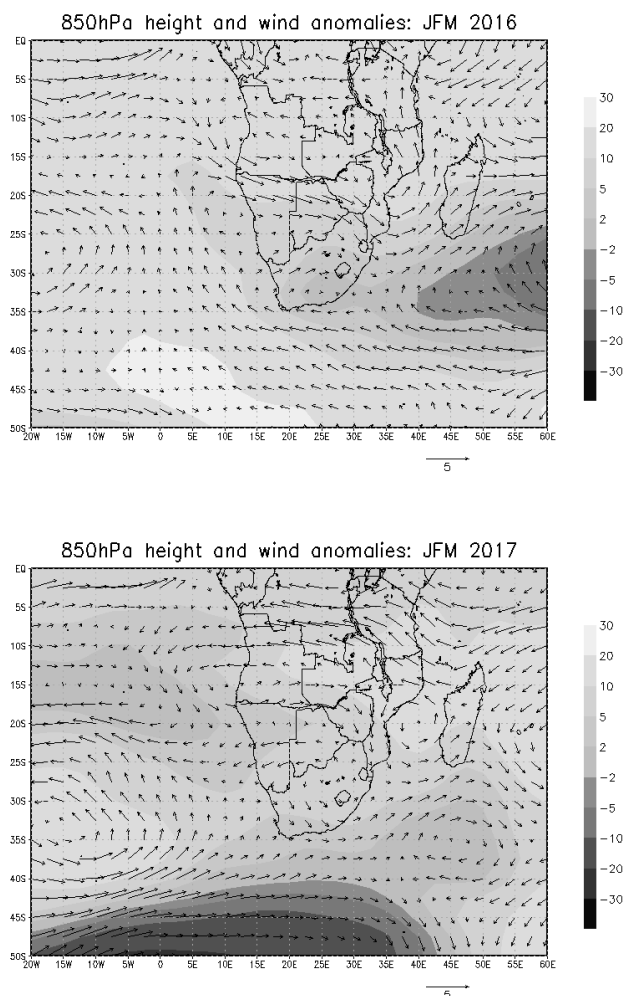


**Figure 4** 850 hPa anomalies in geo-potential meters (shading - gpm) and wind anomaly vectors (arrows - m/s) for JFM 2016 (strong El Niño and high SAM - top) and JFM 2017 (weak LA Niña, relatively low SAM - bottom).

Given the negative correlation between the SAM and rainfall over the Lowveld during the high phase of the bidecadal cycle, it may be expected that a similar weakened association between the SAM in JFM and the SOI will also be present. This is the case, as demonstrated by Figure 5.

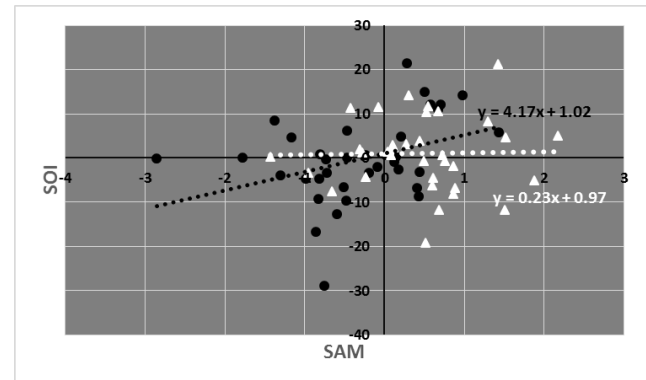


**Figure 5** Scatterplot showing the association between the SOI (y-axis) with the JFM SAM (x-axis). The 2 series are for the wet phase of the cycle (as per Malherbe et al. 2014) (white triangles and white trend line) and dry phase of the cycle (black circles and black trend line).

Figure 5 shows a weakened correlation between the SOI and the SAM during the wet phase of the cycle ( $R^2 < 0.01$ ) as opposed to during the dry phase ( $R^2 = 1.2$ ).

### Conclusion

The bidecadal climate cycle remains present in rainfall anomalies over the northeastern parts of South Africa until 2018. Here we also observed a weak correlation between rainfall and large-scale circulation anomalies over the Southern Hemisphere changing in association with the cycle, a feature that is also reflected in a similar change in the ENSO-SAM correlation at the bi-decadal time scale. It is outside the scope of the current work to consider reasons for the change in the SAM-SOI correlation, but changes in the driving mechanism of ENSO, as modulated at the bidecadal time scale, may possibly explain the feature.

### References

- Archer ERM, Landman WA, Tadross MA, Malherbe J, Weepener H, Maluleke P and Marumbwa FM, 2017. Understanding the evolution of the 2014–2016 summer

- rainfall seasons in southern Africa: Key lessons. *Climate Risk Management*, 16, pp.22-28.
- Kalnay E et al. 1996. The NCEP/NCAR 40-year reanalysis project. *Bulletin of the American Meteorological Society* 77:437-457.
- Malherbe J, Dieppois B, Maluleke M, Van Staden M, Pillay DL. 2016. South African droughts and decadal variability. *Natural Hazards*. 80: 657 – 681. DOI 10.1007/s11069-015-1989-y
- Malherbe J, Engelbrecht FA, Landman WA and Engelbrecht CJ. 2012. Tropical systems from the Southwest Indian Ocean making landfall over the Limpopo River Basin, southern Africa: a historical perspective. *International Journal of Climatology* 32:1018-1032. doi: 10.1002/joc.2320.
- Malherbe J, Landman WA and Engelbrecht FA. 2014. The decadal-scale rainfall cycle, Southern Annular Mode and tropical cyclones over the Limpopo River Basin, southern Africa. *Climate Dynamics* 42:3121-3138.
- Pohl B, Fauchereau N, Reason CJC, Rouault M. 2010. Relationships between the Antarctic oscillation, the Madden-Julian oscillation, and ENSO, and consequences for rainfall analysis. *J Clim* 23:238–254. doi:10.1175/2009JCLI2443.1
- Tyson PD, Cooper GRJ, McCarthy TS. 2002. Millennial to multi-decadal variability in the climate of southern Africa. *International Journal of Climatology* 22, 1105–1117, doi:10.1002/joc.787.
- Tyson PD. 1980. Temporal and spatial variation of rainfall anomalies in Africa south of latitude 22 during the period of meteorological record. *Climatic Change*, 2(4), pp.363-371.

## Present and future variability of heat units for Mpumalanga Province

Thato Masithela<sup>1</sup>, Thabo E. Mokgoale<sup>1</sup>, Joel Botai<sup>1</sup>, Michael Mengistu<sup>1</sup>

<sup>1</sup>South African Weather Service, Eco Glades 1 Eco Park, Centurion, Pretoria, 0157, South Africa

### Abstract

Heat units often known as Growing Degree Days (GDD) are frequently used to describe the timing of plants' biological processes. GDD units can be useful for a variety of activities in agricultural sector. The current study aims to investigate present and future change in accumulated GDD for warm season crops over Mpumalanga province using the Coordinated Regional Climate Downscaling Experiment (CORDEX) Africa models. The maximum and minimum daily temperature from the Rossby Centre Regional Atmospheric Model (RCA4) driven by the nine Global Climate Models participating in the Coupled Model Inter-comparison Project Phase 5 (CMIP5) was utilized to calculate the accumulated GDD. Accumulated GDD was calculated for historical period from 1976 – 2005 and GDD projections were done for near period 2036 – 2065 and far period 2066 – 2095 under Regional Climate Projection (RCP) 4.5 and RCP 8.5 concentration pathways. In general, the GDD are projected to change in space and magnitude for both RCP 4.5 and 8.5. The degree of change is more pronounced in far period under RCP8.5. The underlying magnitude and pattern change in GDD under global warming will have significant impacts on warm season crops over Mpumalanga area.

**Keywords: GDD, CORDEX, Temperature**

### Introduction

Temperature is a key factor that influences the timing of biological processes. The growth and development of plants depends on temperature and specific amount of heat is required for plants to develop from one stage in their lifecycle to another, such as from emergence to harvest (Parthasarathi *et al.*, 2013). Heat units, often known as Growing Degree-Days (GDD) are used frequently to assess the timing of biological processes (McMaster and Wilhelm, 1997). The concept of heat units was introduced in 1730 by Reaumur and calculating heat units has been used effectively in agricultural sciences (Neild and Seeley, 1977). The GDD is an indicator used to measure amount of heat accumulated above a specific base temperature, and plays an important role to predict plant and insect developmental stages (Castillo *et al.*, 2016). The base temperature (T<sub>base</sub>) is the temperature below which development does not occur and varies among crop species and different organisms. Heat units are used to assess the suitability of a region for crop production, estimate heat stress on crops, predict maturity and harvest dates and determine the developmental stages of crops (Parthasarathi *et al.*, 2013). Generally, temperature affects the developmental stages, phenology and the length of growing season in crop production (Castillo *et al.*, 2016). Global climate change affects and causes shifts in phenology, or the timing of certain growth stages on plants and animals (Cayton *et al.*, 2015). GDD can account for both spatial and temporal variation in temperature, and constrains the thermal limits within which growth is possible. Therefore, GDD should be used as a strong, integrative measure of climate change (Cayton *et al.*, 2015). The aim of this study is to estimate the future variation of GDD for the periods of 2036-2065 and 2066-2095 under Regional Climate Projection (RCP) 4.5 and RCP 8.5 emission scenarios in relation to the reference period (i.e. 1976-2005) for the Mpumalanga province, South Africa.

### Data and methodology

Mpumalanga province is located in the eastern part of South Africa, bordered by Mozambique and Swaziland in the east and Gauteng in the west. It is situated mainly on the high plateau grasslands of the Middle veld, which roll eastwards for hundreds of kilometres. It has an area of 76 495 km<sup>2</sup> and total population of 4.4 million (StatsSA, 2016). Mpumalanga is a temperate region with a mean annual precipitation greater than 700 mm and the mean annual temperature between 24.5° C - 25°C (Blignaut *et al.*, 2009). Figure 1 represents the digital elevation map of the study area, while Table 1 represents the cultivations, their characteristics and the planting date.

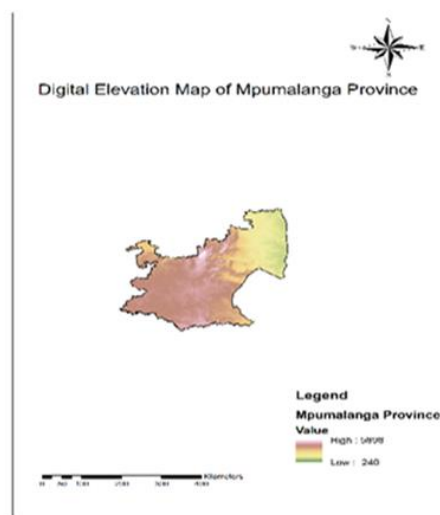


Figure 1. Digital elevation map for Mpumalanga province

Table 1. Warm season crops and their characteristics cultivated in Mpumalanga Province (DAFF, 2016)

Study area	Cultivations	Scientific name	Planting date	GDD maturity
Mpumalanga	Maize	<i>Zea Mays</i>	Oct-Nov	800-2400
	Sorghum	<i>Sorghum Bicolor</i>	Oct-Dec	1400-1800
	Sunflower seed	<i>Helianthus annuus</i>	Nov-Mid Jan	1700-1900
	Soya-beans	<i>Glycine max</i>	Mid Nov	2450-2550
	Dry beans	<i>Phaseolus Vulgaris</i>	Oct-Nov	1100-1300
	Sugarcane	<i>Saccharum Offinarum</i>	Feb-Apr	3000

Present GDD for warm season crops were calculated using daily air temperature data values obtained from point observed data and interpolation to create gridded air temperature fields (SAWS-obs) and output from RCA4 regional climate model (RCMs) driven by nine CMIP5 GCMs models which are, CanESM2, CNRM, CSIRO, IPSL, MIROC5, HadGEM2, MPI-ESM, NorESM1, GFDL and the ENSMEAN was calculated using all the nine models for the period of 1975 – 2005. Out of the nine models only performing models were selected and then future GDD for warm season crops were calculated using performing models for periods of 2036-2065 and 2066-2095 under RCP 4.5 and RCP 8.5 emission scenarios. Accumulated GDD were also calculated for both present and future periods. The model simulations were validated with point observed data from SAWS and interpolation to create gridded air temperature fields. The formula in Eq. 1 was used to calculate the number of GDDs for the Mpumalanga province. Base temperatures of 10° C for the warm season crops was used to calculate GDD.

$$GDD = \left( \frac{T_{max} + T_{min}}{2} \right) - T_{base} \quad \text{Eq.(1)}$$

Where Tmax represents daily maximum temperature (°C); Tmin is daily minimum temperature (°C); Tbase is the temperature below which process development does not occur. The GDD Eq. 1 was applied every day of the growing season over a period of Oct-Apr each year for 30 years and the daily GDD were accumulated into seasonal averages.

**Results and discussion**

Fig. 2 illustrates the performance of the nine models in representing the historical period accumulated GDD and its ENSEMBLE and the simulations are compared to SAWS-obs to check which models perform better within a reference period of 1975-2005 for the month of Oct – Apr. Models CanESM2 and IPSL perform better than the other seven models including ENSEMBLE. Therefore, the two models were used to predict future accumulated GDD for the reference period, 2036-2065 and 2066-2095 periods under RCP 4.5 and RCP 8.5 emission scenarios.

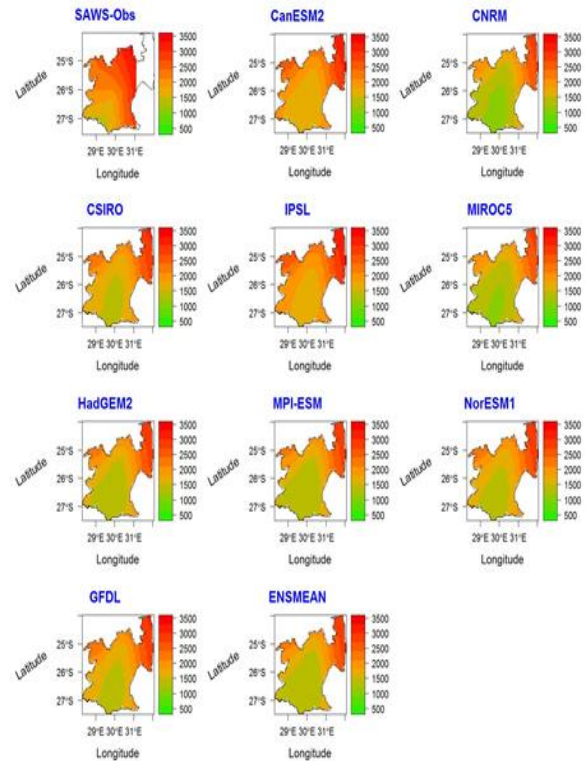


Figure 2. Seasonal Accumulated GDD from historical dataset.

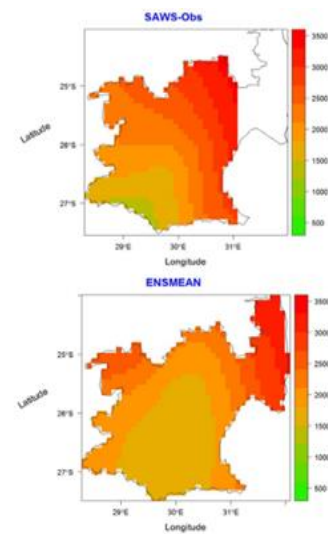


Figure 3. Seasonal Accumulated GDD of SAWS-obs and ENSEMBLE of CanESM2 and IPSL model from historical dataset.

The historical GDD simulations from the two models, CanESM2 and IPSL, (Figure 3) were used to obtain the ENSEMBLE and compared to SAWS observations (SAWS-obs). The analysis showed that, GDD for ENSEMBLE ranged between 1500 - 3500 which was similar to historical observed data, which ranged from 1300-3500 accumulated GDD (Figure 3). This showed that the ensemble mean for the nine models

corresponded with the observed data. These GDD values indicate that Mpumalanga province is suitable for warm season crops, which require GDD values between 800 and 3000 to

Scenarios	Mean GDD	Historical GDD	Change in GDD
RCP 4.5(2036-2065)	2837.82	2412.62	425.2
RCP 4.5(2066-2095)	2960.7	2412.62	548.05
RCP 8.5(2036-2065)	2986.15	2412.62	573.5
RCP 8.5(2066-2095)	3394	2412.62	981.35

reach maturity. The two models were then used for future GDD projections under RCP 4.5 and RCP 8.5 emission scenarios over reference period of 2036-2095.

The future projections were obtained under RCP 4.5 and RCP 8.5 and analyzed covering the growing seasons from 2036-2095. The results were derived using historical data for present seasonal accumulated GDD and from two performing models which are CanESM2 and IPSL model for future seasonal accumulated GDD (Figure 4). The GDD are expected to increase under both RCPs (Figure 4). The future mean GDD could increase between 425.5 – 528.05 under RCP 4.5 and between 573.5 – 981.35 under RCP 8.5. The GDD are directly dependent on temperature, therefore the change in temperature results in the change in GDD.

data was obtained from SAWS. The two performing models, CanESM2 and IPSL, were selected and compared to observed data from SAWS using the ENSEMBLE for both models. The future projections of the seasonal accumulated GDD for the periods of 2036-2065 and 2066-2095 under RCP 4.5 and RCP 8.5 emission scenarios using data from CanESM2 and IPSL were performed for Mpumalanga province. The results indicated that there will be an increase of GDDs under both RCPs. The increase of accumulated GDDs would have an impact on growth and development of crops, thus shorten the length of growing season, the maturity and harvest dates for warm season crops.

**Acknowledgments**

The authors acknowledge South African Weather Service for providing with the support during the entire work.

**References**

Blignaut, J., Ueckermann, L., Arosonc, J. (2009). Agriculture production’s sensitivity to changes in climate in South Africa. South African Journal of Science 105.  
 Castillo, N.R., and Gaitán Ospina, C.F. (2016). Projecting Future Change in Growing Degree Days for Winter Wheat. Agriculture, 6: 47.  
 Cayton, H.L., Haddad, N.M., Diamond, S.E., Gross, K., and Ries, L. (2015). Do growing degree days predict

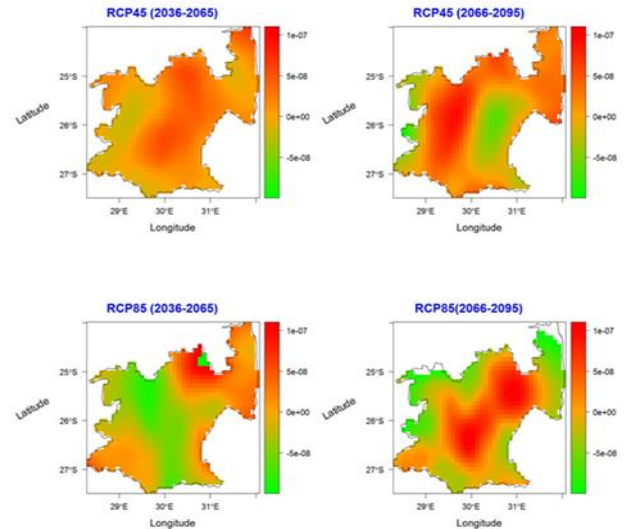


Figure 4. Future GDD results in Mpumalanga Province

Table 2. Change in Growing degree days for period of 30 years

**Conclusions**

In the current research, the present seasonal accumulated GDDs for the period of 1975-2005 were done and historical data was obtained from several RCMs models and observed

phenology across butterfly species? Ecology, 96(6): 1473–1479.  
 Department of Agriculture, Forestry and Fisheries (2016). The South African year book agriculture (2015/2016) Pretoria, South Africa.  
 McMaster, G.S., and Wilhelm, W.W. (1997). Growing degree-days: one equation, two interpretations. Agricultural and Forest Meteorology 87: 291-300.  
 Neild, R. E., and Seeley, M. W. (1977). Growing Degree Days Predictions for Corn and Sorghum Development and Some Applications to Crop Production in Nebraska. Univ. of Nebraska, Lt, Coln libraries.  
 Parthasarathi, T., Velu, G., and Jeyakumar, P. (2013). Impact of Crop Heat Units on Growth and Developmental Physiology of Future Crop Production: A Review. A Journal of Crop Science and Technology Volume 2, Issue 1: 2319–3395.  
 StatsSA, (2016). Provincial profile: Mpumalanga Community Survey 2016. Statistics South Africa.

## ***An Era-Interim hail climatology for South Africa***

Liesl L Dyson\* and Nita Pienaar\*\*

\*Department of Geography Geoinformatics and Meteorology, University of Pretoria

\*\*Life Insurance Solutions, MMI Holdings, South Africa

### ***Abstract***

Understanding the character of hail is important. In November 2013, two hail events in Gauteng cost the insurance industry ± R2 billion. The hailstorm of 28 November 2013 “was the single worst insurance event in South Africa’s history”. The question is how common are these destructive events and how likely are they to occur at any geographical location in South Africa? In order to answer these questions an Era-Interim hail climatology is created from 1979-2017 using the HAILCAST model. Results show geographical distribution patterns very recognisable when compared to observed climatologies over the summer rainfall area. There is a direct relationship between increased number of hail days and height above sea level. Eastern Lesotho has the highest annual hail day frequency over southern Africa – 70 days. Between 80-90% of hail events occur in summer and there are between 5-10 hail days per annum over the mountains of the South Western (winter) and Southern Cape (summer). November is the month with the most hail days over the entire southern Africa with the exception of the South Western Cape (August) and Lesotho (December). Additional information not available from observed climatologies are, amongst others, hail day frequency for different hail sizes as well as the seasonal and temporal hail frequency distribution. The Era-Interim HAILCAST climatology captures the general hail pattern over South Africa very well. However, larger hail (> 3cm) seems to be over predicted.

*Keywords:* Hail day frequency, hail climatology, South Africa, Era-Interim. HAILCAST

### ***Introduction***

The observational record of hail in South Africa is particularly poor. The official source of hail information is from the South African Weather Service (SAWS) where a few manned stations report hail if it occurred *at a station close* to the time of observation. The only size criteria available from the SAWS database is that the hail was > 5mm in diameter. The distribution of weather stations used by SAWS is coarse and not all of them are manned, making the capture of local-scale hail events unreliable. The lack of reliable hail observations is a global issue. Punge and Kunz (2016) describe how hailstorms in Europe are inaccurately captured due to the lack of observing systems. In Australia the environments connected to severe thunderstorms, including those producing hail, are poorly observed (Allen and Karoly, 2014). The USA, on the other hand, has an exceptional observational hail database record, *Storm Data*, which is maintained by the National Climatic Data Center. *Storm Data* currently contains data from January 1950 to February 2018 and consists of data from (amongst others) emergency managers, spotters, damage surveys, newspaper reports, insurers and the general public (NOAA, 2018). However, there are some reporting biases in Storm Data as non-severe hail events are under reported and population density substantially influence reporting (Allen et al., 2015).

Despite the lack of observational hail data there is a dire need to understand the character of hail. Hail climatologies help to pinpoint where improvements are needed in understanding atmospheric conditions leading to hail. Determining hail risk from climatologies is important to insurers and economists while farmers may make informed decision on hail threat if long-term hail data are available (Punge and Kunz, 2016). Several attempts have been made in recent years to create hail

or severe thunderstorm climatologies using re-analysis data. In the early 2000’s Brooks et al., (2003) and (2007), started using re-analysis data to determine characteristics of severe thunderstorms globally. Examples of this also include Eccel et al. (2012) who integrated hailpad observations and instability parameters from ERA-interim data to create a hail climatology over the Alps. Karoly and Allen (2014) used the same approach over Australia and Burcea et al. (2016) over Romania. In Europe, Punga et al. (2017) estimated hail frequency by combining the detection of overshooting tops from satellite observations with convective parameters in Era-Interim. Allen et al. (2015) used monthly averages of several parameters from the North American Regional Reanalysis dataset to determine the predictability of hail from monthly averaged datasets.

In this paper the HAILCAST (Brimelow et al., 2002) model was run from 1979-2017 on Era-Interim pseudo proximity soundings over South Africa in order to create a hail climatology.

### ***Instrumentation and Method***

ERA-Interim reanalysis (Dee et al., 2011) from the European Centre of Medium Range Weather Forecast (ECMWF) was used to create pseudo proximity soundings over South Africa. Temperature, dew point temperature, geopotential height as well as wind direction and speed were isolated on all the levels at every grid point over South Africa for 0000, 0600, 1200 and 1800 UTC for every day from 1979 to 2017. One of the major constraints in the ERA-interim data set is that the horizontal resolution of 0.75° requires the use of convective and boundary layer parametrisation schemes. This may result in inaccurate vertical profiles of temperature and dew point temperature (Taszarek et al., 2018). Convective parametrisation

schemes are not developed to represent single convective storms (Sanderson et al., 2015) and the number and intensity of convective storms may therefore be inaccurately captured by the reanalysis dataset. There will therefore be spatial and temporal differences between observed and modelled hail climatologies. Another limitation in the creation of the pseudo soundings is that the horizontal resolution of ERA-interim in areas with significant variation in topography may result in the soundings not representing the spatial variability of an area accurately. A drawback of reanalysis data, in general, is that strong vertical gradients are not represented well (Allen and Karoly, 2014; Brooks et al. 2003). This is of particular concern when simulating severe storm soundings as the thermal (capping) inversion could be misrepresented.

HAILCAST is a combination of a steady-state cloud model with a time-dependent hail growth model (see Brimelow et al., 2002 and Poolman 1992 for detail description of HAILCAST) predicting a maximum hail size diameter. In this paper HAILCAST is run on the ERA-interim pseudosoundings. Thunderstorms are very sensitive to slight changes in surface temperature and moisture (Crook et al., 1996). Following the method of Brimelow et al. (2006) the uncertainty in surface variables is compensated for by running HAILCAST several times with different input data, creating an ensemble of forecasts. The ensembles are produced by adding perturbations of +1.0°C, +0.5°C, -0.5°C, -1.0°C to ERA-interim surface temperature and dewpoint temperature at each grid point and running HAILCAST for all the combinations. 25 individual hail diameter forecasts are created this way and the average hail size is the arithmetic mean of the hail sizes of each ensemble member. This mean value is used to represent the hail diameter on any specific day.

Brimelow et al. (2006) found that HAILCAST has a tendency to over predict the size of hail. In order to compensate for this, in this paper only hail with a diameter > 1cm is considered with the upper limit at > 3 cm. An Era-Interim HAILCAST (EIH) hail day is defined as a day when the average ensemble hail size was > 1 cm. Hail-day frequency was calculated for 2 classes, when the average ensemble hail size was > 1 cm (HDF1) and > 3cm (HDF3).

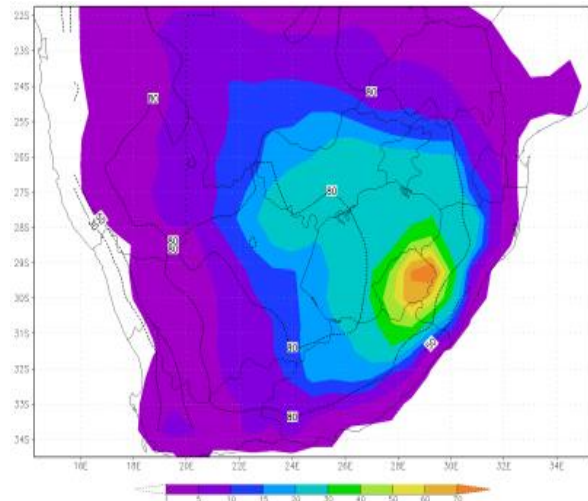
*Results and Discussion*

The EIH hail day frequency (> 1cm) for summer is shown in Fig. 1a and is compared to the observational climatology of Le Roux and Olivier (1996) in Fig. 1b. Perfect agreement cannot be expected between the 2 datasets as the Le Roux and Olivier (1996) climatology represents hail frequency at a point location while EIH hail day frequency is a numerical grid box which incorporates an area of approximately 5000 km<sup>2</sup>. There is nevertheless remarkable parity between the geographical distributions of hail in these 2 images. The highest HDF1 on both images is over the eastern parts of Lesotho with tight gradients between the coast of KwaZulu-Natal and the mountains. There are also relatively high HDF1 values over the Witwatersrand extending to the escarpment of Mpumalanga. One of the noticeable differences between these 2 maps is that the HDF1 over Mpumalanga in the EIH climatology is not as high as the frequency over Lesotho as is the case in Fig. 1b.

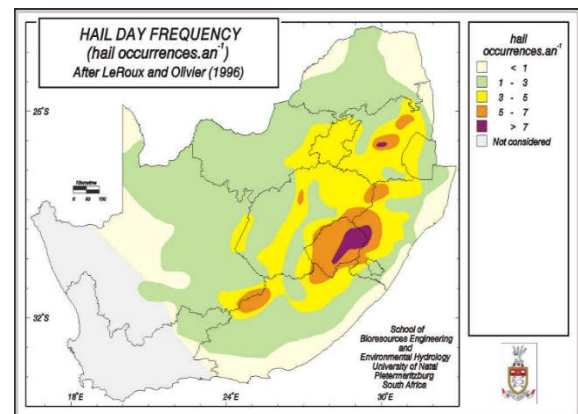
Figure 1a: The Era-Interim HAILCAST hail day frequency for summer (October to March) for hail with diameter > 1 cm.  
 Figure 1b: The annual hail day frequency at point location over the summer rainfall area (after Le Roux and Olivier (1996))

The EIH climatology also extends an area of higher HDF1 into the south-western parts of the North-West Province which is

absent in the Le Roux and Olivier (1996) map. Nevertheless,



the EIH climatology provides information not previously available over the winter rainfall areas and outside the borders

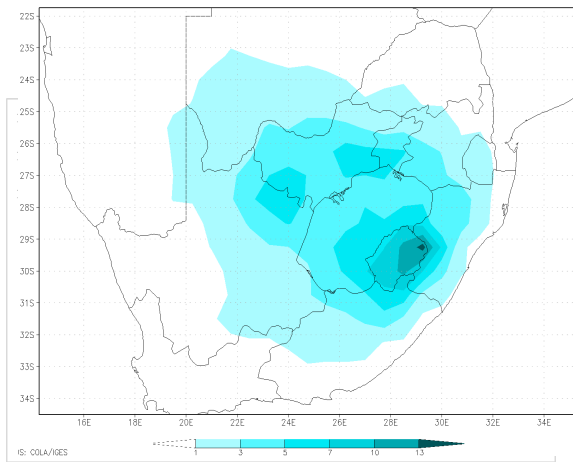


of South Africa. The mountains of the Southern and Western Cape receive 5-10 hail days per annum and there are between 10-20 hail days over southern Botswana. This area is the corridor through which moist tropical air flows from the ITCZ into South-Africa. The EIH climatology confirms that most hail days occur in austral summer (October to March) as more than 80% of hail days occur in summer over most of southern Africa (dotted lines in Fig 1a). It is only the extreme South-western parts where 70% of all hail days are in winter.

The EIH climatology also provides information on the frequency of larger hail which was not previously available. The HDF3 (Fig 2) are as high as 13 over eastern Lesotho and with generally high values over the Drakensburg. Southern Gauteng and south-western North West provinces all have more than 5 days per annum when hail > 3cm occurs. HDF3 is less than 1 per annum over the western half of the country. For the entire area with an HDF3 of more than 1, the percentage occurrence in summer is larger than 90% and approaching 100% over Lesotho. Although small hail may occur over the South-western Cape in winter from mid-latitude cyclones, the EIH climatology reveals that large hail is very rare and seldom occurs even in winter.

Figure 2: The Era-Interim HAILCAST hail day frequency for summer (October to March) for hail with diameter > 3 cm.

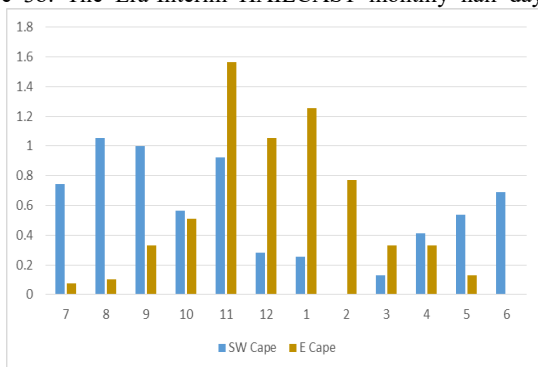
October is the start of the hail season over southern Africa. During October and November months the middle and upper troposphere is still cold after winter while surface temperatures rise quickly and moist air starts to flow into the eastern interior from the Mozambique Channel. The availability of surface moisture, steep vertical temperature lapse rates and large wind shear values make conditions during early summer ideal for



hail over the eastern interior (Simpson and Dyson, 2018). November has the highest frequency of hail days over the entire summer rainfall season with the exception of Lesotho which has the highest frequency in December months (Fig. 3a). There is a sharp decrease in hail day frequency as summer progress with February having the lowest values. It is during this time of year, when tropical air flows into southern Africa, that the hail frequency decreases notably. Over the South-western Cape, August has the highest HDF1 with higher values during winter months (Fig. 3b). There is nevertheless an increase in HDF1 during November even in this winter rainfall area.

Figure 3a: The Era-Interim HAILCAST monthly hail day frequency over Lesotho (blue) and Gauteng (orange)

Figure 3b: The Era-Interim HAILCAST monthly hail day



frequency over SW Cape (blue) and Eastern Cape (tan)

Conclusions

The EIH hail climatology provides a reasonable representation of the occurrence of hail over southern Africa. For smaller hail (> 1cm) there is remarkable parity with previously established observational climatologies. Although it is very difficult to verify it is likely that EIH climatology overestimates the frequency of larger hail (> 3cm). There is nevertheless detailed information available from the EIH climatology which was not previously available. These include the spatial, temporal and seasonal distribution of hail over the entire southern Africa.

References

Allen JT, and Karoly DJ (2014). A climatology of Australian severe thunderstorm environments 1979–2011: Inter-annual variability and ENSO influence. *Int J Climatol* 2014;34:81–97.  
 Allen JT, Tippett MK and Sobel AH (2015) An empirical model relating U.S. monthly hail occurrence to large-scale meteorological environment. *J. Adv. Model. Earth Syst.*, 7, 226–243

Brimelow JC, Reuter GW, and Poolman ER (2002). Modeling maximum hail size in Alberta thunderstorms. *Wea. Forecasting*, 17, 1048–1062  
 Brimelow JC, Reuter GW and Goodson R (2006). Spatial forecasts of maximum hail size using prognostic model soundings and HAILCAST. *Weather Forecasting*, 21 206–219  
 Brooks HJ, Lee J and Craven J. (2003). The spatial distribution of severe thunderstorm and tornado environments from global reanalysis data. *Atmospheric Research* 67: 73–94.  
 Brooks HE, Anderson AR, Riemann K, Ebberts I and Flachs H. (2007). Climatological aspects of convective parameters from the NCAR/ NCEP reanalysis. *Atmospheric Research* 83: 294–305.  
 Burcea S, Cică R, Bojariu R (2016). Hail climatology and trends in Romania: 1961–2014. *Mon. Weather Rev.*, 144 4289–4299  
 Crook NA (1996). Sensitivity of moist convection forced by boundary layer processes to low-level thermodynamic fields. *Mon. Wea. Rev.* 124: 1767–1785.  
 Dee D and Coauthors (2011). The ERA-Interim reanalysis: Configuration and performance of the data assimilation system. *Quart. J. Roy. Meteor. Soc.*, 137, 553–597.  
 Eccel E, Cau P, Riemann-Campe K, Biasioli F (2012). Quantitative hail monitoring in an alpine area: 35-year climatology and links with atmospheric variables. *Int J Climatol* 32:503–17.  
 Le Roux NJ and Olivier J (1996). Modelling hail frequency using a generalized additive interactive technique. *South African Geographical Journal*, 78: 7 - 12.  
 NOAA (2018). Storm Events Database. <https://www.ncdc.noaa.gov/stormevents/faq.jsp>  
 Poolman ER (1992). Die voorspelling van haelkorrelgroei in Suid-Afrika (The forecasting of hail growth in South Africa). M.S. thesis, Faculty of Engineering, University of Pretoria, 113 pp.  
 Punge HJ and Kunz M (2016). Hail observations and hailstorm characteristics in Europe: A review. *Atmos. Res.*, 176–177, 159–184  
 Sanderson M, Hand W, Groenemeijer P, Boorman P, Webb J, McColl L. (2015) Projected changes in hailstorms during the 21st century over the UK. *Int J Climatol*.  
 Simpson L, Dyson LL (2018). Severe weather over the Highveld of South Africa during November 2016. *Water SA*, 44, 75–85  
 Taszarek M, Brooks H, Czernecki B, Szuster P and Fortuniak K (2018) Climatological aspects of convective parameters over Europe: a comparison of ERA-Interim and sounding data. *J Clim.* <https://doi.org/10.1175/JCLI-D-17-0596.1>

# The Trends of Thermodynamic Indices Over Irene

H HAVENGA, R.P BURGER & S.J PIKETH

North-West University Potchefstroom

22743259@nwu.ac.za, roelof.burger@nwu.ac.za, & stuart.piketh@nwu.ac.za

## Abstract

*Radiosondes are a valuable tool to analyze the vertical profile of the atmosphere. From these soundings we can derive several thermodynamic indices to evaluate the state of the atmosphere and the possibility of certain weather phenomena. This study examines some of the commonly used indices over Irene by examining data from the Integrated Global Radiosonde Archive (IGRA) to evaluate the changing nature of the atmosphere over the Highveld. Early results show a marginal increase towards a convective favoring atmosphere when analyzing the 12:00 UTC values of several thermodynamic derived variables including CAPE, CIN, KI, SI and LI possibly indicating an increasingly convective favoring atmosphere. The implications of this include the possibility of an increased frequency in events such as hailstorms, thunderstorms and flash floods.*

## 1. INTRODUCTION

Radiosonde data has proven to be a valuable tool for weather services and atmospheric scientists around the world. These products are often used to forecasts of severe weather events while providing data that feeds into global forecasting models used to drive numerical weather predictions. The data also provides a recent historical record of possible changes in the atmosphere. Considering the potential impacts of a changing climate, radiosondes provides a valuable tool in understanding our changing atmosphere in relation to an increasingly warmer climate. This increase in temperature can be linked to a convective favoring atmosphere as every 1°C increase in temperature allows for the atmosphere to *hold* more moisture and also increases the rate of evaporation. Over areas like Johannesburg and Pretoria where we already see extreme damage as a result of convective driven weather events like hail and flash floods, a warmer atmosphere could lead to an increase in these events. To understand this possible trend it is worth looking at radiosonde data instead of surface temperature alone to understand the change within the vertical profile of the atmosphere. Variables such as convective available potential energy (CAPE), convective inhibition (CIN), Showalter Index (SI), K-index, lifted-index (LI) and totals-totals index (TT) are derived from radiosonde soundings and are commonly used for the forecasting and prediction of convective events.

The main aim of this study is to assess the long term trends of thermodynamic variables from radiosonde data over South-Africa and the Highveld. The Irene weather station (see figure 1)

has been consistently launching weather balloons since the 1970s data is available through the SAWS and also in global radiosonde databases such as the Integrated Global Radiosonde Archive (IGRA) which will be used to achieve this objective.

## 2. THE USE OF THERMODYNAMIC VARIABLES IN WEATHER FORECASTING

The thermodynamics of convection play an important part in understanding severe storm formation. Through the use thermodynamic diagrams scientists have been able to represent processes in the atmosphere related to various atmospheric conditions including severe, high impact events. Research related to sounding derived severe storm climatologies is relatively abundant for Europe (see Berthet et al. (2013); Groenemeijer and Van Delden (2007); Mohr and Kunz (2013); Sánchez et al. (2003, 2009)) and North-America (see Allen et al. (2015); Doswell and Schultz (2006); Dupilka and Reuter (2006); Rasmussen and Blanchard (1998)). Over South-Africa Blamey et al. (2016); Dyson (2013); Dyson et al. (2015); Rae (2014) research is related to the topic of thermodynamic characteristics of weather events. Dyson et al. (2015) focused on the examining sounding derived parameters from 1977 to 2015 to assess storm environments and found that most severe convective indices that were recorded during summer months were CAPE and wind shear, furthermore these indices were comparable to that of severe events observed in the United States. Rae (2014) had a similar finding, showing that most unstable CAPE (MUCAPE) values are the highest during summer and also noting

the sudden increase in observed MUCAPE from September to October. Blamey et al. (2016) analysis of convective indices over South-Africa supports these findings, they show that a marked increase in CAPE is observed over the spring and summer months.

To record these thermodynamic indicators mentioned meteorological agencies typically launch weather balloons known as soundings at certain points to gather atmospheric data. In South-Africa this occurs at Cape-Town and Irene on a daily basis while other sites have a more irregular frequency of launches. The basic movement of a parcel of air in a warm unstable environment can be summed up as follows: as a parcel is lifted through a colder region of stable air it becomes saturated and reaches the lifting condensation level (LCL) where clouds typically form. In a warm unstable environment the parcel continues lifting to its level of free convection (LFC). To achieve this the parcel requires a certain amount of energy to *break* through the stable atmosphere known as CIN. If a parcel is warm it will continue to rise to the equilibrium level (EL) where it has the same density to that of the surrounding environment. When this occurs a parcel is said to be positively buoyant and this is represented by the function CAPE. Thermodynamic indicators derived from these soundings are used to evaluate the thermodynamic structure of the atmosphere and the possibility of severe weather occurrence.

Johns and Doswell (1992); Sánchez et al. (2009) mentions three *ingredients* that indicate an environment ideal for storm formation; this includes a moist deep layer in the low/mid troposphere, instability and a triggering mechanism which can be deduced from sounding observations and the derived indicators.

### 3. DATA AND METHODS

The study area (see figure 1) is located in the South-African interior plateau known as the Highveld. At a mean altitude of 1500m - 1700m above sea level and covering an area of 30000km<sup>2</sup> (Freiman and Piketh, 2003), the Highveld extends across several provinces in South-Africa; the Free-State, Gauteng and Mpumalanga. The region is the location of some of Africa's most industrialised areas and accounts for 75% of South-Africa's industrial activities. Around 70% of the Highveld is covered by grasslands and utilized for agriculture (Collett et al., 2010; Scheifinger and Held, 1997).

The IGRA database is used to analyze 5 derived

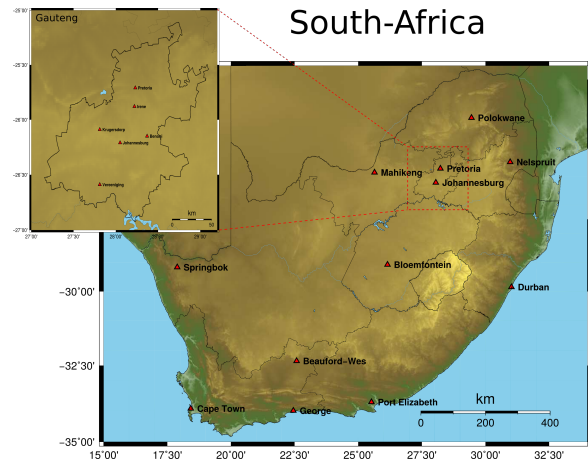


**Figure 1:** Located in the South-African Highveld, Irene is home to the SAWS weather radar the location for daily radiosonde launches. The area is important as it provides valuable weather related information to the Gauteng province, which is South-Africa's economic hub and frequently the location of high impact weather such as hail and glash floods

variables namely CAPE, CIN, SI, KI, LI, TT. The IGRA does have a quality control procedure, but as noted by (Durre et al., 2006) the IGRA data set may have some discrepancies, to account for this the data set underwent a basic quality control procedure to correct for unrealistic values. Furthermore, only the 12 UTC sounding was utilized as most convective activity over the Highveld occurs in the afternoon, reducing the number of data points. A Theil-sen slope analysis is used to determine the trends of the selected parameters along the 95% confidence interval of the slopes. Two major analyzes where done, first the complete data set for the time period to examine the long term trend and secondly the data was examined per season for the time period. Seasons are defined as summer (December, January & February), autumn (March, April & May), winter (June, July & August) and spring (September, October & November) in the analysis the trends of thermodynamic indicators for a period of 45 years. Each indicator was analyzed for seasonal and long term trends.

Radiosonde data is prone to failures and within the scope of this study the data underwent a minimum sanity check as the IGRA already undergoes a quality control procedure (Durre et al., 2006). Dyson (2013) advises against the use of the IGRA database as data for some periods is missing and erroneous dew point are could impact soundings on convective days. It is important to note that Dyson (2013) emphasizes that thermodynamic variables and values associated convection may differ across geographic locations.

An regression analysis is performed by using the Thiel-Sen slope analysis on the IGRA data for the time period. This allows for the analysis of seasonality and long term trends in the data. The Thiel-Sen determines the trend slope of  $n$ -pairs of data as;

$$T_i = \frac{x_j - x_i}{j - i} \quad (1)$$

where  $x_j$  and  $x_i$  represents time at  $j$  and  $i$  (Khan et al., 2015). The Thiel-Sen has the advantage of being 'robust' (Dennison et al., 2014; Sen, 1968; Theil, 1992) to outliers as it is based on the median slope, this is a advantage when using a radiosonde dataset where outlier values are frequent.

#### 4. RESULTS

##### 4.1. The seasonal trends of thermodynamic indicators

The IGRA dataset for the Irene weather station was used to analyze the trends of thermodynamic indicators for a period of 45 years. Each indicator was analyzed for seasonal and long term trends. The section is similar to Dyson (2013) analysis of heavy rainfall events using sounding derived indicators. The exception is that Dyson (2013) used radiosonde data from the UWYO database while the IGRA database is used in this study.

Figure 2 shows a clear indication of the seasonal variation observed in CAPE. Spring and summer months are associated with the highest average CAPE values and summer averages slightly over 1000 J/kg. This is ideal for the formation of convective storms. The high values are expected as the circulation over South-Africa during summer is associated warm tropical circulation which is highly unstable and increases the amount of buoyant energy in the atmosphere. There is also a significant upward trend in the buoyant energy available in the atmosphere over the last 40+ years, particularly in the spring and summer months. The Thiel-Sen slope analysis indicates a significant trend of 0.59 and 0.46 for the spring and summer months respectively. No significant trend is observed in the autumn and winter months and CAPE values seem to be relatively stable. These observations support Dyson (2013) findings that CAPE values peak in December and January. The positive seasonal trend that is observed in the CAPE values indicate that the atmosphere is becoming increasingly favorable for the formation of severe events associated with convection.

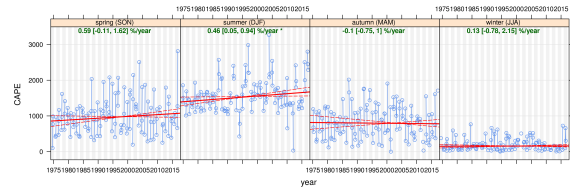


Figure 2: The seasonal distribution of CAPE

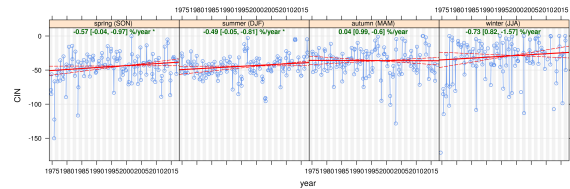


Figure 3: The seasonal distribution of CIN

In Figure 3 we see that the seasonal trend of CIN is less variable than that of CAPE. The lowest values of CIN is observed during the summer months from November to February with only a marginal difference between the seasons. The fine balance between CIN and CAPE is emphasized again and if the CIN is too low severe storms will not appear and only cumulus clouds will form while high CIN can completely prevent storm formation. According to Grieser (2012) values between -15 and -200 is favorable for convective activity. The values remain stable throughout the year and no significant difference is observed between the seasons.

The KI based on the vertical temperature gradient between 850hPa and 500hPa has a well-defined seasonal variation (see Figure 4). The highest KI values are observed in the summer months and there is also an observed positive trend in this value indicating an increasingly convective favoring atmosphere during summer months. A positive trend is also observed during spring months, although not that significant. Autumn and winter months show no significant positive trend but it is observed that the winter months show a trend towards a more stable atmosphere with a slight decreasing trend. This is similar to that observed by Dyson (2013).

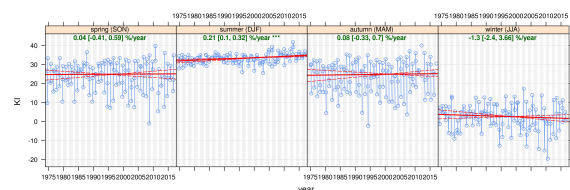


Figure 4: The seasonal distribution of the K-Index

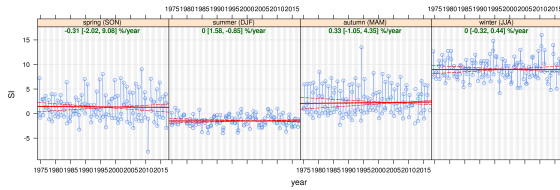


Figure 5: The seasonal distribution of the Showalter index

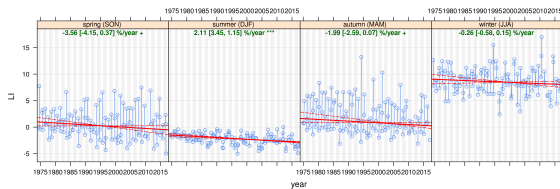


Figure 6: The seasonal distribution of the Lifted index

In Figure 5 the SI shows a well-defined seasonal variation. The summer months have an average of  $-3^{\circ}\text{C}$  indicating an unstable atmosphere favoring convection but this is only observed in the summer months. In autumn, winter and spring all SI values are slightly positive (stable atmosphere). The SI values also show no significant trend towards a convective favoring atmosphere in any of the seasons. The LI, Figure 6, shows a similar seasonal variation to the SI, however there is a significant trend seen in summer, spring and autumn months towards a more unstable atmosphere. Winter LI values show no significant positive trend indicating that the atmosphere remains in a relatively stable state.

The TT values observed at the Irene weather station show a clear seasonal variation, similar to the indicators already discussed. The TT value is useful in that it provides a measure of possible storm intensity as well as instability (Grieser, 2012). In Figure 7 no significant trend is observed in the TT values. The seasonal variation between spring and summer is minimal while the winter conditions are stable as expected. According to Dyson (2013) summer highs are in the order of  $\pm 53^{\circ}\text{C}$ , however Figure 7 indicates marginally lower values compared to work by Dyson (2013).

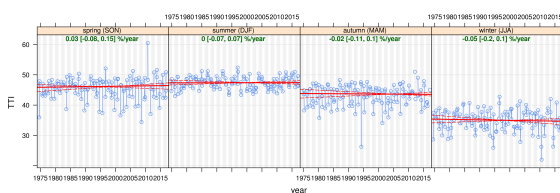
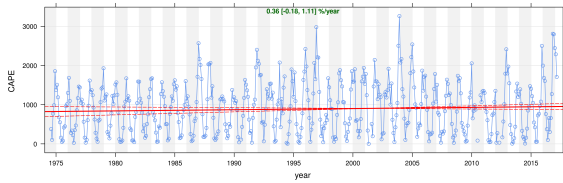


Figure 7: The seasonal distribution of the total totals index trends

In this section the seasonal trends and variations of selected sounding derived variables were evaluated. The Thiel-sen slope analysis was used to evaluate the seasonal trends of the selected indicators from 1975 to 2016. Six thermodynamic variables were analyzed namely CAPE, CIN, KI, SI, LI and TT. Three indicators showed a significant trend towards a convective a favoring atmosphere, this was CAPE, KI and LI. A significant increase in CAPE is observed during spring and summer months while winter and autumn remain stable. The KI only showed a positive trend during summer months for convective favoring atmosphere while LI indicated that spring, summer and autumn had a significant trend towards a more unstable atmosphere. CIN also showed a significant positive trend, however, the indicator is difficult to evaluate as there is a balance between the stable layer represented by CIN and buoyancy represented by CAPE. If CIN values are too low ( $\leq -15$ ) only minor convection will occur and storms could form too early for powerful storms to occur. High CIN,  $\geq -200$  could prevent lifting and convection might not occur either. If CIN is evaluated along with the increasing CAPE observed during spring and summer, it could be that the positive CIN trend observed shows an atmosphere where lifting is increasingly favoured. The SI and TT show no significant trend in the seasonal analysis.

#### 4.2. The long term thermodynamic trends of thermodynamic indicators

Over South-Africa scientists have stated that climate change could result in an increase in extreme events associated with heavy rainfall, flooding and possibly more severe hailstorms. The  $4^{\circ}\text{C}$  increase projected would have a strong effect on convective nature of the atmosphere (Engelbrecht et al., 2013; Piketh et al., 2014). More heat allows the atmosphere to hold more moisture and also increases the amount of convective energy. Figure 8 indicates that CAPE has increased significantly over the last three decades (0.36). The increased CAPE supports the climate change predictions of (Engelbrecht et al., 2013; Piketh et al., 2014) as the variable is a function of the energy in the atmosphere which effects the convection type and intensity. When the seasonal analysis is considered we can observe the increase in CAPE in the spring and summer months while winter and autumn remain stable. This is expected as CAPE is a function of heat and moisture, with a warming atmosphere both these variables can be expected to increase, the freezing levels also play an important



**Figure 8:** The long term trend of CAPE based on the IGRA dataset and a Thiel-Sen slope analysis

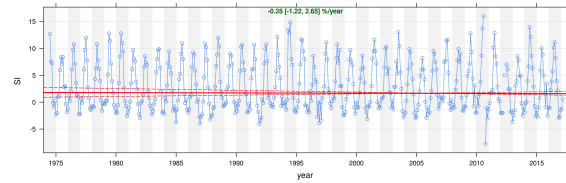


**Figure 10:** The long term trend of SI based on the IGRA dataset and a Thiel-Sen slope analysis

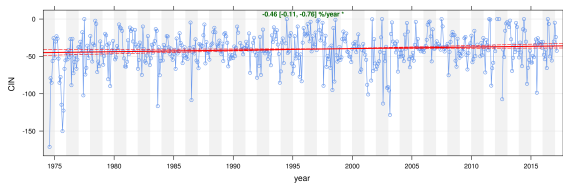


**Figure 9:** The long term trend of CIN based on the IGRA dataset and a Thiel-Sen slope analysis

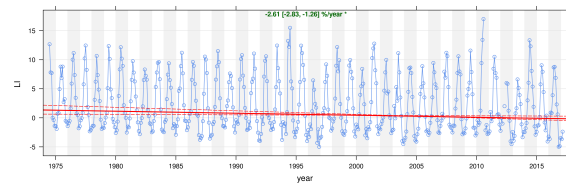


**Figure 11:** The long term trend of LI based on the IGRA dataset and a Thiel-Sen slope analysis

role in ice formation, if more heat and moisture is lifted into the atmosphere and freezing levels allow for ice formation we can expect an increase in hail events. The long term trends from the IGRA dataset indicate that CIN is significantly decreasing (-0.46) (Figure 9). The decreasing CIN value is still within the thunderstorm threshold as described by Grieser (2012). However, the CIN value should be evaluated concurrently to CAPE. The increasing CAPE value along with the observed CIN value could indicate that the conditions for thunderstorm formation is becoming more favorable and the CIN is not increasing to a level where convection is completely halted neither do we observe low CIN where convection is triggered too early.

Figure 10 indicates that the low value of the SI shows a slightly decreasing trend over the last three decades. This decreasing SI supports the CAPE observations that an increasingly unstable atmosphere is ever more present over Gauteng. However, the trend is marginal and by referring back to the seasonal variation of the SI index this can also be seen. The slight decreasing value is however important to observe and when the rare spatio-temporal nature of severe events is taken into account this trend is significant. The LI is similar to the SI but a stronger trend towards convective favoring atmosphere is observed with a Thiel-Sen slope of -2.61 (Figure 11).

The KI (Figure 12) also indicates a marginal increase towards a slightly more convective favoring atmosphere, the Thiel-Sen slope analysis indicates a positive trend over the last three decades. The seasonal analysis of the KI shows that this in-

crease is observed in spring and summer, similar to CAPE, SI and LI variables.

The TT does not show the same significant trend towards a convective favoring atmosphere. The seasonal analysis of the TT shows supports this and although a slight increase in the seasonal analysis is observed, it is insignificant. The long term analysis indicates a 0.01 increase which is also not significant.

The section investigated the long term trends of thermodynamic indicators associated with severe events usually occurring along with convective storms. Each of the selected variables are popular derivatives of sounding data used to evaluate the possibility of severe storm occurrences. Data was gathered from the IGRA database and starting in 1975 until early 2017. The long term trend analysis indicated that the atmosphere is increasingly becoming favorable for convective storms. CAPE shows a significant increase with a Thiel-Sen value of 0.36. The next three variables analyzed all showed the same trend towards a marginally more unstable atmosphere. The SI and LI again indicated a trend towards a convective favoring environment. This increase is mainly

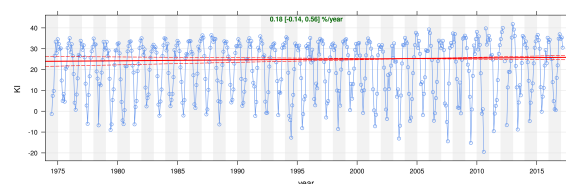


**Figure 12:** The long term trend of KI based on the IGRA dataset and a Thiel-Sen slope analysis

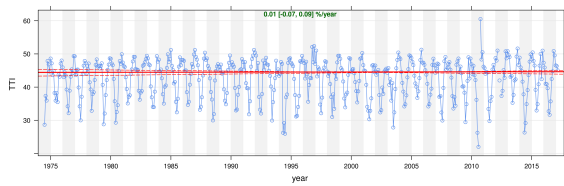


**Figure 13:** The long term trend of TT based on the IGRA dataset and a Thiel-Sen slope analysis

observed in the spring and summer months. The TT did not indicate a significant increase or decrease and this was also observed in the seasonal observations.

## 5. DISCUSSION

The Thiel-sen slope analysis was used to evaluate the seasonal trends of the selected indicators from 1975 to 2016. The Thiel-Sen analysis is robust and depends on the median slope of the data this means that outliers influence the data less. Furthermore, only the 12:00 UTC sounding was extracted from the dataset as convective storms occur within the early to later afternoon. Six thermodynamic variables were analyzed namely CAPE, CIN, KI, SI, LI and TT. Three indicators showed a significant trend towards a convective favoring atmosphere, this was CAPE, KI and LI. CAPE. The seasonal distribution of the total totals index trends significant increase in CAPE is observed during spring and summer months while winter and autumn remain stable. The KI only showed a positive trend during summer months for convective favoring atmosphere while LI indicated that spring, summer and autumn had a significant trend towards a more unstable atmosphere. CIN also showed a significant positive trend, however, the indicator is difficult to evaluate as there is a balance between the stable layer represented by CIN and buoyancy represented by CAPE. If CIN values are too low ( $\leq -15$ ) only minor convection will occur and storms could form too early for powerful storms to occur. High CIN,  $\geq -200$  could prevent lifting and convection might not occur either. If CIN is evaluated along with the increasing CAPE observed during spring and summer, it could be that the positive CIN trend observed shows an atmosphere where lifting is increasingly favored. The SI and TT show no significant trend in the seasonal analysis.

The long term trend analysis indicated that the atmosphere is increasingly becoming favorable for convective storms. CAPE shows a significant increase with a Thiel-Sen value of 0.36. The

next three variables analyzed all showed the same trend towards a marginally more unstable atmosphere. The SI and LI again indicated a trend towards a convective favoring environment. This increase is mainly observed in the spring and summer months. The TT did not indicate a significant increase or decrease and this was also observed in the seasonal observations.

## 6. CONCLUSION

Apart from the TT index, all the sounding derived variables indicated a trend towards conditions favoring an increasingly convective environment. The effects of high impact events will especially be felt by those in impoverished areas where infrastructure and emergency services are least prepared to handle events convective weather.

Although the use of severe weather indicators from radiosondes is valuable, they are prone to errors in instrumentation and/or calibration. According to Doswell and Schultz (2006); Markowski et al. (2003) the combination of various indicators should be used as an assistance to meteorologist and as the sole predictor for storm possibility, as these measurements are limited in space and time. Other tools such as numerical weather prediction, radar and satellite can assist us to better understand the thermodynamic properties of events with less space-time limitations.

## REFERENCES

- Allen, J. T., Tippett, M. K. and Sobel, A. H. (2015), 'An empirical model relating US monthly hail occurrence to large-scale meteorological environment', *Journal of Advances in Modeling Earth Systems* 7(1), 226–243. 1
- Berthet, C., Wesolek, E., Dessens, J. and Sanchez, J. (2013), 'Extreme hail day climatology in Southwestern France', *Atmospheric Research* 123, 139–150. 1
- Blamey, R., Middleton, C., Lennard, C. and Reason, C. (2016), 'A climatology of potential severe convective environments across South Africa', *Climate Dynamics* pp. 1–18. 1, 2
- Collett, K. S., Piketh, S. J. and Ross, K. E. (2010), 'An assessment of the atmospheric nitrogen budget on the South African Highveld', *South African Journal of Science* 106(5-6), 35–43. 2
- Dennison, P. E., Brewer, S. C., Arnold, J. D. and Moritz, M. A. (2014), 'Large wildfire trends in the western United States, 1984–2011', *Geophysical Research Letters* 41(8), 2928–2933. 3
- Doswell, C. A. and Schultz, D. M. (2006), 'On the use of indices and parameters in forecasting

- severe storms', *Electronic J. Severe Storms Meteor* 1(3), 1–22. 1, 6
- Dupilka, M. L. and Reuter, G. W. (2006), 'Forecasting tornadic thunderstorm potential in Alberta using environmental sounding data. Part I: Wind shear and buoyancy', *Weather and forecasting* 21(3), 325–335. 1
- Durre, I., Vose, R. S. and Wuertz, D. B. (2006), 'Overview of the integrated global radiosonde archive', *Journal of Climate* 19(1), 53–68. 2
- Dyson, L. L. (2013), Atmospheric thermodynamics and circulation associated with heavy rainfall over the Gauteng Province, South Africa, PhD thesis, University of Pretoria. 1, 2, 3, 4
- Dyson, L. L., Van Heerden, J. and Sumner, P. D. (2015), 'A baseline climatology of sounding-derived parameters associated with heavy rainfall over Gauteng, South Africa', *International Journal of Climatology* 35(1), 114–127. 1
- Engelbrecht, C., Engelbrecht, F. and Dyson, L. (2013), 'High-resolution model-projected changes in mid-tropospheric closed-lows and extreme rainfall events over southern Africa', *International Journal of Climatology* 33(1), 173–187. 4
- Freiman, M. and Piketh, S. (2003), 'Air transport into and out of the industrial Highveld region of South Africa', *Journal of Applied Meteorology* 42(7), 994–1002. 2
- Grieser, J. (2012), 'Convection Parameters'. 3, 4, 5
- Groenemeijer, P. and Van Delden, A. (2007), 'Sounding-derived parameters associated with large hail and tornadoes in the Netherlands', *Atmospheric research* 83(2), 473–487. 1
- Johns, R. H. and Doswell, C. A. (1992), 'Severe local storms forecasting', *Weather and Forecasting* 7(4), 588–612. 2
- Khan, A., Chatterjee, S. and Bisai, D. (2015), 'On the long-term variability of temperature trends and changes in surface air temperature in Kolkata Weather Observatory, West Bengal, India', *Meteorology Hydrology and Water Management. Research and Operational Applications* 3. 3
- Markowski, P., Hannon, C., Frame, J., Lancaster, E., Pietrycha, A., Edwards, R. and Thompson, R. L. (2003), 'Characteristics of vertical wind profiles near supercells obtained from the Rapid Update Cycle', *Weather and forecasting* 18(6), 1262–1272. 6
- Mohr, S. and Kunz, M. (2013), 'Recent trends and variabilities of convective parameters relevant for hail events in Germany and Europe', *Atmospheric Research* 123, 211–228. 1
- Piketh, S., Vogel, C., Dunsmore, S., Culwick, C., Engelbrecht, F. and Akoon, I. (2014), 'Climate change and urban development in southern Africa: The case of Ekurhuleni Municipality (EMM) in South Africa', *Water SA* 40(4), 749–758. 4
- Rae, K. (2014), A Modified Supercell Composite Parameter for Supercell thunderstorms over the Gauteng Province, South-Africa, PhD thesis, University of Pretoria. 1
- Rasmussen, E. N. and Blanchard, D. O. (1998), 'A baseline climatology of sounding-derived supercell and tornado forecast parameters', *Weather and Forecasting* 13(4), 1148–1164. 1
- Sánchez, J., Fernández, M., Fernández, J., Tuduri, E. and Ramis, C. (2003), 'Analysis of mesoscale convective systems with hail precipitation', *Atmospheric research* 67, 573–588. 1
- Sánchez, J. L., Marcos, J. L., Dessens, J., López, L., Bustos, C. and García-Ortega, E. (2009), 'Assessing sounding-derived parameters as storm predictors in different latitudes', *Atmospheric Research* 93(1), 446–456. 1, 2
- Scheifinger, H. and Held, G. (1997), 'Aerosol behaviour on the South African highveld', *Atmospheric Environment* 31(21), 3497–3509. 2
- Sen, P. K. (1968), 'Estimates of the regression coefficient based on Kendall's tau', *Journal of the American Statistical Association* 63(324), 1379–1389. 3
- Theil, H. (1992), A rank-invariant method of linear and polynomial regression analysis, in 'Henri Theils Contributions to Economics and Econometrics', Springer, pp. 345–381. 3

## 7. ACKNOWLEDGMENTS

A large part of this work was completed as part of my masters degree and has yet to be published. I would like to thank Dr. R.P Burger and Prof. S.J Piketh for their financial support. The IGRA data is freely available on the for anyone to use and download (see <https://www.ncdc.noaa.gov/data-access/weather-balloon/integrated-global-radiosonde-archive>). My greatest gratitude to the scientists around the world that make it possible for access to their data without any restrictions.

## ***The sensitivity of simulated temperatures in climate models to aerosols over southern Africa***

TE Makgoale<sup>1,3</sup>, RM Garland<sup>2,3</sup>, RP Burger<sup>3</sup>, J. Botai<sup>1</sup>, FA Engelbrecht<sup>2,4</sup> and SE Bauer<sup>5,6</sup>

<sup>1</sup>South African Weather Service – Research, Pretoria, South Africa

<sup>2</sup>Climate Studies, Modelling and Environmental Health research Group, CSIR, Pretoria, South Africa

<sup>3</sup>Climatology Research Group, Unit for Environmental Sciences and Management, North West University, Potchefstroom, South Africa

<sup>4</sup>School of Geography, Archaeology and Environmental Studies, University of the Witwatersrand, South Africa

<sup>5</sup>Center for Climate Systems Research, Columbia University, New York, NY, USA

<sup>6</sup>NASA Goddard Institute for Space Studies, New York, NY, USA

### ***Abstract***

The sensitivity of surface air temperature to atmospheric aerosols over southern Africa is being studied using the Conformal Cubic Atmospheric Model (CCAM) that uses the Coupled Model Intercomparison Project Phase 5 (CMIP5) emission inventory. Control simulation of surface air temperature were carried out without the effect of atmosphere aerosols. With regard to standard experiment, simulations of aerosol optical depth (AOD) at 550nm and surface air temperature were carried out with the implementation of aerosol scheme into CCAM. The model results show that there is spatial variability of AOD at 550nm over southern Africa. The variability of AOD in both space and time results in surface air temperature change ( $\Delta T$ ), leading to surface air cooling that ranges between -1.0 to -4.0 °C. The surface air temperature change ( $\Delta T$ ) was quantified using the statistical analysis of symmetric mean absolute percentage error (*SMAPE*), mean absolute error (*MAE*), root-mean-square error (*RMSE*) and mean error (*ME*) between surface air temperature simulated with and without the effect of atmosphere aerosols.

Keywords: Aerosols, Climate Models, Surface Air Temperature

### ***Introduction***

Atmospheric aerosol from human activity can influence climate directly through scattering and absorbing of solar radiation. The scattering and absorbing ability of particles differ with respect to their properties. Aerosol particles such as sulphates and nitrates scatter incoming solar radiation hence causes cooling at surface of the Earth (Hatzianastassiou *et al.*, 2007; Podgorny and Ramanathan, 2001; Rap *et al.*, 2013). In contrast, absorbing aerosol, such as black carbon, absorbs solar radiation which consequently warms the layer of the atmosphere around the particles (Zhang and Wang, 2011; Bond *et al.*, 2013). Aerosol can also impact the climate indirectly through modifying radiative properties of clouds (Lohman and Feichter, 2005; Rap *et al.*, 2013). Due to relatively short atmospheric lifetime and heterogeneous distributions through space and time, the impact of aerosol on radiative balance remains highly uncertain (Myhre *et al.*, 2013). This uncertainty limits our knowledge about climate change. The impact of aerosol on regional climate, particularly temperature, is important for developing regions such as southern Africa because of high vulnerability to climate variability and limited resources for adaption (Solomon *et al.*, 2007). The Southern African region is affected by various kinds of aerosol. Their variability is due to various formation mechanisms and different kinds of emitting sources. Southern Africa's aerosol loading comprises of carbonaceous aerosol (which include organic carbon (OC) and black carbon (BC), marine aerosol and dust.

Dynamic models are important tools for simulating climate variability and change. However, in order to reduce uncertainty, the effect of aerosol must be realistically represented. The aerosol module in climate models should be able to treat all important aerosol processes such as transport, particle formation, emissions, deposition and interactions with clouds and other components. Over Africa, a successful representation of aerosol particles and their transport in climate models (i.e. Conformal Cubic Atmospheric Model –CCAM) has been achieved using the CMIP5 historical emissions inventory (Garland *et al.*, 2016). The model captures monthly trends of aerosol optical depth (AOD) over Africa. This study aims at complementing the study of Garland *et al.* (2016) through investigating the sensitivity of simulated temperature in climate models to aerosol over southern Africa using the CCAM model forced with CMIP5 emissions.

### ***Study Area***

The analysis area considered for this study extents from 10 °N to 50 ° S and 0 °W to 60 °E (Figure 1). The area is comprised of various economic activities such as industries, mines and farm areas that contribute to aerosol loading in the atmosphere. The seasonal biomass burning, and plant microbial materials are the source of carbonaceous aerosol. The surrounding oceans modulate large scale winds that are responsible for the transportation of aerosol particles to

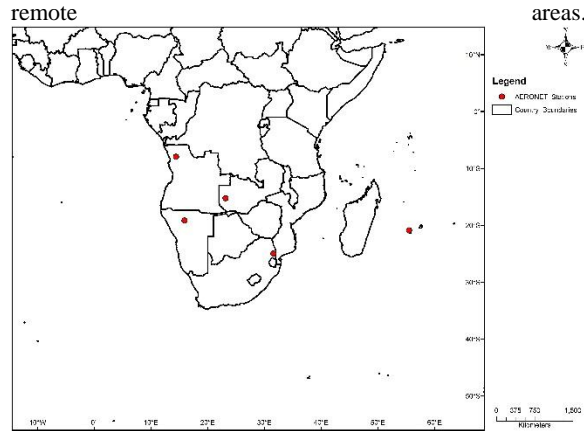


Figure1: The Southern African region with major Aerosol Robotic Network (AERONET) stations.

### Data

#### Model Simulations

Simulations were performed with the CCAM (McGregor, 2005) using the CMIP5 emissions inventory with and without interactive aerosol effect. CCAM has been widely applied in regional studies over Africa (e.g. Engelbrecht *et al.*, 2015; Landman *et al.*; 2012). The model runs in a quasi-uniform grid with resolution of about 210 km and it can alternatively be applied at high resolution (stretched grid mode) over areas of interest using Schmidt transformation (Schmidt, 1977). This avoids lateral boundary conditions and also yields flexibility in dynamical downscaling from Global Climate Models (GCM).

#### Model dynamics

The CCAM model make use of the 2-time level semi-Lagrangian, semi-implicit method to derive the solution of the hydrostatic equations. The horizontal advection is used with total-variation-diminishing (TVD scheme) vertical advection (McGregor, 1996). The semi-Lagrangian horizontal advection together with TVD scheme are able handles tropopause temperature gradient. The model uses a reversibly-staggered grid that pivots between the Arakawa A and C-grids. This results in better dispersive behaviour for both the atmosphere and ocean models. The model incorporates a fairly a wide range of physical parameterizations. The physical parameterization include Geophysical Fluid Dynamics Laboratory (GFDL) long-wave and short-wave radiation parameterisation (Lacis and Hansen, 1974; McGregor and Dix, 2001) and Rotstayn, (1997) liquid and ice water scheme is employed to parameterize micro-physical processes (e.g. precipitation formation in warm, strati-form and mixed phase clouds). The CCAM model uses CSIRO mass-flux cumulus convection scheme that includes down drafts, detrainment and a gravity wave drag scheme. The stability dependent boundary layer scheme used is based on Monin-Obukhov similarity theory (McGregor *et al.*, 1993). The boundary layer scheme together with the non-local vertical mixing enhances the mixing of cloudy boundary layer air. A canopy scheme of

six layers for soil moisture, six layers for soil temperature and three layers for snow is included.

#### Aerosols Scheme

The interactive aerosol treatment is from the CSIRO atmospheric Global Climate Model (Gordon *et al.*, 2002). The aerosol scheme used treats the effect of carbonaceous aerosol, sulphate, sea salt and mineral dust (Rotstayn *et al.*, 2012). The direct effect of aerosol species on shortwave radiation and dust impact on longwave radiation is handled by the radiation scheme (Rotstayn *et al.*, 2007). The transportation of aerosol and other atmospheric spatial variables, such as atmospheric water vapour, occurs by vertical advection within convective clouds, horizontal advection and vertical turbulence mixing (Rotstayn and Lohmann, 2002). The flux-corrected transport scheme is responsible to drive vertical advection (Van Leer, 1977). The semi-lagrangian scheme (McGregor, 1993) is used to handle the horizontal advection, and vertical turbulence mixing treatment is based on stability depended K-theory (Louis, 1979). Convective processes e.g. shallow; mid-level and deep convection are represented by the convective scheme (Gregory and Rowntree, 1990).

The carbonaceous aerosol and the sulphur cycle are handled by the single moment prognostic scheme with prognostic variables being sulphur dioxide (SO<sub>2</sub>), sulphate and dimethyl sulphide (DMS). The sulphur emission, chemistry and, its wet and dry deposition is calculated online with meteorology in the GCM. The sulphate mass distribution, chemistry and radiative forcing treatment are similar to that in the fourth-generation atmospheric general circulation model (ECHAM4) developed at the Max Planck Institute for Meteorology (MPIM) (Feichter *et al.*, 1996). The reaction with hydroxyl (OH) oxidises both DMS and SO<sub>2</sub> during the day while the DMS react with nitrate radical (NO<sub>3</sub>) at night. The oxidation product considered is only SO<sub>2</sub> thus ignoring the other small yield like methane sulfonic acid (MSA) (Rotstayn, 2002). Black carbon (BC) module as in Cooke *et al.* (1996) is used to model carbonaceous aerosol. The module assumes 80% emission of BC and organic matter to be hydrophobic. It took one and half days to convert these to hydrophilic forms (Rotstayn *et al.*, 2007). The carbonaceous aerosol lifetime in the atmosphere is modulated by both dry and wet deposits. The sea-salt aerosol is diagnosed at each time step as a function of wind speed in the marine boundary layer and is assumed to be well mixed in the marine boundary layer (O'Dowd *et al.*, 1997).

The shortwave and longwave effects of different types of aerosol species are treated by the radiation scheme. The aerosol species include BC, tropospheric sulphate, sea salt, stratospheric aerosol, particulate organic matter (POM) and dust particles (Rotstayn *et al.*, 2007). In the radiation scheme, carbonaceous aerosol are assumed to be an internal mixture while other aerosol species are treated as external mixture (Rotstayn *et al.*, 2013). The treatment of aerosol first and second indirect effects on liquid water clouds is also included (Rotstayn *et al.*, 2013). The calculation of the first indirect effect follows Rotstayn and Liu (2009) and the calculation of second indirect effect follows Rotstayn and Liu (2005).

**Methodology**

To investigating the sensitivity of simulated temperatures to aerosol, two set of simulation experiments are needed namely *control* and *standard simulations*:

- I. Control Simulation: 14 - year temperature simulations were carried out without the effect of atmospheric aerosol (i.e. aerosol set to 0). The output from this experiment is compared against observed data to establish how well the model simulate present climate of southern Africa.
- II. Standard Simulation: The standard simulation was carried out with the effect of atmospheric aerosol. In this experiment temperature and AOD at 550nm were simulated with the implementation of prognostic aerosol scheme into CCAM. This implementation provides comprehensive characterisation of aerosol and their interactions with climate. For the purpose of sensitivity analysis, seasonal spatial anomalies between temperature simulated with implementation of prognostic aerosol scheme and temperature simulated without aerosol effect, were investigated. To quantify any underlying pattern or anomalies statistical calculations were carried out, these include *SMAPE*, *MAE*, *RMSE* and *ME*.

effect of atmospheric aerosol particles. The ME ranges between -0.5 and -1 °C over western part and -1.5 and -2.0 °C over the eastern part of southern Africa. The mean MAE ranges between 1.5 to 3.0 °C. The significance difference found in RMSE, ME and MAE confirms the difference in surface air temperature simulated without and with aerosol effect (Fig. 4).

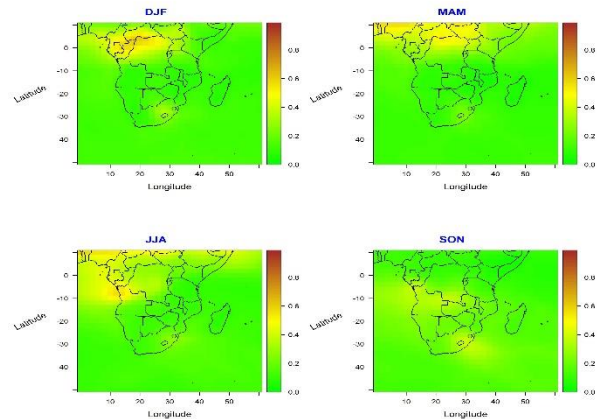


Figure2: The distribution of seasonal AOD at 550nm according to CCAM, which has been averaged over a period (2000 to 2014).

**Results and Discussion**

**Simulated Aerosols Optical Depth (AOD)**

Figure 2 shows the spatial variability of AOD at 550nm, which has been averaged over year 2000 – 2014. According to CCAM, spatial variability and peak of AOD at 550nm varies from one season to another. On average the magnitude of simulated AOD at 550nm ranges between 0.2 to 0.7. Maximum AOD was simulated for DJF, MAM and JJA season over the region of central and West Africa situated approximately 5 – 10 °N. There is a peak in AOD at 550nm of magnitude 0.4 over eastern South Africa and western Angola during SON season. This corresponds to biomass burning period over southern Africa.

**Simulated Aerosol Induced Surface Air Temperature**

Figure 3 display seasonal simulated surface air temperature (°C) changes ( $\Delta T$ ) induced by aerosol. The CCAM simulate cooling over southern Africa especially during DJF, MAM and SON season. Aerosol induced seasonal surface cooling ranges between -4 to -1°C over southern Africa from 2000 to 2014. The exception is JJA season where there is a slight warming which ranges between 0.5 to 1.1°C. This warming is pronounced over region of Botswana, Zimbabwe and Madagascar.

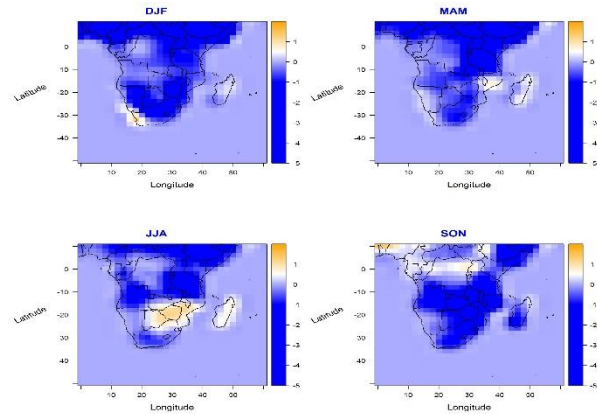


Figure 3: Simulated seasonal mean aerosol –induced changes in surface air temperature (°C) according to the CCAM, which has been averaged over a period (2000 to 2014).

Figure 4 displays a spatial map of statistical analysis between surface air temperatures simulated with and without the/a prognostic aerosol scheme. The RMSE between surface air temperature simulated with and without aerosol is mostly above 1 over southern Africa. High value (greater than 1) of RMSE indicate that there is difference in surface temperature simulated with the effect of atmospheric aerosol particles and surface temperature simulated without the

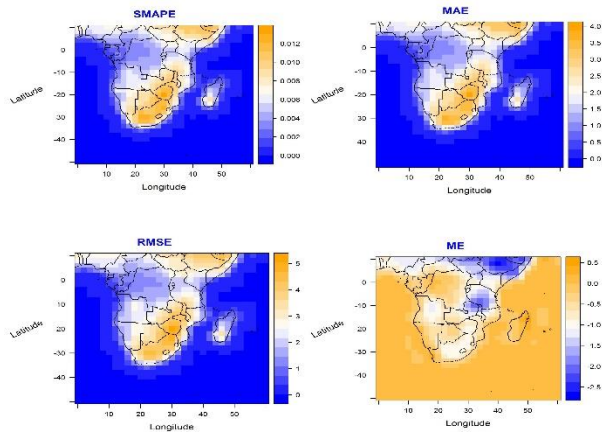


Figure 3: Statistical analysis of simulated mean aerosol induced changes in surface air temperature according to CCAM, the statistic include symmetric mean absolute percentage error (*SMAPE*), mean absolute error (*MAE*), root-mean-square error (*RMSE*) and mean error (*ME*).

### Conclusion

In this study the CCAM was used to investigate seasonal spatial distribution and magnitude of AOD at 550nm as well as the associate surface air temperature response over southern Africa averaged over period (2000 to 2014). The results show that CCAM is able to simulate seasonal spatial variability of AOD at 550nm over southern Africa. In general, atmospheric aerosol induce surface air temperature change in southern Africa. Strong seasonal cooling is simulated when the effect of atmospheric aerosol particles is included in climate models, however there is slight warming pronounced over regions of Botswana and Zimbabwe during winter season. Realistic representation of aerosol effects in climate models is an important step towards reducing the uncertainties in model predictions of climate.

### Acknowledgements

This research would never been possible without the financial support from National Research Foundation (NRF) and the South African Weather Service (SAWS) facilities.

### References

Bond, T. C., Doherty, S. J., Fahey, D. W., Forster, P. M., Berntsen, T., DeAngelo, B. J., Flanner, M. G., Ghan, S., Karcher, B., Koch, D., Kinne, S., Kondo, Y., Quinn, P. K., Sarofim, M. C., Schultz, M. G., Schulz, M., Venkataraman, C., Zhang, H., Zhang, S., Bellouin, N., Guttikunda, S. K., Hopke, P. K., Jacobson, M. Z., Kaiser, J. W., Klimont, U., Lohman, U., Schwarz, J. P., Shindell, D., Storelvmo, T., Warren, S. G. and Zender, C. S., 2013: Bounding the role of black carbon in the climate system: A scientific assessment. *Journal of Geophysical Research*. 118, 5380-5552.

Cooke, W. F., Wilson, J. J. N., A global black carbon aerosol model. *J. Geophys. Res.*, 101, 19395-19409.

Feichter, J., Kjellstrom, E., Rodhe, H., Dentener, F., Lelieveld, J. and Roelofs, G. J., 1996: Simulation of the tropospheric sulphur cycle in a global climate model, *Atmos. Environ.*, 30, 1693-1707.

Garland, R.M., Horowitz, H.M, Engelbrecht, C.J, Dedkind, Z, Bopape, M.M, Piketh, S.J and Engelbrecht, F.A., 2016: Representation of aerosol particles and associated transport pathways in regional climate modelling in Africa.

Gordon, H. B., Rotstayn, L. D., McGregor, J. L., Dix, M. R., Kowalczyk, E. A., O'Farrel, S. P., Waterman, L. J., Hirst, A. C., Wilson, S. G., Collier, M. A., Watterson, I. G. and Elliott, T. I., 2002: The CSIRO MK3 Climate System Model. CSIRO Atmospheric Research Technical Paper No. 60.

Gregory, D. and Rowntree, P. R., 1990: A mass flux convection scheme with representation of cloud ensemble characteristics and stability dependent closure. *Monthly Weather Review*, 118, 1483- 1506.

Hatzianastassiou, N., Matsoukas, C., Drakakis, E., Stackhouse Jr, P. W., Koepke, P., Fotiadi, A., Pavlakis, K. G. and Vardavas, I. 2007: The direct effect of aerosols on solar radiation based on satellite observations, reanalysis datasets, and spectral aerosol optical properties from Global Aerosol Data Set (GADS). *Atmos. Chem. Phys.*, 7, 2585-2599.

IPCC, 2007: *Climate Change 2007: The Physical Science Basis. Contribution of Working Group I to the Fourth Assessment*

Lacis, A. A. and Hansen, J. E., 1974: A parameterization for the absorption of solar radiation in the Earth's atmosphere. *Journal of the Atmospheric Sciences*, 31, 118-133.

Landman, S., Engelbrecht, F. A., Engelbrecht, C. J., Dyson, L. L. and Landman, W. A., 2012: A short-range weather prediction system for South Africa based on a multi-model approach, 38, ISSN 1816-7950.

Lohmann, U., Feichter, J., 2005: Global indirect aerosol effects: a review. *Atmos. Chem. Phys.*, 5, 715-737.

Louis, J. F., 1979: A parametric model of vertical eddy fluxes in the atmosphere. *Boundary Layer Meteorology*, 17, 187-202.

McGregor, J. L., Gordon, H. B., Watterson, I. G., Dix, M. R. and Rotstayn, L. D., 1993: The CSIRO 9-level atmospheric general circulation model. CSIRO Aust. Div. Atmos. Res. Technical Paper, 26, 1-89.

McGregor, J. L., 1996: Semi-Lagrangian advection on conformal-cubic grids. *Mon. Wea. Rev.*, 124, 1311-1322.

McGregor, J. L. and M. R. Dix, 2001: The CSIRO conformal-cubic atmospheric GCM. IUTAM Symposium on Advances in Mathematical Modelling of Atmosphere and Ocean Dynamics, P. F. Hodnett, Ed., Kluwer, 197-202.

McGregor, J. L., 2005: C-CAM: Geometric aspects and dynamical formulation [electronic publication]. Technical Report 70, CSIRO Atmospheric Research, 43 pp.

Myhre, G., Shindell, D., Breon, F. M., Collins, W., Fuglestedt, J., Haug, J., Koch, D., Lamarque, J. F., Lee, D., Mendoza, B., Nakajima, T., Robock, A.,

- Stephens, G., Takemura, T. and Zhang, H., 2013: Anthropogenic and Natural Radiative forcing. In: Climate Change 2013: The Physical Science basis. Contributing of working Group I to the Fifth Assessment Report of the Intergovernmental Panel on Climate Change [Stocker, T. F., D. Qin, G. K. Plattner, M. Tignor, S. K. Allen, J. Boschung, A. Nauels, Y. Xia, V. Bex and P. M. Midgley (eds.)]. Cambridge University Press, Cambridge, United Kingdom and New York, NY, USA, pp. 741-866, doi:
- O'Dowd, C. D., Smith, M. H., Consterdine, I. E. and Lowe, J. A., 1997: Marine aerosol, sea-salt, and the marine sulphur cycle: A short review. *Atmospheric Environment*, 31, 73-80.
- Podgorny, I. A. and Ramanathan, V. 2001: A modelling study of the direct effect of aerosols over the tropical Indian Ocean. *Journal of Geophysical Research*, 106, 24097-24105
- Rap, A., Scott, C. E., Spracklen, D. V., Bellouin, N., Forster, P. M., Carslaw, K. S., Schmidt, A. and Mann, G., 2013: Natural aerosol direct and indirect radiative effects. *Geophysical Research Letters*, 40, 3297-3301.
- Report of the Intergovernmental Panel on Climate Change* [Solomon, S., D. Qin, M. Manning, Z. Chen, M. Marquis, K.B. Averyt,
- Rotstayn, L. D., 1997: A physical based scheme for the treatment of stratiform clouds and precipitation in large-scale models. I: Description and evaluation of the microphysical processes. *Quart. J. Roy. Meteor. Soc.*, 123, 1227-1282.
- Rotstayn, L. D. and Lohmann, U., 2002: Simulation of the tropospheric sulphur cycle in a global model with a physically based cloud scheme. *Journal of Geophysical Research*, 107, D21.
- Rotstayn, L. D. and Liu, Y., 2005: A smaller global estimate of the second indirect aerosol effect. *Geophysical Research Letters*, 32, L10801. doi:10.1029/2005GL020001
- Rotstayn, L. D. and Liu, Y., 2009: Cloud droplet spectral dispersion and the indirect aerosol effect: Comparison of two treatments in a GCM. *Geophysical Research Letters*, 36, L10801. doi:10.1029/2009GL012001
- Rotstayn, L. D., Chai, W., Dix, M. R., Farquhar, G. D., Feng, Y., Ginoux, P., Herzog, M., Ito, A., Penner, J. E., Roderick, M. L. and Wang, M., 2007: Have Australian rainfall and cloudiness increased to the remote effects of Asian anthropogenic aerosols? *Journal of Geophysical Research*, 112, D09202.
- Rotstayn, L. D. and Liu, Y., 2009: Cloud droplet spectral dispersion and the indirect aerosol effect: Comparison of two treatments in a GCM. *Geophysical Research Letters*, 36, L10801.
- Rotstayn, L. D., Jeffrey, S. J., Collier, M. A., Dravitzki, S. M., Hirst, A. C., Syktus, J. I. and Wong, K. K., 2012: Aerosol- and greenhouse gas-induced changes in summer rainfall and circulation in the Australasian region: a study using single-forcing climate simulations. *Atmos. Chem. Phys.*, 12, 6377-6404.
- Rotstayn, L. D., Collier, M. A., Chrastansky, A., Jeffrey, S. J. and Luo, J. J., 2013: Projected effects of declining aerosols in RCP4.5: unmasking global warming? *Atmos. Chem. Phys.*, 13, 10883-10905.
- Schmidt, F., 1977: Variable fine mesh in spectral global model. *Beitr. Atmos.*, 50, 211-217.
- Van Leer, B., 1977: Towards the ultimate conservation difference scheme. V. A new approach to numerical convection. *J. Comp. Phys.*, 23, 276-299.
- Zhang, H. and Wang, Z. 2011: Advances in the study of black carbon effects on climate. *Advances in Climate Change Research*, 2, 23-30.

## Analysis of the atmospheric conditions during 2014 – 2017 for the winter rainfall season of South Africa

Stephanie Landman<sup>1</sup>, Cobus Olivier<sup>1</sup>, Christien Engelbrecht<sup>2</sup>

<sup>1</sup>South African Weather Service, Pretoria, South Africa

<sup>2</sup>Agricultural Research Council, Pretoria, South Africa

### Abstract

The south western parts of South Africa experienced its worst drought in a century during 2014 to 2017, with water resources reaching critically low levels. This was mainly due to a lack of sufficient rainfall during multiple back-to-back winter seasons. This study illustrates the important rainfall bearing and blocking systems for the south western parts of the country by way of Self-Organising Maps. It is found that during the drought period there was both an increase in frontal blocking systems and a decrease in frontal activity reaching South Africa. Also shown here is the relationship between these important circulation patterns and the Antarctic Oscillation, which influence the frequency of these systems depending on its phase.

Keywords: Western Cape, Synoptic patterns, Drought,

### Introduction

All observation data point towards a drought over South Africa's winter rainfall region during 2014 to 2017. The Western Cape dam levels reached levels as low as ~16% by the end of April 2018 (ENCA 2018). This sparked intense water restrictions for both the city of Cape Town as well as the surrounding agricultural sector.

This region, the south-western parts of South Africa and the southern coastal areas westwards of the all-year rainfall region receives its rainfall primarily during May to August (Schulze et al, 2007). The rainfall distribution over these regions are predominantly due to the westerly flows associated with mid-latitude low pressure systems situated to the south of the continent during this period (van Heerden and Hurry, 1987).

Based on three rainfall stations surrounding the Cape Town region and its major catchment area (Western Cape Water Supply System), there was a decrease in average annual rainfall since 2014 (Wolski, 2018). The question to be addressed in this preliminary study, which forms part of a greater analysis, is not how severe the drought was but rather examining the possible changes in the driving dynamical and synoptic atmospheric processes contributing to this decrease in rainfall.

### Data and Methodology

In order to establish the past synoptic patterns with its associated rainfall, Self-Organising Maps (SOM; Kohonen, 2001) was used to do a synoptic classification for the period 1 January 1983 to 31 October 2017. ERA-Interim data (ERA-Int; Dee et al, 2011) were used to determine the daily 12 UTC circulation patterns at the 850 hPa pressure level together with the accompanying African Rainfall Climatology (ARC2) data set which is based on satellite estimated and rainfall observed data (Novella and Thiaw, 2013). The SOM was able to determine the 850 hPa circulation patterns with associated daily rainfall totals. From the resulting 35 nodes, six nodes were classified as being synoptic conditions largely associated with South Africa's winter rainfall seasons.

A first attempt to attribute the rainfall variability to seasonal fluctuations, is to consider the Antarctic Oscillation (AAO) (Mo, 2000) also known as the Southern Annular Mode (SAM). This climate driver focuses on the strength of the polar vortex

and is thought to affect the mid-latitude system activity over the Southern Ocean.

The daily AAO Index was used to determine whether there is any change in the occurrence of specific winter nodes during a particular phase (positive or negative) of the AAO. The daily AAO index was obtained through the Climate Prediction Centre (CPC) at the National Centre for Environmental Protection (NCEP) (CPC Internet Team 2018). Both the AAO index and the Node occurrence data was converted to monthly averages (AAO) and totals (nodes) before analysis. A baseline monthly occurrence frequency of all the nodes (1-35) was first established for the period May-September for all years. This was then compared with occurrence frequencies during only positive AAO phases, and similarly during only negative AAO phases.

### Results

The circulation patterns of the six "winter" nodes (Figs. 1a and b) are, as expected, mostly associated with the west to east passing of mid-latitude systems to the south, as well as cold air onshore flow from the south (e.g. Node 14). From Fig. 1b, the months of May to September are further analysed. The average monthly occurrence of each node for the period 1983 to 2010 was calculated (LTA) and then the following seven year's monthly occurrence were compared to the LTA values (Fig. 2). Together with the node distributions in Fig. 1b for Nodes 14, 21, 28 and the accompanying panels in Fig. 2 it is noted that these three nodes occurred less often and have a weaker winter distribution than Nodes 33 to 35. Focussing on the month of June from 2014 to 2017, the synoptic conditions occurred less than the LTA since 2014 (except Nodes 14 and 33 for 2017). However, for Node 28 the conditions occurred more frequently during June. On the contrary for July from 2014 to 2017, most of the nodes occurred more often, except for Nodes 33 and 34. By just concentrating on the last three years corresponding with the drought, there seems to be almost an exchange in the synoptic patterns between June and July. Overall what is concerning, is that during some years there were no occurrences of some nodes during June and July, e.g. June 2017 in Node 35 and June 2015 for Node 34. The non-occurrence for some of these nodes during the drought period is considered to have had a big impact on an area which typically rely on a relatively low frequency of these system occurring, but by a large extend contribute to the total winter rainfall.

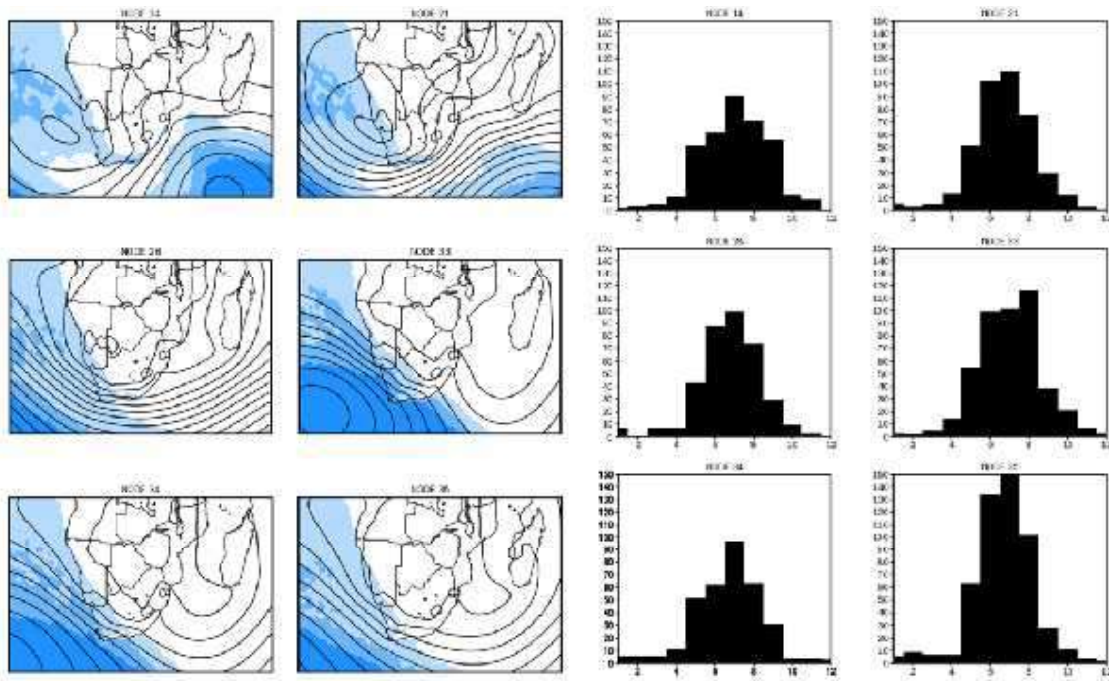


Figure 1: a) The six nodes indicating the 850 hPa circulation (contours) associated with the surface rainfall (shaded) pattern and b) the corresponding nodes indicating the annual distribution of the frequency of occurrence of the six patterns (months are on the x-axis).

In Fig. 3, which indicates the overall deviation of node events from their respective LTA, it is evident that Node 28 occurred more frequently during 2010-2017. This might be an indication of the change in the transition between more or less than average seasonal rainfall. Node 35, on the other hand which has the highest frequency during the winter months (Fig. 1b), had an overall decrease in occurrences from 2014 to 2017 apart from 2016 where each month exceeded the average number of events.

The increase in the number of events for Node 14 (Fig. 3) which is associated with cold air onshore flow following relatively strong cold fronts, may perhaps indicate a reason for lower rainfall totals. The decrease in Node 35 events can in turn be attributed to the increase in Node 28 events, which blocks the frontal systems and preventing northwards advection of the systems and hence prevent any associated frontal rain.

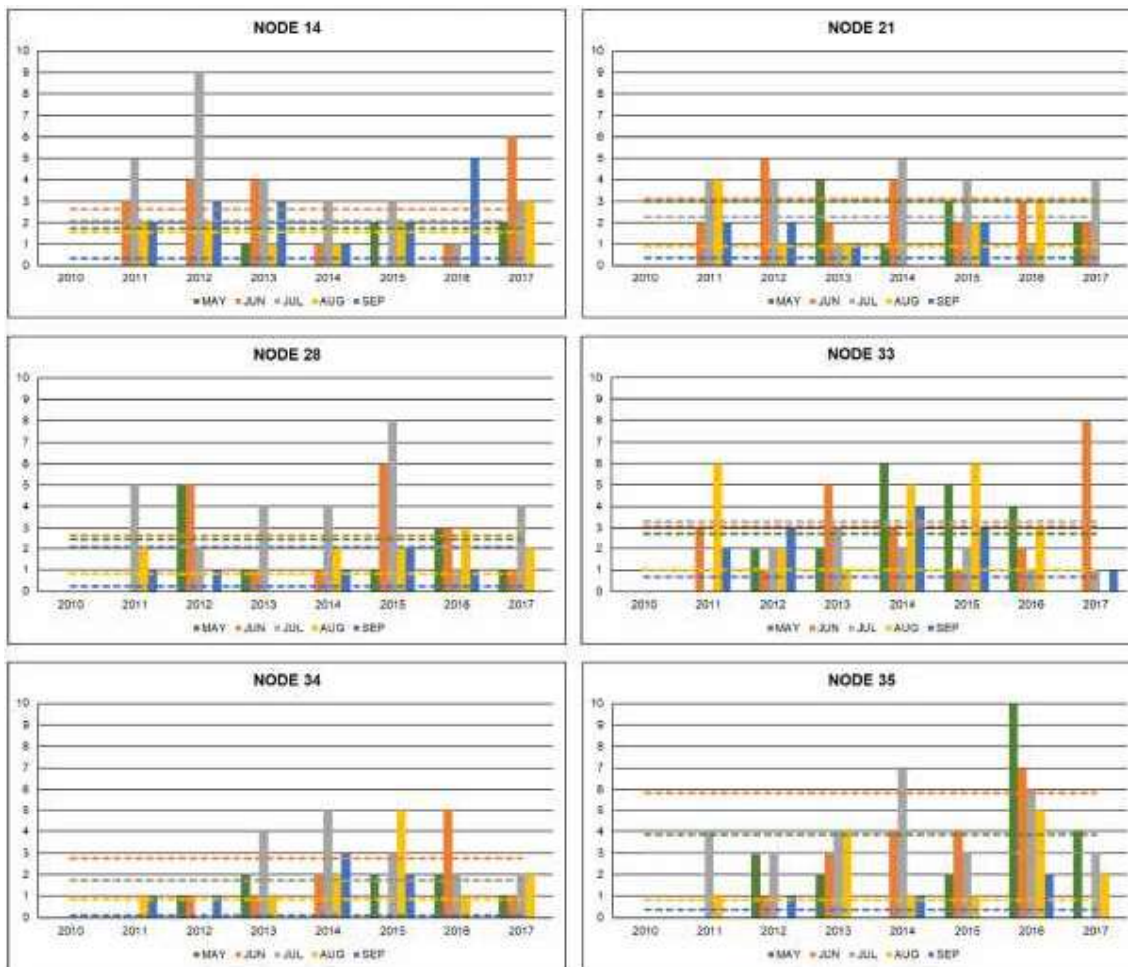


Figure 2: Monthly frequency and long term mean of occurrence for the five months associated with winter rainfall

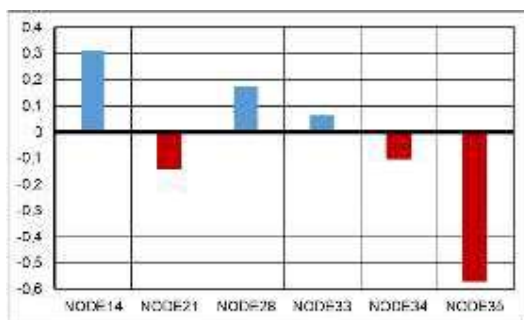


Figure 3: Changes in the occurrence of each Node for the past 7 years based on long term averages.

In Fig. 4 it is seen that during the period under investigation, the AAO was mostly positive, which is believed to have a negative impact on these important rainfall bearing systems to reach South Africa. Figure 5 shows that during a positive phase of the AAO (stronger polar vortex), nodes 28, 34, and 35 tend to be more frequent while the rest of the nodes tend to occur less. These nodes (28, 34 and 35) are indicative of the mid-latitude cyclones either being blocked by the sub-tropical ridge or the development of the mid-latitude cyclones further south than normal. The reverse is seen during a negative phase of the AAO (weaker polar vortex). Nodes 29-33 occur more frequently during negative AAO phases, and seem to be associated with either equatorward development of the mid-latitude cyclones or a lack of blocking systems in the sub-tropics.

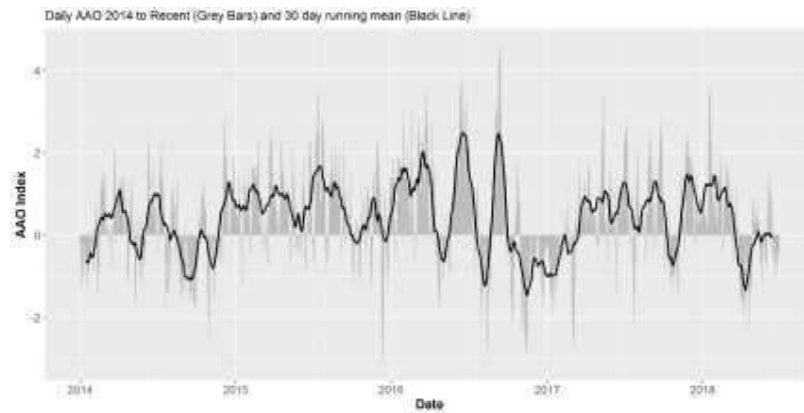


Figure 4: Daily AAO Index with a 30 day running mean.

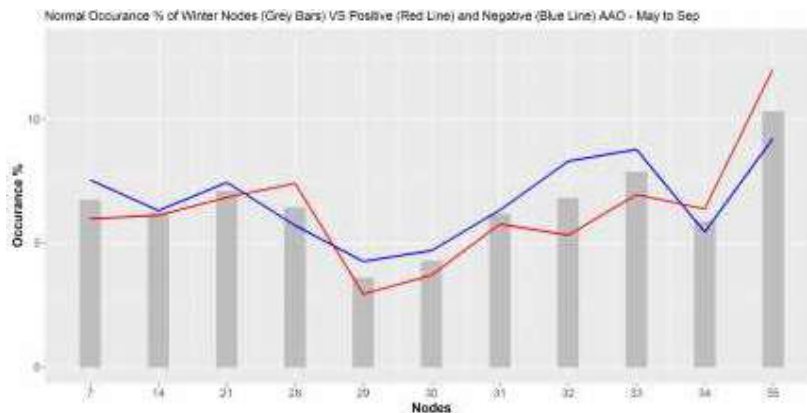


Figure 5: The most frequent occurring nodes during May to Sep. Grey bars indicate the normal percentage (relative to all 35 nodes) of occurrence since 1983-2016. Red and blue lines indicate the change in overall occurrence during a positive and negative AAO index

### Conclusion

With the initial results, there are signs on the weather timescale of variability in the daily circulation patterns associated with the winter rainfall season. Adding to this, the positive AAO during the drought period (2015-2017) suggests a possible relationship between the synoptic (weather) and planetary (seasonal) scale processes. To establish the possible cause of the daily deviations from the long term means, further studies and greater scrutiny into the seasonal and climate drivers will be investigated. The study will also be extended to include the dry conditions currently being experienced over the Eastern Cape region.

### References

Climate Prediction Center Internet Team. 2018. *Antarctic Oscillation (AAO)*. [ONLINE] Available at: [http://www.cpc.ncep.noaa.gov/products/precip/CWlink/daily\\_ao\\_index/ao/ao.shtml](http://www.cpc.ncep.noaa.gov/products/precip/CWlink/daily_ao_index/ao/ao.shtml). [Accessed 20 July 2018].

Dee D.P. and Co-authors, 2011: The ERA-Interim reanalysis: configuration and performance of the data assimilation system. *Q. J. R. Meteorol. Soc.* **137**: 553–597

ENCA. 2018. *Relief as dam levels in Cape Town rise above 50%*. [ONLINE] Available at: <https://www.enca.com/south-africa/relief-as-dam-levels-in-cape-town-go-above-50>. [Accessed 23 July 2018].

Kohonen T. 2001, 'Self-organizing maps'. 3rd ed. Springer

Mo, K. C., 2000: Relationships between Low-Frequency Variability in the Southern Hemisphere and Sea Surface Temperature Anomalies. *J. Climate*, **13**, 3599-3610.

Novella N.S. and W.M. Thiaw, 2013: African Rainfall Climatology Version 2 for Famine Early Warning Systems. *J. App. Met. Clim.*, **52**: 588-606

Schulze, R.E, Maharaj, M., Warburton, M.L., Gers, C.J., Horan, M.J.C., Kunz, R.P. and Clark, D.J., 2008: South African Atlas of Climatology and Agrohydrology

Van Heerden J. and L. Hurry, 1987: Southern Africa's Weather Patterns: an Introductory Guide. 2<sup>nd</sup> Edition. Acacia

## ***Five Minute to Yearly Record Highest Rainfalls for South Africa (excluding Lesotho) from 1860 to 2017***

Jan H. Vermeulen, Disaster Risk Reduction, SA Weather Service, Tshwane

### ***Abstract***

South African (SA) and world rainfall records are compared and the new 5-minute, 10-minute, 15-minute and yearly records for SA is reported. 42.4 mm, 70.8 and 76.0 mm were recorded by an Automatic Weather Station (AWS) at Levubu in Limpopo province for 5, 10 and 15 minutes respectively from a thunderstorm 26 February 2016. A rainfall of 4359 mm was recorded for the year 2000 at Woodbush in Greater Tzaneen district of Limpopo from Tropical Cyclone Eline and other systems that affected the area for the whole year. Swartkoppies 22 km to south of Johannesburg recorded 218 mm in 40 minutes ending 18:30 from a severe thunderstorms 13 January 1951. Swartkoppies is the SA record rainfall intensity for one hour. The clock hourly rainfall record according to the Climate database is 125 mm at 19:00 5 March 1997 at Bisho in Eastern Cape. Adcockvale in Port Elizabeth recorded 470 mm in 4 hours ending 12:00 from a cut-off low system 1 September 1968. Adcockvale is the SA 4-hour rainfall record. A cloudburst occurs if rainfall intensity is equal to or greater than 100 mm per hour. The above record events of less than 6 hours are all cloudbursts with Levubu's 504 mm/h a record highest rainfall intensity.

Key words: Cloudburst, Rainfall Intensity, Autographic Charts, Automatic Weather Stations.

### ***Introduction***

Highest rainfall records from 5-minutes to one year are reported for South Africa from 1860 until 30 June 2017. June is the end of rainfall year for the summer rainfall areas that covers most of the country. Comparing South African records with world records available online from National Oceanic and Atmospheric Administration (NOAA) of the United States of America (USA), it is seen that none are world records.

Instrumentation used for record measurements are discussed. Archiving of rainfall observations and its effect

on records are also investigated. Weather systems causing the records are also indicated.

### ***Results***

A comparison of SA and world records is shown in Figure 1 that also indicates the exponential functions fitted to the World and SA record rainfall series. Table 1 summarises the comparisons giving places and dates that records occurred with notes indicating disparities in record time periods.

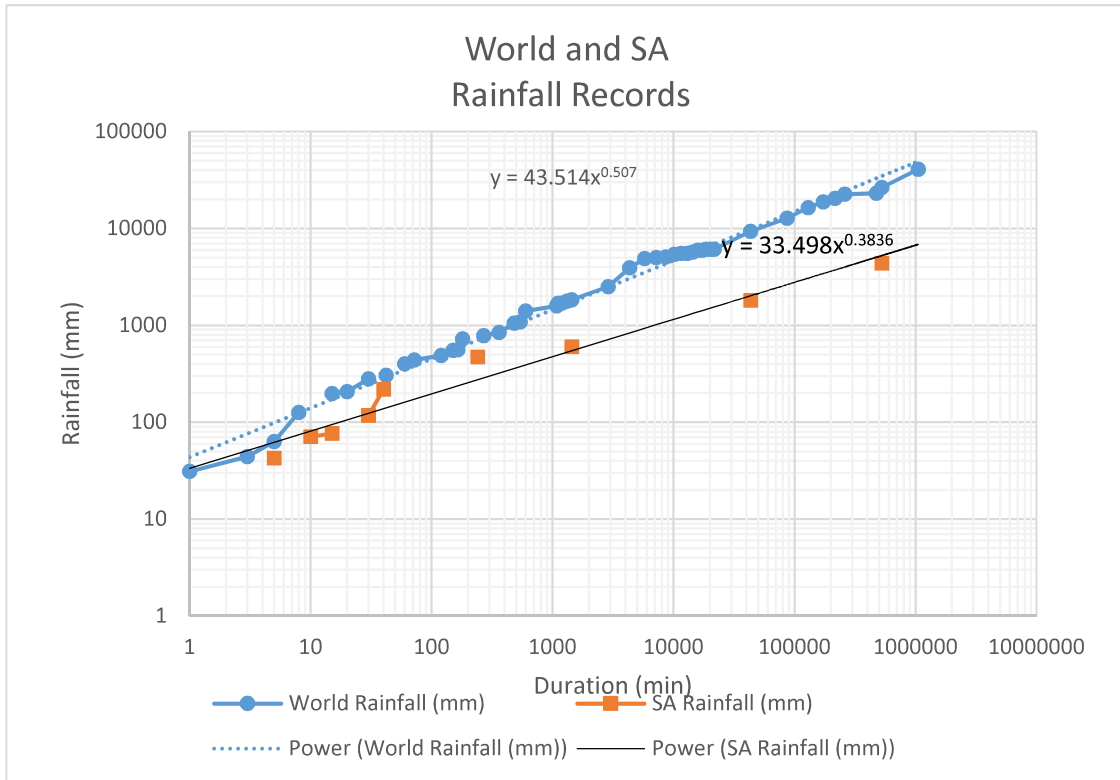


Figure 1. World versus South African record rainfall comparison.

Table 1: Comparison of South African and World rainfall records for 5-minute to one year periods.

Period		South Africa			World		
Minutes	Day	Rainfall	Place	Date	Rainfall	Place	Date
5		42	Levubu, Limpopo	26/2/2016	63	Porto Bello, Panama	11/29/1911
10		71	Levubu, Limpopo	26/2/2016	126	Fussen, Germany*	11/6/1972
15		76	Levubu, Limpopo	26/2/2016	198	Plumb Point, Jamaica	12/5/1916
30		116	Bisho, Eastern Cape	5/3/1997	280	Sikeshugou, China	3/7/1974
60		218	Johannesburg, Gauteng**	13/1/1951	401	Shangdi, China	3/7/1975
240		470	Port Elizabeth, Eastern Cape	1/9/1968	724	Smethport, USA***	18/7/1942
1440	1	597	St Lucia, KwaZulu-Natal	31/1/1984	1825	Foc-Foc, Reunion	7/1/1966
	30	1803	Matiwa, Limpopo	February 2000	9300	Cherrapunji, India	July 1861
	365	4359	Woodbush, Limpopo	2000	26461	Cherrapunji, India	1860

Notes:

- \* Rain over 8 minutes at Fussen, Bavaria
- \*\* Rain over 40 minutes at Swartkoppies, Johannesburg
- \*\*\* Rain over 180 minutes at Smethport, Pennsylvania

No South African records are World records, but the closest graphically is the 218 mm in 40 minutes at Johannesburg (see Figure 1).

Discussion

1) Johannesburg – Swartkoppies record:

218 mm Measured over 40 minutes ending at 18:30 from a thunderstorm at Swartkoppies a farm 22 km to south of Johannesburg on 13 January 1951 is the oldest SA record. This event is documented in the Weather Bureau Newsletter (1951). Sikesugou in China's 280 mm in 30 minute's world record (Burt C, 2007) is higher than Swartkoppies' 218 mm in 40 minutes.

The Swartkoppies rainfall was measured by two standard 8-inch rain gauges at a third order climate station. The WB36 (1974) climate publication of South African Weather Service

(SAWS) reports that Port Elizabeth Regional Office's 112.4 mm on 1 September 1968 is the highest hourly rainfall for the period that it covers (1938 to 1972). Last mentioned used autographic rain gauge charts to compile the statistics. 218 mm at Johannesburg - Swartkoppies 31 January 2017 is the SA record highest rainfall for one hour.

The clock hourly rainfall record according to the database of the Climate Service of SAWS is 125 mm 19:00 at Bisho on 5 March 1997. This event also gave the 30-minute rainfall record of 116 mm for SA and was measured with an automatic weather station (AWS). An AWS has a tipping bucket digital rain gauge with a resolution of 0.2 mm that reports 5-minute rainfalls. The AWS technology was experimented with in the 80's and officially introduced in the 90's making it feasible to have 5-minute and 10-minute rainfall records for a nearly 30-year climate period. As an example of this technology the Levubu 5-, 10- and 15-minutes rainfall record is shown in Figure 2 below.

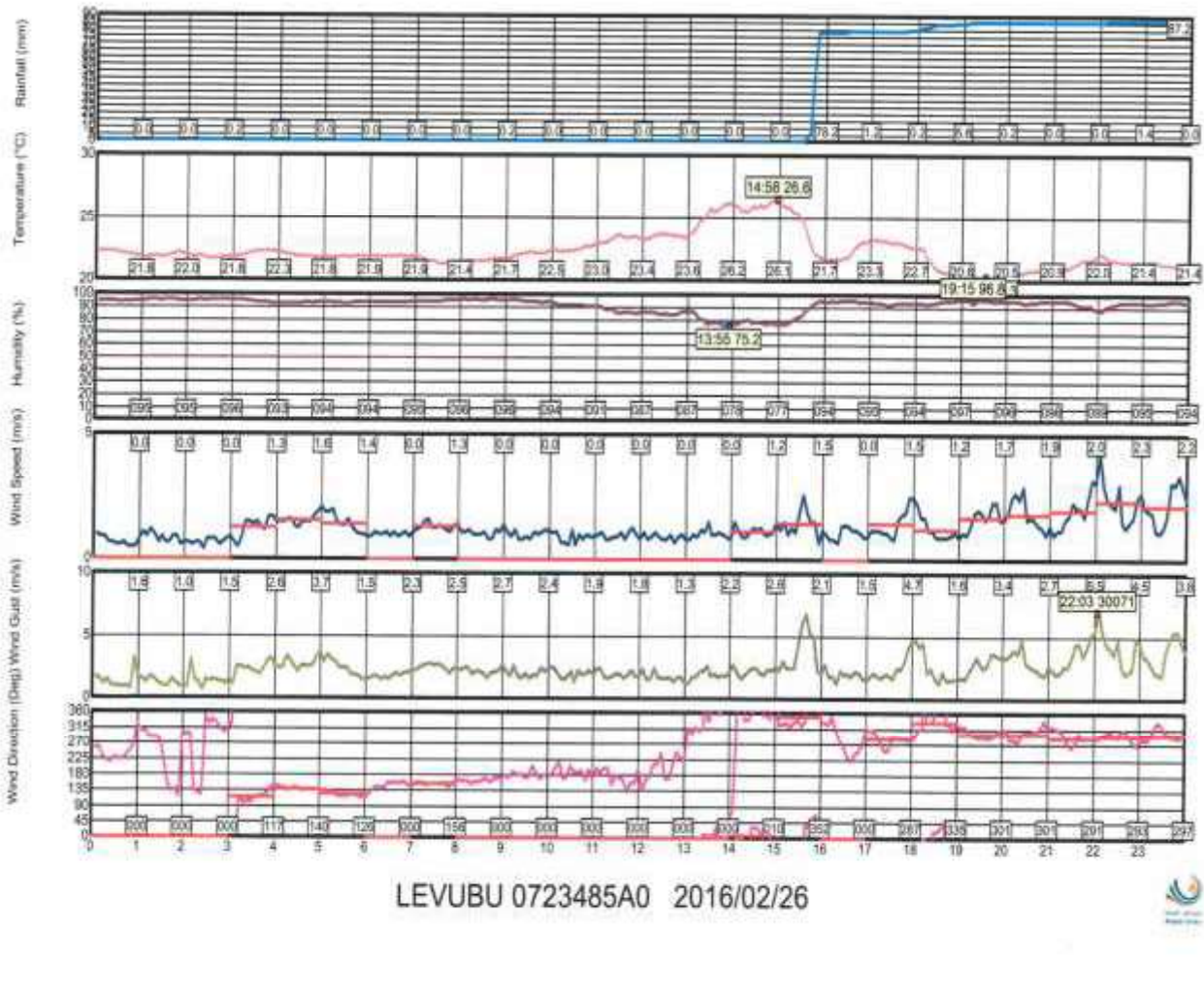


Figure 2: 5-Minute weather graph of Levubu for 26 February 2016 with the rainfall graph on top.

2) Port Elizabeth – Adcockvale record:

Hayward and Van den Berg (1968) reports that the Cut-off low of 1 September 1968 at Port Elizabeth (PE) gave 552 mm at Adcockvale of which 470 mm of the rain fell between 8:00 and 12:00 the Sunday morning. The 470 mm was measured by an autographic rain gauge of the municipality. Rainfall intensities at the Airport exceeded 30 mm per 15 minutes during this storm. World record for 3

hours is 724 mm at Smethport, USA 18 July 1942 (Burt, 2007). The event at Smethport gave 782 mm over 4.5 hours. The PE event is a once in a century event according to Hayward and Van den Berg (1968).

According to the exponential function for SA rainfall records (see Fig. 1) an estimate for four hour's rainfall record is 274.2 mm. Thus the 4 hours' rain 1st September 1968 at PE is a SA record. Fig. 3 below shows the daily rainfall map and an autographic rainfall record for the PE event.

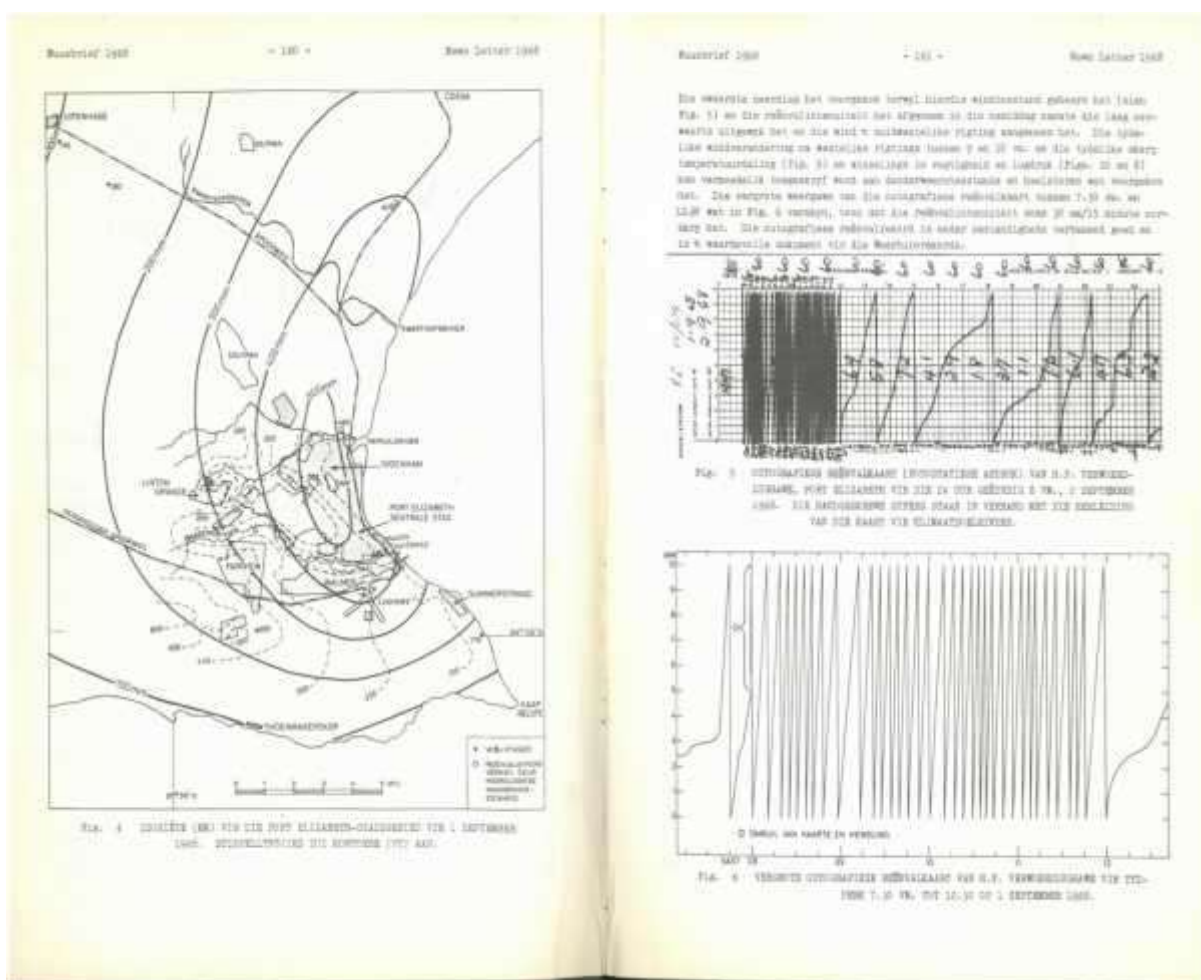


Figure 3: Daily Rainfall map and an Autographic rainfall record of 1 September 1968 at Port Elizabeth.

3) Cloudbursts:

Cloudburst is a sudden and heavy fall of rain, almost always of the shower type. The Meteorological Glossary of the America Meteorological Society (AMS) further says that an unofficial criterion sometimes used specifies a rate of fall equal to or greater than 100 mm

(3.94 inches) per hour. Applying last mentioned criteria all the SA records from 5 minutes to 4 hours (see Table 1) were cloudbursts. Rainfall rates/ intensities for the SA records of  $\leq$  one hour varied from 232 mm/h at Bisho to 504 mm/h at Levubu. The Port Elizabeth's storm average rainfall rate was 117.5 mm/h for the 4 hours at Adcockvale. All the SA rainfall records of less than a day are then per definition cloudbursts.

*Conclusions*

All SA rainfall records below World records are as expected since RSA is climatologically a dry land due to its location in the sub-tropical high pressure belt. It is possible that SA could measure a World record.

42.4 mm measured 15:45 by an AWS at Levubu 26 February 2016 is the SA record rainfall for 5-minutes.

218 mm measured in 40 minutes ending 18:30 by a Third order climate station from a thunderstorm at Johannesburg - Swartkoppies 31 January 2017 is the SA record rainfall for one hour.

The 470 mm over 4 hours ending 12:00 1<sup>st</sup> September 1968 from a cut-off low system at Port Elizabeth - Adcockvale is a SA record.

The best fit exponential or power function can be used for estimates of SA or World record rainfalls for any time period.

The 5-minute, half-hourly, hourly and four-hourly SA record events were all cloudbursts.

Levubu's 504 mm/h on 26 February 2016 is the record highest rainfall intensity measured in South Africa.

Highest record or extreme rainfalls invariably leads to impacts such as flash floods, river floods, lives lost and extensive damage to infrastructure.

*Acknowledgements*

Elsa de Jager and Charlotte McBride from Climate Service.

Karin Oxley from the Library.

Other colleagues especially forecasters and technicians for help and discussions.

Mr Jerry Lengoasa CEO of SAWS.

*References*

Burt C. C, 2007, Extreme Weather – A Guide and Record Book, W. W. Norton & Company, New York.

Glossary of Meteorology (AMS):  
[http://glossary.ametsoc.org/wiki/Main Page](http://glossary.ametsoc.org/wiki/Main_Page)

Hayward Q. L, Van den Berg H. J. C, 1968, Die Port Elizabeth-stortreëns van 1 September 1968, Weather Bureau News Letter, No. 234

NOAA, USA, World record rainfall data:  
[http://www.weather.gov/oh/hdsc/record\\_precip/record\\_precip.html](http://www.weather.gov/oh/hdsc/record_precip/record_precip.html)

WB 36, 1974, Climate of South Africa: Weather Bureau (WB) 36 Part II

Weather Bureau News Letter, 1951, Agt en 'n half duim reën in 40 minute, No. 22. January 1951.

# Annual and Seasonal Spatial Analysis of Rainfall Variability in Western Cape, South Africa

Willard Zvarevashe<sup>1\*</sup>, Syamala Krishnannair<sup>1</sup> and Venkataraman Sivakumar<sup>2</sup>

<sup>1</sup>*Department of Mathematical Sciences, University of Zululand, Private Bag X1001, KwaDlangezwa, 3886, South Africa*

<sup>2</sup>*Department of Chemistry and Physics, University of Kwazulu-Natal, Private Bag X54001, Durban, South Africa*

## **Abstract**

An understanding of the trend and the spatial shifts of the rainfall is very important for the development and management of water resources so that there is greater sustainability especially in the rainfed agriculture. Mann-Kendall test was applied to 20 stations scattered in Western Cape. An analysis of spatial variability, monthly and seasonal variability for the period from 1980 to 2017 showed that there was a monotonic decrease in rainfall in most of the stations except for stations located further north in the province. There was also a variability of up to 127% in the annual and seasonal rainfall in some of the stations. These rainfall trend analyses may help to predict future rainfall patterns and thereby allowing planning and better water resources management.

**Keywords:** Rainfall, Trend Analysis, Spatial Analysis

## **1. Introduction**

Change in the rainfall patterns have adverse effects on all the earth's spheres particularly the hydrosphere, biosphere and lithosphere. Therefore, study of the climate trends such as temperature and rainfall trends becomes very essential, which is the first step towards systematic study of climate change (Nema *et al.*, 2018). The whole of Southern Africa is prone to relatively high rainfall variability and there are numerous recorded floods and draughts occurrences (Usman and Reason, 2004). Most of agricultural production in Africa depends heavily on the rainfall (Kijazi and Reason, 2005). Western Cape in South Africa, has not been spared from this rainfall variability. Some of the regions in the province have been facing water challenges in the last decade because of general decrease of rainfall (Kruger and Nxumalo, 2017; Zvarevashe *et al.*, 2018). It becomes important to carry out an analysis of the rainfall trends for different rainfall periods and different regions to find out if the trend is similar throughout the province and for different seasons.

In view of the precarious position that Western Cape find itself in, this study seeks to investigate precipitation patterns in the province. Although there have been several studies that have investigated the variability of rainfall patterns in South Africa, very few concentrated on Western

Cape. Furthermore, there are few spatial statistics based studies for South Africa in general. In this study, Mann-Kendall Test (MK) will be used, which is a non-parametric method that can be used to detect trends in a time series for any period (MacKellar *et al.*, 2014; Nema *et al.*, 2018). Additionally, coefficient of variation (CV%) is calculated and used to carry out spatial analysis using Inverse Distance Weighted (IDW) method.

## **2. Data and Method**

### **2.1 Study Area**

Monthly rainfall data was used to generate annual, summer covering the period December, January and February (DJF), autumn covering the period March, April and May (MAM), winter covering the period June, July and August (JJA) and spring covering the period September, October and November (SON). The data was obtained from South African Weather Service. It was collected from the weather stations in Western Cape for the period from 1980 to 2017. The study area and location of the weather stations are shown in figure 1.

### **2.2 Mann-Kendall and Coefficient of Variation**

Trends in the rainfall data for the period from 1980 to 2017 were evaluated using Mann-Kendall trend Test (MK) and variability was calculated using Coefficient of Variation (CV%). MK has an

advantage of not having any underlying assumptions about the distribution of the data. It can indicate the temporal patterns in yearly and season precipitation (Kendall, 1980). A correlation coefficient,  $\tau$ , which denotes relative strength of the trend of the time series is computed. It takes on a value between -1 and 1. The probability of this trend occurring by chance is also estimated, from which a measure of statistical significance can be assigned.

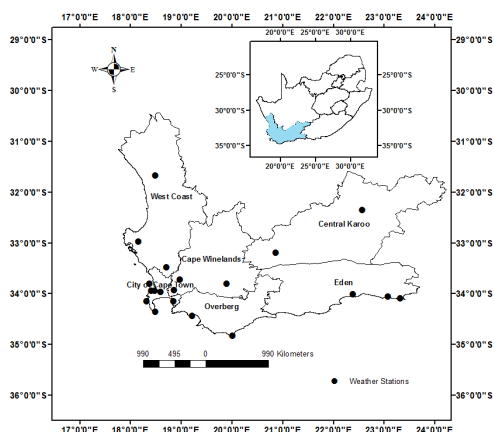


**Figure 1:** The location of Western Cape province in South Africa, its magisterial districts and the location of weather stations used in the study.

A 5% level of significance is used such that if the probability estimate was less than 0.05, the trend was deemed to be significant. The trend estimates were calculated for seasonal and totals for all the stations.

Given the time series  $x_1, x_2, x_3, \dots, x_n$  then the MK statistic,  $S$ , is defined as:

$$S = \sum_{i=1}^{n-1} \sum_{j=i+1}^n \text{sgn}(x_j - x_i) \quad (1)$$

Where  $x_j$  and  $x_i$  are the data values in years  $j$  and  $i$ , respectively, with  $j > i$ ,  $n$  is the total number of years and  $\text{sgn}()$  is the sign function. Let  $x_j - x_i = \theta$  then

$$\text{sgn}(\theta) = \begin{cases} 1 & \text{if } \theta > 0 \\ 0 & \text{if } \theta = 0 \\ -1 & \text{if } \theta < 0 \end{cases} \quad (2)$$

The statistics  $S$  is approximately normally distributed, with mean zero and variance given by:

$$\text{Var}(S) = N(N - 1)(2N + 5)/18.$$

The standard normal variable  $Z$  is then formulated as

$$z = \begin{cases} \frac{S-1}{\sqrt{\text{Var}(S)}} & \text{if } S > 0 \\ 0 & \text{if } \theta = 0 \\ \frac{S+1}{\sqrt{\text{Var}(S)}} & \text{if } S < 0 \end{cases} \quad (3)$$

The coefficient of variation (CV%) is then calculated. CV%, also known as “relative variability”, equals the standard deviation divided by the mean. It measures how a value is varied around the mean (Label et al., 1987).

Using the CV% for each station the Inverse Distance Weighted method (IDW) is used to investigate spatially fleeting precipitation variability over the regions using ArcGIS (Singh et al., 1987; Zuo et al., 2016). IDW is a deterministic method for multivariate interpolation which uses exact points to calculate the nearest points using a weight. Therefore, using the rainfall data from the stations available an estimate of monthly rainfall for areas without stations can be done using IDW. (Moeletsi et al., 2016).

### 3. Results and Discussion

#### 3.1 Statistical Characteristics of Annual and Seasonal Rainfall

Table 1 shows the z-statistics of the seasonal and annual rainfall of selected stations in Western Cape province using MK. Negative z-statistic shows that there is a monotonic downward trend in the rainfall whereas a positive z-statistic shows that there is a monotonic upward trend. There is generally monotonic downward trend in most of the stations for different seasons. Paarl station has a significant downward trend for annual ( $p = 0.003$ ), DJF ( $p = 0.006$ ), MAM ( $p = 0.001$ ) and SON ( $p = 0.046$ ). Stellenbosch station which is also located in the same district with Paarl station has almost similar trend with a significant downward trend in DJF ( $p = 0.008$ ) and MAM ( $p = 0.004$ ). It was also noted that significant upward trend only recorded in Strand ( $p = 0.009$ ) and Hermanus ( $p = 0.007$ ) stations for the period JJA and Cape Point ( $p = 0.033$  for the period SON). George WO and Knysna stations have significant monotonic downward trend for 2 consecutive seasons of DJF and MAM. This is expected as they are also located in the same district. Almost similar trend was observed at Plettenbergbaai station which is another station located in the same district. These results agreed with what was found by MacKellar et al. (2014) and Kruger et al. (2017).

The results from MK Test showed that there is generally monotonic decreasing rainfall trend. A

further investigation of this decrease is then done to analyse the variability of the rainfall over different seasons.

**Table 1:** Z-statistic values of seasonal rainfall using MK for Stations in Western Cape Province

Station	Annual	DJF	MAM	JJA	SON
Beaufort-Wes	-1.0666	-0.372	-1.215	0.397	-0.223
Cape Agulhas	-0.955	-0.528	-2.489*	0.163	0.427
Cape Point	0.453	-0.653	-1.333	0.805	2.138*
Cape Town Slangkop	-0.113	-0.733	-0.733	0.508	0
Cape Town WO	-1.986*	-0.864	-1.191	-0.911	-0.864
George WO	-1.985	-1.939*	-1.985*	0.981	-0.490
Hermanus	0.27177	-0.513	-1.782*	2.689**	-0.393
Knysna	-1.238	-2.386*	-1.962*	-0.634	0.030
Laingsburg	-0.620	-1.213	-0.226	0.056	0.338
Langebaanweg Aws	-1.685	-0.805	-2.578**	-0.289	-0.226
Malmesbury	-0.521	-0.447	0.024	0.174	-0.620
Molteno Reservoir	-1.612	-1.662	-1.860	-0.620	-0.174
Paarl	-3**	-3.438**	-3.147**	-0.924	-1.995*
Plettenbergbaai	-1.3778	-1.985*	-0.537	0.210	-1.098
Robbeneiland	-0.537	0.093	-0.210	0.817	0.817
Robertson	0.42257	-0.950	-2.774**	1.321	0.898
S. A. Astronomical Observatory	-1.609	-1.911	-1.660*	-0.981	0.063
Stellenbosch	-1.785	-2.665**	-2.879**	0	-0.289
Strand	1.1279	-0.931	0.649	2.594**	-0.620
Vredendal	-1.195	-1.245	-1.597	-0.101	-1.685

\*z-statistic is significant at 0.05 level and \*\* z-statistic is significant 0.01 level

### 3.2 Annual and Seasonal Analysis

CV% was calculated for the different stations and IDW was used to find the spatial patterns of the rainfall. The results are shown in figure 2 which shows the variability of rainfall for annual and seasonal rainfall. Generally, there is a variability of between 19% to 127%. Annual Rainfall is less variable in City of Cape Town, greater part of Overberg and part of West Coast and Cape Winelands. The wettest months JJA, are also less variable for the same areas as compared to the northern areas. A variability of between 25 to 33% is observed. Whilst the northern part of West Coast is more variable with a variability of up to 126% for DJF period. Figure 2 (c) shows that MAM is more variable with most of the province having a CV% of between 40% to 50% whilst for JJA most of the province has CV% of between 30% and 40%. Annual rainfall is least variable as compared to the seasons, with CV% of between 19% and 36%.

### 4. Conclusions

An analysis of the rainfall trend was carried out for annual, DJF, MAM, JJA and SON rainfall totals for the period 1980 to 2017 over Western Cape. Mann-Kendall test and inverse distance weighted method were used to explore these variability. The results showed that there is generally downward trend of rainfall in most part of Western Cape. Coefficient of variation for the whole province showed that there is variability of between 19% and 126%. The highest variability was recorded in the driest period of DJF and the lowest variability were recorded in the wettest months of JJA.

It was observed that although there is generally monotonic decreasing rainfall pattern (from table 1) over the study period the variability is mostly observed in the seasonality of the rainfall than in the annual rainfall.

### Acknowledgement

The author would like to acknowledge South African Weather Service for the data that was used in this study and NRF for the funding of the work.

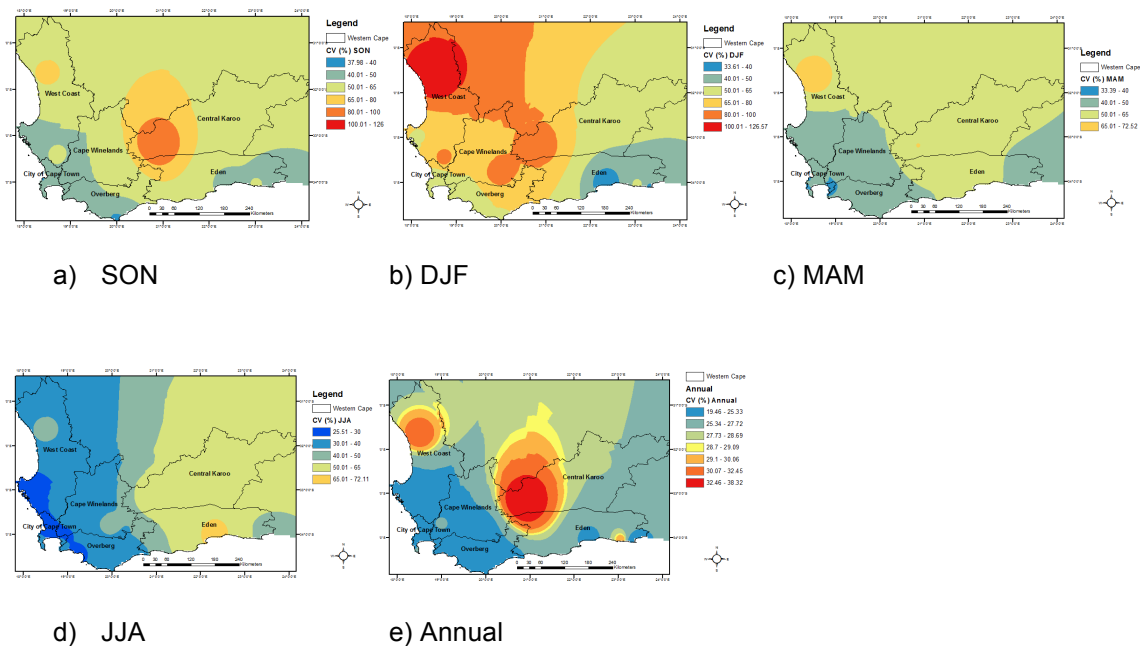


**Figure 2:** Annual and seasonal rainfall variability (CV%) in Western Cape a) annual b) DJF c) MAM d) JJA e) SON.

#### 4. Reference

- Kijazi A.L. and C.J.C. Reason. 2005, Relationships between intraseasonal rainfall variability of Coastal Tanzania and ENSO, *Theoretical and Applied Climatology*, 82: 153-176.
- Kendall, M. (1980). *Multivariate Analysis*, (London, Charles Griffin).
- Kruger, A. C., & Nxumalo, M. P. (2017). Historical rainfall trends in South Africa: 1921–2015. *Water SA*, 43(2), 285-297.
- Lebel, T., Bastin, G., Obled, C., & Creutin, J. D. (1987). On the accuracy of areal rainfall estimation: a case study. *Water Resources Research*, 23(11), 2123-2134.
- MacKellar, N., New, M., & Jack, C. (2014). Observed and modelled trends in rainfall and temperature for South Africa: 1960-2010. *South African Journal of Science*, 110(7-8), 1-13.
- Moeletsi, M. E., Shabalala, Z. P., De Nysschen, G., & Walker, S. (2016). Evaluation of an inverse distance weighting method for patching daily and dekadal rainfall over the Free State Province, South Africa. *Water SA*, 42(3), 466-474.
- Nema, M. K., Khare, D., Adamowski, J., & Chandniha, S. K. (2018). Spatio-temporal analysis of rainfall trends in Chhattisgarh State, Central India over the last 115 years. *Journal of Water and Land Development*, 36(1), 117-128.
- Singh, V. P., & Chowdhury, P. K. (1986). Comparing Some Methods Of Estimating Mean Areal Rainfall 1. *Jawra Journal of the American Water Resources Association*, 22(2), 275-282.
- Usman M.T. and C.J.C. Reason. 2004, Dry spell frequencies and their variability over southern Africa, *Climate Research*, 26: 199-211.
- Zuo, R., Carranza, E. J. M., & Wang, J. (2016). Spatial analysis and visualization of exploration geochemical data. *Earth-Science Reviews*, 158, 9-18.
- Zvarevashe, W., Krishnannair, S., & Sivakumar, V. (2018). Analysis of Austral Summer and Winter Rainfall Variability in South Africa Using Ensemble Empirical Mode Decomposition. *IFAC-PapersOnLine*, 51(5), 132-1.

## ***Coastal marine weather and safety: towards an integrated understanding for marine weather services***

Marc de Vos <sup>\*1, 2, 3</sup> and Christo Rautenbach <sup>1, 2</sup>

<sup>1</sup>South African Weather Service, Marine Unit, Cape Town, South Africa

<sup>2</sup>Oceanography department and Marine Research Institute, University of Cape Town, South Africa

<sup>3</sup>National Sea Rescue Institute, Cape Town, South Africa

### ***Abstract***

South Africa boasts an extensive coastline which hosts a multitude of activities and interests. The coastline and the coastal waters bordering it represent significant economic, recreational and cultural value. It follows that producers of marine weather (taken here to mean the combination of meteorological and oceanographic parameters) information products and services have a critical role to play in supporting these interests; both in terms of maximising safety and efficiency for coastal users. However, challenges surrounding uptake and usability of critical marine weather products and services remain. Here, we present findings from research into the relationship between weather and safety of coastal activity, and insight into obstacles to weather information uptake, which may modulate this relationship. We show that sensitivity to marine weather (and specific parameters) varies according to activity type and location. We also show that innovative techniques are required in the presentation of forecast data to inform decisions involved with these activities, where accuracy and consistency (forecast skill) are unable to add value to the value chain by themselves.

**Keywords:** Marine Weather, Coastal Safety, Coastal Management, Ocean Forecasting

### ***Introduction***

South Africa has a challenging coastline to manage. Whilst it is generally considered to be geologically rugged (Wigley, 2011), it is highly dynamic, with many bays, headlands, beaches, rocky shores and cliffs. At around 3000 km in length (Lombard et al., 2004), the coastline is extensive, with an equally sizeable Exclusive Economic Zone (EEZ) of just over 291, 550 NM<sup>2</sup> (Griffiths et al., 2010) extending from it. Much of the activity occurring within this EEZ and contributing to South Africa's GDP (either directly, e.g. through commercial activity, or indirectly e.g. through recreation and tourism) occurs along the coastline, or in coastal South African waters. Operation Phakisa, the South African governmental initiative to enhance the economic contribution of ocean-related products and services such as transport and manufacturing, offshore oil and gas, aquaculture and protection and governance (Spamer, 2015), can be expected to further increase coastal activity. This makes the domain an important one to manage. In this regard, the importance of marine meteorological services, taken to mean services provided in respect of meteorological and oceanographic parameters, is formally acknowledged by the World Meteorological Organisation (WMO, 2017). It is also broadly acknowledged by coastal users themselves, with many users having favourite weather information platforms and intuitive calibration techniques which they use to inform decisions. This paper aims to improve coastal weather information service delivery by 1) developing a basic quantitative understanding of the relationship between marine weather and coastal activity, and 2) investigating the way in which some users of these services interact with them. It is proposed that this would assist in the strategic development or adaptation of marine weather information services

such that they address current key gaps. It would also help to ensure that they are

presented in such a way as to be useful and understandable by their intended users.

### ***Methods***

#### ***Establishing the relationship between weather and safety.***

Little objective data and analyses are available detailing the relationship between weather and coastal marine activity (de Vos and Rautenbach, 2018: in prep). However, the reporting system and associated archived incident reports of the National Sea Rescue Institute (NSRI) provide a valuable opportunity to investigate patterns in respect of marine weather and coastal safety. As the only mandated coastal search and rescue (SAR) agency, its archives provide the best collection of incident reports describing coastal safety incidents. Reports cover incidents involving anything from swimmers at the shore to commercial vessels within 150 NM of the coast. Reports are compiled via a bespoke Management Information System (MIS). In each report, marine meteorological parameters (wind speed, wind direction, wave height and visibility) are entered via drop down menus with pre-defined magnitude bins. Personnel can also enter qualitative descriptions of weather conditions and other details in text fields. In order to impose some structure on this extensive data set, weather severity categories (Good, Marginal, Bad) were defined according to accepted thresholds as informed by discussions with coastal users and SAR operators. Coastal sub-regions were also defined. The reports' standard meteorological data were then filtered in order to assign each report a weather severity (Good, Marginal, Bad) in respect of these thresholds. These thresholds are summarized in Table 1. Thereafter, reports were mined

---

\* Corresponding Author Tel: +27 21 935 5764 | Email: [marc.devos@weathersa.co.za](mailto:marc.devos@weathersa.co.za) | P.O Box 21, Cape Town International Airport, 7525

for commonly used key words and phrases used by SAR personnel in the MIS qualitative text fields to describe weather related ideas. At the time of writing, the archive contained more than 17,000 reports spanning the period from December 2009 until April 2018. After filtering reports for training missions, public relations events, inland stations and spurious records, we arrived at a total of 6,051 incidents reports from 32 coastal NSRI stations. These range from Lamberts Bay in the north-west to Richard’s Bay in the north-east. For a complete description of the dataset and the methods used to mine it, please refer to de Vos and Rautenbach (2018: in prep).

		Visibility	Swell (m)	Wind (kt)
Lower Severity ↑ ↓ Higher Severity	Good	Good	0-2	0-6
	Marginal	Average	2-3	11-27
	Bad	Bad	> 3	> 28

Table 1. Classification framework for marine weather conditions as described in NSRI MIS reports. The classification process involves identifying the relevant cells (visibility, swell and wind) for a given incident. The weather is then classified according to the highest severity (Good, Marginal, Bad) of the 3 identified parameter cells

Establishing how users interact with coastal marine meteorological information.

Over a period of 6 months, various coastal ocean users were engaged regarding their favourite marine weather information products. Specifically, a series of workshops was set up to collect feedback from a group of small scale fishers operating out of the eastern and western periphery of False Bay after they had been involved in a trial of a new marine weather information delivery project (a transdisciplinary research approach). Ultimately responses from a total of 78 fishers were recorded, detailing their perception of the accuracy of a forecast product for False Bay. The sea state forecast product was comprised of outputs from a Delft-3D WAVE and FLOW configuration with a horizontal resolution of approximately 200 m (for waves and currents). This configuration was forced by winds from a multi-scale global climate Conformal-Cubic Atmospheric Model (CCAM) (Engelbrecht et al., 2011) run in forecast mode with a horizontal resolution of 1 km. Spectral wave boundary conditions for the wave model were recreated from parameters obtained from the National Centre for Environmental Prediction (NCEP). Then, numerous exchanges from several local activity forums were monitored over 6 months to develop insights into perceptions of commonly used marine weather services. These forums were hosted on *WhatsApp* groups and involved big-wave surfers, regular surfers, SAR personnel and kayakers from a Cape Town paddling club. While these insights have not been quantified, they reveal interesting misconceptions and factors which affect user-uptake and usage of marine meteorological information products.

Results

The relationship between weather and coastal marine safety.

First level analysis reveals a consistent pattern across all coastal sub-regions whereby the highest (lowest) incidents frequency coincides with Good (Bad) weather (Fig. 1). Since it is impossible to normalize data to account for absolute numbers of users engaged in activity on

any given day, this is a logical pattern, whereby higher incident frequency might be related to higher levels of coastal activity during Good weather. For the full analysis, including derived exposure coefficients in respect of varying weather severity, please refer to de Vos and Rautenbach (2018: in prep).

In Fig. 2 the second level analysis reveals that, despite incidents occurring least frequently during Bad weather (likely related to fewer coastal users engaged in activity during at these times), the cause-effect linkage between the weather conditions and incidents appears to be stronger. Whilst this relationship is impossible to prove explicitly, the higher frequency with which SAR personnel make specific mention of weather parameters in their qualitative descriptions (over and above the mandatory drop-down menu weather reporting) for Bad weather incidents implies that weather conditions were more noteworthy in these cases. We can thus infer that they played a more important role in either causing the incident, or at least affecting the response. We assert that, given the coherence of the patterns revealed in the analysis of such a large sample size, the strategy has merit. Furthermore, differences in the relative

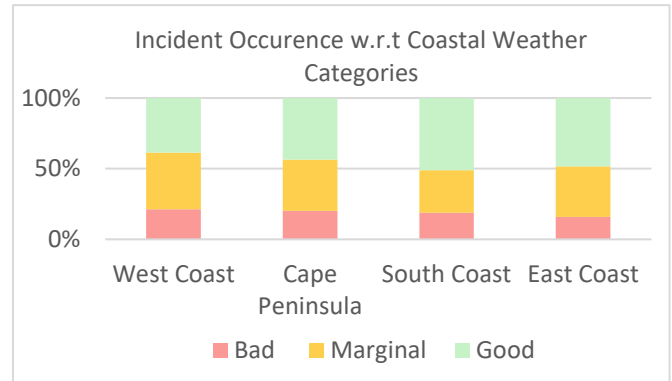


Figure 1. Results of the Level 1 analysis showing the relative occurrence frequencies of incidents in Bad, Marginal and Good weather conditions for each coastal sub-region. The total number of incidents from which these percentages are derived are West Coast: 767; Cape Peninsula: 1,448; South Coast: 2,638 and East Coast: 1,198. This gives rise to the total of 6,051 reports for the entire coastline for the time period in question.

importance of specific marine weather parameters (wind, waves or visibility) appear from this analysis. Along the West Coast, for

example, poor visibility (fog) appears to be an issue more frequently

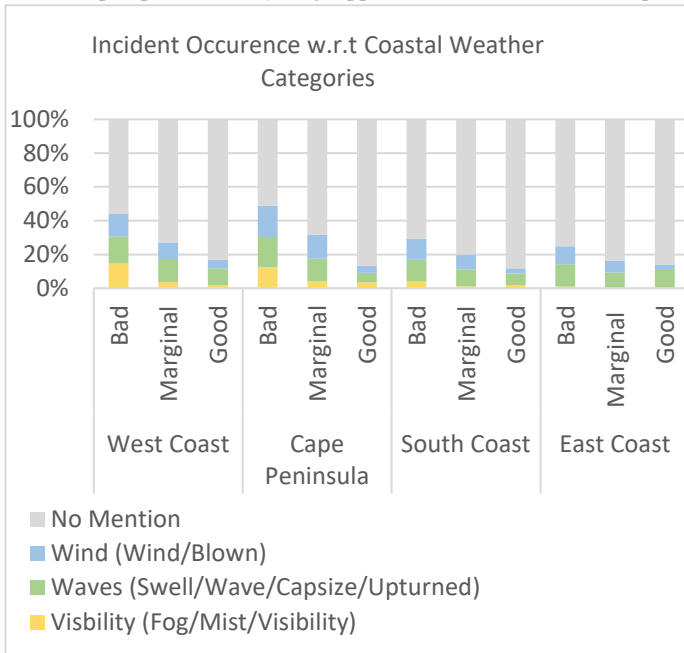


Figure 2. Results of the Level 2 analysis showing the number of times weather conditions were explicitly mentioned in the qualitative descriptive fields of incident reports (in addition to the mandatory weather reporting fields). Each bar represents the total number of reports for a specific weather severity category and location; e.g. for the West Coast, Bad column the shaded portions are proportions of the total number of reports in this subset and not the entire dataset.

than along any other coastal sub-regions, whilst for the Cape Peninsula, wind and waves are mentioned qualitatively more often than anywhere else. Third level analysis of the incident reports are aimed at establishing the sensitivity of specific activity types and areas to different marine weather parameters and severity.

Fig. 3 shows a consistent trend across most coastal sub-regions whereby incidents in which users are more vulnerable (Group 1) are most frequent during Good weather. As weather severity increases (Marginal), so incidents involving personal water craft (Group 2) increase in frequency. The pattern persists, with incidents involving small vessels (Group 3) being most numerous during Bad weather conditions. There does not appear to be a clear relationship between incidents involving larger commercial vessels (Group 4) and marine weather. These results adhere to the logical expectation that the greater the perceived security and safety offered by one's craft (e.g. a kayaker may feel more secure than a swimmer, and a small boat skipper more secure than a kayaker), the more severe the weather one might be inclined to risk putting to sea in. Again, whilst the results cannot be normalized to account for absolute numbers of users engaged during any given weather conditions, it appears that incidents still occur in spite of enhanced perceived security offered by one's craft.

*Perceptions of marine weather information services.*

Results of the perception surveying conducted with small scale fishers revealed that accuracy (and consistency thereof) is not, by themselves, sufficient determinants of usability. The perception of a forecast, which appears to be modulated by various possible ancillary factors in the way it is presented, is important, as it determines trust

in the product and therefore future use and/or reliance on it as a critical decision-making tool. This confirms that even in cases where model performance was high, perceptions of accuracy were not necessarily correspondingly high. As such, producers of marine weather information products and services should ensure that they consider the design of their products right through to the end of the value chain, in order to avoid poor uptake of otherwise well-performing forecasting systems.

In Fig. 4 the summary of user perceptions of a high resolution numerical forecasting model is given. This transdisciplinary model was evaluated by sending out representatives on fishing boats with False Bay fishermen. The 78 participants compared their existing means of predicting metocean condition with the newly developed models. The numerical models provided 9-hour predictions for winds, waves and currents within False Bay.

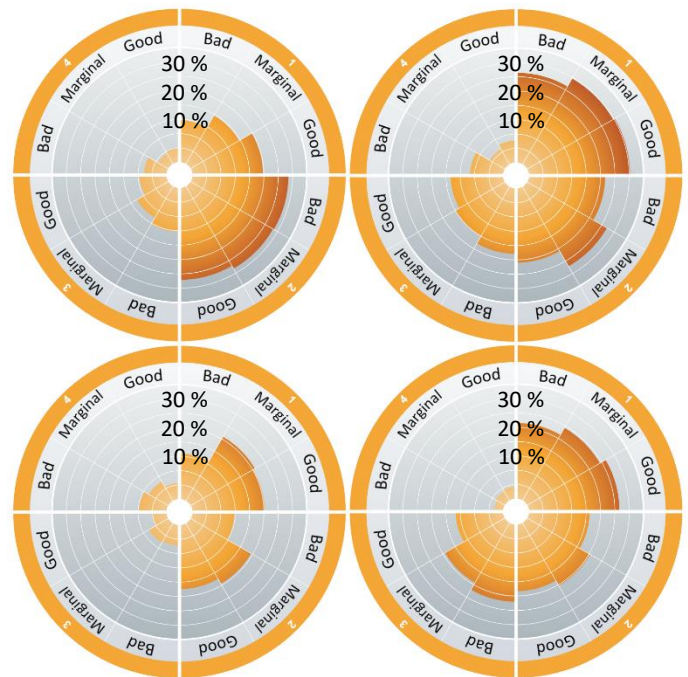


Figure 3. Results of the Level 3 analysis showing incident occurrence per activity group in Good, Marginal and Bad weather conditions, for the (A) West Coast, (B) Cape Peninsula, (C) South Coast and East Coast (D). These results yield insight into the sensitivity of certain activities and locations to certain weather conditions. Activity group numbers are shown in white around the circumference of each circular chart.

The questionnaire used during the user perception quantification process was carefully developed to try and keep the polling of true perceptions as robust as possible. For example, fishermen were not left to fill in the questionnaires of their own accord to avoid careless or non-completion of the forms. Interns and volunteers in charge of the questionnaires were thoroughly briefed to ensure standard wording and scoring systems were followed. In Fig. 4 the individual perceived performance of the numerical models is given. It is clear that the wind model (1 km resolution CCAM) was perceived to perform the best. In total the perception was approximately 50 % acceptable even though the numerical validation of the models performed better than other lower resolution numerical atmospheric and oceanographic forecasting tools widely used among these particular small craft commercial fishermen.

Even though this model was developed in a transdisciplinary fashion (where users requested forecasts via text message) it appears that supplementary information, like apps and websites, are also required. These will likely enhance confidence in products. From discussion with users it was also established that showing that development was based on peer-reviewed processes will enhance trust in tools and services.

sensitivity are the West Coast and Cape Peninsula, which see more reporting involving fog (poor visibility) than the other coastal regions.

For most coastal sub regions, Good weather appears to be a precursor to increased incident frequency for Group 1, marginal weather for Group 2 incidents and Bad weather for Group 3 incidents. From the user perception study it can be concluded that in the context of product uptake into large scale usage, not only is forecast accuracy (skill level) important but also user perception, which may be moderated by considerations other than model performance.

#### References

- de Vos, M., Rautenbach, C., 2018. Investigating the connection between metocean conditions and coastal user safety: an analysis of search and rescue data. *Saf. Sci.*
- Engelbrecht, F.A., Landman, W.A., Engelbrecht, C.J., Landman, S., Bopape, M.M., Roux, B., McGregor, J.L., M, T., 2011. Multi-scale climate modeling over Southern Africa using a variable-resolution global model. *Water SA* 37, 647–658. <https://doi.org/10.4314/wsa.v37i5.2>
- Griffiths, C.L., Robinson, T.B., Lange, L., Mead, A., 2010. Marine biodiversity in south africa: An evaluation of current states of knowledge. *PLoS One* 5. <https://doi.org/10.1371/journal.pone.0012008>
- Lombard, A., Strauss, T., Harris, J., Sink, K., Attwood, C., Hutchings, L., 2004. South African National Spatial Biodiversity Assessment Technical Report Volume 4 : Marine Component.
- Spamer, J., 2015. Riding the African Blue Economy wave: A South African perspective. 2015 4th IEEE Int. Conf. Adv. Logist. Transp. IEEE ICALT 2015 59–64. <https://doi.org/10.1109/ICAdLT.2015.7136591>
- Wigley, R., 2011. Geohazards in Coastal Areas. Cape Town.
- WMO, 2017. Manual of Marine Meteorological Services: Volume 1 - Global Aspects. WMO-No. 558, 2017 draft. ed. World Meteorological Organisation, Geneva.

#### Acknowledgements

The authors would like to thank the National Sea Rescue Institute for the provision of the report data.

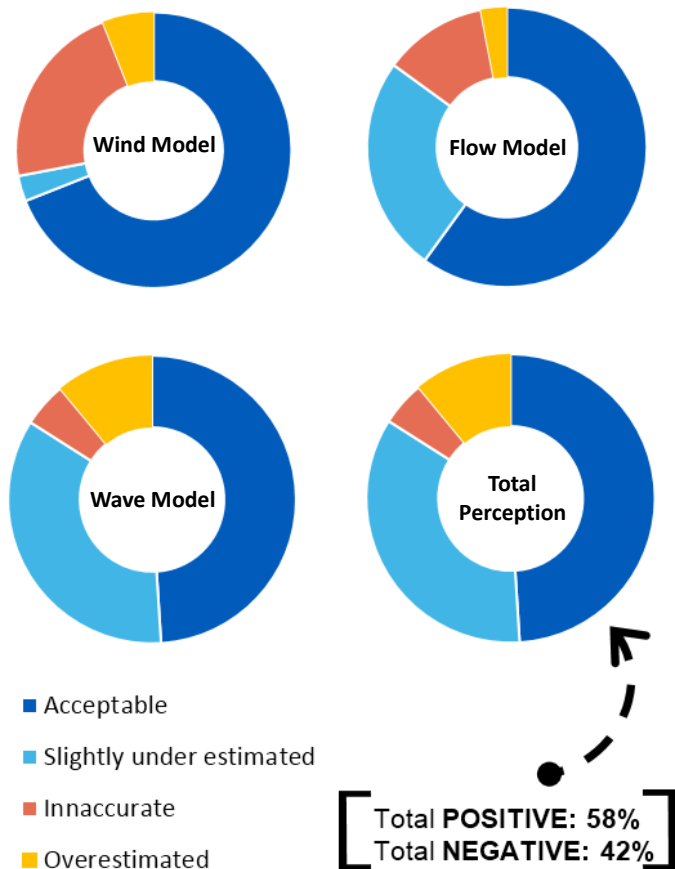


Figure 4. A summary of perception of small scale fisher's during trials of a wind, wave and current forecasting system.

#### Conclusions

With sufficient sample size ( $n = 6,051$ ), meaningful patterns emerged from an NSRI incident report dataset which possibly describe how coastal marine incident occurrence is modulated by weather severity. Whilst, in general, incidents coincide most frequently with Good weather (a result which is likely related to increased coastal activity during Good weather), analyzing different kinds of activities, in different coastal sub regions reveals differing sensitivities to weather severity and parameters. For example, along densely populated coastlines with major metropolitan areas such as the Cape Peninsula, Group 1 activities are of particular concern during Good weather conditions (likely due to high exposure – or the number of users engaged at that time). Where population density is known to be lower, along the West Coast for, the number of Good weather Group 1 incidents is lower. An example of region-specific weather parameter

## Climate Change Impacts on Accumulated Winter Chill for the Western Cape

Siphamandla Daniel<sup>1\*</sup> Michael G. Mengistu<sup>1</sup> Thabo Makgoale<sup>1</sup>

South African Weather Service, Eco Glades 1 Eco Park, Centurion, Pretoria, 0157, South Africa

### Abstract

Temperate fruit trees require exposure to chilling conditions in order to break dormancy and produce high yields. Winter chill accumulation is important for site selection, variety selection and for operational management of orchards. General Circulation Models (GCMs) data from the Coupled Model Intercomparison Project phase 5 (CMIP5) which were downscaled by Rossby Centre Regional Atmospheric Model (RCA4), Regional Climate Model (RCM) under the auspice of Coordinated Regional Climate Downscaling Experiment (CORDEX) Africa models were used. Maximum and minimum daily air temperatures from the Rossby Centre Regional Atmospheric Model (RCA4) were utilized to calculate hourly air temperature data, which was then used to calculate chill units. The study evaluates the projected future changes in positive chill units' accumulation over the Western Cape region. Projections of positive chill units indicate loss of current growing areas in some regions due to insufficient chill units' accumulation caused by the increase in temperatures.

Keywords: Climate change, Chill Units, Western Cape, CMIP5, CORDEX.

### Introduction

Fruit and nut trees annually cycle through different stages in their physiological stages to produce fruits. Deciduous fruit trees fall into dormancy during the winter months, this process enables the fruit tree to tolerate the cold temperatures (Vegis, 1964). During this phase, any dry matter accumulation is suspended within the fruit tree. The process is broken during spring, when warm temperatures are dominating (Luedeling, 2012). Deciduous fruit trees break dormancy after a prescribed 'sum' of winter conditions has passed and the tree has then determined that winter has finished and will begin to flower in response to warm temperatures (Linville, 1990). This sum of cold weather is known as winter chill. The winter chill required to break dormancy differs by fruit type and variety. According to Luedeling (2012), trees must fulfill their chilling and heat requirements in order to break dormancy. Meeting the chilling requirements is important for fruit trees particularly in warmer environments where they are not of origin (Chandler, 1942). Chill units are calculated by using hourly air temperatures and are summed over 24 hours and accumulated for the winter months (Linville, 1990). The cold temperatures of winter months have a major effect on the deciduous fruit yield and quality, as well as the onset of flowering stage (Ballard et al, 1987; Allan, 2004). Chill hour model, Richardson Chill model, Daily Positive Chill Hour model and Dynamic model are all used to measure the chilling requirements of a deciduous fruit (Luedeling et al., 2009)

The Utah model recommends that a full chill unit can be acquired when the temperature in an hour is between 2.4 and 9.2°C. High temperatures  $\geq 12.5^\circ\text{C}$  does not contribute to the chill accumulation, while temperatures below  $1.5^\circ\text{C}$  are also not considered effective for chilling. Higher temperatures counteract the positive effects of chilling and negative chill units are applied when temperatures exceed a threshold of  $16^\circ\text{C}$  (Richardson *et al.*, 1974; Linsley-Noakes *et al.*, 1994). The Utah model was adopted by the South African deciduous fruit industry in the southern part of the Western Cape (Linsley-Noakes *et al.*, 1994). However, Linsley-Noakes *et al.* (1994) found the Utah Model to be inaccurate under South African conditions, especially in the

warm deciduous fruit growing areas with high winter daytime temperatures greater than  $20^\circ\text{C}$ . The high negative totals during warm winter days led to inaccurate and negative Utah chill unit totals, even though adequate chilling was received by low chill trees. A modification of the Utah Chill Unit Model was proposed by Linsley-Noakes *et al.* (1994) which is known as Daily Positive Utah Chill Unit Model. The Daily Positive Utah Chill Unit Model makes use of the same criteria as Utah model with the exception of temperatures above  $15^\circ\text{C}$  being given 0 instead of -1.

The aim of this study is to investigate the effects of climate change on Positive Utah chill units' accumulation for the periods of 2036-2065 as well as 2066-2095 under Representative Concentration Pathway (RCP) 4.5 and under Representative Concentration Pathway (RCP) 8.5 emission scenarios comparative with the reference/observed period between 1976 to 2005 of Western Cape province. RCP8.5 represents the business as usual scenarios where the greenhouse gases concentrations increase abnormally overtime leading to radiative forcing of  $8.5 \text{ W/m}^2$  at the end of the century (Riahi et al, 2011). On the other hand, RCP4.5 represents the scenario where the greenhouse gases and concentrations stabilize at the end of the century to radiative forcing of  $4.5 \text{ W/m}^2$ .

The period of 2036-2065 and 2066-2095 were chosen as the RCP 4.5 illustrates a peak in the 2040s and slowly stabilizing at the end of the century. This is vital to capture the changes that may result thereof. With respect to RCP 8.5 the two periods are vital to check the impacts that the continuous rise in radiative forcing will have on accumulated winter chill.

### Study Area

Western Cape is the fourth largest province in South Africa with a surface area of  $129462 \text{ km}^2$  (WCG, 2013). The province is geographically located between  $-31^\circ$  to  $-35^\circ$  S latitudes and  $18^\circ$  to  $24^\circ$  E longitude. The province is the largest contributor on South African Agricultural export commodities (DEA&DP, 2016). Agriculture in this province is a major contributor to employment as around 150 000 people are employed in the sector (DEA&DP, 2016). Agricultural commodities are as

follows fruit production, wheat, vegetables, oats, forestry, Lucerne, barley and sheep farming. Kruger (2004) identified five climatic zones within the Western Cape induced by the Cape Fold Belt mountains, namely the Great and upper Karoo, Little Karoo, South-Western Cape, Southern Cape, and Southern cape Forest. The Great and Upper Karoo is a dry extreme climate with very high temperatures during the summer and very low temperatures in winter. This region is found along the north-eastern parts of the Western Cape. Little Karoo region is found in the interior of the province, it is characterised by low rainfall with higher rainfall along the mountains and its mainly of cyclonic nature. South-western Cape region receives winter rainfall with very dry summers, temperatures tend to be moderate. Southern Cape is moderate in temperatures, with all-year round rainfall climate, with peaks in autumn and spring (Kruger, 2004). Lastly the Southern Cape Forest is a moist area with high rainfall, three to four months of rainy days are experienced in this region, temperatures are mild and frost is almost non-existent (Kruger, 2004).

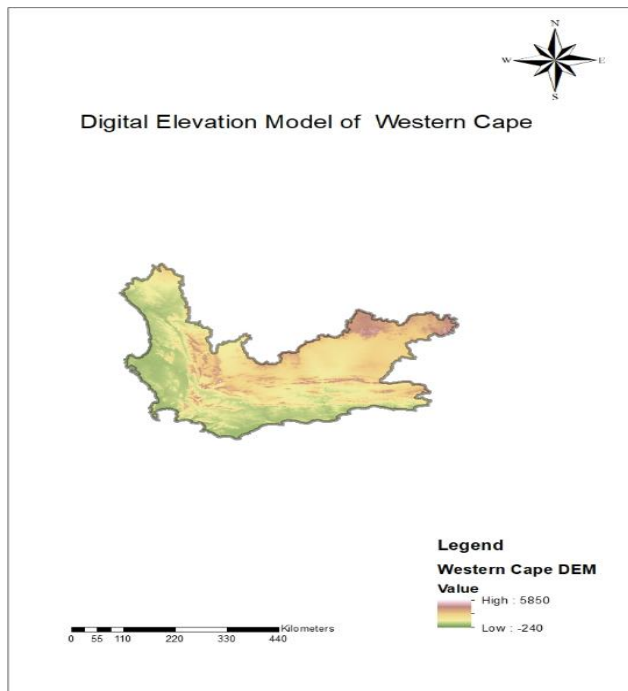


Figure 1: Digital Elevation Model of the Western Cape Province.

Methodology

Hourly temperature data is required for estimating winter chill using all models used to calculate chill units. Hourly air temperature data were simulated using an idealized daily temperature curve that uses a sine curve for daytime warming and a logarithmic decay function for nighttime cooling using the daily maximum and minimum air temperatures (Linville, 1990). Chill units for each hour are summed over every 24 hours and if the total for the 24 hours' period is negative the total chill unit for that day is counted as zero, but if the total is positive, it is added to the already accumulated chill units. Daily observed temperatures were obtained from the South African Weather Service stations for the base period of 1976 to 2005. The daily observed dataset was compared to the nine individual RCA4 model outputs and the ensemble model data.

The Taylor diagram was used to graphically summarize how closely the pattern between the observed and different models was (Taylor, 2001). Taylor diagrams are used in this study to evaluate the skill of individual models. The similarity between two patterns is measured in terms of their correlation, the amplitude of their standard deviation and lastly their centered root mean square difference (Taylor, 2001). RCP 4.5 and 8.5 were used to analyse the predicted change of positive Utah chill units for time periods of 2036-65 and 2066-95.

Table 1: Summary of representative pathway concentration (IPCC, 2007).

Name	Radiative Forcing	Carbon Concentration	Pathway shape
RCP 8.5	>8.5W/m <sup>2</sup> in 2100	~1370 CO <sub>2</sub> -equivalent in 2100	Rising
RCP 4.5	~4.5W/m <sup>2</sup> in 2100	~650 CO <sub>2</sub> -equivalent (at stabilization at 2100)	Stabilization without overshoot

Table 1 summarizes the RCP 8.5 and 4.5 radiative forcing at the end of the century as well as the carbon concentration each pathway will exceed or stabilize in by the end of the century.

Results and Discussion

The relative skill of the 9 CMIP5 GCMs downscaled using the RCA4 regional climate model used to simulate the spatial pattern of daily mean temperature over South Africa is summarised in Fig. 2. Statistics for the nine models were computed, and a different dot colour was assigned to each model considered. The position of each dot colour appearing on the plot quantifies how closely the model's simulated mean temperature pattern matches observations. The results show good correlation between SAWS station data and model data, with the ensemble model output (black dot) being closely correlated to the observed data.

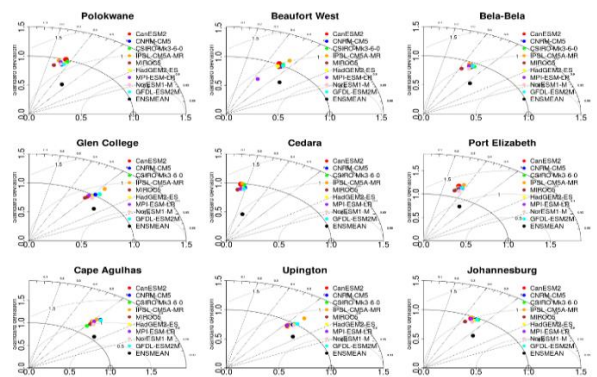


Figure 2: Taylor Diagrams displaying a statistical comparison of daily maximum temperature (°C) between SAWS station data and 9 CMIP5 models which were downscaled by RCA4. The ensemble mean of downscaled CMIP5 GCM simulations is represented by a black dot, while the coloured dots represents individual downscaled CMIP5 GCMs.

Positive Utah chill units' projections using the ensemble model output of the 9 CMIP5 GCMs downscaled using the RCA4 regional climate model for the RCP 4.5 and RCP 8.5 for both study periods are presented in Fig. 3. The results demonstrate that there is a projected change of positive chill units' accumulation in the Western Cape region. The trend in the spatial map shows that there will be a decreasing trend in areas over the coast with marginal increases over the highlands of the province for both RCPs. For the near future period of 2036 to 2065 the coastal areas of the region will experience a decreasing trend in positive chill units' accumulation with the inland areas which are in the highlands experiencing marginal increasing trends for both RCMs. Most parts of the Western Cape will be expected to experience a decrease in positive chill units' accumulation for the later period (2066 to 2095). However, the simulations show no change in the positive chill units' accumulation for the later period in the highlands of the region and RCP8.5 the highlands show a slight increase in positive chill unit accumulation. Therefore, these changes will have a major effect on the traditional production areas, as some areas will not be suitable for production.

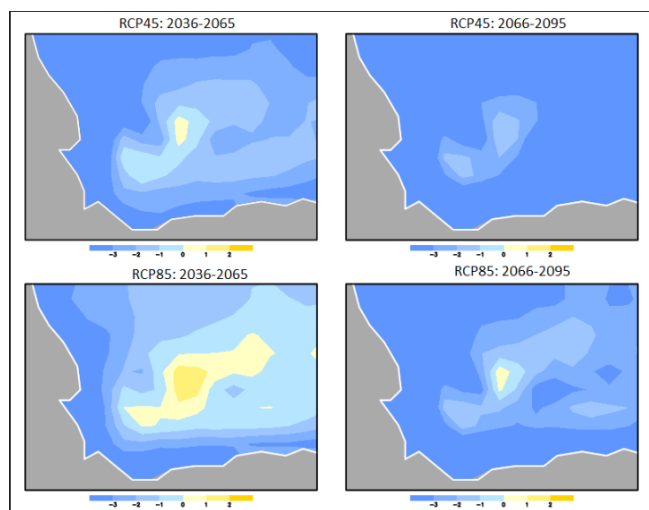


Figure 3: The CORDEX-Africa ensemble average projected changes in chill units over the Western Cape region for 2036-2065 and 2066-2095.

### Conclusion

Climate change is likely to have an effect on the accumulation of chill units in the Western Cape. Deciduous fruit trees' growers are in urgent need of climate change adaptation strategies to reduce losses that the orchards might encounter due to changes in the climate. Due to changes in the climate, many traditional orchards in the region will be affected negatively due to the chilling requirements not being met in these areas. In addition, changes in fruit variety can be proposed to the communities that can still achieve their required chill units' requirements. Therefore, it is critical that more research is conducted at a local level on the impacts of Climate Change on chill units so that stakeholders can be advised properly.

### References

- Ballard, J.K., Proebsting, E.L. & Tukey, R.B., 1987. Apples: Critical temperatures for blossom buds. *Cooperative Extension Bulletin No.0913*. Washington State University, USA.
- Chandler, W.H., 1942. *Deciduous Orchards*. Lea & Febiger, Philadelphia, USA.
- Department of Environmental Affairs & Development Planning, 2016. *State of Environmental Outlook Report for the Western Cape Province*. Stellenbosch, South Africa.
- Engelbrecht, F.A., Landaman, W.A., Engelbrecht, C.J., Landman, S., Bopape, M.M., Roux, B., McGregor, J.L., & Thatcher, M., 2011. Multi-scale climate modelling over Southern Africa using a variable-resolution global model. *Water SA Vol. 37 NO 5*. WRC 40-year Celebration Special Edition, Pretoria, South Africa.
- IPCC, 2007. *Climate Change in 2007 In: Solomon, S., Qin, D., Manning, M., Chen, Z., Marquis, k., Averyt, K.B., Tignor, M., & Miller, H.L. (Eds.). The physical science basis. Contribution of Working Group 1 to the Fourth Assessment Report of the Intergovernmental Panel on Climate Change*. Cambridge University Press, Cambridge, United Kingdom.
- Kruger, A.C., 2004. *Climate of South Africa. Climate Regions. WS45*. South African Weather Service. Pretoria. South Africa.
- Linsley-Noakes, G. C., Allan, P., And Mathee G. W. (1994). Modification of rest completion models for improved accuracy in South African stone fruit. *J. S. Afr. Soc. Hort. Sci.* 4: 13-15.
- Linville, D.E., 1990. Calculating chilling hours and chill units from daily maximum and minimum temperature observations. *HortSci* 25(1): 14-16.
- Luedeling, E., 2012. *Climate change impacts on winter chill for temperate fruit and nut production: A review*. World Agroforestry Centre. Nairobi, Kenya.
- Luedeling, E., Zhang, M., McGranahan, G., & Leslie, C., 2009. Validation of winter chill models using historic records of walnut phenology. *Agric. For. Meteorol.* 149: 1854-1864.
- Middley, S.J.E & Lotze, E., 2011. Climate change in the Western Cape of South Africa: trends, projections and implications of chill unit accumulation. *Acta Hort.* 903: 1127-1134.
- Riahi, K., Rao, S., Krey, V., Cho, C., Chirkov, V., Fischer, G., Kindermann, G., Nakicenovic, N., Rafaj, P., 2011. RCP 8.5-A scenario of comparatively high greenhouse gas emissions. International Institute of Applied Systems Analysis (IIASA). Laxenburg. Austria.
- Taylor, K.E.: Summarizing multiple aspects of model performance in a single diagram. *J. Geophys. Res.*,106, 7183-7192, 2001.
- Thomson, A.M., Calvin, K.V., Smith, S.J., Kyle, G.P., Volke, A., Patel, P., Delgado-Arias, S., Bond-Lamberty, B., Wise, M.A., Clarke, L.E., Edmonds, J.A., 2011. RCP 4.5: a pathway for stabilization of radiative forcing by 2100. Joint Global Change Institute, Pacific Northwest National Laboratory and the University of Maryland. United States of America.
- Vegis, A., 1964. Dormancy in higher plants. *Annu. Rev. Plant Physiol. Plant Mol. Biol.* 15, 185-224.
- WCG., 2013. *State of Environment Outlook Report*. Western Cape Government. South Africa.

## Perceived benefits of hail nowcasts over the Gauteng Highveld (SASAS) 2018

Nisa. Ayob, Roelof. P. Burger and Stuart. J. Piketh

Unit for Environmental Sciences and Management North West University, Potchefstroom,  
2520, South Africa.

### Abstract

Hailstorms are one of the main meteorological phenomena's that signify sources of destruction and damage to property, vehicles, agriculture and infrastructure over the Highveld. This event pose a significant strain to societies and is by far one of the costliest insured natural hazard in South Africa. Nowcasting hailstorms can lead to significant improvement in watches and warnings which is of great practical importance. This study aims to assess the perceived benefits of hail nowcasts and to increase the resilience over the Gauteng Highveld towards hail events. The objectives of this study are two folded: Firstly, to outline the benefits of hail nowcasts used by end-users and secondly, to examine individual's perceptions on hail nowcasts. This was achieved by open-ended interviews to individuals residing within the Gauteng Highveld. It is evident that there are significant benefits in receiving hail nowcasts as well as perceptions as mentioned by different respondents. Nowcasts helps individuals in ensuring the safety of their loved ones. Hence nowcasting hailstorms should be implemented and predicting these storms well in advance may be of use to the public and disaster agencies.

**Keywords:** Gauteng Highveld, Hailstorms, Interviews, Hail nowcasts

### Introduction

Hailstorms are exceptionally hazardous, powerful and destructive meteorological events which cause considerable damage to property, infrastructure, agriculture as well as loss of life Bosco *et al.*, (2015). The amount of damage caused is dependent on the intensity and frequency of the hailstorm event Chantraket *et al.*, (2013). The South African Highveld is typically a home to recurrent occurrences of thunderstorms de Coning and Adam (2000); Gill (2008); Gijben (2012), these storms are frequent during summer during the summer season. Many of these thunderstorms are severe in nature and are related to severe hail, damaging winds, floods and lightning Blamey and Reason (2012).

A disastrous hailstorm in the Gauteng province that occurred on the 28th November 2013 caused an insured loss of over R1.4 billion, hence making it one of the most destructive weather event in the South African insurance history Visser, (2014). This was an example of a classical long-lived hailstorm which in due course travelled into Gauteng and resulted in widespread hail damage, especially in Randburg, where tennis ball sized hail destroyed vehicles and properties as depicted in Fig 1.



Figure 1: Large tennis ball size hailstones cover the ground in Mamelodi on the 28 November 2013. Source: Eye Witness News (ENW), 2013.

Previous research shows a vast amount of studies dedicated to hailstorms, however, unanswered questions remain. Part of the difficulty in advancing our knowledge is the public's perception on hail nowcasts and the maximum benefits received by using nowcasts. Nowcasting is comprised of a full description of current weather conditions attained by extrapolation or nowcast models for a short period of 0 to 2 hours in advance Sun (2012). Nowcasting hail well in advance may act as a powerful tool that can provide benefits to end-users such as: prevent property and vehicle damages, enhance the aviation safety, save lives and support aid agencies Martins *et al.*, (2016). The main aim of this paper is to assess the perceived benefits of hail nowcasts and to increase the resilience over the Gauteng Highveld towards hail events. To achieve this aim, two

primary objectives are followed in this study namely:

1. To examine individual's perceptions on hail nowcasts
2. To evaluate the benefits of hail nowcasts used by end-users

### **Data and methods**

The Highveld is located within the Gauteng, Free State, Mpumalanga and North West province. The Highveld region is notorious to one of the highest rates of thunderstorms in addition to lightning within Southern Africa. Common incidences of severe thunderstorms may consist of large hail, strong damaging winds as well as lightning and flash floods SAWS (2013). This is an explorative study in building end-to-end comprehension from general weather knowledge through to the perceived socio-economic benefits which will aid in guiding investment decisions and product development for SAWS for example; numerical modelling, what nowcast information to provide and when to provide it given limited resources.

### **Methods of data collection**

#### **Interviews**

To conduct interviews the most applicable sampling technique was found to be the non-probability sampling method. Snowball sampling was chosen because these objectives are mainly explorative, qualitative and descriptive. A state-of-the-art method for developing and pretesting interview questions were used. The interview was developed to examine several themes related to these objectives, including: demographics, general weather knowledge, hail warning communication and socio-economic benefits of hail nowcasts. Numerous questions that appeared in the interviews were drawn from previous studies that investigated tornado perception and response in the United States (e.g. Lazo *et al.*, 2009) and Sherman-Morris (2010). The interview script was ordered into four segments:

#### A) Demographics

The purpose of this section was to understand the interviewee's socio-demographic profile. The core aim of these set of questions was to collect statistics on characteristics for example, their gender, age, income group, education background and residential suburb etc. which are known to influence risk propensity, decision making as well as social vulnerability (Silver, 2012).

#### B) General weather knowledge

The questions in this segment were intended to gain an insight of how interviewees perceived general weather and used weather products such as: hail warnings. Considering where, when and how frequent different end-users obtain nowcasts is fundamental to understand the best possible way to supply them with such information. One aspect of how people use nowcasts was assessed namely: for what decisions or activities nowcasts are used. The findings will yield valuable insight into how and why individuals use hail nowcasts.

#### C) Hail warning communication process

The questions in this section was to understand how interviewees gained, interpreted and distributed important information before a hail warning.

#### D) Perceived benefits of hail nowcasts

One of the key thrusts of this objective was understanding the socio-economic value of hail nowcasts which is vital for policy analysis as well as for making decisions about priorities for nowcast delivery. Interviewee's were asked to define what role nowcasts played in the short and long-term recovery process as well as to what typical time scales do they need as an early warning. They were further asked if they valued hail nowcasts. Hail nowcasts are of utmost importance since people's activities are affected by severe hail events. Hence these nowcasts are considered exceptionally valuable.

### **Interview recruitment**

Four potential subjects in the population were identified who resided in different suburbs within the Gauteng province. Thereafter, those potential subjects were asked to recruit other people or to encourage people to come in for a short interview. This was repeated until the necessary sample size was found. All interviews conducted as a part of this study took the form of semi-structured discussions that followed a script, however still acceptable for flexibility and spontaneity of inquiry. The interviews commenced on the 1<sup>st</sup> of October 2017 and were completed on the 5<sup>th</sup> of December 2017. During this period a total of 30 participants were interviewed from different suburbs in Gauteng. These sample sizes are reliable with other studies on hazard perception that incorporated in-person interviews (e.g. Donner 2007). The interviews varied in length from less than 25 minutes to over 40 minutes, with most interviews lasting approximately 35 minutes. It was conducted at a location and time that was accessible and convenient for the participants as well as the student researcher.

### Data analysis

The interviews were first transcribed and then analyzed using thematic analysis to note response patterns within the interview transcripts. The information was analyzed using techniques similar to those defined by McCormack (2000), whereby transcripts are revised numerous times to pick up patterns from different ‘lenses’ (such as context, narration and language). The interviews were formatted for analysis in LibreOffice Calc. LibreOffice Calc was used to determine percentage frequencies and averages as well as to document relationships between variables and across respondent groups using cross-tabulation.

### Results and discussion

The main aim of these interviews was to gain an understanding into the different perceptions and experiences of how individuals perceived benefits of hail nowcasts prior to a hailstorm event. The interviews were also intended to gain an insight of how interviewees obtained and used weather products such as: hail warnings.

The sample consisted of 12 females and 18 males. 30% of the interviewees were categorized in the 40-45-year group whereas, 20% were 45-50years old. In terms of education status, 43% of the participants had a bachelor’s degree with the minority of a PhD and a diploma. 27% of the individuals indicated that they had an honours degree. The residences of the participants were well diverse and included suburbs such as: Soweto; Johannesburg; Roodepoort; Sandton; Randburg; Midrand; Kempton Park; Benoni; Rosebank; Krugersdrop; Randfontein and Boksburg.

The interviewees were further asked how much they earn per month. The monthly household income for the participants ranged from <R10000 to >R30000 with a median value of R15000. 44% of the participants earned a monthly income between R15000-R20000 followed by R20000-R25000 per month. The racial composition was dominated by African 47% followed by 30% of the White participants.

It was found that majority of the participants checked forecasts and identified themselves as ‘weather enthusiasts’. 75% of the interviewees reported they received general weather forecasts in the mornings. This is consistent with results reported in the next section, which shows that several participants used forecasts for deciding on what to wear or daily activities as shown in Fig 2. Most of the respondents obtained weather forecasts from

mass sources (television and radio). Interestingly, majority of the interviewees were unaware of the South African Weather Service (SAWS) website, therefore the most convenient way in receiving this information was from mass sources. Furthermore, interviewees checked weather forecasts for pragmatic reasons (e.g., deciding on what to wear). Lastly, 42% of the respondents stated that an SMS would be the most preferred way of communication in receiving hail nowcasts, followed by social networks such as: Facebook or Twitter.

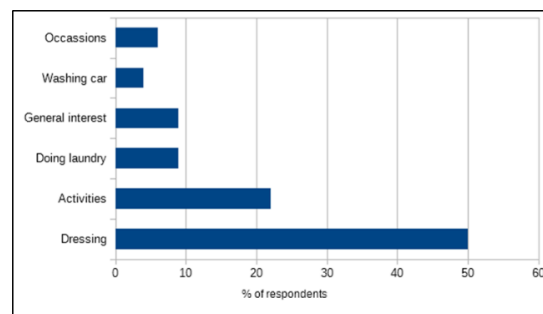


Figure 2: Interviewees were asked why they check the weather forecast.

As expected, majority of the respondents were worried and concerned about severe hailstorms, due to the amount of damage it can bring. It was clear that the respondents were interested in nowcasts because it can minimize costs and damages. It was evident that most of the interviewees received hail warnings, whereas some of them hardly received any warning. Majority of the respondents mentioned that they receive warnings through their insurance company. Interviewees further reported that they would prefer to receive hail warnings as soon as possible. Interviewees were asked at which time intervals they would prefer to receive hail warnings. 61% of the respondents reported that they would prefer at least between 0-2 hours in advance as depicted in Fig 3. Whereas, 23% mentioned they prefer 3-5 hours because they need time to prepare for the hailstorm. Additionally, these results are comparable to other studies such as Ewald and Guyer, (2002). Simmons and Sutter (2008) found that as warnings in advance increases, morbidity drops in a linear manner. Surprisingly, 70% of the respondents reported that they would rather be over warned of hailstorms although it might be a false alarm.

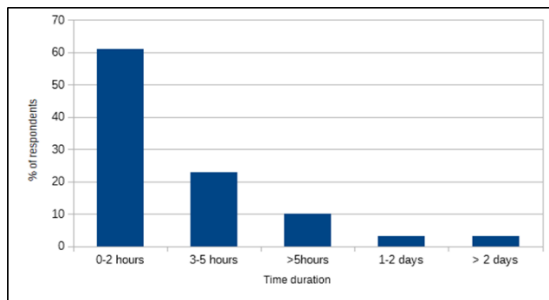


Figure 3: Interviewees were asked at which time intervals they would prefer to receive hail warnings.

80% of the interviewees explained they would save money and they would be relieved if they were prepared for hail events. The majority of the interviewees valued hail warnings and their reasons for valuing warnings varied from individual to individual. They further explained that hail nowcasts can help them in saving money and to cut on unnecessary costs such as damaged vehicles, properties etc. Nowcasts will also help them in ensuring the safety of their loved ones. Interestingly, few interviewees mentioned that it could help city officials in making sure the drainage systems are well organized thus reducing floods caused by severe storms. As expected, most of the interviewees agreed to pay a fee in order to receive hail nowcasts directly from SAWS, however, only if it was affordable. Lastly, 17% of the respondents did not agree into paying a fee because their insurance company does that.

### Conclusions

Hailstorms are meteorological phenomena of great importance and signify one of the main sources of destruction and damage to property, vehicles, agriculture and infrastructure over the Highveld. The main aim of this paper was to assess the perceived benefits of hail nowcasts through interviews. Most of the respondents obtained weather forecasts from mass sources and checked weather forecasts for pragmatic reasons. As expected, majority of the respondents were worried and concerned about severe hailstorms, due to the amount of damage it can bring. 70% of the interviewees reported that they would rather be over warned of hailstorms although it might be a false alarm. Nowcasts helps individuals in ensuring the safety of their loved ones. Interestingly, it was found that hail nowcasts could help city officials in making sure the drainage systems are well-organized thus reducing floods caused by severe storms. It is evident that there are significant benefits in receiving hail nowcasts as mentioned by different respondents, such as: saving end-users from damage

to their property or vehicle, saving lives, reduced damage costs and planning ahead of hailstorms. It can clearly be seen that there is a pressing need for nowcasting, however, the scope and feasibility remains unanswered.

### References

- Bosco, L.C. et al. (2015). Apple production and quality when cultivated under anti-hail cover in southern Brazil. *International Journal of Biometeorology*. 59:773-782.
- Chantraket, P. et al. (2013). Radar reflectivity derived rain-storm characteristics over Northern Thailand. *Environment Asia*. 6:24-33.
- De Coning, E. and Adam, B. (2000). The tornadic thunderstorm events during the 1998-1999 South African summer. *Water SA*. 26:361-376.
- Donner, W. R. (2007). An integrated model of risk perception and protective action: public response to tornado warnings. Doctoral dissertation, Department of Sociology: University of Delaware.
- Ewald, R. and Guyer, J. L. (2002). The ideal lead-time for tornado warnings—a look from the customer’s perspective. Publications, Agencies, and Staff of the U.S. Department of Commerce, Paper 39.
- Lazo, J. K., Morss, R. E. and Demuth, J. L. (2009). 300 Billion Served: sources, perceptions, uses, and values of weather forecasts. *Bulletin of the American Meteorological Society*. 90:785-798.
- Martins, J.A. et al. (2016). Climatology of destructive hailstorms in Brazil. *Journal of Atmospheric Research*. 184:126-138.
- McCormack, C. (2000). From interview transcript to interpretative story: Part 1, viewing the transcript through multiple lenses. *Field Methods*. 12:282-297.
- Silver, A. (2012): Factors influencing individual’s decision making during high risk short notice disasters: the case study of the August 21<sup>st</sup>, 2011, Goderich, Ontario tornado. M.Sc. thesis: University of Waterloo.
- Sherman-Morris, K. (2010). Tornado warning dissemination and response at a university campus. *Natural Hazards*. 52:623-638.
- Simmons, K. and Sutter, D. (2008). Tornado warnings, lead times, and tornado causalities: an empirical investigation. *Weather and Forecasting*. 23:246-258.

South African Weather Service, (2013). Standard Work Instructions (SWI): Weather Related Alerts. Pretoria, South Africa. IS09001 Document reference: FCAST-SWI- Weather Related Alerts-002.0.

Sun, J., Xue, M. D., Wilson, J. W. and Zawadzki, I. (2014). Use of NWP for nowcasting convective precipitation: recent progress and challenges. *American Meteorological Society*. 52:409-426.

Visser, P. (2014). The insurance institute of South Africa-Breakfast Session on “HAIL”, IISA Insurance Forum Presentations, May 2014, The Insurance Institute of South Africa, Hyde Park, Gauteng.

# Temperature anomalies over South Africa during El Niño Modoki and conventional El Niño.

Rakhee Lakhraj-Govender

School of Environmental, Water and Earth Sciences, Tshwane University of Technology, Pretoria, South Africa,

## Abstract

This study investigates the influence of El Niño Modoki and conventional El Niño events on maximum ( $T_{\max}$ ) and minimum temperature ( $T_{\min}$ ) anomalies across 15 stations in South Africa during peak (austral summer) and decaying (autumn) phases of El Niño over the period 1979-2016. For austral summer,  $T_{\min}$  at Zurbekom and  $T_{\max}$  at Cape Columbine record significant differences for El Niño Modoki and conventional El Niño, using Student's t-test. Notably during austral autumn, stations recording significantly different  $T_{\max}$  for conventional and El Niño Modoki events occur over the northern (Messina) and central interior (Marico, Zurbekom and Kimberley) regions of South Africa.

**Keywords:** Teleconnection, Ocean-atmospheric interaction, El Niño Modoki and conventional.

## Introduction

El Niño-Southern Oscillation (ENSO) is a large-scale ocean-atmospheric phenomenon, which alternates between the warm phase (El Niño) and the cold phase (La Niña). ENSO is a primary driver of seasonal to interannual temperature variability over Southern Africa (Archer *et al.*, 2018). The destructive environmental and socio-economic impacts of ENSO (such as drought during strong El Niño events (e.g. 1982/1983, 1991/1992 and 2015/2016) and floods during La Niña events (e.g. 1999/2000, 2010/2011)) over southern Africa emphasizes the increased need to understand ENSO's influence over this region (Landman *et al.*, 2015). Extensive work has been undertaken to develop seasonal forecasting systems over southern Africa based on ENSO for rainfall (e.g. Landman and Beraki, 2012) and temperature (Klopper *et al.*, 1998; Lazenby *et al.*, 2014).

In a departure from forecasting models, observational studies demonstrated the role of the Kalahari Desert and ENSO in producing extreme maximum surface air temperature ( $T_{\max}$ ) over southern Africa during late austral summer for the period 1960-2013, using empirical orthogonal function analysis (Manatsa and Reason, 2017). Also for austral summer, Lakhraj-Govender and Grab (2018) record an increasing influence of El Niño on  $T_{\max}$  through time (1940-1978 compared to 1979-2016), with the strongest responses to El Niño occurring over the central and northern interior regions of South Africa for the period 1940-2016, using composite analysis (Lakhraj-Govender and Grab, 2018). Multiple studies (Larkin and Harrison, 2005; Lakhraj-Govender and Grab, 2018) conclude that since the 1976/1977 ENSO climatic shift, recent decades are more reliable indicators for seasonal forecasting.

In addition to the conventional El Niño (also known as canonical, cold tongue or eastern Pacific), a number of studies detect a change in the frequency of El Niño Modoki (also known as Central Pacific or dateline El Niño) for more recent decades (Radenac *et al.*, 2012). El Niño Modoki (pseudo-El Niño) are unique warming events with a zonal tripole pattern,

different from conventional El Niño, with cold sea surface temperatures (SSTA) centres on both sides (east and west) of the warm centre along the equator (Ashok *et al.*, 2007; Kug and Jin, 2009). During conventional El Niño, large SSTA are evident in the Niño-3 region while SSTA are confined to Niño-4 region during El Niño Modoki (Kug and Jin, 2009). The strength and the frequency of El Niño Modoki has almost doubled over the period 1980-2010 (Lee and McPhaden, 2010) and is expected to continue to increase under global warming (Yeh *et al.*, 2009; Liu *et al.*, 2017). Ashok *et al.* (2007) suggest that the increased frequency and persistence of ENSO Modoki in recent decades may be a result of a recent weakening of equatorial easterlies associated with weakened zonal sea surface temperature (SST) gradient resulting in a flattened thermocline.

As a result of the distinctive SSTs during conventional and ENSO Modoki, the associated atmospheric responses are expected to be different (Kug and Jin, 2009). Different impacts of conventional and El Niño Modoki on weather and climate have been reported both globally (Larkin and Harrison, 2005; Banholzer *et al.*, 2014) and regionally (Li *et al.*, 2011; Yuan and Yang, 2012). However, studies investigating the impact of El Niño Modoki on temperature over South Africa are largely limited or simply do not exist. Therefore, the main aim of this paper is to compare temperature anomalies during peak and decaying phases of conventional El Niño with those of El Niño Modoki events. This is expected to increase our understanding of ENSO's influence on temperature over South Africa for the period 1979-2016 and provide results to increase the accuracy of seasonal forecasts, thereby improving disaster management preparedness.

## Method

$T_{\max}$  and minimum temperature ( $T_{\min}$ ) data were obtained from South African Weather Services (SAWS) for the period 1979-2016. This period was selected because El Niño Modoki events rarely occurred prior to 1980 and became more frequent thereafter (Yuan and Yang, 2012). Monthly temperature

anomalies were computed by subtracting the mean for the base period 1961-1990.  $T_{max}$  and  $T_{min}$  were detrended using differencing, to remove the long-term trend. Austral summer was computed by averaging December, January and February (DJF) temperature anomalies (Lakhraj-Govender and Grab, 2018). Here DJF 1979 refers to December 1978, January 1979 and February 1979. This study examines austral summer and austral autumn (average of March, April and May) because the El Niño events reach peak intensity in summer. In addition, the maximum SSTs anomalies were largely different for El Niño Modoki and conventional El Niño events during the decaying phase (austral autumn) (Paek *et al.*, 2017).

Multiple methods are used to classify the different types of El Niño events. A considerable amount of disagreement exists in the literature on how to distinguish between different types of ENSO events. This study uses events identified by two studies: 3 conventional El Niño (1982–1983, 1991–1992, 1997–1998) and 6 El Niño Modoki (1986–1988, 1990–1991, 1992–1995, 2002–2003, 2004–2005, 2006–2007) El Niño events, identified by Singh *et al.*, (2011). Liu *et al.* (2017) classify 2015/2016 El Niño as a Modoki event.

Composites are used to identify the common features of the different types of ENSO events (Li *et al.*, 2011). The two-tailed Student's t-test was employed to determine if the temperature composites during conventional El Niño years are significantly different from those during El Niño Modoki years.

## Results and Discussion

Conventional El Niño and El Niño Modoki events have different convection patterns and atmospheric responses (Mo, 2010). During peak conventional El Niño, positive SST anomalies are observed from the South American coastline to the equatorial Pacific while the SSTs during peak El Niño Modoki are situated in the central Pacific, which are smaller in magnitude (Hu *et al.*, 2016). Therefore, the different types of El Niño events are expected to produce different impacts on weather. Temperature anomalies associated with conventional and El Niño Modoki events display marked differences across the globe (Larkin and Harrison, 2005). Globally, conventional El Niño years display significantly warmer temperatures compared to the remaining years (Banholzer *et al.*, 2014). Similarly, the results of the current study display different responses to conventional and El Niño Modoki events across different regions of South Africa during austral summer and autumn.

During austral summer,  $T_{max}$  anomalies are insignificantly warmer for El Niño Modoki years compared to the conventional El Niño years at northern stations (Skukuza, Messina, Warmbaths and Marico). In contrast, central interior stations (Vryburg, Glen College, Kimberley and Zuurbekom) record warmer  $T_{max}$  anomalies during conventional El Niño years compared to El Niño Modoki years (Table 1). Similarly, in South America during austral summer, above average temperatures were recorded during conventional El Niño

events while average or marginally above average temperatures were reported during El Niño Modoki events, being less extreme than those for conventional El Niño events (Li *et al.*, 2011). With the exception of  $T_{min}$  at Zuurbekom and  $T_{max}$  at Cape Columbine, the temperature anomalies at the remaining stations are not significantly different during El Niño Modoki years compared to those during conventional El Niño years, as determined by Student's t-test (Table 1).

During austral autumn (representing the decaying phase of El Niño events; Table 2), the number of stations with significantly different temperature anomalies (associated with the conventional and El Niño Modoki events) increased compared to that during austral summer (representative of developing phase; Table 1). This indicates that  $T_{max}$  anomalies during conventional El Niño and El Niño Modoki events on are more prominent during the decaying El Niño phase. During austral autumn,  $T_{max}$  anomalies are significantly different during El Niño Modoki events compared to those during conventional El Niño years at Messina, Marico, Zuurbekom and Kimberley (Table 2). With the exception of Glen College and Kimberley, the remaining northern and central interior stations record warmer  $T_{max}$  anomalies during conventional El Niño events compared to El Niño Modoki events. An example of the  $T_{max}$  anomalies during El Niño Modoki, conventional El Niño events and neutral years at the Kimberley station over the period 1979-2016 is provided in Figure 1. With the exception of Marico, Vryburg and Glen College, the remaining stations record warmer  $T_{min}$  anomalies associated with conventional El Niño years compared to El Niño Modoki events. Different  $T_{max}$  and  $T_{min}$  responses to El Niño events have been previously reported and explained (see Lakhraj-Govender and Grab, 2018). Further investigations are required for the Western Cape region because two of the stations (Cape Columbine and SA Astronomical Observatory) display weak insignificant ( $p=0.09$  and  $0.08$ , respectively)  $T_{max}$  differences when comparing El Niño Modoki with conventional El Niño events during austral autumn (Table 2).

Table 1:  $T_{max}/T_{min}$  anomalies during conventional and El Niño Modoki events for austral summer over the period 1979-2016.

Station name	Conventional El Niño		El Niño Modoki		p-values for Student's t-test	
	$T_{max}$	$T_{min}$	$T_{max}$	$T_{min}$	$T_{max}$	$T_{min}$
	Skukuza	1.28	0.23	1.54	0.65	0.72
Messina	1.11	0.77	1.32	0.61	0.71	0.86
Warmbath	1.28	0.23	1.96	0.32	0.48	0.62
Marico	1.42	0.13	2.44	0.39	0.08	0.62
Vryburg	2.05	0.22	1.13	0.60	0.36	0.59
Zuurbekom	1.61	-2.56	1.45	-0.86	0.13	<b>0.03</b>
Glen College	2.21	0.14	1.60	0.67	0.49	0.56
Kimberley	2.02	0.87	1.51	0.56	0.53	0.36

Cape Columbine	-0.19	0.53	0.51	0.18	<b>0.02</b>	0.21
Cape Agulhas	-0.28	-0.23	0.16	-0.01	0.14	0.42
SA Astronom.	0.08	0.10	0.00	-0.08	0.89	0.62
East London	0.65	-0.12	0.31	0.46	0.29	0.18
Port Elizabeth	0.53	-0.11	0.44	0.26	0.70	0.43
Cedara	0.68	0.46	1.38	0.24	0.31	0.62
Mount						
Edgecombe	0.01	-0.03	0.49	0.25	0.10	0.40

Table 2:  $T_{max}/T_{min}$  anomalies during conventional and El Niño Modoki events associated for austral autumn over the period 1979-2016.

Station	Conventional		El Niño		Student's t-test	
	$T_{max}$	$T_{min}$	$T_{max}$	$T_{min}$	$T_{max}$	$T_{min}$
Skukuza	1.88	1.23	1.24	0.94	0.36	0.37
Messina	2.35	1.50	0.13	-0.18	<b>0.00</b>	<b>0.06</b>
Warmbath	0.79	-1.56	0.10	-2.02	0.22	0.80
Marico	2.08	0.39	0.23	0.41	<b>0.03</b>	0.95
Vryburg	2.02	0.08	1.52	0.09	0.33	0.99
Zuurbekom	2.04	0.38	0.04	0.08	<b>0.03</b>	0.34
Glen College	0.48	-0.42	0.86	0.30	0.71	0.38
Kimberley	2.02	0.87	1.51	0.56	<b>0.04</b>	0.40
Cape Columbine	-0.18	0.10	0.25	0.09	0.09	0.97
Cape Agulhas	0.30	0.37	0.69	0.27	0.18	0.66
SA Astronom	-0.08	-0.15	0.59	0.19	0.08	0.34
East London	0.74	0.35	0.83	0.26	0.72	0.76
Port Elizabeth	0.43	0.00	0.66	-0.30	0.44	0.39
Cedara	1.49	0.68	0.99	0.84	0.43	0.73
Mount Edgecombe	1.31	0.61	0.95	0.30	0.37	0.46

Bold=Significant

Given the destructive nature of the impacts of ENSO events on South African climate, the results of this study, further studies are required to determine the impact of El Niño Modoki events on extreme temperatures and rainfall across South Africa. These studies are expected to improve seasonal forecasts and assist with disaster preparedness.

### Conclusions

Despite the limited number of stations to represent the different regions, this study provides important information with regard to the influence of conventional El Niño and El Niño Modoki events on temperature across South Africa. For austral summer, only  $T_{min}$  at Zuurbekom and  $T_{max}$  at Cape Columbine record significant differences during El Niño Modoki compared to conventional El Niño events, using Student's t-test. For austral autumn,  $T_{max}$  anomalies during El Niño Modoki events are significantly different compared to those during conventional El Niño events at Messina, Marico, Zuurbekom and Kimberley stations in South Africa. This indicates that the differences between  $T_{max}$  anomalies associated with the two types of El Niño events are more prominent during the decaying El Niño phase.

Bold=Significant

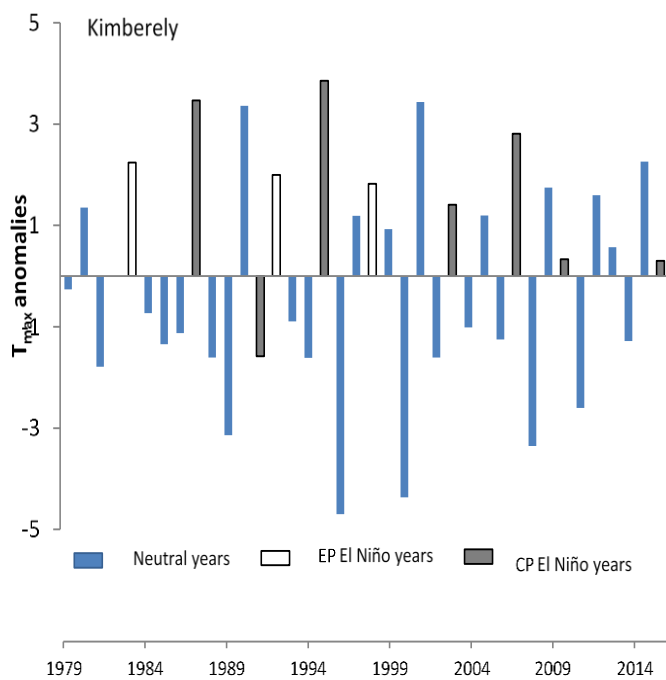


Figure 1: Detrended  $T_{max}$  anomalies for El Niño Modoki and conventional El Niño events during austral autumn at Kimberley over the period 1979-2016.  $T_{max}$  anomalies associated with El Niño Modoki events are significantly different compared to conventional El Niño years, determined by Student's t-test.

One of the limitations of this study is the uncertainties produced by composites, given that stronger events may overpower weaker events (Mo, 2010). An additional limitation is the classification of ENSO events into two broad categories while each ENSO event is actually unique (Paek *et al.*, 2017). In addition, numerous studies are investigating new methods to classify ENSO events resulting in different criterion used to select the events (Jeong *et al.*, 2017). For instance, Liu *et al.* (2017) classify the 2015/2016 El Niño as a Modoki event because maximum SST warming was observed in the central Pacific. In contrast, Paek *et al.* (2017) suggest that the 2015/2016 event may be a mixture of conventional and El Niño Modoki.

## Acknowledgements

Thank you to South African Weather Services for the temperature data. Thank you to the Departmental Committee for Postgraduate Studies (DCPS) at the Department of Environmental, Water and Earth Science (Tshwane University of Technology) for providing funds to attend the conference.

## References

1. Archer, E., Engelbrecht, F., Hänsler, A., Landman, W., Tadross, M. and Helmschrot, J. (2018). Seasonal prediction and regional climate projections for southern Africa. In: *Climate change and adaptive land management in southern Africa – assessments, changes, challenges, and solutions* Revermann, R., Krewenka, K.M., Schmiedel, U., Olwoch, J.M., Helmschrot, J. and Jürgens, N. (Eds.), *Biodiversity & Ecology*, 6, Klaus Hess Publishers, Göttingen & Windhoek, pp. 14-21, doi:10.7809/b-e.00296.
2. Ashok, K., Behera S.K., Rao S.A., Weng H, Yamagata T. (2007). El Niño Modoki and its possible teleconnection. *Journal of Geophysical Research* 112:C11007, doi:10.1029/2006JC003798
3. Banholzer, S. and Donner, S. (2014). The influence of different El Niño types on global temperature. *Geophysical Research Letters*. 41:2093-2099, doi:10.1002/2014GL059520.
4. Hu, X., Yang, S. and Cal, M. (2016). Contrasting the eastern Pacific El Niño and the central Pacific El Niño: process-based feedback attribution. *Climate Dynamics*. 27:2413-2424.
5. Klopper, E., Landman, W.A. and van Heerden, J. (1998). The predictability of seasonal maximum temperature in South Africa. *International Journal of Climatology*. 18: 741-758.
6. Kug, J.-S. and Jin, F.-F. (2009) Two types of El Niño events: cold tongue El Niño and warm pool El Niño. *Journal of Climate*. 22:1499-1514.
7. Lakhraj-Govender, R. and Grab, S. (2018). Assessing the impact of ENSO on South African temperatures during austral summer. *International Journal of Climatology*. (online). doi.org/10.1002/joc.5791.
8. Landman, W.A. and Beraki, A. (2012). Multi-model forecast skill for mid-summer rainfall over southern Africa. *International Journal of Climatology*. 32: 303–314.
9. Landman, W.A., Barnston, A.G. and Vogel, C. (2015). Ranking seasonal rainfall forecast skill of emerging and developing economies. 31st Conference of the South African Society for Atmospheric Science: Applying the weather, Hennops River Valley, Centurion, South Africa, 21-22 September 2015.
10. Larkin, N.K. and Harrison, D.E. (2005). Global seasonal temperature and precipitation anomalies during El Niño autumn and winter. *Geophysical Research Letters*. 32: L16705, doi:10.1029/2005GL022860.
11. Lazenby, M.J., Landman, W.A., Garland, R.M. and de Witt, D.G. (2014). Seasonal temperature prediction skill over South Africa and human health. *Meteorological Applications*. 21:963-974.
12. Lee, T. and McPhaden, M.J. (2010). Increasing intensity of El Niño in the central-equatorial Pacific. *Geophysical Research Letters*. 37: 1-5, doi:10.1029/2010GL044007.
13. Li, W., Zhang, P., Ye, J., Li, L. and Baker, P.A. (2011). Impact of two different types of El Niño events on the Amazon climate and ecosystem productivity. *Journal of Plant Ecology*. 4:91-99.
14. Liu, Y., Cobb, K.M., Song, H., Li, Q., Li, C., Nakatsuka, T., An, Z., Zhou, W., Cai, Q., Li, J., Leavitt, S.W., Sun, C., Mei, R., Shen, C., Chan, M., Sun, J., Yan, L., Lei, Y., Ma, Y., Li, X., Chen, D. and Linderholm, H.W. (2017). Recent enhancement of central Pacific El Niño variability relative to last eight centuries. *Nature Communications*. doi: 10.1038/ncomms15386
15. Manatsa, D, Reason C. (2017). ENSO–Kalahari Desert linkages on southern Africa summer surface air temperature variability. *International Journal of Climatology*. 37: 1728-1745.
16. Mo, K.C. (2010). Interdecadal modulation of the impact of ENSO on precipitation and temperature over the United States. *Journal of Climate*. 23:3639-3656.
17. Paek, H., Yu, J.-Y. and Qian, C. (2017). Why were the 2015/2016 and 1997/1998 extreme El Niño different? *Geophysical Research Letters*. 44: doi:10.1002/2016GL071515.
18. Radenac, M-H., Léger, F., Singh A. and Delcroix T. (2012). Sea surface chlorophyll signature in the tropical Pacific during eastern and central Pacific ENSO events. *Journal of Geophysical Research Letters*. 117:C04007 doi:10.1029/2011JC007841.
19. Singh, A., Delcroix, T., and Cravatte S. (2011). Contrasting flavors of El Niño-Southern Oscillation using surface salinity observations. *Journal of Geophysical Research*. 116: 1-16.
20. Yeh, S-W., Kug, J-S., Dewitte, B., Kwon, M-H., Kirtman, B.P. and Jin F-F. (2009). El Niño in a changing climate. *Nature*. 461: 511-515.
21. Yuan, Y. and Yang, S. (2012). Impacts of different types of El Niño on the East Asian Climate: Focus on ENSO cycles. *Journal of Climate*. 25: 7702-7722.



**Data and Methods**

Ideally, for the forecast technique developed in this paper, sugarcane yield was supposed to be used as a ‘target’ for prediction but this could be misleading. Sugarcane has a long-cycle of 12-18 months, which implies depending on a number of factors other than climate.

Thus, summer (December-March) Palmer Drought Severity Index (PDSI) was used as ‘target’ for prediction and a proxy for sugarcane yield. PDSI data was obtained from KNMI climate explorer, and it is precipitation minus potential evaporation from station-based data. All climatic data were obtained from KNMI climate explorer.

Predictors of sugar-PDSI were selected using signal and determinants of remote influences such as Sea Surface Temperature (SST) patterns. Monthly NOAA reconstructed SST4 is interpolated to 1° and it is based on data from ship, buoys and infrared satellites.

Allan and Ansell (2006) described the Sea Level Pressure (SLP) data employed in this study which was computed from HadSLP2 reanalysis interpolation system.

Era-interim data for both meridional flow, (V component) and zonal wind (U component) was employed as predictor candidates for sugar-PDSI. The atmospheric levels examined include 850 and 200 hPa, respectively.

Sugarcane yield data was obtained from Food and Agriculture Organisation (FAO) of the United Nations (UN). South African and Swaziland yields were combined into one sugar index, this was made by use of the total annual productions.

Prior spring (August-November) predictor candidates were extracted from correlation maps with respect to December-March PDSI for the period 1980-2014. The duration of the rainy season over southeast southern African is from December-March (Mbhama *et al.* 2017). A step-wise multi-variate and cross correlation were performed, and less influential predictor candidates were eliminated until a final model was reached with the least number of predictors.

The model was screened to check for over-fitting and co-linearity between predictor candidates. The multi-variate algorithm should have a standardised coefficient for each predictor of value < 1 and be of the same sign as the pair-wise association.

**Results and Discussion**

The results presented in this section were obtained using the methodology outlined above, and correlation search maps derive from globally gridded data. Subsequently, predictor candidates were selected from those which reveal significant correlations, and the results are presented below.

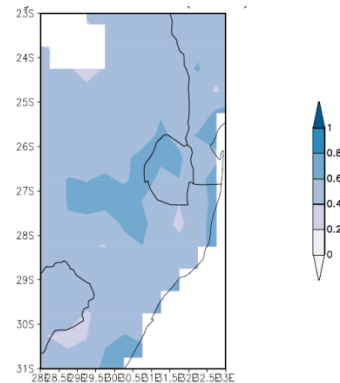


Figure 2: Correlation of Dec-May PDSI and sugarcane yield in southeastern southern Africa for the period 1970-2014.

The study found a strong positive correlation ( $r \geq \pm 0.5$ ) between annual sugarcane yield and preceding year PDSI (Fig. 2), this implies that negative December-March PDSI is characterised by suppressed yield in the next season. Hence, the necessary assumption is that: owing to the significant correlation (Fig. 2), PDSI could be a good proxy for sugarcane yield.

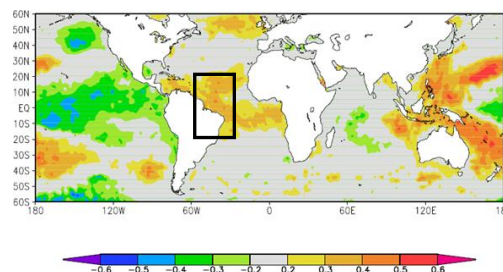


Figure 2: Aug-Nov year-1 SST correlated with Dec-Mar PDSI covering the adjacent oceans for the period 1980-2014. Predictors selected are shown by boxes.

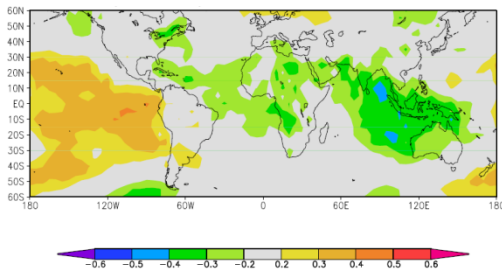


Figure 3: Correlation of year-1 Aug-Nov SLP with Dec-Mar sugar PDSI, to assess ENSO influence in sugar yield prediction.

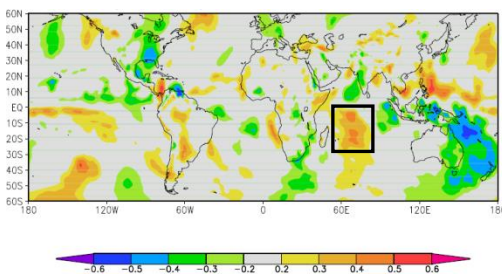


Figure 4: Meridional wind for Aug-Nov year-1 (V 850 hPa) correlation against Dec-Mar sugar PDSI. Box shows the predictor selected.

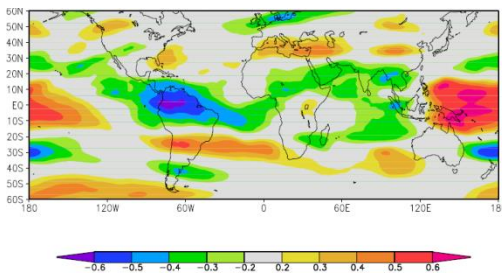


Figure 5: Zonal wind (U 200 hPa) correlated with PDSI, which is a predictor and proxy of sugarcane yield.

The statistical correlations suggest the influence of both local and global climate on sugar (Figs. 2, 3 and 6). When SSTs are cooler and SLP is increased in the Pacific Ocean, the next year will be characterised by increased sugarcane yield.

The model was then developed and the predictors were screened according to the method described in this study under methods section, and the predictor candidates are defined below.

Table 1: Geographical boundaries of year-1 Aug-Nov predictor-candidates for southeast southern Africa averaged Dec-Mar PDSI (23-31°S; 28-33°E).

Predictor	Parameter	Area-averaged	Boundaries (lat. long)
SST1	sea surface temperature	East Pacific Ocean	15°S-15°N; 120-80°W
SST2	sea surface temperature	West Atlantic Ocean	20°S-20°N; 45-60°W
SST3	sea surface temperature	Indonesia	5°N-20°S; 80-120°E
SST4	sea surface temperature	SW Indian Ocean	15-30°S; 60-70°E
SLP1	sea level pressure	West Indian Ocean	30°S-5°N; 60-90°E
SLP2	sea level pressure	East Pacific Ocean	30°S-5°N; 120-80°W
V1	meridional wind (850 hPa)	West Indian Ocean	0°Eq-25°S; 50-80°E
V2	meridional wind (850 hPa)	Southern Ocean	35-60°S; 50-40°E
V3	meridional wind (850 hPa)	East Australia	10-25°S; 140-160°E
U1	zonal wind (200 hPa)	Amazon	15°S-15°N; 50-100°W
U2	zonal wind (200 hPa)	West Pacific Ocean	15°S-15°N; 180-120°W
U3	zonal wind (200 hPa)	Northern Australia	10°S-20°N; 120-180°E

Table 2: Pair-wise correlation for screening predictor candidates

	SST1	SST2	SST3	SST4	SLP1	SLP2	V1	V2	V3	U1	U2	U3
SST1												
SST2	<b>0.89</b>											
SST3	<b>0.49</b>	0.12										
SST4	0.21	0.24	0.04									
SLP1	0.09	<b>0.40</b>	<b>-0.53</b>	-0.15								
SLP2	0.24	0.29	-0.18	0.12	<b>0.51</b>							
V1	-0.11	-0.31	<b>0.54</b>	-0.39	-0.27	-0.24						
V2	-0.11	-0.18	0.18	<b>0.40</b>	-0.24	-0.02	-0.09					
V3	0.04	0.36	<b>-0.57</b>	0.30	<b>0.53</b>	0.34	<b>-0.63</b>	0				
U1	0.09	0.38	<b>-0.63</b>	0.02	<b>0.59</b>	0.18	<b>-0.65</b>	-0.18	<b>0.52</b>			
U2	-0.18	0.10	<b>-0.56</b>	-0.14	<b>0.50</b>	-0.07	-0.24	-0.20	0.20	<b>0.76</b>		
U3	0.16	-0.26	<b>0.72</b>	-0.14	-0.64	-0.12	<b>0.51</b>	-0.02	<b>-0.79</b>	<b>-0.63</b>	<b>-0.52</b>	
PDSI	-0.15	-0.37	<b>0.51</b>	-0.03	-0.33	-0.25	<b>0.66</b>	0.22	<b>-0.57</b>	<b>-0.61</b>	-0.25	<b>0.46</b>

Most predictors show significant influence but co-linearity observed in Table 2, suggest that they must be removed from the multi-variate regression analysis. Only SST2 and V1 we fitted in the model. The model output is illustrated in the next page (Table 3).

Table 3: Representation of the model output summary

Regression Statistics				
Multiple R	0.69			
R Square	0.47			
Adj R Square	0.44			
Standard Error	0.73			
Observations	34			
ANOVA				
	df	SS	MS	F
Regression	2.00	14.81	7.40	13.91
Residual	31.00	16.49	0.53	
Total	33.00	31.30		
	Coefficients	Standard Error	t Stat	P-value
Intercept	0	0.13	-7.40	2.50E-08
SST2	-0.18	0.13	-1.37	1.80E-01
V1	0.58	0.13	4.43	1.10E-04

From the technique employed, the multi-variate regression equation is given by: December-March

sugar PDSI =  $-0.18(\text{SST2}) + 0.58(\text{V1})$  using August-November predictors. Therefore, these two predictors have the teleconnections SST2 -0.18 and V1 +0.58, and predicted sugar-PDSI accounts for 47% of the variance for the observed PDSI. The model created is significant for prediction of PDSI (proxy for sugarcane yield) since it has an adjusted R Square of 0.44. Positive value of PDSI in year-1 indicates increased summer rainfall, and sugarcane could grow well while negative sugar-PDSI might be characterised by warm and dry weather condition that could be detrimental to sugarcane.

### **Conclusions**

Palmer Drought Severity Index (PDSI) is given by precipitation minus potential evaporation. There is a significant positive correlation ( $r \geq +0.5$ ) between PDSI and sugarcane yield over southeast southern Africa.

During Pacific El Niño, trade winds weaken and sugarcane yield diminishes in the upcoming season. La Niña is linked to cooler SST patterns in southwest Indian Ocean and cooler warmer in the Atlantic Ocean, which positively benefit the growth of sugarcane.

The model created in this study is statistical significant and it could be used in seasonal climate forecasting and crop modelling. Hence, sugarcane growers can inform their decisions based on this forecast technique.

### **Acknowledgements**

I wish to thank Prof. Mark R. Jury of the University of Puerto Rico (supervisor), Dr. Nkanyiso B. Mbatha and Dr. Nozipho M. Motsa of the University of Zululand (co-supervisors), for their inputs to make this study a success. I also acknowledge the work done by KNMI climate explorer and FAO for archiving data that was used in this research.

### **References**

Allan, R. and Ansell, T., 2006. A new globally complete monthly historical gridded mean sea level pressure dataset (HadSLP2): 1850–2004. *Journal of Climate*, 19(22), pp.5816-5842.

Chikoore, H., 2017. Drought in Southern Africa: structure, characteristics and impacts. PhD thesis, Department of Geography and Environmental Studies, University of Zululand.

Gbetibouo, G.A. and Hassan, R.M., 2005. Measuring the economic impact of climate change on major South African field crops: a Ricardian approach. *Global and Planetary Change*, 47(2-4), pp.143-152.

Jury, M, R., 2002. Economic impacts of climate variability in South Africa and development of resource prediction models. *Journal of Applied Meteorology*, 41, pp.46–55.

Kew.org, 2018. *Saccharum officinarum* (sugar cane). Plants and Fungi at Kew. Available online at: <http://www.kew.org> (viewed 13 May 2018).

Khan, M.T., Seema, N., Khan, I.A. and Yasmine, S., 2017. Applications and potential of sugarcane as an energy crop. *Agricultural Research Updates*. Nova Science Publishers, USA, pp.1-24.

Mbhamali, T.W., Jury, M.R., Motsa, N.M. and Mbatha, N.B., 2017. Climate impacts on sugarcane yield in the eastern part of southern Africa, Proc. of 33rd Annual conference of South African society for atmospheric sciences, ISBN 978-0-620-77401-7, 21-22 September 2017, Polokwane, Limpopo (South Africa), pp. 58-61.

## ***Exploring the predictability of lightning-caused wildfires in the Western Cape***

Serafini, ACC<sup>1\*</sup>, du Preez DJ,<sup>2</sup> Landman WA<sup>1</sup> and Wright CY<sup>1,3</sup>

<sup>1</sup>Department of Geography, Geoinformatics and Meteorology, University of Pretoria, Pretoria.

<sup>2</sup>South African Weather Services.

<sup>3</sup>Environment and Health Research Unit, South African Medical Research Council, Pretoria.

\* Email: [aimeeserafini@gmail.com](mailto:aimeeserafini@gmail.com)

### ***Abstract***

The Western Cape comprises land area that consists of vegetation that is susceptible to ignition and typically experiences their fire season during their dry summers. Cross validation and retroactive probability forecasting were used to investigate any predictability in lightning-caused wildfires by exploring the relationship between lightning wildfire occurrence and meteorological variables during December through February from 1980-2012 for the Western Cape. Merged variables outperformed single variables by showing the most predictive skill. Precipitable water, relative humidity at 925 hPa and V-wind at 925 hPa performed best as single variables and as merged data sets.

*Keywords: Wildfire, Lightning-caused fire, Canonical Correlation Analysis, Western Cape*

### ***Introduction***

Lightning is one of the six main causes of wildfires within the Western Cape (Western Cape Government, 2017). It is also, possibly, one of the most dangerous because, unlike other wildfire ignition causes, lightning can ignite fires in areas that are remote which makes detection and extinction difficult (Read et al., 2018). Lightning-caused fires usually burn for longer periods of time and may be widespread before they are extinguished (Podur et al., 2002). These types of wildfires usually occur during severe thunderstorms and dry thunderstorms. Both types of thunderstorms are often associated with strong winds which makes aerial extinction resources redundant (Nieto et al., 2012).

Lightning generation requires a mixture of positively charged ice particles and negatively charged graupel particles to be present during the development of a cumulonimbus (thunderstorm cloud). In general, positive charges gather below the cloud and follow it. The large charge difference within the cloud and between the cloud and ground results in an electrostatic discharge commonly known as "lightning" (Frenkel, 1947). There are four types of lightning: intra-cloud - the connection of charge within the cloud; inter-cloud - the connection of charge between two separate clouds; air discharge - links the main negative charge within a cloud with a small area of positive charge lower down in the cloud, and cloud-to-ground - the connection of charge between the ground and the cloud. South Africa has one of the world's highest ground flash densities, accounting for 10% of the daily global statistic. However, the Western Cape has a relatively low ground flash density, ranging from 0.1-1 flashes per kilometre along the coast and interior, increasing to 2-3 and 3-4 flashes per kilometres over the north-eastern parts of the province (Gijben, 2012).

Although many wildfires in the Western Cape are caused by people, lightning fires also occur and are a cause for concern for fire management agencies (Read et al., 2018). Lightning fire ignition can be attributed to three processes: the occurrences of cloud-to-ground lightning strikes, ignition caused by the strike

and the ignited flame surviving long enough to be detected (Anderson, 2002). If a lightning strike occurs, fuel moisture and weather conditions determine whether ignition will occur and if the flame can be sustained until detection. For the flame to be sustained fuel sources must be continuous (Read et al., 2018). Meteorological variables that are directly related to lightning occurrence and fire growth and indirectly related to fuel moisture include temperature, relative humidity, wind speed and precipitation. While strong correlations between these weather conditions and lightning-caused wildfires have been demonstrated (Read et al., 2018) there is still a great deal that is unknown about the likelihood of ignition during a season.

The aim of this study is to investigate the relationship between lightning-caused wildfires and various meteorological variables over the Western Cape, South Africa during the summer season (December, January and February). This study will test the meteorological variables' relationship with the lightning data to determine which variables perform best.

### ***Data and Methods***

#### ***Study Area***

The Western Cape (Fig. 1) is located on the South Western coast of South Africa and is the fourth largest province. The dominant vegetation is Fynbos and Renosterveld; both species are very susceptible to fires because they require burning for growth and regeneration (Privett, 2011). The climate along the coast is Mediterranean with hot, dry summers and cool, wet winters and average summer (winter) temperatures ranging between 15 - 27°C (5 - 22 °C)



Figure 1: Map indicating the study area and SANParks within the study area (red dots).

(Botai et al., 2017). The province has three dominant rainfall areas: the winter rainfall region (the Cape Peninsula and Cape Winelands), the late summer rainfall region (the Great Karoo) and year-round rainfall regions (includes areas along the southern coast) (Botai et al., 2017). Average annual rainfall ranges from approximately 300 mm to greater than 900 mm; some areas receive as much as 3345mm and as little as 60mm (Botai et al., 2017). Due to hot and mostly dry summer conditions, wildfires are more prevalent in the Western Cape during the summer months of December, January and February (DJF).

*Lightning Fire Data*

The occurrences of fires caused by lightning are extracted from a fire occurrence database compiled by Cape Nature. The lightning data for this study covered all seven South African National (SAN) Parks within the Western Cape (Fig. 1) (South African National Parks, 2018). The fire data have been recorded by park managers for many decades. Since the very early data records are less reliable, the data used in this study dates to 1980. The raw data consists of polygons of the mapped extent of the fires that occurred. The extent of the fires was measured by park rangers using field mapping techniques. These mapped areas were then combined with other attribute fields such as the date on which the fire occurred and the cause of the fire (van Wilgen et al., 2010). The raw data records were converted into a specific format recognised by the Climate Predictability Tool (CPT). Data from 1993 was missing.

*Meteorological Data*

Monthly, averaged National Oceanic and Atmospheric Administration (NOAA) National Centres for Environmental Prediction (NCEP) Climate Data Assimilation System (CDAS)-I meteorological data sets are obtained from the International Research Institute for Climatology and Society (IRI) archives. The data are for the 32-year period (1980-2012) for the Western Cape’s summer months and fire season of DJF. The data is at 2.5-degree horizontal resolution and a 6-hour

*Results and Discussion*

Table 1: List of variables and variable merges showing correlation, significance and ROC scores. The best predictor variables and merges are indicated by an \*.

Meteorological Variable/s	Unit	Pressure level (hPa)	Pearson Correlation	Spearman Correlation	p-value	ROC Score (above-normal)	ROC Score (below-normal)
---------------------------	------	----------------------	---------------------	----------------------	---------	--------------------------	--------------------------

temporal resolution. The data are created using a forecast system that performs data assimilation using past data from 1980 to present, for the DJF period.

*Methods*

Each meteorological data set is averaged over the three-month period of DJF from 1980-2012. The averaged data set is analysed separately for a correlation with the lightning fire data using Canonical Correlation Analysis (CCA). CCA was chosen because it finds the optimum combination of predictor data that shows the most variance in the predictand (Barnett and Preisendorfer, 1987); with the meteorological variables as predictors and lightning data as the predictand. The analysis is done using a 32-year training period and using 9 modes (which is the maximum number of modes usable with a training period of 32 years). The advantage of using 9 modes is that no potentially useful information about the predictors is excluded (Barnett and Preisendorfer, 1987). For each variable, cross validation is performed. The SST data domain covers the Equatorial Pacific Ocean: 5° N to 5° S and 170° W to 130° W. For consistency 9 modes are used for the SST data, although the maximum number of modes for a domain of that size is 26. By restricting the number of modes, as in the case with SSTs, it ensures that no false correlation is created. From the cross validation, the variables that exhibit the highest Spearman and Pearson correlations are deemed the best predictors and further investigation is done using these variables. The best predictor variables will then undergo significance testing (p-value) indicating the probability that the sample score would be improved by chance. These variables are then merged using various combinations to determine whether correlation improved when two of the best predictor variables were combined. Merging data sets within CPT does not average the variables but rather stacks the data sets.

Retroactive probability forecasts are performed using the variables deemed the best predictors, using an 8-year initial training period. This is done to show discrimination between above-normal and below-normal lightning-fire seasons and explore the probabilities and reliability of forecasts. Forecast probabilities and skill are explored using Receiver Operating Characteristic (ROC) scores. A ROC score value of a category must be above 0.5 for the forecast to be considered skillful. There is usually very little skill to be determined from predicting the near-normal category (Landman et al., 2012) therefore, in this study, that category is ignored. Reliability of forecast probabilities are investigated using attribute diagrams following framework described by Hsu and Murphy (1986); a comparison of the straight-line curves and the perfect reliability line for each variable in each category is used to show over- and under-forecasting. The variables are merged again using the same combinations as before to determine whether the reliability and discrimination are improved when two of the predictor variables, previously deemed the best, are merged.

Precipitable water*	kg/m <sup>2</sup>	n/a	0.439	0.511	0.012	0.492	0.389
Relative humidity*	%	925	0.524	0.422	0.001	0.527	0.317
Relative humidity	%	1000	0.346	0.340	n/a	n/a	n/a
U-wind	m/s	925	0.132	0.147	n/a	n/a	n/a
V-wind*	m/s	925	0.548	0.423	0.001	0.527	0.456
SSTs over the Equatorial Pacific Ocean*	°C	n/a	0.260	0.327	0.167	0.585	0.283
Surface Pressure	hPa	n/a	0.345	0.329	n/a	n/a	n/a
Mean sea level pressure	hPa	n/a	0.338	0.310	n/a	n/a	n/a
Temperature	°C	925	0.286	0.328	n/a	n/a	n/a
Temperature	°C	1000	0.291	0.332	n/a	n/a	n/a
Precipitable water-relative humidity merge*	kg/m <sup>2</sup> and %	925 (relative humidity)	0.503	0.581	0.012	0.515	0.422
V-wind-precipitable water merge*	kg/m <sup>2</sup> and m/s	925 (V-wind)	0.535	0.615	0.002	0.646	0.444
V-wind-relative humidity merge*	% and m/s	925	0.636	0.550	0.000	0.550	0.394

After cross validation, it is evident that precipitable water, relative humidity at 925hPa and V-wind showed the highest correlation with the lightning data and are therefore deemed the best predictors (Table 1). SSTs, although they do not outperform other variables, will undergo further investigation based on the findings presented by Chen et al., (2016). Highly correlated merges included precipitable water-relative humidity, V-wind-precipitable water and V-wind-relative humidity. All merge correlations outperform all single variable correlations (Table 1).

The ROC scores for relative humidity, V-wind and SSTs show skill in the above-normal category (Table 1). The above-normal ROC scores for the variable merges perform better than the single variable ROC scores. The below-normal category scores, in all cases, displays little to no skill (Table 1).

For precipitable water, the above-normal category attributes diagram shows over-confidence when making forecasts (Figure 2). In contrast, the relative humidity above-normal attributes diagram shows under-confidence when making forecasts (Figure 3). The V-wind-precipitable water merge attributes diagram for above-normal outperforms all other variables in all categories, with forecasts showing over-confidence (Figure 4). All other attribute diagrams for all other variables and variable merges show little to no skill (not shown). The above-normal category in each of the above-mentioned cases (Figures 2, 3, and 4) shows forecast probability of approximately 45%. This value, being greater than 33% (a climatological forecast that uses three equiprobable categories), indicates a degree of reliability.

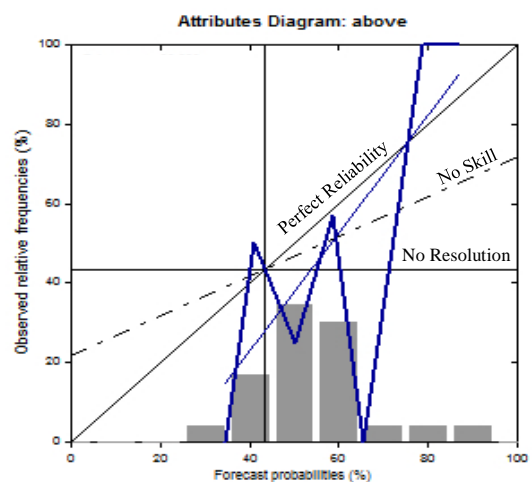


Figure 2: The above-normal attribute diagram for precipitable water with the perfect reliability, no skill and no resolution lines indicated.

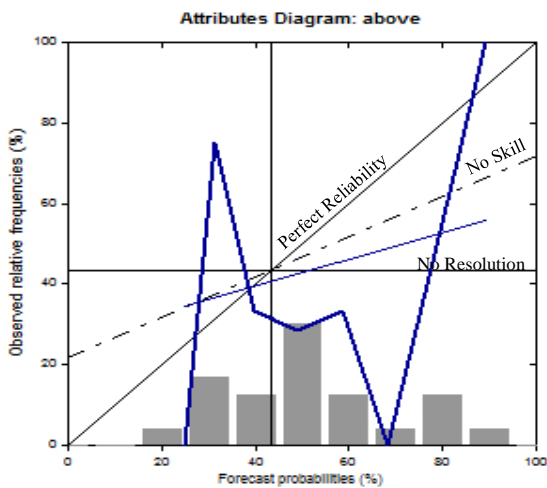


Figure 3: The above-normal attribute diagram for relative humidity with the perfect reliability, no skill and no resolution lines indicated.

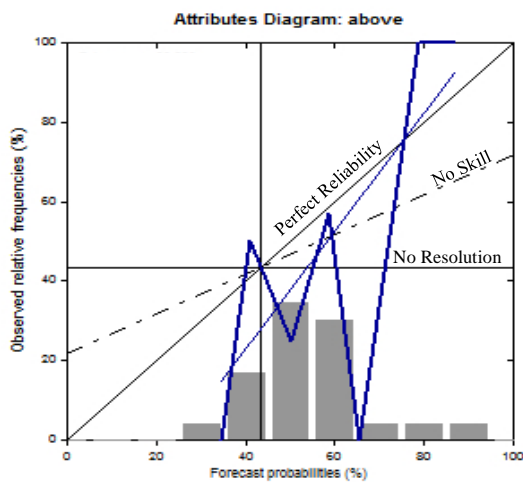


Figure 4: The above-normal attribute diagram for the V-wind-precipitable water merge with the perfect reliability, no skill and no resolution lines indicated.

### Conclusion

Precipitable water and relative humidity show the highest correlation with lightning fires. Merged variables outperform all single variables in terms of correlations, with the V-wind-relative humidity merge showing the highest overall correlations. All single and merged variables display at least 90% significance with the V-wind-relative humidity merge showing the highest level of significance, outperforming all other variables and merges. This shows that all correlations are reliable. It is demonstrated that three of the four single variables were skillful predictors of lightning fire occurrence, only in the above-normal category. All variable merges show some predictive skill in the above-normal category, with the V-wind-precipitable water merge showing the most skill. The above-normal category forecasts show sharpness that can be interpreted as a degree of reliability of the forecasts.

Managers of SANParks within the Western Cape could benefit from skillful forecasts of lightning-caused wildfires, as it could help with early preparation and decision-making. It is recommended that this research contribute toward the creation of a prediction model to assist in the prediction of lightning-caused wildfires by using the demonstrated best performing single and merged variables (precipitable water, relative humidity, V-wind, the V-wind-relative humidity

merge and the V-wind-precipitable water merge) as data sets sourced from a global model.

### References

- Anderson, K. (2002). A model to predict lightning caused fire occurrences. *Int. J. Wildland Fire*. 11:163–172.
- Barnett, T.P. and Preisendorfer, R. (1987). Origins and Levels of Monthly and Seasonal Forecast Skill for United States Surface Air Temperatures Determined by Canonical Correlation Analysis. *Monthly Weather Review*. 15:1825-1850
- Botai, C.M., Botai, J.O., de Wit, J.P., Ncongwane, K.P. and Adeola, A.M. (2017). Drought Characteristics over the Western Cape Province, South Africa. *Water*. 9:876
- Chen, Y., Morton, D.C., Andela, N., Giglio, L. and Randerson, J.T. (2016). How much global burned area can be forecast on seasonal time scales using sea surface temperatures? *Environ. Res. Lett.* 11: 045001
- Frenkel, J. (1947). Atmospheric electricity and lightning. *Journal of the Franklin Institute*. 243(4): 287-307
- Gijben, M. (2012). The lightning climatology of South Africa. *South African Journal of Science*. 108(3/4).
- Hsu, W. and Murphy, A.H. (1986). The attributes diagram A geometrical framework for assessing the quality of probability forecasts. *International Journal of Forecasting*. 2:285-293.
- Landman, W.A., DeWitt, D., Lee, D.E., Beraki, A. and Lotter, D. (2012). Seasonal Rainfall Prediction Skill over South Africa: One- versus Two- Tiered Forecasting Systems. *Weather and Forecasting*. 27:489-501.
- Nieto, H., Aguado, I., García, M. and Chuvieco, E. (2012). Lightning-caused fires in Central Spain: Development of a probability model of occurrence for two Spanish regions. *Agricultural and Forest Meteorology*. 162(3): 35-43
- Privett, S. 2011. *Fynbos and Fire*. [Online] Available at: <http://www.fynboshub.co.za/fynbos-and-fire/>. [Accessed 08 03 2018]
- Read, N., Duff, T.J. and Peter G. Taylor, P.G. (2018). A lightning-caused wildfire ignition forecasting model for operational use. *Agricultural and Forest Meteorology*. 253(4):233-246
- South African National Parks, 2018. *Explore Parks*. [Online] Available at: <https://www.sanparks.org/parks/> [Accessed 18 06 2018]
- van Wilgen, B.W., Forsyth, G.G., de Klerk, H., Das, S., Read, N., Duff, T.J. and Taylor, P.G. (2018). A lightning-caused wildfire ignition forecasting model for operational use. *Agricultural and Forest Meteorology*. 253-254: 233-246.
- Western Cape Government, 2017. *Wildfire Season*. [Online] Available at: <https://www.westerncape.gov.za/general-publication/wildfire-season> [Accessed 18 06 2018]

## **Inter-comparison of total column ozone from ozonesonde with the Dobson spectrophotometer measurements from Irene, South Africa: 2012 - 2017.**

**Tshidi Machinini<sup>1</sup> and Gerrie Coetzee<sup>1</sup>**

<sup>1</sup>South African weather service, Eco-glades 1B Eco-park, CnrOlievenhoutboschand Ribbon Grass street, Centurion, 0157, South Africa

Phone: +27-12-367-6240, Email: [tshidi.machinini@weathersa.co.za](mailto:tshidi.machinini@weathersa.co.za)

### **Abstract**

Ozone layer plays an important role as it absorbs most of the ultraviolet (UV) radiation preventing the potentially harmful radiation from reaching the earth's surface. This study assessed similarity of observed total column ozone measurements through inter-comparison of data from ground-based ozone measuring instruments, the Dobson spectrophotometer and balloon-borne ozonesonde over Irene. Root mean square error (RMSE), BIAS and percentage difference were used. RMSE value of 35.1 DU was found with a BIAS of 32.05 DU and the percentage difference showed that the ozonesonde data are lower than the Dobson data mostly by 5-15%. Although the ozonesonde and Dobson measurements follow a similar pattern, the variation between them is slightly high. This was expected as the sonde balloon does not reach through the upper part of the stratosphere.

**Key words:** *Total column ozone, bias, root mean square error, percentage difference.*

### **Introduction**

Ozone is an important but toxic molecular species in the troposphere, but in the stratosphere ozone is important as it absorbs most of the ultraviolet (UV) radiation preventing the potentially harmful radiation from reaching the earth's surface (Bramstedt *et al.*, 2002). Ozone is formed and destroyed in complex non-linear systems of atmospheric chemical reactions, catalysed by various other gases. About 90% of ozone is found in the stratosphere (10 – 50km above the surface), which is referred to as “Good ozone”, and about 10% of ozone is found in the troposphere, and which is sometimes referred to as “Bad ozone” (Fabian & Dameris, 2014).

Detection of stratospheric ozone decline and the expected future recovery requires long-term records of ozone measurements (Fioletov *et al.*, 1999). Various techniques have been developed and utilized to monitor ozone concentrations in the atmosphere over the years. Ozone is monitored worldwide using ground-based and space and airborne measurements. The most commonly used instrumentation to measure total column ozone from the ground is the Dobson and Brewer spectrophotometer (Vanicek, 2006).

Vertical distribution of ozone is critical to our understanding of both photochemical and dynamic processes that are operating in the atmosphere and contributing to the tropospheric ozone budget (Diabet *et al.*, 2003). Balloon-borne ozonesondes play an essential role in monitoring stratospheric and

tropospheric ozone and are also used to validate and improve satellite remote sensing techniques (Thompson *et al.*, 2003). Ozone depletion in the stratosphere increases the ultraviolet and visible radiation reaching the troposphere. Therefore monitoring the total column ozone is important.

The South African Weather Service (SAWS) monitors total column ozone using the Dobson spectrophotometer at Irene D#089 since 1989 and at Springbok D#132 since 1995. These Dobson measurements are supplemented by balloon-borne ozonesondes conducted at Irene station (25.9° S, 28.2° E, 1523m) (illustrated in figure 1) that provides a detailed vertical profile of ozone concentrations throughout the atmosphere. Ozonesondes started at Irene since 1990 using the Vaisala MW15 Digicora and RS80 GPS sondes and 1200g Totex balloons; Irene is also a component of the Southern Hemisphere additional ozonesondes (SHADOZ) network since 1998 (Thompson *et al.*, 2003). Sounding was conducted weekly with a few gaps. The ozone sounding program, after new equipment the MW31 processor and RS92 GPS sondes were purchased, was then reinstated in September 2012 after a three year break. The aim of this study was to assess the similarity of the observed total column ozone data from the ground-based instruments, that is the Dobson spectrophotometer, and ozonesonde data over Irene through inter-comparison of the datasets. Regular validation of ozone measuring instruments on a regular basis will increase reliability of the measurements.

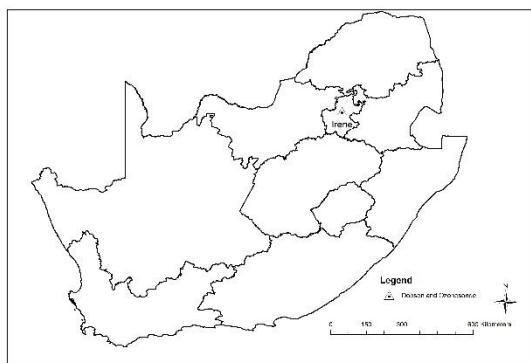


Figure 1: Geographical location of Irene, South Africa

## Instrumentation and methods

Measurements from the ground-based Dobson spectrophotometer and ozonesonde at Irene are used in this study. Daily total column ozone measurements from the Dobson spectrophotometer (D#089) are observed since 1989 and weekly ozonesonde measurements were conducted at Irene since 1990 until 2007 and due to financial limitations the data is characterised with gaps. The ozonesondes measurements were stopped in 2007 and later re-instated again in September 2012. There are three types of measurements that can be taken with the Dobson; the direct sun (DS) made only when there is no obstruction from the clouds, zenith blue (ZB) taken when there is no clouds around the zenith angle and zenith clouds (ZC) taken when there are clouds on the zenith angle. In this study only the DS measurements taken around the sounding release were used for the analysis.

Ozonesondes play an important role in monitoring the stratospheric ozone layer where harmful ultraviolet radiation is absorbed by ozone thus protecting the biosphere (Stolarski, 2002). Ozonesondes measures the ozone profile in the atmosphere by a chemical reaction and a weather balloon carries the sounding instrument from the surface of the earth to 30-35km above the surface. The ozone sensor used within the ozonesonde is an iodine-iodide redox electrochemical concentration cell (ECC), which is interfaced with a radiosonde to transmit the ozone data to the surface. Ozonesonde profiles provide high resolution data throughout the ascent, providing measurements roughly every 10 meters. Ozonesondes measurements are made on a bi-weekly basis on Wednesdays (around 10 am local time).

## Statistical methods

The bi-weekly datasets from the ozonesondes measurements made around 10 am (only soundings that burst above 30 km were used, to homogenise the data) and the corresponding Dobson measurements (average readings within 10 am) between 2012 and 2017 from Irene are used in this study. The inter-comparison based on root mean square error (RMSE), BIAS and percentage difference were used to determine the datasets relationship between the different ozone measurements for ozonesondes and the Dobson spectrophotometer. The Bias is mathematically calculated as:

$$B = \left\{ \frac{1}{N} \sum_{i=1}^n O_{ref} - O_{obs} \right\}$$

The RMSE is defined as:

$$RMSE = \sqrt{\frac{\sum_{i=1}^n (O_{ref} - O_{obs})^2}{n}}$$

The percentage difference is a way of expressing how large a quantity is relative to another quantity. It is given by the formula:

$$Percentage\ difference = \frac{(O_{obs} - O_{ref})}{O_{ref}} \times 100$$

Where,  $O_{obs}$  is the ozonesonde data (observed), while  $O_{ref}$  is the Dobson measurements (reference). A time series analysis was also used in the study, which involved plotting a line graph against time. The time series was used to show the inter-annual variability of the datasets for both the ozonesonde and Dobson spectrophotometer instruments.

## Results and Discussion

Figure 2 below shows the inter-annual variability of ozone over Irene as represented by measurements from the ozonesonde and the Dobson spectrophotometer (only DS) datasets. It can be observed that the ozonesonde and the Dobson follow a similar pattern, with the Dobson being generally greater than the ozonesonde. The inter-comparison of ozonesonde and Dobson (as reference) had a bias of 32.05 with a RMSE value of 35.1. Figure 4 shows that ozone from the soundings are lower than the Dobson, mostly between 5-15% lower than Dobson. On the 25 November 2015 the ozonesonde

measured more ozone than the Dobson. The cause of this higher ozonesonde reading might be as a result of the Dobson's sensitivity, this needs to be investigated further. Thompson *et al.*, 2012, demonstrated that the ozonesonde measurements are lower than the Dobson mostly at 5-10%. Venkataraman and Ogunniyi, (2017) showed that the maximum ozone concentration is found in the altitude between 23-27 km over Irene using the ozonesonde measurements for the period 2004-2007. The bias and the percentage difference are shown in detail in figure 3 and figure 4 below.

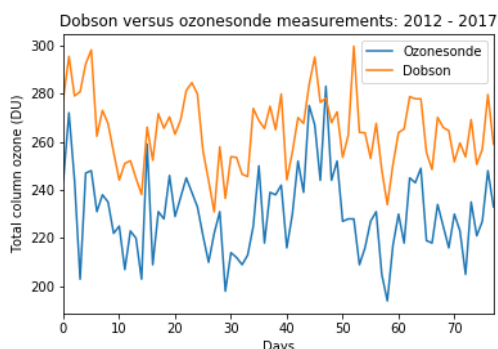


Figure 2: Comparison of ozonesonde and Dobson data over Irene: 2012-2017.

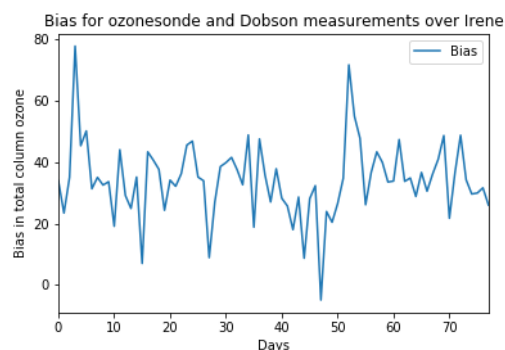


Figure 3: The BIAS for ozonesonde and Dobson ozone measurements over Irene.

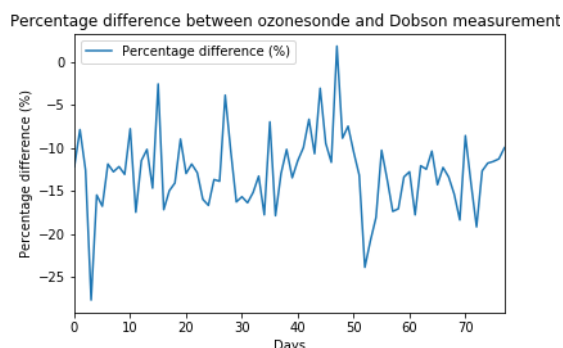


Figure 4: The percentage difference between ozonesonde and Dobson ozone data over Irene.

## Conclusion

The inter-comparison study between ozonesonde and Dobson measurements of total column ozone over Irene shows that the two measurements follow a similar pattern. The percentage difference shows that the ozonesonde measurements are lower than the Dobson measurements mostly by 5-15%. The RMSE, BIAS and the percentage difference values shows a slightly high deviation between the two instruments. Previous studies have shown that the maximum ozone to be found between the altitude 23-27km by the ozonesonde measurements.

## Acknowledgement

The following are thanked for their contribution and help in this study: Irene meteorological technicians for taking Dobson measurements and Mr Gerrie Coetzee for his continued supervision.

## References

- Bramstedt. K.,*et al.*, (2002). Comparison of total column ozone from the satellite measurements GOME and TOMS with measurements from the Dobson network 1996-2000. *Atmos. Chem. Phys. Discuss.* 3, 1409-1419.
- Diab. R. D.,*et al.*, (2003). Classification of tropospheric ozone profiles over Johannesburg based on MOZAIC aircraft data. *Atmospheric Chemistry and Physics discussions*, European Geosciences Union.
- Diab. R. D.,*et al.*, (2004). Tropospheric ozone climatology over Irene, South Africa, from 1990 to 1994 and 1998 to 2002, *J. Geophys. Res.*, 109, D20301.
- Fioletov. V. E.,*et al.*, (1999). An assessment of the world ground-based total ozone network performance from the comparison with satellite data. *J. Geophys. Res.*, 104, 1737 – 1747.
- Fabian. P. & Dameris. M. (2014). Ozone in the atmosphere. Basic principles, natural and human impacts. DOI 10.1007/978-3-642-54099-8\_2
- Thompson. A. M.,*et al.*, (2003). Southern hemisphere additional ozonesondes (SHADOZ) 1998 – 2000 tropical ozone climatology. 2. Tropospheric variability and the zonal wave-one. *J. Geophys. Res.*, 108(D2), 8241.

- Thompson, A. M. *et. Al.* (2012). Southern Hemisphere Additional Ozonesondes (SHADOZ) ozone climatology (2005-2009): Tropospheric and tropical tropopause layer (TTL) profiles with comparisons to OMI-based ozone products. *J. Geophys. Res.*, 117, D23301, doi: 10.1029/2011JD016911. Vanicek, K. (2006). Differences between ground Dobson, Brewer and satellite TOMS-8, GOME-WFDOAS total ozone observations at Hradec Kralove, Czech. Solar and ozone observatory, Czech Hydrometeorological Institute, Hvezdrana 456, 50008.
- Stolarski, R.S.,*et. al.*, (2002). Combined total ozone record from TOMS and SBUV instruments, [http://code916.gsfc.nasa.gov/Data services/merged/mod data.public.html](http://code916.gsfc.nasa.gov/Data/services/merged/mod%20data.public.html).

## Assessment of cloud types over Durban, South Africa, using only day time cloud cover observations: an initial study

P. Govender<sup>1</sup> and V. Sivakumar<sup>1</sup>

<sup>1</sup>School of Chemistry and Physics, University of KwaZulu-Natal, Durban, 4041.

### Abstract

Durban (29.87° S; 30.98° E), situated on the east coast of South Africa, is a location with humid sub-tropical climate that experiences a variety of cloud cover dynamics. This study focuses on analyzing cloud data to investigate the dominant cloud types and the frequency over the Durban area. Analysis of a 3-year (2014-2016) cloud observer record show that the most dominant cloud types were found to be Stratocumulus, Altocumulus (translucidus and altocumulus in two or more layers) and Cirrus in the low, middle and high cloud levels, respectively. Total cloud coverage show that most days in Durban consist of either very clear conditions (0 oktas) or very cloudy/overcast conditions (7 or 8 oktas). Total cloud coverage of 4 and 5 oktas were found to be fairly uncommon for Durban. Knowledge of cloud patterns may contribute to the understanding of climate patterns over Durban.

Keywords: Clouds, Stratocumulus, Altocumulus, Cirrus, Okta

### Introduction

Clouds are an essential component of the Earth-atmosphere system and they have a significant influence on the Earth's hydrological cycle and radiation budget. Therefore, an understanding of clouds is fundamental to understand the Earth's climate (Lohnman *et al.* 2016). A cloud is described by Lohmann *et al.* (2016) as "an aggregate of water droplets or ice crystals, or a combination of both, suspended in air". As described by Rogers and Yau (1989), the existence of clouds is due to the physical process of condensation however, condensation occurs primarily in response to dynamic processes that include widely distributed vertical air movement, convection and mixing. Within a cloud system there can be individual cloud structures or elements of a cloud that can be identified by their shape and size. Their sizes could range from 1 to 100 km in spatial extent and have lifetimes from minutes to hours. Together, they constitute the cloud system. As described by Tapakis and Charalambides, (2013), clouds can also be broadly classified based on their altitude:

- Low level clouds: Cumulus (Cu), Stratocumulus (Sc), Stratus (St), and Cumulonimbus (Cb).
- Mid-level clouds: Altocumulus (Ac), Altostratus (As) and Nimbostratus (Ns).
- High level clouds: Cirrus (Ci), Cirrocumulus (Cc) and Cirrostratus (Cs).

Their composition can be either water droplets (low level clouds), ice crystals (high level clouds) or a combination of both phases mid-level clouds). Measurements of cloud amount are either made automatically i.e. by satellites and ground-based imagers, or from the ground by visual observation. The total cloud amount, or total cloud

cover, is the fraction of the celestial dome covered by all clouds visible (Castro-Almazan *et al.* 2015). The assessment of the total amount of cloud, therefore, consists in estimating how much of the total apparent area of the sky is covered with clouds (WMO, 2008). According to the World Meteorological Organization (WMO), the proportion of cloud amount is given in eighths or oktas as in Table 1, which was used for the present study. Cloud type classification is given according to WMO cloud classification coding system. A description of the codes is given in Table 2. Each category i.e. low, middle and high has a numeric code that corresponds to the cloud type at the time of the observation. For the present study, the cloud types were analyzed to

investigate which are the most common clouds that occur over Durban and their corresponding frequency. In addition, total cloud amounts were also investigated.

Analyzing clouds over a location, in particular the type, frequency and seasonal distribution can assist in the understanding of the local climate and possibly in the design and implementation of efficient solar powered systems. Durban, South Africa (29.87° S; 30.98° E) lies in a region that has been classified as having sub-tropical humid climate and thus significant cloud variation. There are limited studies that have focused on investigating cloud cover patterns over Durban. Shikwambana and Sivakumar (2016) presented a study on cloud observations over Durban using Light Detection and Ranging (LIDAR), however these were night-time measurements conducted for a short period of time, and seasonal distributions and dominant patterns were not investigated. The present study focuses on analyzing cloud types over Durban, in order to investigate cloud patterns, if any, over the region. Knowledge of the dominant cloud types in Durban will assist in the design of efficient solar power systems, and in the general understanding of the local climate.

Table 1: Total cloud amount in oktas and corresponding sky condition, according to WMO standards. Adapted from Castro-Almazan *et al.* (2015).

Oktas	Description of sky condition
0	Completely clear
1	Clear
2	Clear
3	Partly cloudy
4	Partly cloudy
5	Partly cloudy
6	Cloudy
7	Cloudy
8	Overcast

Table 2: WMO cloud classification of cloud types in each category (WMO, 2008).

Code	Low	Middle	High
1	Cumulus	Altostratus translucidus	Cirrus fibratus
2	Cumulus congestus	Altostratus opacus	Cirrus spissatus
3	Cumulonimbus calvus	Alto cumulus translucidus	Cirrus spissatus cumulonimbogenitus
4	Stratocumulus cumulogenitus	Alto cumulus lenticularis	Cirrus uncinus
5	Stratocumulus	Semi-transparent Alto cumulus	Cirrus/Cirrostratus
6	Stratus	Alto cumulus cumulogenitus	Cirrus/Cirrostratus
7	Stratus fractus and Cumulus	Alto cumulus in two or more layers	Cirrostratus covering whole sky
8	Cumulus and Stratocumulus	Alto cumulus castellanus	Cirrostratus not covering whole sky
9	Cumulonimbus	Alto cumulus	Cirrocumulus

\*The reader is referred to WMO manual on the observation of clouds and other meteors (WMO, 1975) for a detailed description of the cloud observation procedures and specific cloud genera, species and varieties in each cloud level.

**Instrumentation and Method**

The cloud data used for this study was provided by the South African Weather Service (SAWS). Cloud observations including the type and amount used for this analysis was obtained from the meteorological station located at the Durban, King Shaka Airport (29.61° S; 31.11° E) and was recorded by a weather observer. Daily cloud observations were recorded at 08:00, 14:00 and 20:00 (SAST), for a period of 3 years (2014-2016) i.e. a total of 1095 days, and which includes both wet and dry periods. For the purpose of this study, we have restricted the analysis to day-time readings only, since this is the most useful period for the operation of solar powered systems and the time during which clouds interact with the incoming solar irradiance, hence affecting the performance of these systems.

**Results and Discussion**

Cloud observations during 08:00 and 14:00 for each cloud level i.e. low middle and high were analyzed, and Table 2 was used to find the description of the cloud type in the corresponding level. Fig. 1 and Fig. 2 show the frequency of occurrence for cloud type in the low cloud level at 08:00 and 14:00, respectively. For low level clouds at both these times, the most dominant type was found to be stratocumulus (i.e. code 5). This is consistent with the findings presented in Shikwambana and Sivakumar (2016) where low level clouds were classified as stratocumulus. Although the study by Shikwambana and Sivakumar (2016) was based on night-time measurements, they are still in agreement with the findings of the present study that only involved day-time measurements. In addition, the present study found that stratocumulus clouds occur most frequently during the months of October, November and December. Stratus occurs as the second most frequent low cloud type in the

morning, however cumulus occurs most frequently in the afternoon.

Fig. 3 and 4 show the frequency of occurrence for middle cloud types at 08:00 and 14:00, respectively. Both mornings and afternoons are dominated by cloud codes 3, 7 and 8 corresponding to Alto cumulus translucidus, Alto cumulus and Alto cumulus castellanus types. All months almost equally experience Alto cumulus translucidus and Alto cumulus cloud types during 08:00 and 14:00. Mid-level clouds of Alto cumulus castellanus type have a fairly low frequency of occurrence during all months, but tend to show a slight increase in the afternoon.

Fig. 5 and 6 show the frequency of occurrence for high cloud types at 08:00 and 14:00, respectively. Cirrus fibratus and cirrus spissatus are the most frequently occurring cloud types in the mornings and afternoons. The occurrence of Cirrostratus is more prevalent during the afternoon than in the morning. In the afternoon, cirrus uncinus and cirrus/cirrostratus show almost equal frequency.

Overall, the most dominant cloud types were found to be Stratocumulus, Alto cumulus (translucidus and Alto cumulus in two or more layers) and Cirrus in the low, middle and high cloud levels, respectively. In the mornings and afternoons, Stratocumulus clouds comprise 53% and 60% of days, respectively. For middle clouds at 08:00, 26% of days are distributed across Alto cumulus translucidus, Alto cumulus and Alto cumulus castellanus types. At 14:00, the proportion of days with the same distribution is reduced to 20%. For high clouds in the mornings, 23% of days are distributed across Cirrus fibratus, Cirrus spissatus and Cirrostratus. High clouds in the afternoon follow a similar distribution with almost equal proportion of days i.e. 26%.

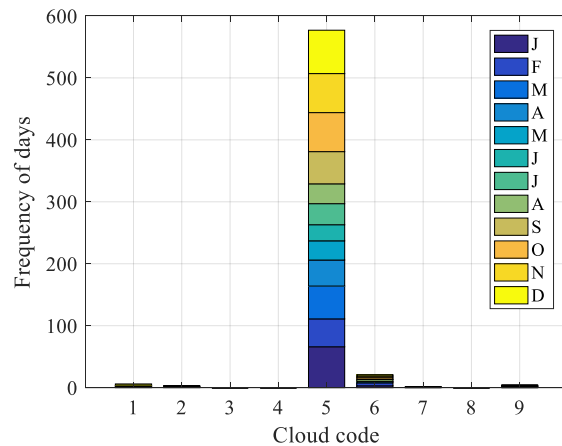


Figure 1: Frequency of days for low cloud level for each cloud code at 08:00.

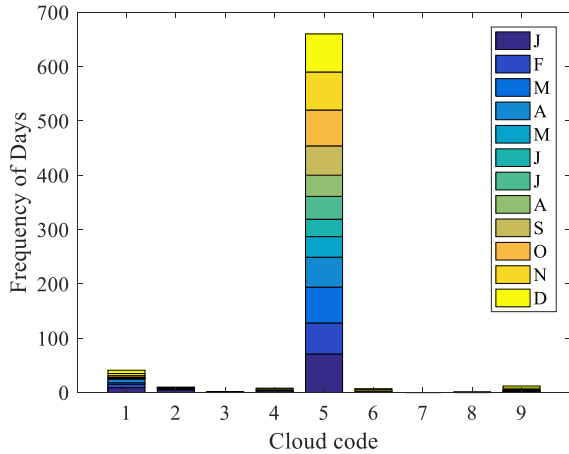


Figure 2: Frequency of days for low cloud level for each cloud code at 14:00.

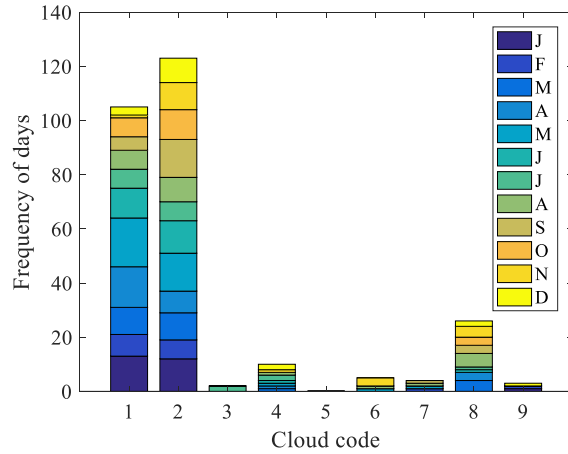


Figure 5: Frequency of days for high cloud level for each cloud code at 08:00.

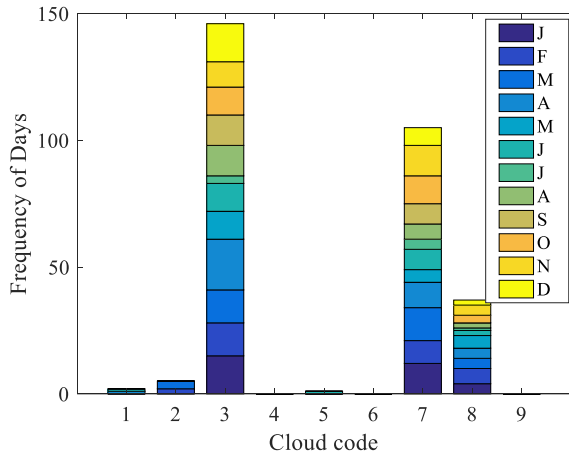


Figure 3: Frequency of days for middle cloud level for each cloud code at 08:00.

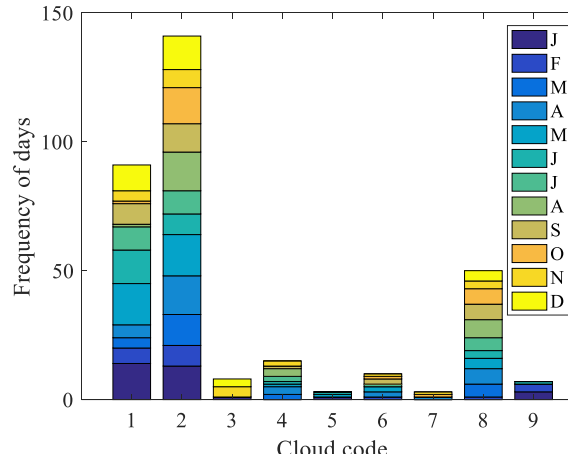


Figure 6: Frequency of days for high cloud level for each cloud code at 14:00.

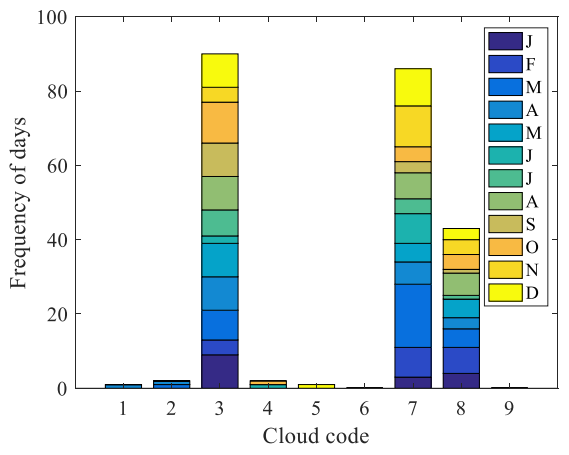


Figure 4: Frequency of days for middle cloud level for each cloud code at 14:00.

Annual Total Cloud Cover (TCC) is presented in Fig. 7 and Fig. 8 for 08:00 and 14:00, respectively. Approximately 11% of days across all months have a total cloud coverage of 4 and 5 Oktas for the morning and afternoon, respectively. This suggests that morning and afternoon sky coverage, where half the sky or slightly less than half the sky is obscured by clouds, is fairly uncommon for Durban. Cloud types and their frequency were analyzed over Durban for a period of 3 years. This study showed that the dominant cloud types were found to be Stratocumulus, Altopumulus (translucidus and Altopumulus in two or more layers) and Cirrus in the low, middle and high cloud levels, respectively. In addition, June-July were found to be the clearest months (lowest TCC), while March, October-December were found to be the most cloudy (highest TCC).

In the mornings, 57% of days have either 0, 7 or 8 Oktas of cloud cover, indicating that Durban experiences a majority of very clear or very overcast/cloudy sky conditions. This is consistent with the study presented by Govender *et al.* (2018), where daily solar irradiance levels were classified as either very high or very low, corresponding to sunny and overcast/cloudy conditions, respectively.

Months that had the most number of days with a TCC of zero Oktas were June and July, which indicates that these months comprised

mostly sunny days. Durban experiences most cloudiness during the months of March, October, November and December.

In the afternoons, 12% of days have 4 or 5 oktas of cloud cover, while 88% of days are distributed across 0, 1, 2, 3, 6, 7 and 8 oktas. This shows that Durban has larger variation of cloud cover in the afternoons as compared to the mornings. Afternoons show an increase in days that have either 1, 2, 3 or 4 oktas of cloud cover as compared to mornings, and which are fairly evenly distributed across all months.

**Conclusion**

This study analyzed cloud observations to investigate dominant cloud types over Durban. Based on the 3-year period (2014-2016), the most dominant cloud types were found to be Stratocumulus, Altostratus (translucidus and Altostratus in two or more layers), and Cirrus in the low, middle and high cloud levels, respectively.

However, there may be some variation between the years. Total cloud coverage showed that most days in Durban consist of either very clear conditions (0 oktas) or very overcast/cloudy conditions (7 or 8 oktas). Total cloud coverage of 4 and 5 oktas were found to be fairly uncommon for Durban. The results of this study contribute to the understanding of the dominant cloud types and the associated climate patterns in Durban. Future work will include investigating the irradiance levels associated with the dominant cloud types, as this would assist in the design and implementation of efficient solar power systems.

**Acknowledgements**

The authors would like to acknowledge the South African Weather Service (SAWS) for providing the cloud data required for the study.

**References**

Castro-Almazan, J., Varela, A. and Munoz-Tunona, C. (2015). Day time cloud cover at Teide Observatory. Canarian Observatories.

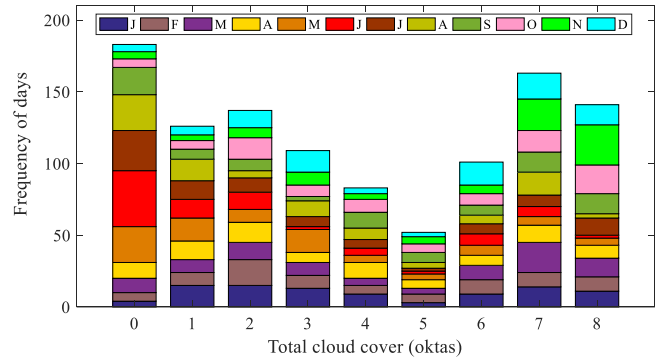


Figure 8: Distribution of total cloud cover for Durban at 14:00.

Updates, Institute of Astrophysics of the Canary Islands (IAC), 1-4  
 Govender, P., Brooks, M.J., Matthews, A.P. (2018). Cluster analysis for classification and forecasting of solar irradiance in Durban, South Africa. *Journal of Energy in Southern Africa*, 29 (2), 51-62.  
 Lohmann, U., Luond, F. and Mahrt, F. (2016). An introduction to clouds: from the microscale to climate. Cambridge University Press, UK.  
 Rogers, R. R. and Yau, M. K. (1989). A short course in cloud physics. Elsevier, USA.  
 Shikwambana, L. and Sivakumar, V. (2016). Observation of Clouds using the CSIR transportable LIDAR: a case study over Durban, South Africa, *Advances in Meteorology*, 1-9.  
 Tapakis, R. and Charalambides, A. (2013). Equipment and methodologies for cloud detection and classification: a review. *Solar Energy* 95, 392-430.  
 World Meteorological Organization (WMO) (2008). Guide to meteorological instruments and methods of observation (WMO-No. 8). <http://www.wmo.int/pages/prog/www/IMOP/CIMO-Guide.html>. Accessed October 2017.  
 World Meteorological Organization (WMO) (1975). Manual on the observation of clouds and other meteors (WMO-No. 407). [http://www.wmo.int/pages/governance/policy/tech\\_regu\\_en.html](http://www.wmo.int/pages/governance/policy/tech_regu_en.html). Accessed February 2018.

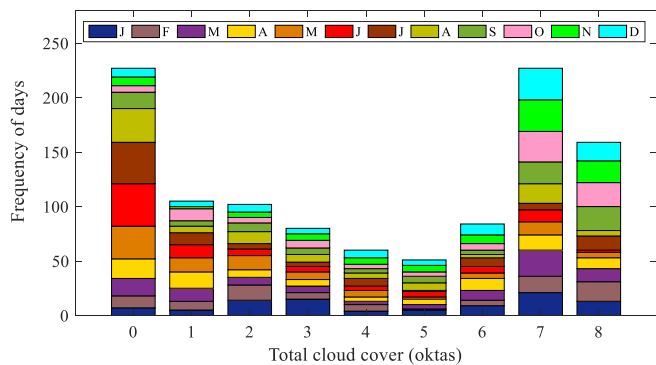


Figure 7: Distribution of total cloud cover for Durban at 08:00.

## ***Interannual variability correlation between the Cape Point wave record and large-scale climate modes***

Christo Rautenbach<sup>1,2</sup>, Jennifer Veitch<sup>3</sup>, Juliet Hermes<sup>3</sup>, Chris Reason<sup>2</sup>

<sup>1</sup>South African Weather Service, Marine Unit, Cape Town, South Africa

<sup>2</sup>Oceanography department and Marine Research Institute, University of Cape Town, South Africa

<sup>3</sup>South African Environmental Observation Network, Egagasini Node

### ***Abstract***

A 31-year wave model record is analysed in comparison with two major large-scale measures of climate modes. It is postulated that these modes will play a role on the location, density and intensity (depths) of mid-latitude cyclones and will influence the characteristics observed in the Cape Point wave record. Wavelet analysis were performed on both the wave record parameters and the large-scale climate mode indexes to quantify the underlying signals easily missed by traditional frequency analysis technique due to their design to assume a stationary timeseries. Results indicate that a shift in the wave record occurred in the early 1990s and that this shift corresponds to common cycles identifies in both atmospheric and oceanic timeseries.

*Keywords: Waves, Cape Point, SAM, ENSO, Wavelet analysis*

### ***Introduction***

To set the scene, we begin with a description of the seasonal cycle of the Cape Point wave record, as reproduced by the 31-year CSIRO wave model within the broader context of the seasonal fluctuations of cyclone density and intensity in the South Atlantic and the Atlantic section of the Southern Ocean. Cape Point's wave record is subject to a very marked seasonal signal. Bigger waves with larger periods occur during winter while summer waves are known to have smaller periods (by about 1 m and 0.6 s respectively). The predominant swell direction is southwesterly throughout the year with more of a westerly component during winter and more of a southerly component during summer. Plotting wave roses show that during winter there is a greater directional spread than during summer with southwesterly waves occurring about 55% of the time, as opposed to more than 65% of the time in summer. They also reveal that during winter the bigger waves tend to be more westerly, while in summer they tend to be more southerly. The strong seasonal variations in the number and depth (or intensity) of cyclones in the South Atlantic and Atlantic sector of the Southern Ocean is apparent in Figure 1 that shows the variations of the seasonal mean from the long term mean for each of the metrics based on the NCEP-2 dataset.

During winter months, higher than usual densities of cyclones are typically found south of the African continent with large numbers particularly on and flanking 45°S, spanning 45°W to 30°E, with particular 'hotspots' just south west of the African continent. A second band of high cyclone densities in winter months is further south, flanking 60°S from about 15°W, eastward to beyond 60°E. Cyclones are

'deeper' (i.e. more intense) during winter months in a 15° 'swath' that extends southwestward from about 22°S to 55°S and particularly so, approximately 1000 km to the west and southwest of Cape Point. In summer a zone of enhanced cyclone activity exists between about 50-60°S, from approximately 60°W to 45°E, north of this toward the African continent cyclone activity is reduced.

The cyclones everywhere in the South Atlantic and south of the African continent tends to be weaker, except for two isolated regions where cyclone intensities are slightly enhanced during summer; one to the southwest of Cape Point at about 15°E, 50°S and a smaller one about 30° westward of this. The maps of seasonal anomalies of cyclone density and depth are consistent with the seasonal variability of wave properties at Cape Point whereby during winter when the waves tend to be larger and are slightly more westerly, the band of preferential cyclone formation in the Southern Ocean shifts northward, closer to the African continent and the cyclones are more intense in an extensive band spanning from the west toward the southeast of the African continent.

On the other hand, during summer when the waves are smaller and with a more southerly component, the region of preferential cyclone formation shifts southward and cyclones are slightly more intense than the annual average in an isolated region about 15° south of Cape Point. For a more in-depth discussion please refer to Veitch et al, 2018: *in prep*. The aim of the present study is to illustrate the usefulness of applying Continuous Wavelet Transforms (CWT) and the Cross Wavelet Transform (XWT) to geographical time series and to the interannual variability of the Cape Point wave

record in relation to the large scale atmospheric variations. In particular the Southern Annular Mode (SAM) and the El Niño – Southern Oscillation (ENSO). Taking the connection between the variability of the Cape Point wave record and cyclone statistics further, we investigate the climate modes of various phases of SAM and ENSO.

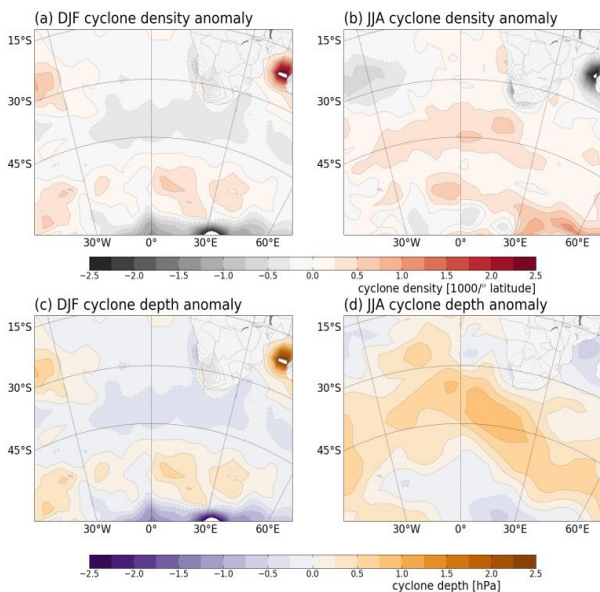


Figure 1: Austral summer (DJF) and winter (JJA) mid-latitude cyclone density and intensity (depth) deviations from the annual means, based on NCEP2 monthly mean sea level pressures.

#### Methods: The use of wavelets

According to Grinsted *et al.*, 2004 there exists two types or classes of wavelets, the Continuous and Discrete wavelet transform (CWT and DWT respectively). The CWT transform is usually used for feature extraction and will thus be employed in the present study to investigate the potential connection between the signals represented by the monthly SAM and ENSO indexes and the mean monthly wave anomalies. The CWT applied to a single time series will prove useful in identifying localized intermitted oscillations while the current study also explores the potential relationship between two timeseries (e.g. the relationship between our monthly mean wave anomalies and SAM or ENSO). By using the cross wavelet (XWT) and wavelet coherence (WTC) technique, suggested by Grinsted *et al.*, 2004, it was possible to investigate the regions in time-frequency space with common power. It is now also possible to link these high common power areas with a phase relationship. If the areas or regions with large common power are consisted within their phase relationship, it implies that

the large common power and/ or coherence regions are more than just coincidental (Grinsted *et al.*, 2004).

Similar to numerous other statistical procedures based on probability density functions, it is also assumed that the timeseries should be close to normally distributed as timeseries deviating far from this distribution might produce misleading significance values through the CWT (Grinsted *et al.*, 2004). Both the SAM and ENSO index timeseries were checked and both had near normal distributions (Marshall Index (Marshall, 2003) and Nino3.4 (Trenberth, 1980) respectively). The raw time series of significant, 3 hourly, wave heights were not normally distributed. After processing the CSIRO Wave Watch 3 model output data into mean monthly anomalies, it followed that the timeseries was near normal, as the seasonality was effectively also removed. In this geophysical application of the CWT the distribution of the timeseries (the not-normal distributed 3 hourly and normal distributed mean monthly anomalies wave time series) did not make a difference in the resulting XWT. Indicating that the strong common power signal in the time-frequency domain was not an artefact of seasonality nor sample frequency. For the purposes of the present study the SAM and ENSO time series were standardized (e.g. zero mean and unit variance).

According to the recommendation of Grinsted *et al.*, 2004, an appropriate wavelet for feature identification with equal variance in time and frequency in geophysical signals in the *Morlet* wavelet. The motivation for using wavelet analysis rather than the typical Fourier analysis is because we suspect the underlying processes (atmospheric ocean interaction) not to be stationary. Wavelets thus allow the identification of localised intermitted periodicities in the time frequency space (Torrence and Compo, 1998; Grinsted *et al.*, 2004). Examples of studies following a similar methodology to link geophysical timeseries may be found in the studies by (Torrence and Webster, 1999; Jevrejeva, 2003; Anctil and Coulibaly, 2004).

#### Results: Inter annual variability of wave record.

The standardized monthly anomalies of each of the model-derived wave variables that are being analysed (i.e. significant wave height ( $H_{m0}$ ), peak wave period ( $T_p$ ) and peak wave direction) for 1980-2010 are given in Figure 2. A 12-month running mean is given as a bold line in order to better visualize the potential trends and cycles. Bigger waves are associated with higher periods and are significantly correlated (Pearson's correlation between significant wave heights and peak wave periods:  $r=0.5$ ,  $p<<0.05$ ). While there is not a clear relationship between wave height and direction, there is a correlation between direction and wave period, but

only during austral spring and summer (with  $r$ -values of 0.4 and 0.5 respectively, both with  $p$ -values of less than 0.05). The  $T_p$  and  $H_{m0}$  timeseries undergo a definite shift in the early-mid 1990s, beyond which a period of predominantly negative anomalies exists for more than a decade. This suggests that  $T_p$ s and  $H_{m0}$ s tended to be bigger (smaller) before (after) the shift. While the wave direction does not similarly display a distinct shift toward more negative or positive anomalies from the early-mid 1990s, it does tend to be more variable with many more instances of extreme westerly or southerly wave directions. Likewise, the  $H_{m0}$  tends to become more variable during the later period. This more intense variability during the later period (i.e. after the early-to-mid 1990s) in wave direction and  $H_{m0}$ s is reflected

in the accompanying wavelet plots in Figure 2 that show significant peak power at return periods ranging from 2-12 months that span isolated time periods of 6 months to 2-3 years. This pattern is not present in the earlier period. However, lower frequency cycles are particularly apparent in the low-pass filter timeseries of  $T_p$ s in the period prior to the early-mid 1990s shift, during which an approximately 3.5-year cycle is evident. This signal is reflected in the wavelet analysis. The wavelet analysis picks up an approximately 8-year cycle in  $H_{m0}$  that persists throughout much of the timeseries, despite the clear shift toward smaller wave heights in the early-to-mid 1990s. However, the edges of the signal are out of the bounds of significance, being on the leading and trailing edge of the timeseries.

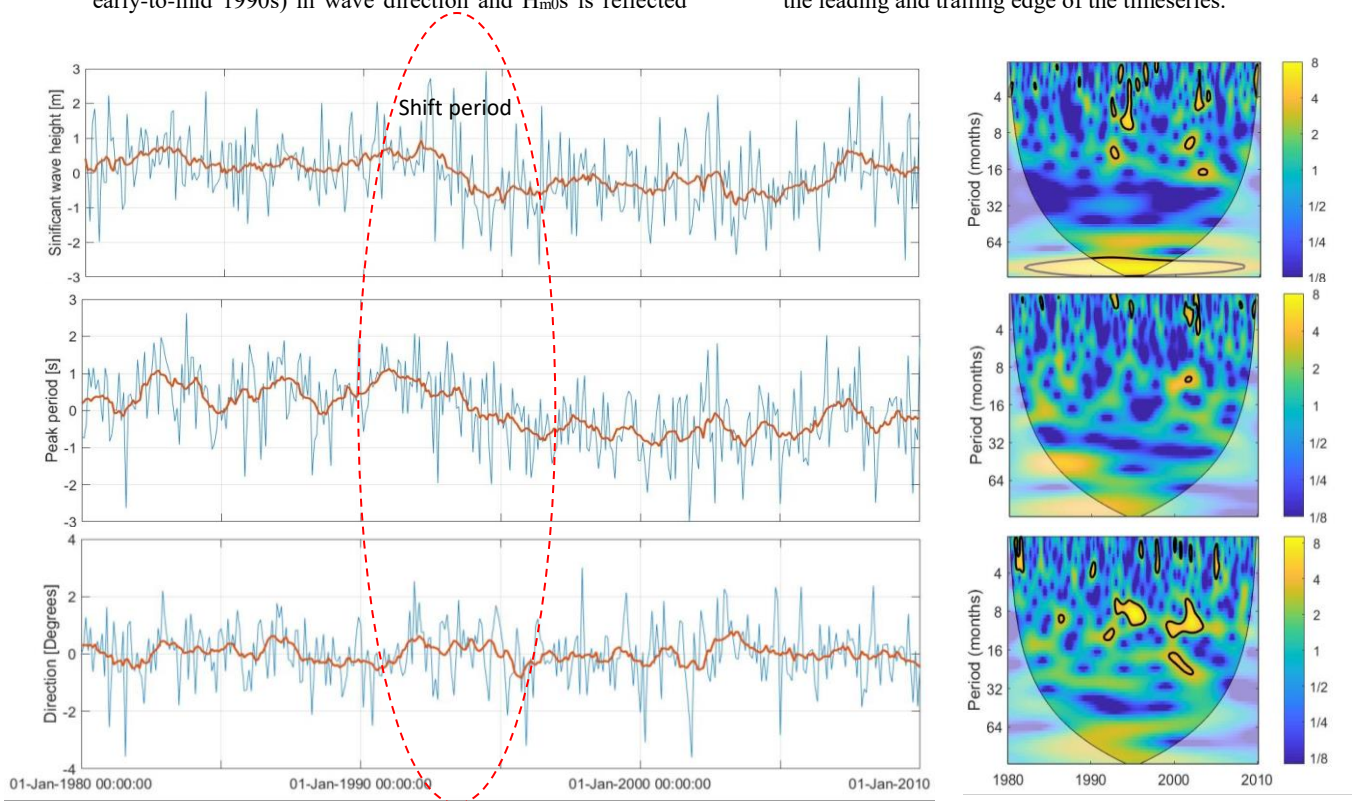


Figure 2: Standardized  $H_{m0}$ ,  $T_p$  and peak wave direction monthly anomalies and 12 month low-pass filter (thick orange line) along with the associated wavelet analysis for each. 5% significance level against red noise is given in thick contours. The cone of influence (where the edges of the time series start causing uncertainties, are given in the lighter shaded area).

*Inter annual variability of wave record and SAM and ENSO.*

An explanation of the shift period indicated in Figure 2 may be found in Figure 3 where the Cross Wavelet Transforms (XWT) are given between SAM and ENSO and the  $H_{m0}$ ,  $T_p$  and peak wave direction. XWT find regions in time and frequency space where the two timeseries indicate high common power. From Figure 3 (a) and (b) it is clear that both SAM and ENSO had regions of high common power with  $H_{m0}$  at a 3.5-year return cycle. It is interesting to note that the appearance of the high common power with SAM coincides with the approximate start of the shift indicated in Figure 2. As the SAM high common power dissipates the  $H_{m0}$  in Figure 2

starts increasing again. Similar to the pre-1990s. An in-phase relationship is given by the arrows in the XWT pointing right, anti-phase with arrows pointing left and SAM and/ or ENSO leading the wave parameters by  $90^\circ$  if the arrows point straight down. Thus, SAM is leading the  $H_{m0}$  by approximately  $135^\circ$  while ENSO and  $H_{m0}$  is approximately in-phase (with the  $H_{m0}$  trailing behind only slightly). The XWT highlight the common feature revealed in the CWT. For a relationship between atmospheric phenomena and oceanic response to be linked through cause and effect, Grinsted *et al.*, 2004 suggested that the common power be phase locked. E.g. the area of high common power should have

similar phasing throughout. Figure 3 clearly confirms this behavior  $T_p$  and peak wave direction with SAM and ENSO. It can be concluded that  $H_{m0}$  is almost mirroring SAM (as they are approximately in anti-phase, refer to Fig 3. (a)) during the significant period areas. This almost out of phase behaviours of SAM and  $H_{m0}$  might also explain the period of decreased  $H_{m0}$  (early 1990s to early 2000s) and increased variability observed in Figure 2. This is also the period during which there were a strong common power between  $H_{m0}$  and ENSO at a 3.5-year return period which dissipates towards the early 2000s.

From Figure 3 (c) and (d) no apparent areas of strong common power was found between  $T_p$  and SAM. Over lapping the cone of influence, there were a strong common power with ENSO with return cycles ranging from 3 to 4 years. This signal is present before the early 1990s shift and not afterwards. Indicating that in the absence of this cycle, the  $T_p$ s decreased and did not recover fully in the early 2000s without this signal returning.

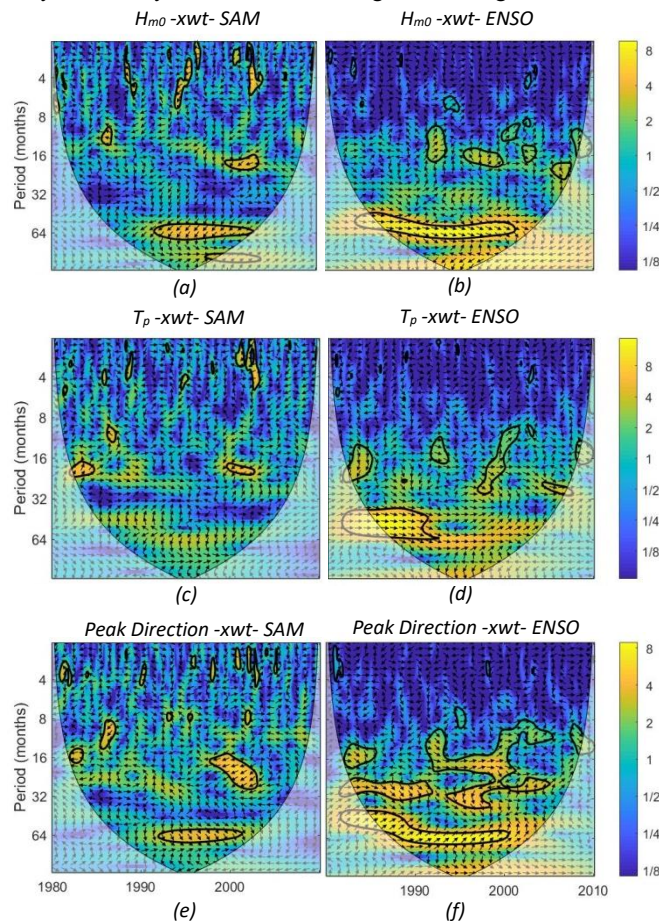


Figure 3: Cross wavelet transform of the standardized (a), (c), (e) SAM index and (b), (d), (f) ENSO index and the (a), (b) significant wave height and (c), (d) peak wave period and (e), (f) peak wave direction. The 5% significance levels are given with the bold lines and the phase relationship is given by the arrows.

Again, an approximate in-phase, phase locked behavior is observed with ENSO. The other areas of significance are not considered as they did not reflect a phase locked behaviour and could probably be due to coincidental common power.

for both the relationship between  $H_{m0}$ ,

In Figure 3 (e) and (f) the peak wave directional common power with SAM and ENSO is given. A similar common power with SAM and ENSO is observed as with  $H_{m0}$ . With SAM the cross transform shows significant peak power at return periods ranging from 2-12 months that span isolated time periods of 6 months to 2-3 years. Both  $H_{m0}$ ,  $T_p$  and the peak direction also show an area of large common power with a 16-month return cycle at the mid-1990s. This area of common power is particularly strong between the peak wave direction and SAM and spans from 16 months to an almost 2-year cycle. As in Figure 2, the increased variability observed after the 1990s seem to be caused by SAM as the higher frequency signals are only observed with SAM's XWTs. The peak wave directional common power with ENSO gives large area of common power but only one large area, again around a 3.5-year cycle, which is phased locked. Around the early 1990s a shift occurs where the common power moves to a higher cycle period. In this case the peak wave direction is leading the phase slightly (or trailing almost completely). From Figure 2 this time period agrees with a period (1990s) when the directional record was characterized with more extreme anomalies and higher variability. For a through discussion on the relationship between the phasing of SAM, ENSO and wave parameters please refer to Veitch et al, 2018: *in prep*.

Wavelet coherence testing (resembling traditional correlation coefficients) can also be performed on geophysical time series. Instead of highlighting areas of common power the co-varying nature of two signals are retrieved in the time-frequency space. For the atmospheric and wave parameters considered in the present study significant areas of co-variance we obtained, consistent with the discussion thus far.

### Conclusions

A 3.5-year cycle that was observed in the  $T_p$  timeseries seems to persist after the early 1990s shift. XWT indicated that the 3.5-year return cycle were present in both the atmospheric and oceanic signals, as indicated by the XWT areas of high significant common power. XWT was thus useful in identifying common oscillations too weak to identify in the individual signals and could in turn explain shifts observed in traditional time-frequency analysis (Cui, Bryant and Reiss, 2012).

### Acknowledgements

We would like to acknowledge the kind contribution of C. Torrence, G. Compo, A. Grinsted and E. K. W. Ng for making the wavelet transform, cross wavelet transform, wavelet coherence and geometric significance testing packages freely available.

*References*

- Ancil, F. and Coulibaly, P. (2004) 'Wavelet Analysis of the Interannual Variability in Southern Québec Streamflow', *Journal of Climate*, 17(1), pp. 163–173.
- Cui, X., Bryant, D. M. and Reiss, A. L. (2012) 'NIRS-based hyperscanning reveals increased interpersonal coherence in superior frontal cortex during cooperation', *NeuroImage*, 59(3), pp. 2430–2437.
- Grinsted, A. *et al.* (2004) 'Application of the cross wavelet transform and wavelet coherence to geophysical time series', *EGU*, 11(5/6), pp. 561–566.
- Jevrejeva, S. (2003) 'Influence of the Arctic Oscillation and El Niño-Southern Oscillation (ENSO) on ice conditions in the Baltic Sea: The wavelet approach', *Journal of Geophysical Research*, 108(D21), pp. 1–11.
- Marshall, G. J. (2003) 'Trends in the Southern Annular Mode from observations and reanalyses', *Journal of Climate*, 16(24), pp. 4134–4143.
- Torrence, C. and Compo, G. P. (1998) 'A Practical Guide to Wavelet Analysis', *Bulletin of the American Meteorological Society*, 79(1), pp. 61–78.
- Torrence, C. and Webster, P. J. (1999) 'Interdecadal changes in the ENSO-monsoon system', *Journal of Climate*, 12(8 PART 2), pp. 2679–2690.
- Trenberth, K. E. (1980) 'Planetary Waves at 500 mb in the Southern Hemisphere', *Monthly Weather Review*, 108(9), pp. 1378–1389.

## Seasonal rainfall anomalies over the all-year and winter rainfall regions of South Africa

Christien J. Engelbrecht<sup>1,3</sup>, Stephanie Landman<sup>2</sup>, Liesl Dyson<sup>3</sup>, Reneilwe Maake<sup>1</sup> and Winston Muthaphuli<sup>3</sup>

<sup>1</sup>Agricultural Research Council, Pretoria, 0001, South Africa

<sup>2</sup>South African Weather Service, Pretoria, 0001, South Africa

<sup>3</sup>University of Pretoria, Pretoria, 0001, South Africa

### Abstract

Seasonal rainfall anomalies over the all-year rainfall region and the southwestern Cape for the period 1901-2017 and March-April-May (MAM) 2018 were used to contextualize the recent/current multiyear droughts over the southwestern Cape and the Cape south coast region. Over both regions, seasonal rainfall deficits of similar magnitude than during the recent/current multiyear droughts have occurred previously. However, the MAM seasons during the recent/current multiyear droughts were notably drier than almost all previous MAM seasons used in this analysis, in particular over the Cape south coast region. It also seems that dry MAM seasons, and not JJA seasons contributed more to the southwestern Cape drought.

Keywords: Drought, Seasonal rainfall anomalies, All-year rainfall region, Winter rainfall region

### Introduction

Between 2014 and 2017 the winter rainfall region of South Africa experienced below-normal rainfall each rainfall season, resulting in extraordinary water shortages by the beginning of 2018. Further to the east along the Cape south coast, 2016 and 2017 were very dry and these conditions continued into 2018, whilst some relief was experienced at last over the far southwestern parts of the country with the start of the 2018 winter rainfall season. The response of the vegetation activity as represented by the Vegetation Condition Index (VCI) to the rainfall conditions can be seen in Figure 1. From the VCI map it is clear that the entire Cape south coast region as well as the adjacent southern interior is under tremendous stress. Apart from below-normal vegetation activity, water storage is also at critical low levels over the Cape south coast region.

The far southwestern part of South Africa receives most of its rainfall during the austral winter, whilst the Cape south coast receives rainfall throughout the year, but with peaks during the transitional seasons (Taljaard 1996). Over the Cape south coast rainfall-producing weather systems of both the winter and summer rainfall regions of South Africa occur.

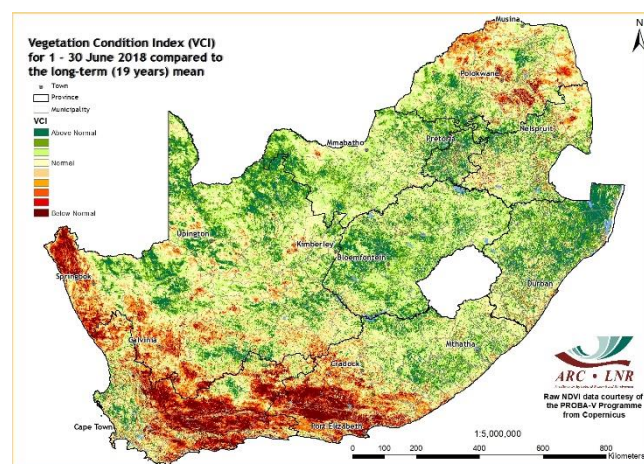


Figure 1: VCI for June 2018 relative to a 19-year long-term mean.

The weather system responsible for the largest contribution to the annual rainfall over the Cape south coast is high pressure systems ridging from the southwest (Engelbrecht *et al.* 2015), and this system is also linked to interannual variability of seasonal rainfall during all the seasons, but less so during summer (Engelbrecht and Landman 2016). Over the winter rainfall region frontal systems are the main rain-producing weather systems as the westerly wind regime shifts toward the equator during austral winter. An equatorward displacement of storm tracks, i.e. cold fronts has been linked to wet years over southwestern Cape (Reason and Rouault 2005; Philippon

et al. 2012). Ridging highs from the southwest typically follow in the wake of frontal systems and exhibit seasonality in their configuration in response to the meridional movement of the westerly wind regime between austral winter and summer. Other important rain-producing systems over the Cape south coast region include tropical-temperate troughs – which have also been linked to interannual rainfall variability of seasonal rainfall (Engelbrecht and Landman 2016). The most intense form of westerly waves, namely cut-off lows (Taljaard 1996), are important rain producing weather systems over both the winter rainfall and the all-year rainfall region.

In this study, the most recent drought conditions over the winter rainfall region and the Cape south coast region are put into a historical context. The aim is not limited to contextualization of the recent/current drought conditions, but also to further our understanding in the processes leading to droughts and to investigate whether there is a link between the droughts over these two adjacent but very distinct climate regions.

**Data and Method**

The Climate Prediction Center (CPC) rainfall data (<https://www.esrl.noaa.gov/psd/>) are used to construct a time-series of area-averaged normalized rainfall for each season (March-May (MAM), June-August (JJA), September-November (SON), December-February (DJF)) over the winter rainfall region and the all-year rainfall region of South Africa. Additional to the four conventional seasons, the winter half-year – defined as April-September (AMJJAS), is also considered in this analysis. The CPC dataset has rainfall data available since 1979 and is updated daily with the most current data having a lag of about 2 days. The CRU TS v. 4.01 rainfall data (Harris et al. 2014) are used to expand the constructed seasonal time-series back to 1901. The overlapping period of the CPC and CRU datasets were used to assess the viability of the construction of a combined normalized rainfall time-series. Very good agreement exist between these 2 datasets for the overlapping period over the

all-year rainfall region (Kendall Tau = 0.8 at the 99<sup>th</sup> confidence level). Over the winter rainfall region, the correlation between these 2 rainfall datasets is also statistically significant, though at the 95<sup>th</sup> confidence level and with a lower correlation (Kendall Tau=0.38) compared to the correlation applicable to the all-year rainfall region. The domains over which the area-averaged rainfall were calculated focussed on the catchment regions of the important water storage dams and is indicated in the legend of Figure 2.

**Results and Discussion**

The annual rainfall cycles over the winter rainfall region and the all-year rainfall region for 4 non-overlapping periods during 1901-2016 is shown in Figure 2 and indicates that the month or months (in the case of the all-year rainfall region) of maximum rainfall is not consistent.

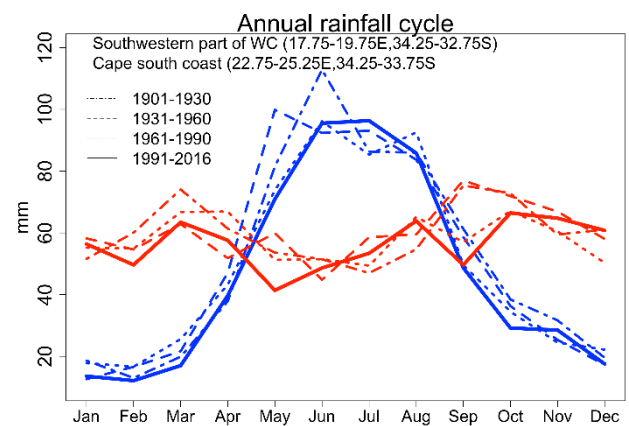


Figure 2: : Area-averaged annual rainfall cycle for four 30-year periods (1901-1930, 1931-1960, 1961-1990, 1991-2016) over the southwestern part of the Western Cape (blue) and the Cape south coast (red).

Over the all-year rainfall region that a change is observed in the second rainfall peak of the year. During the 1901-1930 and 1931-1960 periods, a September rainfall peak is very prominent, but is absent during the 1961-1990 and 1991-2016 periods. Over the winter rainfall region, the start of the winter rainfall season seems to be more conservative during the 1961-1990 and 1991-2016 periods compared to the earlier periods. These observed climatological changes in the annual rainfall cycle might be indicative of synoptic-scale circulation changes which might be in-turn driven by larger-scale climate

modes. Annual rainfall totals for these four non-overlapping periods between 1901-2016 exhibit a decline in rainfall that took place over about the past 60 years (Table 1), more or less coinciding with the timing of the observed changes in the annual rainfall cycle. However, it has not yet been investigated whether there is a physical relationship between these observed changes.

Table 1: Long-term mean area-averaged rainfall totals (mm) over the southwestern Western Cape and the Cape south coast for 1901-1930, 1931-1960, 1961-1990 and 1991-2016

	1901-1930	1931-1960	1961-1990	1991-2016
<b>southwestern Cape</b>	600	599	576	549
<b>Cape south coast</b>	717	716	691	669

The relative contribution of rainfall during AMJJAS, MAM, JJA, SON and DJF to the annual rainfall over the winter rainfall region (all-year rainfall region) ranges from 76-78.8% (46.4-49%), 22.8-27.8% (24-26.4%), 44.7-50.2% (21-24.5%), 18.5-21.6% (26.6-29.7%) and 7.5-9.5% (23.2-24.6%) between the 4 non-overlapping periods between 1901-2016. Over the winter rainfall region, it is not just the rainfall during the winter months that is important, but also rainfall during MAM and to a lesser extent SON.

The normalized rainfall anomalies as computed from the CPC data for the different seasons are shown in Figure 3 and that computed from the CRU data in Figure 4. Over the winter rainfall region, during all the seasons other periods such as around the year 2000 (Figure 3, AMJJAS), between 1960-1980 (Figure 4, AMJJAS, JJA) and between 1920-1930 (Figure 4, MAM), experienced below-normal rainfall conditions of a similar magnitude to the recent drought.

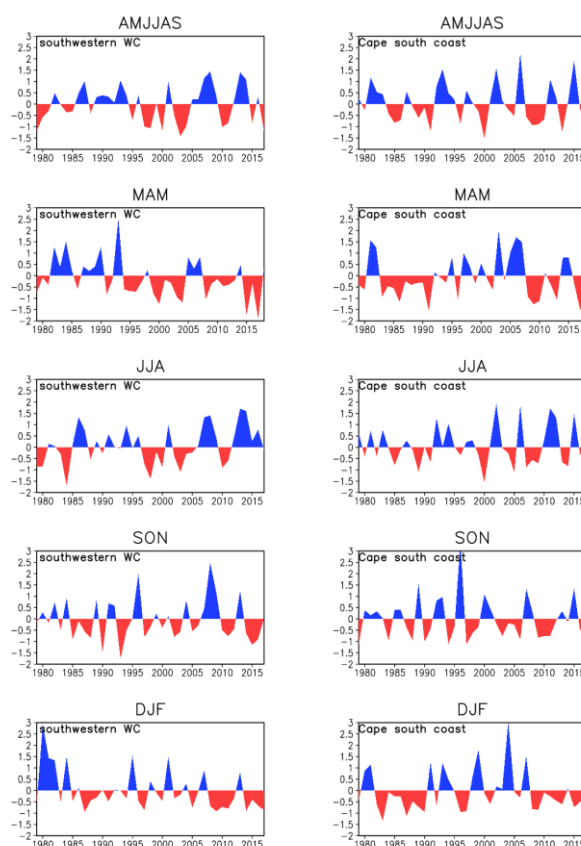


Figure 3: CPC area-averaged normalized rainfall anomalies over the southwestern part of the Western Cape (left panel) and the Cape south coast (right panel) for the 1979-2017 winter half-years, 1979-2018 autumn seasons, 1979-2017 winter seasons, 1979-2017 spring seasons and 1979-2017 summer seasons

However, it seems that the frequency and magnitude of below-normal rainfall during MAM over the winter rainfall region has been increasing since about 1995, and could be contributing more to the drought conditions than the below-normal JJA rainfall. Over the all-year rainfall region, the normalized seasonal rainfall anomalies of the current drought are comparable to seasons of previous years, except for MAM when only 1970 were drier than MAM of 2018.

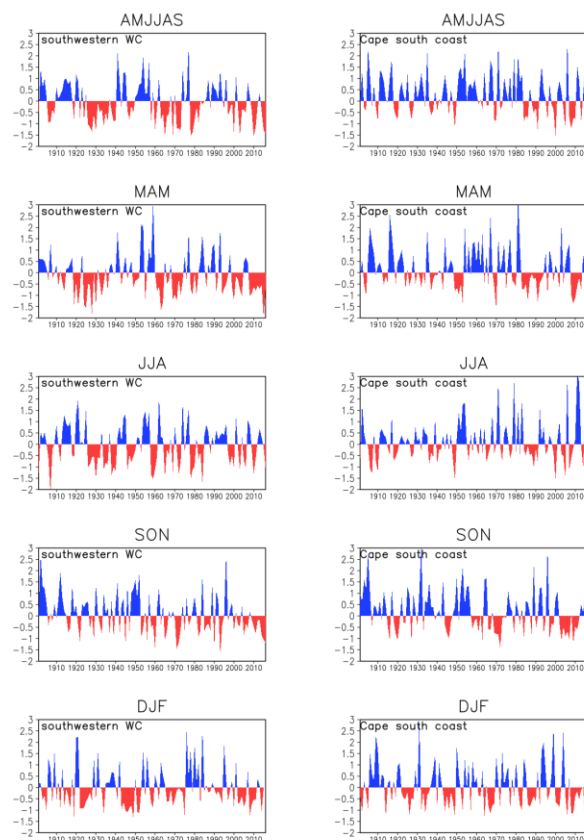


Figure 4: As for Figure 3, but based on CRU TS v. 4.01 rainfall data for the period 1901-2016.

### Conclusions

Generally, annual rainfall totals over both the winter and all-year rainfall regions seem to be on the decline when the climatological annual rainfall totals for 4 non-overlapping periods during 1901-2016 is considered. Long-term mean annual rainfall totals during 1901-1930 and 1931-1960 is stable, but declines during both the following periods (1961-1990, 1991-2016). Some changes are also observed in the annual rainfall cycle, coinciding with the start of the decline in the long-term mean annual rainfall totals. These changes involve differences in the month(s) of maximum rainfall. Over the southwestern Cape the magnitude of the months of maximum rainfall were larger during the first 2 periods and earlier in the rainfall season. Over the all-year rainfall region, the most striking change in the annual rainfall cycle is the absence of the September rainfall peak during the last 2 periods. With respect to the recent/current multiyear droughts over the southwestern Cape and the Cape south coast, seasonal rainfall deficits of a comparable magnitude have

occurred historically in all the seasons, but to a lesser extent in MAM. It seems that failure of rainfall during especially MAM (except over the southwestern Cape in 2018) contributed to the droughts over both regions during these multiyear droughts, and surprisingly not JJA in the case of the southwestern Cape. The MAM 2018 rainfall over the Cape south coast, is the lowest in 40 years.

### Acknowledgements

WRC project K5/2832 titled, “Causes of the 2015-2017 drought over the Western Cape, South Africa”.

### References

- Engelbrecht, C.J., Landman, W.A., Engelbrecht, F.A., Malherbe, J. (2015). A synoptic decomposition of rainfall over the Cape south coast of South Africa. *Climate Dynamics* 44: 2589-2607.
- Engelbrecht, C.J. and Landman, W.A. (2016). Interannual variability of seasonal rainfall over the Cape south coast of South Africa and synoptic type association. *Climate Dynamics* 47: 295-313.
- Harris, I., Jones, P.D., Osborn, T.J. (2014). Updated high-resolution grids of monthly climatic observations – the CRU TS3.10 Dataset. *International Journal of Climatology* 34: 623-642.
- Philippon, N., Rouault, M., Richard, Y., Favre, A. (2012). The influence of ENSO on winter rainfall in South Africa. *International Journal of Climatology* 32: 2333-2347.
- Reason, C.J., Rouault, M. (2005). Links between the Antarctic Oscillation and winter rainfall over western South Africa. *Geophysical Research Letters* 32: L07705. Doi:10.1029/2005GL022419.
- Taljaard, J.J. (1996). Atmospheric circulation systems, synoptic climatology and weather phenomena of South Africa. Part 6: Rainfall in South Africa. South African Weather Bureau, Technical paper 32.

## The influence of thermal and vorticity advection on the development of continental tropical low-pressure systems over southern Africa

Lehlohonolo M F Thobela and Liesl L Dyson

Department of Geography, Geo-informatics and Meteorology, University of Pretoria

South African Weather Service

### Abstract

A dynamical analysis of the development, life cycle and decay of continental tropical low-pressure systems over Southern Africa is presented. The analysis is done using National Centre for Environmental Prediction (NCEP) data. The aim is to investigate the influence of thermal and vorticity advection on the development and movement of continental tropical low-pressure systems over southern Africa. To aid in understanding the deepening and sustainability of the low-pressure system's energy through its migration over time. The investigation is based on a recent example of a continental tropical low-pressure system which occurred between 7 and 10 January 2017. The analysis is done through the application of thermal and vorticity advection in order to explain the dynamical properties of development of these weather systems. The parameters are calculated and displayed at different cross-sections of the vertical atmosphere. Cross-section displays are done in association with time sections to enhance the ability of analysis of the continental tropical low-pressure systems. It has been observed overtime that easterly waves develop into continental tropical low-pressure systems but no further investigations have been done. The research aspires to better the understanding of thermal and vorticity advection in the intensification and motions of developed continental tropical lows. Findings of the research were close to the assumptions of the quasi-geostrophic analysis in terms of correspondence between vorticity advection and thermal advection to development but not all results supported the notions of the quasi-geostrophic analysis. Such as there were instances within the study where there was no support between vorticity advection and thermal advection. With a yield of one term dominating over the other and there being an opposition of the quasi geostrophic theory's assumption in instances where cold-air-advection present below a low-pressure at 500-hPa level does not result in a fall in geopotentials as it would be expected in the extra-tropical regions.

### 1. Introduction

Continental tropical low-pressure systems are defined as systems that have a characteristic structure with relatively cool but very humid air at the surface up to 700 hPa (Taljaard, 1995). These systems are very important weather systems that occur over southern Africa between the months of late December to March. They are observed to have the centre of the low located over Botswana or Namibia and consist of an extending trough towards the south to reach the border of South Africa and Botswana. The influence of the low-pressure system to South Africa extends to cover the northern parts of the country including the Free State (Taljaard, 1995).



Fig.1 Map of South Africa with provinces that are usually affected by Continental Tropical Lows.

The understanding of tropical and dynamical developments plays an important role in grasping the link of the formation of continental tropical low-pressure systems. The storage of available potential energy in the tropics is small. This is due to very small temperature gradients that occur in the tropical atmosphere (Holton, 2004).

Latent heat release is considered to be the primary energy source for disturbances that form within the equatorial zone. It is associated with convective cloud systems but much of the precipitation falls from the strati form clouds in the mesoscale regions (Holton, 2004). Taljaard (1995) explained that continental tropical low-pressure systems may be tropical systems but their development is not within the equatorial region. The centre of the trough being identified over the Namibia or Botswana region but not along the Inter Tropical Convergence Zone.

These conditions bring about attention to the disturbances that have an impact in the tropical development in Southern Africa. The African wave disturbances are associated with convection but they do not appear to be driven by latent heat release. These waves depend on barotropic and baroclinic conversions of energy from the easterly jet (Holton, 2004).

Santurette and Georgiev (2005) described that a negative vorticity gradient serves as an indication that African jets satisfy the conditions for barotropic instability. The baroclinic instabilities cannot be neglected due to the

influence of easterly shear in the lower troposphere. Depicting that both barotropic and baroclinic conversions from the mean flow energy appear to be important for the development of African disturbances (Holton, 2004).

Due to observations explained (Holton, 2004), these disturbances continue to exist in the absence of mean wind shears. It is improbable that baroclinic or barotropic instability act as primary energy source for maintenance. Diabatic heating through precipitating convective systems appears to be the main energy source for African waves over the ocean.

A recent example of a continental tropical low-pressure system occurred between 7 and 10 January 2017. The low-pressure system developed over Botswana and at a slow pace moved south-eastwards to the border of South Africa and Botswana. As significant these systems can be to the meteorological environment and rainfall in Southern Africa, very little is known about how they develop, what sustains their energy and how they cease. Information about the identification of these systems has surfaced but none has been done in relation to what actual needs to happen for these systems to exist. Taljaard (1995) elaborated on the features of these low-pressure systems after development. These low-pressure systems tend to deepen from the lower ground upwards to 700 hPa but they always show a characteristic of disappearance above 500-hPa which eventually gets replaced by an anticyclonic circulation in the upper troposphere (Taljaard, 1995).

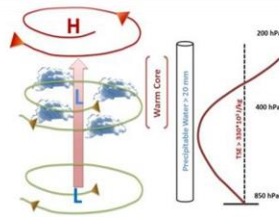


Fig. 2 Image shows the concept and main developmental features of a Continental tropical low pressure system.

After the development of these low-pressure systems, heavy rainfall occur at the eastern side of the developed low-pressure systems. Overtime it has been witnessed that due to weak vertical wind shear and light steering winds in the mid troposphere, the convective cells that develop within the lows tend to be semi-stationary which assists in the efficiency of delivering precipitation (EUmeTrain, 2012).

The hypothetical question to be addressed in the paper is what role the influence of thermal and vorticity advection has on the development of continental tropical low-pressure systems over southern Africa

## 1. 2. Data and methods

### 2.1 Re-analysis Data

Synoptic circulation patterns description over southern Africa is done using the National Centre for Environmental Prediction (NCEP) reanalysis data. It is a merge of observations and model data that is available from the year 1948. The introduction of meteorological satellites as a collection of tools occurred in 1979 (Kanamitsu et al., 2002).

This research uses reanalysis-2 with a horizontal resolution of  $2.5^\circ \times 2.5^\circ$  and a temporal resolution of six hours (Kanamitsu et al., 2002). The reanalysis-2 dataset is preferred because errors of reanalysis-1 have been corrected within it (reanalysis-2). The modification has produced better reanalysis together with an introduction of parameterization schemes. NCEP reanalysis-2 dataset consists of variables such as surface pressure (P), Temperature (T), Zonal winds (U), Meridional winds (V), vertical velocity ( $\omega$ ), Relative Humidity (Rh) and Geopotential height (z) (Kanamitsu et al., 2002).

### 2.2 Apparatus and application

In this study, an investigation of meteorological parameters at different levels is done using Grids Analysis and Display System (GrADS). Application is to calculate, display, and analyse the meteorological variables at different levels (Doty, 2014). The levels assisting in portraying properties of continental tropical low-pressure systems. The program allows for the adaptation of a dynamic set of target resources and combines enormous quantities of information from different sources (Berman et al., 2001).

The research area is southern Africa ( $35^\circ\text{S}$  to  $10^\circ\text{S}$  and  $10^\circ\text{E}$  to  $40^\circ\text{E}$ ). The study includes the calculation of meteorological parameters that are dynamic and thermodynamic such as vorticity, vorticity advection, and thermal advection to investigate the effect these parameters have on the development of continental tropical low-pressure systems over southern Africa. Following the assumption that when wind flows through a temperature gradient it results in the production of positive or negative vorticity advection (Carroll, 1997).

The application of GrADS is used in the diagnosis and assessment of development and movement of continental low-pressure systems. Vorticity calculations done are used in order to be able to apply the importance of vorticity advection in the development of the low-pressure systems. In consideration that vorticity advection is more effective at the surface for development (Holton, 2004). Vorticity advection is defined as the transfer of vorticity horizontally or vertically during the flow of the wind. As a meteorological variable, it is used in the prediction of vertical motion in the atmosphere. Vorticity advection enhances a surface low-pressure system by making it spin faster and cyclonic vorticity advection causes a decrease in geopotential. Cyclonic vorticity advection is responsible with

-the movement of low-pressure systems whereas anti cyclonic vorticity advection is responsible for the movement

of high-pressure systems (American Meteorological Society, 2012; Holton, 2004).

The practice of the Quasi-geostrophic vorticity and thickness equations build a system that can be used to explain and describe the behaviour of synoptic-scale weather systems. A difference between fields of ageostrophic wind at a low level and at a middle or high tropospheric level can be computed then the horizontal divergence can be deduced. In this regard, regions of rising surface pressure over air that is subsiding surface pressure over air that is rising can be located. Cold-air advection at surface and warm-air advection above 500-hPa level assist in explaining the idea that a surface trough and a ridge will tend to be displaced in the direction of shear by an action of development. Considering the effect of divergence and defining it as an outflow of mass from a central point. Its importance being that upper divergence (200-hPa) results in an enhancement or intensification of low-level (850-hPa) convergence (Holton, 2004 and Lackmann, 2011).

The Quasi-Geostrophic height tendency equation is applied to infer change in the height field of the atmosphere. The analysis and conclusions are made based on the signs and the magnitude of two forcing terms. These are advection of absolute geostrophic vorticity by the geostrophic wind and

the vertical variation of geostrophic thickness advection (Holton, 2004).

$$\left(\nabla^2 + \frac{f^2}{\sigma} \frac{\partial^2}{\partial p^2}\right) = -fv_g \cdot \nabla \eta_g + \frac{f^2}{\sigma} \frac{\partial}{\partial p} [-v_g \cdot \nabla \left(\frac{\partial \Phi}{\partial p}\right)] \cdot \nabla \left(\frac{\partial \Phi}{\partial p}\right)$$

(1)                      (2)                      (3)

Where term 1 is the three dimensional Laplacian of height tendency, term 2 the advection of absolute geostrophic vorticity by the geostrophic wind and term 3 the vertical variation of geostrophic thickness advection (Holton, 2004).

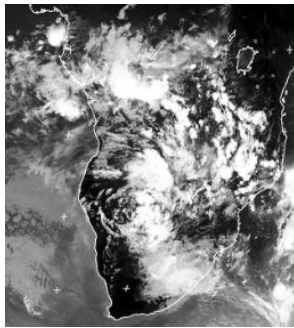
**Table 1:** Meteorological parameters used in the investigation of development with synoptic scale values.

Parameter	Equation	Units	Level (hpa)	Synoptic scale
Vorticity advection	$-fv_g \cdot \nabla \eta_g$	s <sup>-2</sup>	Average (1000-700)	10 <sup>-10</sup>
Thickness advection	$-v_g \cdot \nabla \left(\frac{\partial \Phi}{\partial p}\right)$	k·s <sup>-1</sup>	500	10 <sup>-4</sup>

3. Results and discussions

3. Case study 4-14 January 2017

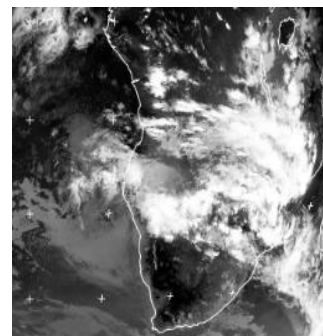
Initial- 04/01/2017



Mature-07/01/2017



Dissipation-14/01/2017



Satellite images of the initial, matured and dissipation stage of the continental tropical low-pressure system over southern Africa for the 4<sup>th</sup>, 7<sup>th</sup> and 14<sup>th</sup> January 2017 at 14:00 Z.

3.1 Developmental stage of continental tropical lows analysis

On January 3rd and 4<sup>th</sup> 2017 a continental tropical low-pressure system started to develop over Botswana. Figure 3.1.1A shows the presence of cold-air advection at the development of the low-pressure system, with a positive value of 24 in the core of the low. Cold-air advection is represented by the colour light to dark red and warm-air advection is represented by light purple to dark purple. The darker the colour, the greater the intensity. Cold-air

advection is supported by cyclonic vorticity advection at 500-hpa level (figure 3.1.1B), where the colour light peach to dark peach represents cyclonic vorticity advection and light green to dark green represents anticyclonic vorticity advection. There is also a fall in geopotentials around the low at the 500hPa level from 5856 to 5848 gpm of which by the quasi geostrophic approximation, supports the notion of development.

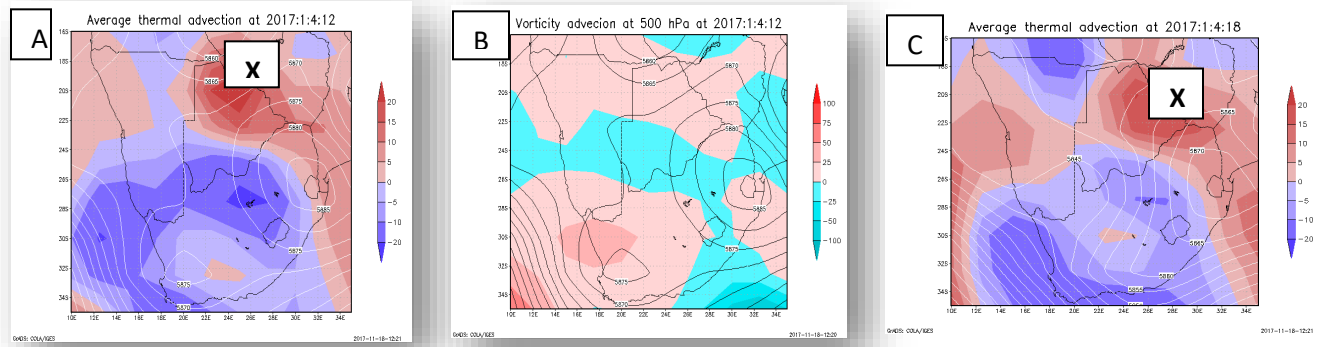


FIGURE 3.1.1: (A) average thickness advection, (B) vorticity advection at 500 hPa and (C) average thickness advection for January 4<sup>th</sup> 2017.

In consideration that thickness advection plays a role on the deepening of a low-pressure system at 500-hPa provided there is evidence of cold-air advection below the low, the geopotentials are expected to fall. In figure (B), with the presence of cyclonic vorticity advection the continental tropical low-pressure system showed a drastic fall of geopotential with a difference of 8 gpm during the initial

stages of development. With vorticity advection as a facilitator of the motion of the low, the low-pressure system was expected to move east from its initial position. Following from the time step on the two figures A and B, the low-pressure system moved slightly to the southeast rather than to the east directly on the next image, C. The movement is illustrated by an **X** on image A and C.

### 3.2 Matured stage of development

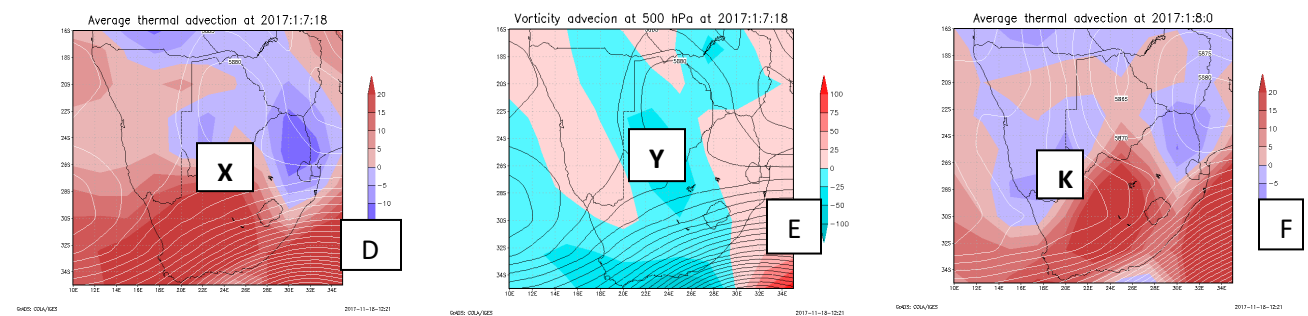


FIGURE 3.2.1: (D) Thickness average advection and (E) vorticity advection at 500-hPa level, for 7 January 2017 and (F) Average thermal advection for 8 January 2017 at 00:00 Zulu.

No presence of cyclonic vorticity was observed on the 500-hPa map of 6 January 2017. There was anticyclonic vorticity advection on the western side of the developed continental tropical low, which supported a development and movement of a ridge on the western parts of South Africa. Vorticity advection assumed the ridge to move in a north-westerly direction. Although the anticyclonic vorticity advection was present over the location of the continental tropical low, it had no impact on geopotentials around and in its core. The low remained as it was stationary and the movement presumed by vorticity advection for the high-pressure system certainly occurred as the high started to ridge over the northwest of the continent.

There was cold-air advection on the day as can be seen by **X** on figure D, which seemed to have dominated on the day to sustain the life cycle of the continental tropical low concurrently with presence of anticyclonic vorticity advection at the 500-hPa level as can be seen by **Y** on figure

E. This would be associated with a rise in geopotentials and high pressures. Geopotentials fell from 5875 to 5865 around the presence of cold-air advection. An observation was made where there was also presence of warm-air advection further southeast of South Africa, which resulted in a rise of geopotentials and a development of a ridge on the eastern parts of the country. The high pressure may have also played a role in bringing moisture to the interior as it assumed the direction of the warm-air advection and strengthened into the country from the northeast of the country.

On 7 January 2017 (figure: 3.2.1 D and E) the continental tropical low-pressure system moved southeast of Botswana touching the border of South Africa. There was little or no cyclonic vorticity advection in and around the continental tropical low pressure system on the 500-hPa level map. On the eastern side of the matured low-pressure system, there was anticyclonic vorticity advection that supported a development and movement of a ridge as indicated by a **K**

on figure F. Thickness advection seems to have dominated over vorticity advection as it can be seen by an X on figure D. Due to the observation that even though the two figures (D and E) do not correspond with each other in terms of the Low-pressure development, there was strong cold-air advection with deepening of the low-pressure system. The geopotentials in and around the continental tropical low-pressure system at level 500-hPa appeared to have been falling. With the core value of the low-pressure system being 5870 gpm from being 5885 gpm, which is a difference of 15 gpm in 6 hours.

### 3.3 Weakening stage of the continental tropical low

On 12 January 2017, the continental tropical low-pressure system moved slightly in a northerly direction over South Africa, leaving the border between South Africa and Botswana and moving back to Botswana.

The interior of South Africa was dominated by anticyclonic vorticity advection over the 500-hPa map covering the Botswana border too. There was minimal amounts of cyclonic vorticity advection enough to identify the low-

pressure system and its location. The available cyclonic vorticity advection assumed a north-westerly direction. Moving back to the area of initial development in Botswana but with less energy and deepening. As the motion of advection predicted, the low-pressure system moved back to its initial position and assumed the direction of the minimal cyclonic vorticity advection available. On the eastern parts of South Africa, there was presence of anticyclonic vorticity advection which supported the development of a ridge on the east of South Africa. Anticyclonic vorticity advection present on the 500-hPa level showed signs of acting independently from the continental tropical low but had a big impact in assuming the direction of the developed ridge.

Cold-air advection dominated over interior with presence of vorticity advection in and around the weakening continental tropical low-pressure system. The geopotentials were still falling but not as deep as they were falling during the above explained time steps, with a difference of 5gpm. Where geopotentials around the low fell from 5890 to 5885gpm. Even though the cold-air advection was not strong, it was still enough for the identification of the location of the continental tropical low and for geopotentials to fall.

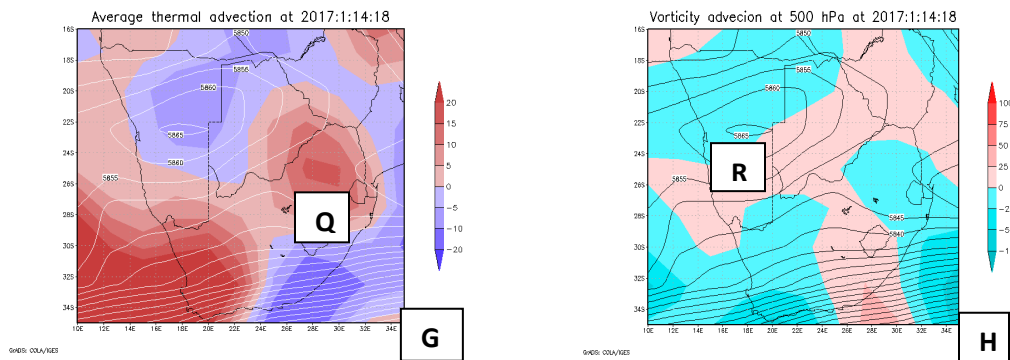


FIGURE 3.3.1: (G) Thickness average advection for January 14<sup>th</sup> 2017 and (H) Vorticity advection at 500 hPa

Cyclonic vorticity advection is present over the interior of the continent as it can be observed on Figure 3.3.1 H, in and around the weakening continental tropical low-pressure system. It's not intense but still enough for the characteristics of the low-pressure system to be identified. The low-pressure has moved further away from the South African border towards Botswana. It has followed the direction of movement of vorticity advection. On the west of the weakening low-pressure system, there was presence of anticyclonic vorticity advection as indicated by **R** on Figure 3.3.1 H, which serve assistance with the development of a ridge and also predicts the movement of the ridge to move northeast of Botswana and from areas around Namibia.

On the eastern parts of South Africa, there is cold-air advection which does not have any influence on the continental tropical low-pressure system situated in Botswana (Figure 3.3.1G). The cold-air advection assists in deepening the easterlies developed along the region of Durban and also deepens the trough along areas of Swaziland indicated by **Q** on figure G. Around the area of the weakening continental tropical low-pressure system, warm air advection is present but with geopotentials falling as opposed to them rising by the quasi-geostrophic approximation (Carroll, 1997). This is an indication that cyclonic vorticity advection was dominating over the warm-air advection present resulting in the existence of the low-pressure system and falling of geopotentials at the 500-hPa level.

**Table 2:** Meteorology data collected for the 3<sup>rd</sup> of January 2017 at 18:00 Z to the 5<sup>th</sup> of January 2017 at 18:00Z

Date	(3 January 2017)	(4 January 2017)	(4 January 2017)	(4 January 2017)	(4 January 2017)	(5 January 2017)	(5 January 2017)	(5 January 2017)	(5 January 2017)
Cold air advection	YES	YES	YES	NO	NO	NO	NO	YES	YES
Geopotential before	5856	5855	5855	5855	5860	5855	5865	5875	5870
Geopotential after	5848	5855	5855	5860	5850	5865	5870	5870	5870
Cyclonic vorticity advection	YES								

**Table 3:** Meteorology data collected for the 6<sup>th</sup> of January 2017 at 00:00 Z to the 8<sup>th</sup> of January 2017 at 00:00 Z

Date	(6 January 2017)	(6 January 2017)	(6 January 2017)	(6 January 2017)	(7 January 2017)	(7 January 2017)	(7 January 2017)	(7 January 2017)	(8 January 2017)
Cold air advection	YES	0	0	NO	YES	0	NO	0	YES
Geopotential before	5875	5880	5880	5880	5885	5865	5855	5850	5855
Geopotential after	5865	5880	5880	5880	5870	5855	5850	5850	5855
Cyclonic vorticity advection	NO	NO	NO	YES	NO	YES	YES	YES	NO

**Table 4:** Meteorology data collected for the 8<sup>th</sup> of January 2017 at 06:00 Z to the 10<sup>th</sup> of January 2017 at 06:00 Z

Date	(8 January 2017)	(8 January 2017)	(8 January 2017)	(9 January 2017)	(9 January 2017)	(9 January 2017)	(9 January 2017)	(10 January 2017)	(10 January 2017)
Cold air advection	YES	YES	YES	YES	YES	YES	NO	YES	0
Geopotential before	5855	5835	5850	5850	5845	5850	5850	5850	5845
Geopotential after	5835	5850	5850	5845	5845	5845	5850	5845	5850
Cyclonic vorticity advection	YES	NO	YES	YES	YES	YES	YES	YES	NO

**Table 5:** Meteorology data collected for the 10<sup>th</sup> of January 2017 at 12:00 Z to the 12 of January 2017 at 12:00 Z

Date	(10 January 2017)	(10 January 2017)	(11 January 2017)	(11 January 2017)	(11 January 2017)	(11 January 2017)	(12 January 2017)	(12 January 2017)	(12 January 2017)
Cold air advection	YES	YES	YES	YES	NO	NO	YES	YES	YES
Geopotential before	5855	5860	5860	5870	5855	5860	5890	5865	5845
Geopotential after	5850	5855	5870	5855	5860	5865	5885	5845	5860
Cyclonic vorticity advection	YES	YES	NO						

**Table 6:** Meteorology data collected for the 12 of January 2017 at 18:00 Z to the 14<sup>th</sup> of January 2017 at 00:00 Z

Date	(12 January 2017)	(13 January 2017)	(13 January 2017)	(13 January 2017)	(13 January 2017)	(14 January 2017)
Cold air advection	YES	YES	YES	YES	0	NO
Geopotential before	5860	5850	5850	5855	5850	5850
Geopotential after	5850	5850	5855	5850	5850	5845
Cyclonic vorticity advection	YES	NO	NO	NO	0	YES

The tables above show periods of when the quasi-geostrophic approximation assumptions occurred and the results expected were observed. That is, cold-air advection to occur simultaneously with cyclonic vorticity advection and geopotentials falling. Warm-air advection occurring simultaneously with anticyclonic vorticity advection and as a result, a rise in geopotentials.

Take into account that geopotentials observed were not all taken from the core of the developed low-pressure system, but areas around the low-pressure system. The colour green represents areas and time steps where there was correspondence between vorticity advection at 500-hPa and

the average thickness advection. The red colour represents areas where there was no correspondence between the observed parameters but there was still a change in geopotentials due to one meteorology parameter dominating over the other.

There are instances where vorticity advection and thickness advection would not influence the continental tropical low in terms of movement or deepening. Geopotentials would remain the same. At times, there would be cold-air advection, cyclonic vorticity advection and the geopotentials do not fall.

4. Conclusions

- Thermal and vorticity advection influence the movement and deepening of continental tropical low-pressure systems over southern Africa. Thermal and vorticity advection in the tropics

do not always have to be present at the same time for the low-pressure system at 500-hPa to assume its properties. At some cases, one term dominates over the other during the development and maturity stages of the continental tropical low-pressure system.

It is recommended that the study is carried out in a more detailed approach where by other parameters of the atmosphere are considered and observed in order to better the understanding of how continental tropical low- pressure systems develop. Parameters such as the omega equation, thermodynamic equation, and application of models that will give independent calculations of the vorticity advection and thermal advection in much more advanced display. To also help in the understanding of the influence of relative vorticity over land during development. Secondly, the study should be carried out in comparison with the applications and assumptions of Petterssen's development equation.

### **Acknowledgements**

My study leader Dr L.L. Dyson is acknowledged with gratitude of all her guidance and efforts as my supervisor. The South African Weather Service for sponsoring my studies and the Water Research Commission for the sponsor of the research.

### **References**

American Meteorological Society: Vorticity advection, 2012, <http://www.glossary.ametsoc.org/wiki/vorticity> advection, 2017.

Berman F., Chien A., Cooper K., Kennedy K., Torczon L., Dongarra J., Foster I., Gannon D., Johnsson L., Kesselman C., Reed D., Wolski R., 2001: The GrADS Project: Software support for High-Level Grid Application Development; The international journal of High Performance computing Applications, vol 15, No.4, P. 327- 344

Carroll, E.B., 1997: Use of dynamical concepts in weather forecasting. *Meteorology Applications*, 4, p. 340-352.

EUmetrain: Tropical Lows in Southern Africa, 2012, <http://www.eumetrain.org/satmanu/CMs/CTL/print.htm#header>, 2017.

Holton, J.R., 2004: An introduction to Dynamic Meteorology, Fourth edition, Elsevier academic press, California USA, p. 157 – 394

Kanamitsu, M., Ebisukazi, W., Woollen, J., Kengyang, S., Hnilo, J., Fiorino, M., Potter, G.L., 2002: NCEO-DOE AMIP-II REANALYSIS (R2):AN updated NCEP/NCAR reanalysis covering 1971- present feature new physics and observed soil moisture forcing and also eliminates several previous errors (2002) *American Meteorological society*, Bams, 83-11-1631.

Lackmann, G., 2011: Midlatitude Synoptic Meteorology: dynamics, analysis, and forecasting, *American Meteorological Society*, USA, p.105 -113

Santurette P., Georgiev C. G., 2005: Weather Analysis and Forecasting, Applying Satellite Water Vapour Imagery and Potential Vorticity Analysis, Elsevier academic press, California USA, p. 03-11

Taljaard J.J. 1995: The Synoptic Climatology of South Africa in January and July. South African Weather Bureau, Technical paper no -14, p.28

# A DECADE OF HEAT STRESS CONDITIONS OVER GAUTENG PROVINCE, SOUTH AFRICA

Katlego Ncongwane<sup>1</sup>, Venkataraman Sivakumar<sup>2</sup>, Joel Botai<sup>1</sup>, Siphesihle Sithole<sup>1</sup>, Christina Botai<sup>1</sup>, Nosipho Zwane<sup>1</sup>, Abiodun Adeola<sup>1</sup>

<sup>1</sup>South African Weather Service, 01 Ecopark, Ecogrades Block B, Cnr Olievenhoutbosch and Ribbon Grass Streets, Centurion, 0157, South Africa

<sup>2</sup>University of KwaZulu-Natal, South Africa, Durban, South Africa

## Abstract

Exposure to extreme heat conditions can pose significant health risks, especially for the population with pre-existing medical conditions. This work aims to calculate, evaluate and develop an operational heat stress tool hereafter the Heat Stress Watch Index for South Africa based on Apparent Temperature AT°C index. AT°C was used to evaluate the thermal components and develop a climatology of different locations across the Gauteng Province. The results pointed that areas in Gauteng with relatively more hours characterized by hot conditions are located mostly in the northern region of the province, notwithstanding inherent Urban Heat Island (UHI) characteristics.

**Keywords:** Apparent Temperature, Heat stress, Health-risk, Urban-Heat-Island, Medical conditions

## 1. Introduction

The Intergovernmental Panel on Climate Change (IPCC) models show that air temperature will continue to rise into the 21<sup>st</sup> century both locally and globally. Models and published scientific papers (Kruger and Shongwe, 2004; Department of Environmental Affairs, 2012; Kruger and Sekele, 2013; Garland *et al.*, 2015) are showing an increase in temperature for the most part of South Africa which combined with high humidity can have adverse effects on the human body. Climate change is projected to increase the severity, frequency, and duration of extreme heat events, which may put more people at risk for heat-related mortality and morbidity. Negative implications of heat are well documented and include both acute and chronic effects. Acute effects include heat edema, rash, cramps, stroke and heat exhaustion with the following symptoms: heavy sweating, weakness, dizziness, visual disturbances, intense thirst, nausea, headache, vomiting, diarrhoea, muscle cramps, breathlessness, palpitations, tingling and numbness of the hands and feet (Opitz-Stapleton, 2016). In worse cases leading to brain damage, internal organ failure which may lead to coma (King and Crews, 2013). People often use air temperature as an indicator of how comfortable they feel. However, air temperature is only one factor in the assessment of thermal stress or comfort. A realistic assessment considers environmental factors such as air temperature, air humidity, and radiation from the sun, personal factors such as clothing being worn and the person's level of physical activity. This work will calculate heat stress levels based on Apparent Temperature AT°C (Steadman, 1984; 1994; Buzan, Oleson and Huber, 2015) for the Gauteng Province. AT°C was invented in the late 1970s (Steadman, 1979) and it was modified in the early 1980s and 1990s to include the effect of sun and wind (Steadman, 1984; 1994). The earlier AT°C version (Steadman, 1979) assume there is no solar radiation and doesn't provide a correction for wind. AT°C is defined as what the temperature feels like on a human body when relative humidity, wind speed and water vapour is combined with air temperature for outdoor conditions. Several formulations exist for AT°C e.g. Australian (Steadman, 1984; 1994; Buzan, Oleson and Huber, 2015), National Weather Service (NWS) (Steadman, 1979; Rothfus, 1990) and various algorithms compared in Anderson, Bell and Peng (2013).

## Data and Methodology

The Gauteng Province (26°16'14.7360"S, 28°6'44.1648"E; 1500 m) is the smallest of the nine provinces in South Africa, it is located in the northeastern part covering the total land area of about 16,548 km<sup>2</sup> which is approximately 1.4% of South Africa's land area. The province has a total population of 12.27 million (STATS SA, 2011) with about 60 towns. Gauteng is divided into three (3) metropolitan municipality (Figure 1), (1) the City of Ekurhuleni, (2) the City of Johannesburg and (3) the City of Tshwane, metropolitan municipalities, as well as two district municipalities, which are further subdivided into six local municipalities.

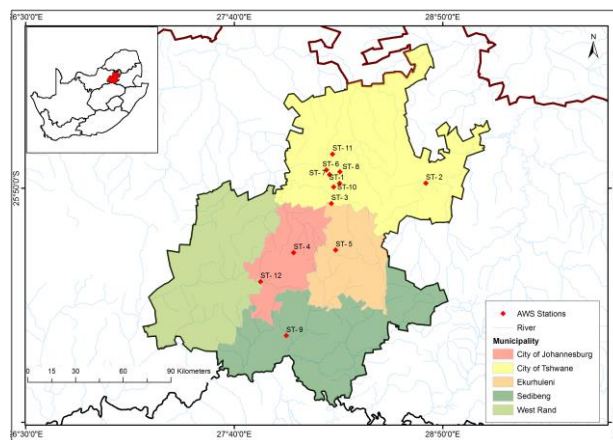


**Figure 1:** Map of Gauteng Province with 12 AWS stations from SAWS

The dataset used consists of 10 years (2006-2016) of datasets from 12 Automatic Weather Stations (AWS) distributed across Gauteng. The data was sourced from climate service at the South African Weather Service (SAWS).

Apparent Temperature was calculated using the Australian Bureau of Meteorology (Eq. 1) (Buzan, Oleson and Huber, 2015).

$$AT = T_c + \frac{3.3e_{RH}}{1000} - 0.7u_{10m} - 4, \quad (1)$$

Where  $T_c$  is the air temperature (°C) or dry bulb temperature (°C),  $u_{10m}$  is the wind velocity (m s<sup>-1</sup>) measured at the 10 m height. Water vapour ( $e_{RH}$ ) in pascals is calculated (Equation (2)) from the relative humidity ( $RH$  in %) and saturated vapor pressure ( $e_{sPa}$ , also in pascals)

The saturated vapour pressure is calculated using the following (Eq. 2).

$$e_{RH} = (RH / 100)e_{sPa} \quad (2)$$

The calculated indices were grouped into risk categories comprising of caution (27-31°C), extreme caution (32-38°C), danger (39-50°C) and extreme danger (>51°C). Values below 26°C, are considered as normal. These categories are accompanied by potential health impact chart messaging adopted by the South African Medical Research Council (SAMRC) from the United States of America National Weather Service (NWS; Figure 2).

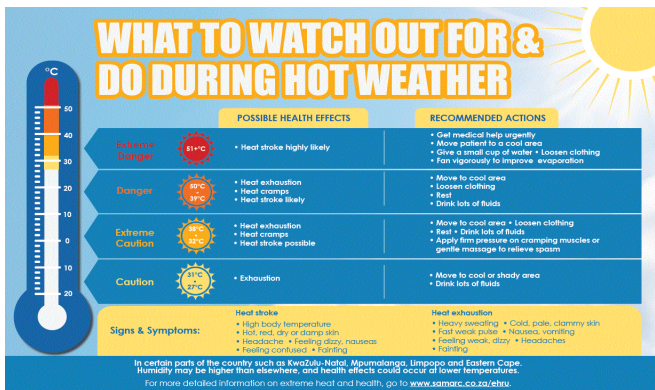


**Figure 2:** Apparent Temperature AT°C thresholds and potential health impacts. Adapted from National Weather Service Weather Forecast Office: Amarillo. What is the Heat Index? Available online: <http://www.srh.noaa.gov/ama/?n=heatindex> by SAMRC

## 2. Results and Discussion

The computed climatology shows that most hours, including night-time hours are characterized by AT°C values of 26°C and below. Figure 3 indicates that when AT°C is within this range, described as “normal”, no health effects are imminent. The first dominant risk category is “caution” (27-31°C) which results in heat exhaustion, which is an acute heat related illness associated with faint or dizziness, excessive sweating and cool, pale and clammy skin symptoms.

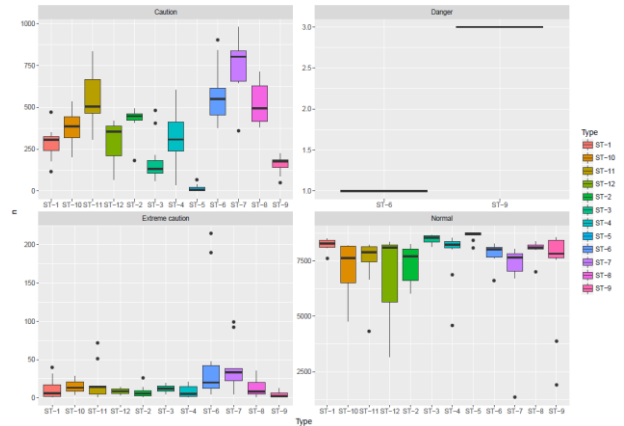


**Figure 3:** Hourly frequency and risk category climatology per station

During the “caution” risk category, people are advised to move to cooler or shady areas and to drink lots of fluids, particularly, water. The second dominant risk category is “extreme caution” (32-38°C). Serious medical conditions can occur as a result of heat during this risk category, includes heat exhaustion, heat cramps and in some cases heat stroke which can cause shock, brain damage, internal organ failure and can lead to coma. For the 10 years of analysed data, only 4 hours (1 hour at Pretoria Eendracht (ST-6) station located in the Central Business District (CBD) and 3 hours at Vereeniging station) reached the danger risk category of 39-50°C. During this extreme heat range, the body overheats, causing severe heat illness which necessitates immediate medical intervention. People who are vulnerable like children, adults, with pre-existing sickness and pregnant woman are at most risk to heat-related illnesses.

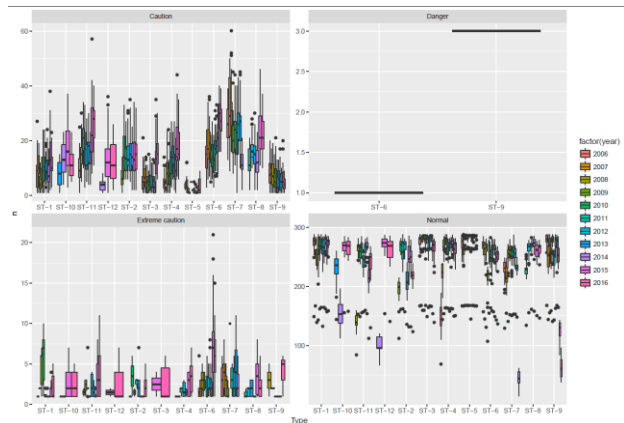


**Figure 4:** Hourly frequency and risk category climatology per station

The hottest area represented by Pretoria Eendracht (ST-6) station is located in the CBD in the inner part of the city. It exhibited higher AT°C heat indices than the neighbouring locations. This may be attributed to the Urban Heat Island (UHI) effect which makes this geographical location prone to increased temperatures of 1-3 °C and in some cases high humidity, thus contributing to general human discomfort and accompanying heat-related illnesses, in worse cases death.

The other stations within Tshwane municipality that experience higher AT°C indices after the CBD station are Unisa (ST-7), Wonderboom (ST-11), Bronkhorspruit (ST-2), University of Pretoria (ST-8) and Bolepi house (ST-1) stations in Erasmusrand. Johannesburg Botanical Gardens station (ST-4), located in the Emmarentia suburb and approximately 6 km from the Johannesburg CBD, is the fourth station exhibiting higher AT°C indices after 3 stations in Pretoria.

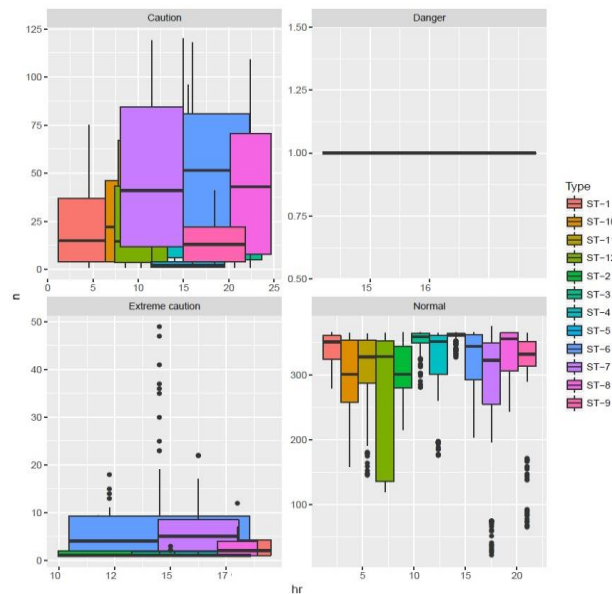


Figure 5: AT°C Diurnal variation per risk category per station

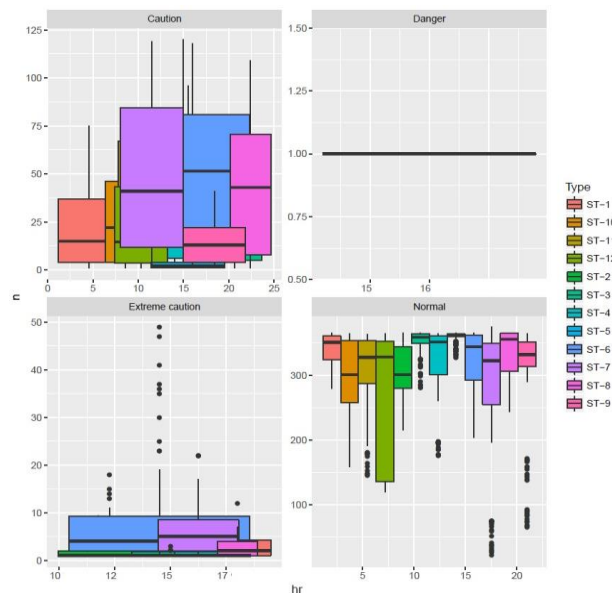


Figure 5 shows AT°C diurnal variation per station. The Pretoria Eendecht (ST-6) station in the CBD experience “caution” and “extreme caution” between 09:00 to 15:00 South African Standard Time (SAST). AT°C values for the University of Pretoria station (ST-8) experience higher AT°C values between 11:00 and 19:30.

As expected higher AT°C values are experienced in spring (SON) and summer (DJF) and some few instances of elevated

heat are noted during autumn (MAM), though very seldom (refer to Figure 6).

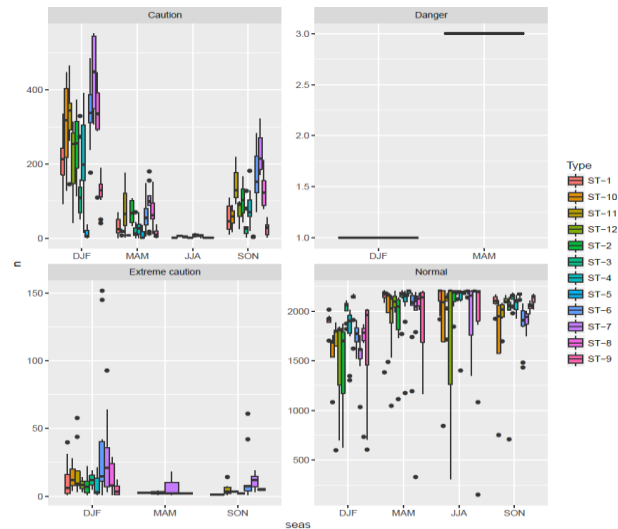


Figure 6: Seasonal AT°C variation per risk category per station

#### 4. Conclusions

Analysis results from this study show an overall increase in the frequency of occurrences across all the risk categories. The most dominant risk categories is caution. The second dominant risk category was determined to be the extreme caution, which is often associated with heat exhaustion, heat cramps and in some cases heat stroke. Caution to extreme caution conditions mostly occurred in the afternoon, just after 15:00 SAST, when the heat stress dangers are not as obvious, especially for school children conducting extramural activities. In addition, results indicate that areas in Gauteng with relatively higher numbers of hours characterized by hot conditions are located mostly in the northern region of the province, notwithstanding the UHI characteristics. The results of this study highlight the necessity for heat interventions such as heat advisory warnings to help avert the effects of the dangerous combination of high temperatures and humidity that can lead to heat-related illnesses.

#### 5. Acknowledgments

The authors acknowledge the invaluable support of the South African Weather Service’s staff and express thanks to the South African Medical Research Council for allowing SAWS to use the adapted apparent temperature thresholds.

#### 6. References

Anderson, G.B, Bell, M.L, Peng, R.D. (2013). ‘Methods to calculate the heat index as an exposure metric in environmental health research’. *Environmental Health Perspectives* 121(10):1111-1119

Buza, J.R. Oleson, K. and Huber, M. (2015) ‘Implementation and comparison of a suite of heat stress metrics within the Community Land Model version 4.5’ *Geosci. Model Dev.*, 8, 151–170, 2015

- King, B. and Crews, K. (2013) 'Ecologies and politics of health', Routledge Press/Taylor and Frances Group, Routledge Studies in Human Geography Series. doi: 10.4324/9780203115527.
- Kruger, A. C. and Sekele, S. S. (2013) 'Trends in extreme temperature indices in South Africa: 1962-2009', *International Journal of Climatology*, 33(3), pp. 661–676. doi: 10.1002/joc.3455.
- Kruger, A. C. and Shongwe, S. (2004) 'Temperature trends in South Africa: 1960-2003', *International Journal of Climatology*, 24(15), pp. 1929–1945. doi: 10.1002/joc.1096.
- National Weather Service Weather Forecast Office: Amarillo, T.X. What Is the Heat Index?
- Garland, R. et al. (2015) 'Regional projections of extreme apparent temperature days in Africa and the related potential risk to human health', *International Journal of Environmental Research and Public Health*, 12(10), pp. 12577–12604. doi: 10.3390/ijerph121012577.
- Opitz-Stapleton, S. Sabbag, L. Hawley, K. Tranc, P. Hoang, L. Nguyen, P.H. (2016) 'Heat index trends and climate change implications for occupational heat exposure in Da Nang, Vietnam' *Climate Services*, 2(1): 41–51.
- Rothfusz, L.P. (1990) 'The Heat Index "Equation" (or, More Than You Ever Wanted to Know About Heat Index)' SR 90–23. Fort Worth, TX: National Oceanic and Atmospheric Administration, National Weather Service, Office of Meteorology
- Steadman, R.G (1979) 'The assessment of sultriness. Part I: A temperature-Humidity Index based on human physiology and clothing science'. *Journal of applied meteorology*. 18, 862-873
- Steadman, R.G. (1984) 'A universal scale of Apparent temperature'. *Journal of climate and applied meteorology*. 23, 1674-1687
- Steadman, R.G. (1994) 'Norms of apparent temperature in Australia'. *Aust Met Mag* 43:1–16.

## ***An evaluation of a ten-year lightning variability over the Western Cape Province, South Africa using weather circulation classification***

Samkelisiwe Thwala<sup>1</sup>, Stephanie Landman<sup>2</sup>, Morné Gijben<sup>2</sup>, Christien J. Engelbrecht<sup>3,1</sup>

<sup>1</sup>University of Pretoria, Pretoria, South Africa

<sup>2</sup>South African Weather Service, Pretoria, South Africa

<sup>3</sup>Agricultural Research Council, Pretoria, South Africa

### ***Abstract***

The aim of this study was to analyse the general circulation patterns and compare it to corresponding rainfall patterns and lightning events for a ten-year period over the Western Cape Province of South Africa from 2007 to 2017, by applying an atmospheric circulation classification method. This assisted in the understanding of the relationship between synoptic circulation and lightning variability. It was found that there was a significant deviation in frequency of circulation types between 2011 and 2017 resulting in an increase in lightning activity but not necessarily in rainfall averages.

Keywords: Lightning, Drought, Circulation weather patterns, Winter rainfall region, SOM, Clusters

### ***Introduction***

South Africa is regarded as a country that is prone to lightning, since it receives on average between 10 to 15 lightning flashes per kilometre squared per year in regions over the eastern escarpment and the Highveld (Gijben, 2012). Lightning events usually occur during October to March in the country, especially in the month of December (Bhavika, 2007; Gijben, 2012).

Since South Africa is prone to lightning events, the South African Weather Service (SAWS) installed a Vaisala lightning detection network (LDN) throughout the country in 2005 (Gijben, 2012). Sensors are used to measure cloud-to-ground lightning with great precision, with a small percentage of cloud lightning also detectable (Gijben, 2012).

The annual update of the LDN data for 2017 indicated an overall increase in lightning activity over the Western Cape Province (WCP; Fig 1), which is in contrast to the drought experienced over the region between 2014 and 2017. South Africa is divided into  $0.1 \times 0.1$  degree grid boxes. Lightning flash data for each year is utilised to calculate the lightning flash density. This is achieved by counting the amount of lightning flashes that occurred inside each grid box during the year and dividing this total by the area of the grid box. This gives the lightning ground flash density per square kilometre per year (flashes/km<sup>2</sup>/year). It is seen in Fig 1 that the lightning flash density over the WCP had a larger area where the density falls between 0.1 and 1. The only other year comparable to 2017 is 2009.

This increase in lightning activity could be an indication of more extreme events. Several studies have shown that lightning variability can be influenced by changes in local

weather patterns and that there's a relationship between weather patterns, lightning and precipitation type (Felix *et al*, 2010; Ramos *et al*, 2011).

In this study, similar to determining the relationship between rainfall and circulation patterns over South Africa (Landman *et al*, 2016), the relationship between circulation, rainfall and lightning can be done. The aim of this study is to lay a sound scientific foundation to determine the possible causes of lightning variability in order to expand it to the whole of South Africa. This study also forms part of a greater in-depth research on the dynamics, causes and impacts of the 2014 – 2017 drought over South Africa's winter rainfall region.

### ***Data and Methodology***

Three sets of data were used in this study; lightning, daily rainfall estimates and synoptic circulation patterns. The period under investigation is January 2007 to December 2017 and the domain of interest is  $16.05^{\circ}\text{S}$  to  $35.9625^{\circ}\text{S}$  and  $10.95^{\circ}\text{E}$  –  $38.85^{\circ}\text{E}$  which corresponds to the range of detection of the LDN. The Self-Organising Maps (SOM) technique was used to determine the synoptic circulation types during the 10-year period. The classification was done using 12 UTC geopotential meters at 850 hPa pressure level ERA-Interim data (ERA-Int).

Both data sets, after being normalized, was ingested into the SOM software to create a  $7 \times 5$  node matrix. The result is 35 associated circulation and rainfall patterns, which was subsequently ingested into a Wards clustering system which assisted in determining the major circulation patterns.

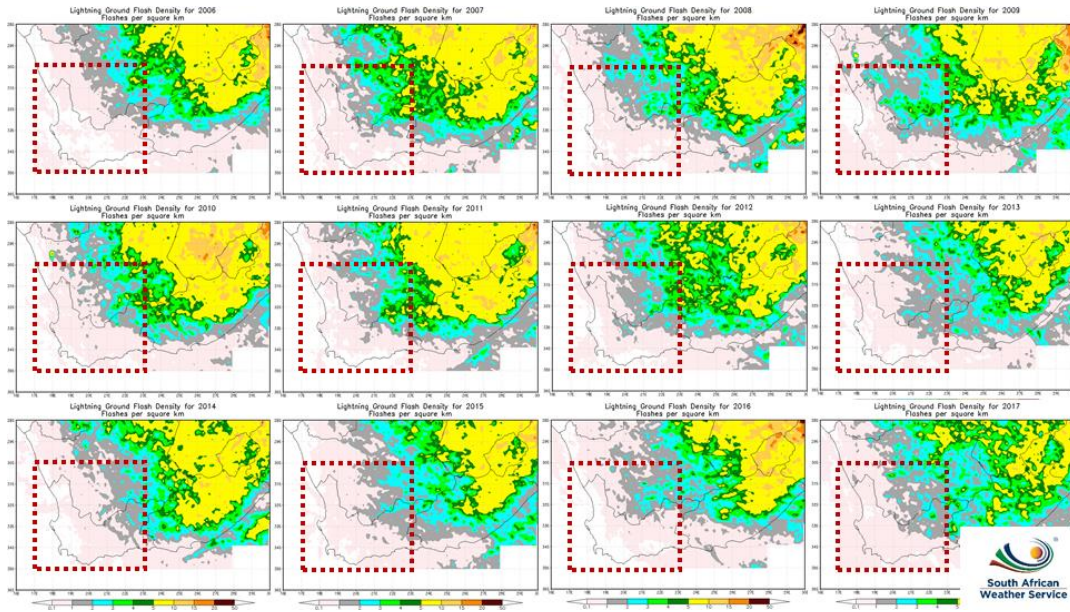


Figure 1: Lightning Ground Flash Density (flashed per square km) for 2007 to 2017 over the southwestern parts of South Africa with the WCP (domain of interest) is indicated by the red square.

The resulting 7 clusters were then named according to the spatial distribution of the rainfall and monthly occurrence of the nodes. The seven seasonal clusters were identified as Summer 1 (S1; October to March with some occurrences May and June), Summer 3 (S3; mostly November to February), Summer 2 (S2; mostly March and October), Transition 1 (T1; occurrences still in summer month but more occurring mid-year), Transition 2 (T2; more occurrences during mid-year but still some events during summer), Winter 1 (W1; mostly June to August) and Winter 2 (W2; mostly May to October).

Lightning data were processed to contain the number of strokes per day on a gridded field with a spatial resolution of  $0.0375^\circ \times 0.0375^\circ$ . The grid then ultimately contains the number of lightning strokes over a 24-hour period from 06:00Z to 06:00Z (corresponding to the daily rainfall totals).

Since the focus of this abstract is the lightning variability over the WCP, the related lightning and rainfall for each node is determined only for this domain. In order to determine the lightning and rainfall associated with each of the 35 nodes, the average daily values were calculated based on the days within each node (equations 1 and 2).

$$AVE = \frac{1}{n} \sum_{i=1}^n rain_i \quad \text{Eq. 1}$$

$$Area\ AVE = \frac{i}{N} \sum_{j=1}^N AVE_j \quad \text{Eq. 2}$$

Where  $n$  is the number of days within the node,  $rain$  is the daily rainfall total,  $N$  is the number of grid points within the domain and  $AVE$  is the average calculated in Eq. (1) per grid box. Lightning was calculated similarly where  $rain$  in Eq. 2 will be replaced by *lightning* (number or strokes per grid box). These values were also calculated for each year individually in order to determine variability in the number of days in each node.

Correlations (Eq. 3) were also calculated in order to determine the relationship of the area averages of lightning and rainfall as well as their relationships to the number of events per node per circulation type.

$$COR = \frac{\sum(i-\bar{i})(j-\bar{j})}{\sqrt{\sum(i-\bar{i})^2 \sum(j-\bar{j})^2}} \quad \text{Eq. 3}$$

In Eq.(3),  $\bar{i}$  and  $\bar{j}$  are the sample means for the nodes contributing to the circulation pattern.

### Results

The  $7 \times 5$  matrix in Fig. 2 indicate the spatial distribution of the rainfall for each node associated with the 850 hPa synoptic circulation. It is seen that there is a clear demarcation of rainfall over the northeastern summer rainfall region (node 7) and the southwestern winter rainfall region (node 29). The monthly indications of event occurrence for each node is indicated in Fig. 3. From these matrices and the results from the Wards clustering, the 7 major clusters were identified and are indicated.

In Fig. 4 the average lightning events per node are indicated, showing that in node 35 which is associated with a winter circulation and rainfall pattern, there is a similar amount of lightning activity as during a node with summer rainfall characteristics (e.g. node 16). When comparing nodes 7 and 19, the number of days are similar but the lightning activity is significantly different. However, both have low to none lightning activity over the south western parts of the WCP domain.

Similar results were found with the average daily rainfall totals (not shown), however as expected node 16 had significantly less rain than node 35; where the lightning were almost similar.

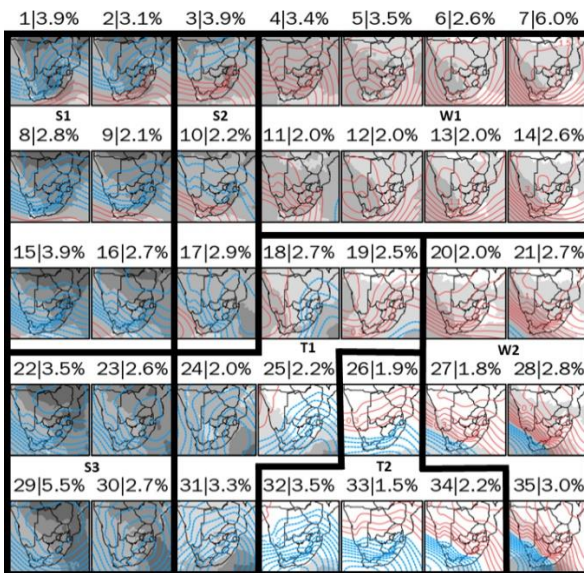


Figure 2: The 35 node matrix indicating 850 hPa circulation patterns (contours) and associated rainfall distribution (shaded). The 7 sub-divided seasonal clusters represent Summer 1 (S1; October to March with some occurrences May and June), Summer 3 (S3; mostly November to February), Summer 2 (S2; mostly March and October), Transition 1 (T1; occurrences still in summer month but more occurring mid-year), Transition 2 (T2; more occurrences during mid-year but still some events during summer), Winter 1 (W1; mostly June to August) and Winter 2 (W2; mostly May to October). The titles for each node indicate the node number and percentage of cases contributing to the node.

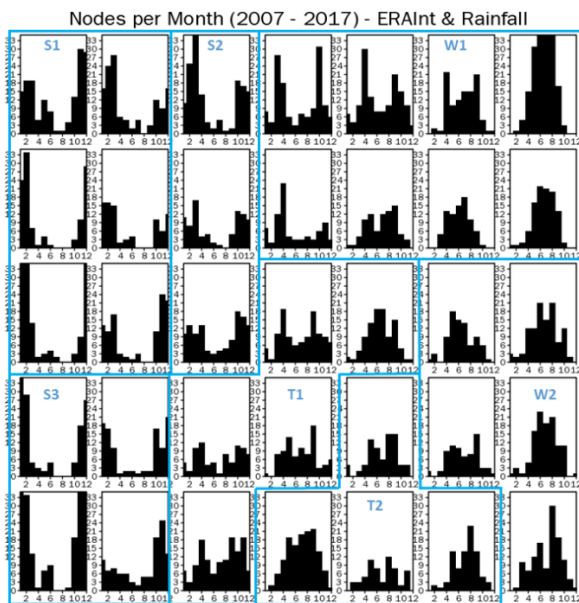


Figure 3: The 35 node matrix indicating the monthly distribution of the occurrence of events within each node (x-axis is 12 months and y-axis occurrences per month).

In Fig. 5 the 7 synoptic types were divided into years and the number of days/events per node captured. In Fig. 5a it is seen

that there was a general decline (increase) in S1 and S3 (S2) events from 2011 to 2016. In 2017 both S1 and S3 events increased while S2 events decreased. Looking at the winter circulation patterns in Fig. 5c, both W1 and W2 patterns had a steady increase in events from 2011 to 2017 (apart from W2 in 2016). For the transition circulation patterns (T1 and T2; Fig. 5c) there is a similar decline in the number of events from 2011 to 2017 as with S1 and S3.

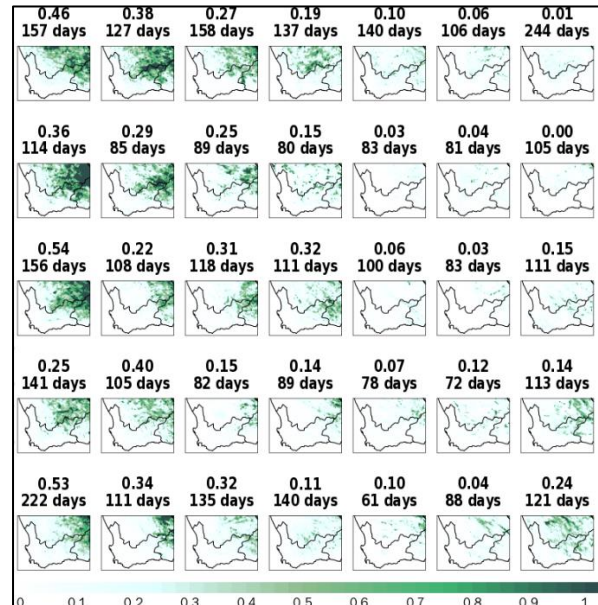


Figure 4: The 35 node matrix indicating the average spatial lightning events for each node (based on Eq. 1). The title indicate the area average of the WCP domain for each node (based on Eq. 2).

The correlation values are represented with each seasonal circulation pattern per year in Figs. 6a to c. Looking at Fig. 6a there is a stronger positive correlation for S1 and W2 patterns indicating that with the increase/decrease in rainfall averages there's also an increase/decrease in lightning averages. However, still focusing on S1 and W2, there's a shift in correlations from 2011 to 2017. The same pattern is seen when looking at the correlation between number of days and average lightning (Fig 6b). The strongest correlation between number of days per node and lightning averages are during W2 conditions. For number of days and rainfall averages (Fig 6c), the correlation is almost similar for S2 and W2 events.

**Conclusion**

It is shown and as expected that different circulation patterns the rainfall and lightning events are different. The results indicate that as there is a positive correlation between S1 and S2, contrasted with the lightning averages. The same also occurs for T1, T2, W1, W2 and lightning averages, as it indicates direct proportionality. There is also a clear indication of deviations of events from 2011 to 2017 (given the relatively small sample size). These deviations in events per node has an effect on the number of lightning events as was shown in Figures 5 and 6. Results of changes in spatial lightning events are not discussed in this paper but will be presented.

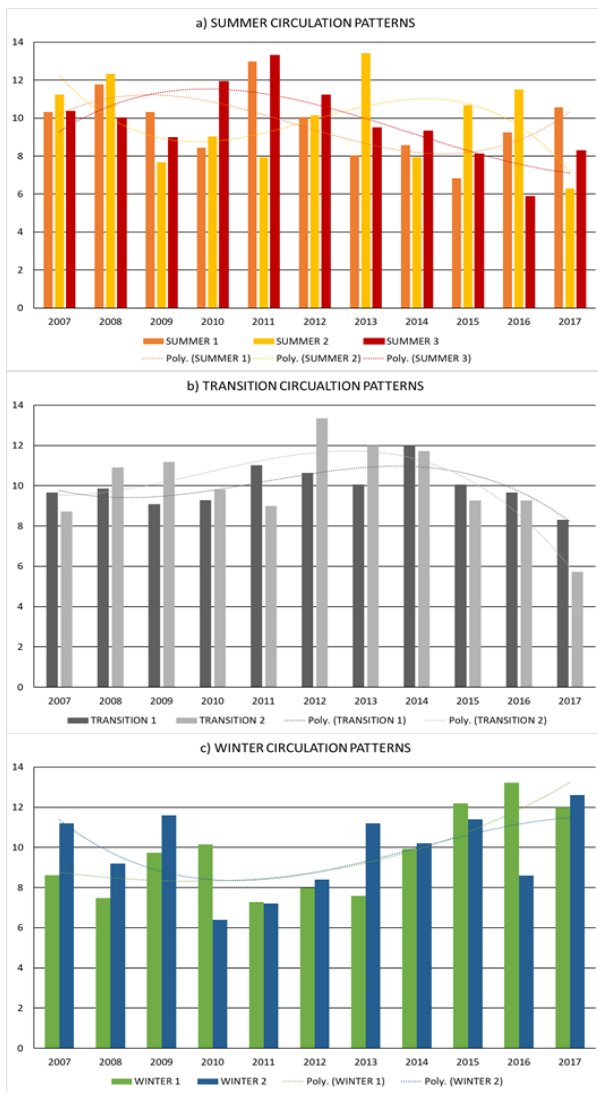


Figure 5: Number of events per circulation pattern per year for a) Summer patterns, b) transition patterns and c) winter patterns. The dotted lines indicate the fitted polynomial trend per circulation pattern.

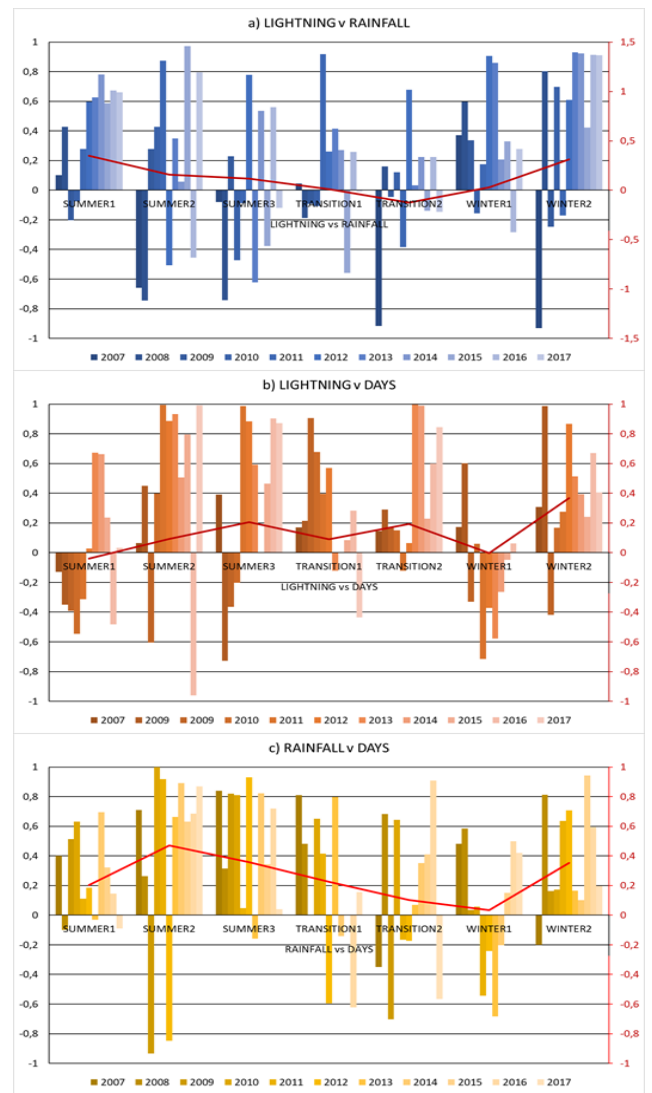


Figure 6: The correlation per year per circulation pattern for a) lightning and rainfall averages, b) lightning averages and number of days c) rainfall averages and number of days. By analysing these graph, it clear that a) lightning and rainfall averages show mostly a positive correlation, with very a more strong positive correlation during S1 and W2. Therefore this indicates that the increase in rainfall averages will lead to an increase in lightning averages during S1 and W2. T2 shows a negative correlation, hence the opposite will occur here

References

Bhavika, B., 2007. The Influence of Terrain on Elevation of Lightning Density in South Africa. 30 November.  
 Felix , P. B., Priyadarsini, G. & Girish, E., 2010. A possible relationship between Global Warming and Lightning Activity in India during the period 1998-2009.  
 Gijben, M., 2012. The Lightning Climatology of South Africa. *South African Journal of Science*, Volume 108, p. 10.  
 Landman, S., Engelbrecht, C., Mason, S. & Pegram, G., 2016. Evaluation of the predictability of rainfall over South Africa by regional and global weather prediction models. *32 Annual conference of South African Society for atmospheric sciences*, Volume 32.  
 Novella, N. S. & Thiaw, W. M., 2012. African Rainfall climatology Version 2 for Famine early Warning System. *Journal of Applied Meteorology and Climatology*, Volume 52.

Ramos, A. M. et al., 2011. Cloud to ground lightning activity over Portugal with circulation weather types. *Elsevier*, pp. 84-104.

## Climatological analysis of temperature and pluviometry in Guinea 1960-2016

R. T. LOUA<sup>a\*,c,e</sup>, H. BENCHERIF<sup>a,d</sup>, N. MBATHA<sup>b</sup>, N. BEGUE<sup>a</sup>, Z. BAMBA<sup>c</sup> and V. SIVAKUMAR<sup>d</sup>.

<sup>a</sup>Laboratoire de l'Atmosphère et des Cyclones, UMR 8105 CNRS, Université de la Réunion, Météo-France, Réunion, France.

<sup>b</sup>University of Zululand, Department of Geography, KwaDlangezwa, 3886, South Africa.

<sup>c</sup>Centre de Recherche Scientifique de Conakry Rogbane, Conakry, BP 1615 Guinea.

<sup>d</sup>School of Chemistry and Physics, Discipline of Physics, University of Kwazulu Natal, Durban, South Africa.

<sup>e</sup>Direction Nationale de la Météorologie de Guinée, Conakry, BP 566, Guinée.

### Abstract

The purpose of this study is to improve the understandings on climate variability in Guinea. The methodology used is based on climatological analysis. The pluviometry and temperature data recorded at 12 meteorological stations were used. The annual variability of temperature shows the semi-annual cycle, and the interannual evolution of monthly mean temperature is characterized by an increasing trend over the years. The pluviometry values seems to indicate a decrease since 1960s, and is characterized by an annual cycle. The northward distributions of the temperature and rainfall show an increase and decrease respectively for the country.

Keywords: Temperature, Pluviometry, Climate variability in Guinea; Climate normal; Semi-annual cycle and annual cycle.

### Introduction

Long-term climate variability can help for estimating its impact on human activities. Climate change can cause prolonged risks leaving people threatened by food shortages and diseases. During the last decade, and particularly since the mid-2000s, the development community has begun to engage seriously with the issue of climate change and its implications for the world's poor, this has led to a growing interaction with the climate research community (Conway, 2011).

Precipitation is a key variable in West Africa in general and more specifically over the Sahel (eco-climatic and biogeographic zone of transition in Africa between the Sahara to the north and the Sudanian Savanna to the south) region where economies, livelihoods and food security are highly dependent on rainfed agriculture Gbobaniyi et al., (2014).

Scientific understanding of the African climate system as a whole is low. For certain regions in Africa, the level of understanding is reasonable, for other parts, such as the Guinea region, very little is known. That's why, in a context of climate change, it is essential to identify the areas or periods which bear the brunt of change and, to analyse the possible variabilities of the climatic parameter such as the temperature.

The specific objective of this study is to provide a climatological analysis of the variability of the temperature as well as the pluviometry in Guinea during 57 years (1960-2016).

Then, after the explanation of methods and instrumentation used, the results are presented and discussed in 4 sections before concluding.

### Data and method of analysis

We first analyzed our data set through statistical approaches. The daily temperature (maximum and minimum) and daily rainfall recorded from 12 stations covering Guinea (Fig. 1) during 57 years (1960-2016) were used. The monthly mean temperatures used in this study were calculated from the daily minimums and maximums measured at these stations.

The monthly rainfall values were obtained by using the sum of daily rainfall for each month. And the annual mean

pluviometry were calculated by averaging the monthly rainfalls for each year. Precipitation and temperature

climatologies, and their interannual variability, were calculated for each station. These climatological means were calculated according to the World Meteorological Organization (WMO) Guidelines on the Calculation of Climate Normals, WMO (2017) by using the reporting period that's from 01 January 1961 to 31 December 1990.

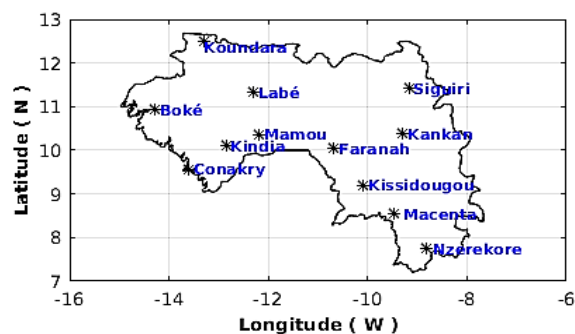


Figure 1: Geo-location of meteorological stations in Guinea.

### Results and discussions

#### Inter annual climatology of temperature and rainfall

Figure 2(a) shows the interannual evolution of monthly mean temperatures measured for the period from 1960 to 2016 for each meteorological stations. A significant observation is that temperatures seems to be higher during March and November. In general, the interannual evolution seems to indicate an increasing temperature trend over the study period. One more thing to point out is the sharp increase of temperatures during 2008 which is consistent with a study by Wang and Wong (2000). In their study, Wang and Wong (2000) reported that the year 1998 temperature averaged for the globe was the highest on record at that time, and the annual mean temperature of China in 1998 was +1.38°C above the normal average.

An exceptional increase in temperature in 1998 is observed in Guinea. This exceptional increase temperatures could be associated to the global warming. Simmons et al., (2008)

highlighted in their global temperature analysis that it was probably only in 1998 that the 1°C above the pre-industrial level was first reached, and this was in the latter stages of a somewhat strong El Niño event. A study by Cleave et al., (2017) confirmed that the 1998 step change was associated with a decrease in winter ice duration of 39 days (a 34% decline), an increase of ~2–3°C in mean surface water temperature (July–September averages), and a 91% increase in July–August evaporation rates, reflecting an earlier start to the summer evaporation season in the Lake Superior.

The figure 2(b) shows the interannual evolution of monthly rainfall from 1960 to 2016 for each station. The annual maximum of the pluviometry is observed in July–August–September. The interannual evolution of the pluviometry shows the inter-seasonality which distinguish between wet years and dry years, and depicts different structure for different station. This variability was also reported by other studies such as Hope et al., (2010) who explained the alternation between dry and wet years in the southwest and southeast of Australia.

In general, the rainfall shows a decreasing trend since 1960's over Guinea. The results reported in this study are consistent with results reported by Villar et al., (2009), where they highlighted that the mean rainfall in the Amazon basin decreases during the 1975–2003 period. Contrary to our result, Descroix et al., (2015) underlined that the pluviometry began to increase in the middle or at the end of decade 1991–2000 for two West-African sub-spaces.

The southern part of Guinea has longest length (8-9 month) of wet season. This observation was also reported in a study by Loua et al., (2017) where they used data from the southern Guinea meteorological station at N'zerekore site.

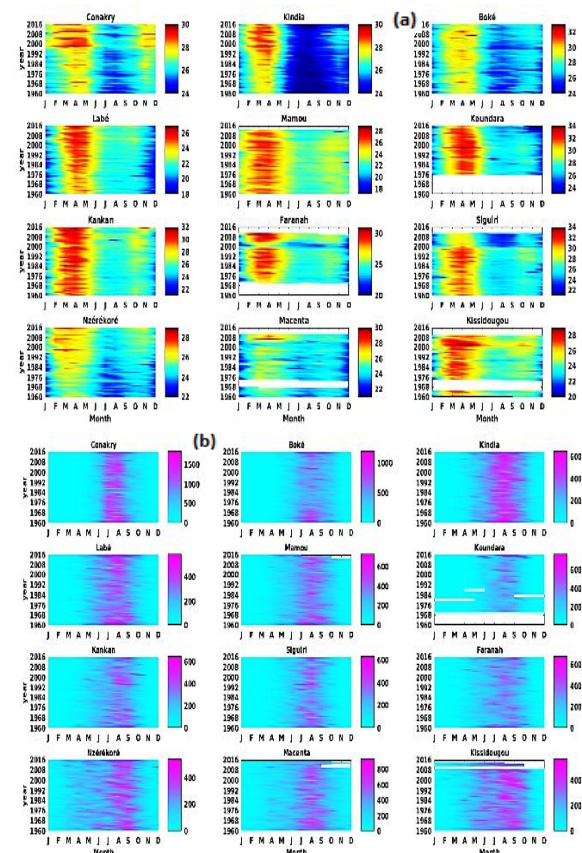


Figure 2: Interannual evolution of temperature (a) and rainfall (b) at 12 stations from 1960 to 2016.

Annual climatology of temperature and rainfall

The yearly variation of the temperature shows an almost identical variability for all the stations, with a bimodal curves (Fig. 3(a)) which correspond to a semi-annual cycle.

It is noteworthy that the temperature is found to be very high in northern part and lowest in the southern and coastal part of the country. Koundara is the hottest region where monthly mean of approximately 32°C is recorded in April. Labé is the coldest region with a yearly mean of approximately 22°C and the minimum value of about 15°C where recorded.

Compared to temperature, pluviometry distribution seem to be opposite, with the coastal and southern regions having high pluviometry relatively compared to the middle and northern parts (Fig. 3(b)). Conakry site seems to be an area most abundantly rainfall with a yearly average of 3753 mm, followed by Macenta with an annual rainfall averaged of 2559 mm. On the other hand, Koundara is observed to be the driest regions with yearly rainfall averaged of 943.4 mm.

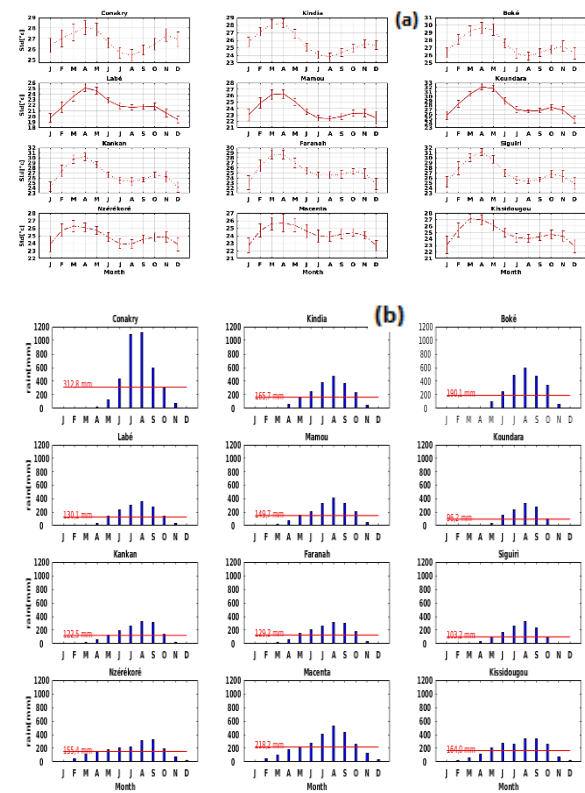


Figure 3: Annual climatology of temperature (a) and rainfall (b) of 12 stations in Guinea.

Global variability of temperature and rainfall

On a national scale, the variability of the temperature and the rainfall is marked by a semi-annual cycle and an annual cycle, respectively. During the year, the minimum temperature may reach 21.6 °C in April and 20.2°C in September, the lowest values are observed in January (15.7°C) and August (20.4°C) (Fig. 4(a)). The maximum temperature rises until about 35.1°C in March and 31.6°C in December and may decrease at the lowest values of 28.3°C in August and 30.6 °C in December. When considering climatological averages, the monthly mean temperature may reach the maximum values of 28.3°C (±2.2) in April and 25.2°C (±1.6) in October with minimum values of 24.0°C (±1.4) in August and 23.8°C (±1.9) in December.

Figure 4(b) shows the monthly climatology of rainfall during the 57 years. In our results, it is observed that in Guinea the rainfall depth can reach 450 mm on average in August and the lowest rainfall quantity in January.

Indeed, this variation is in relationship with the seasonal oscillation of the Inter-Tropical Convergence Zone (ITCZ). A study by Nicholson (1981) reported that the northward displacement of ITCZ may be the first factor responsible for abnormally wet years for the sub-Saharan region. Thus, the rainy season in Guinea as in West Africa is modulated by the West African Monsoon (WAM). Monsoon rainfall over West Africa occurs during the June through September period CLIVR (2017). A study by Cook (2015) also reported that rainfall in the vicinity of the Guinean coast lingers through May and June, while the marine Atlantic ITCZ moves to the north.

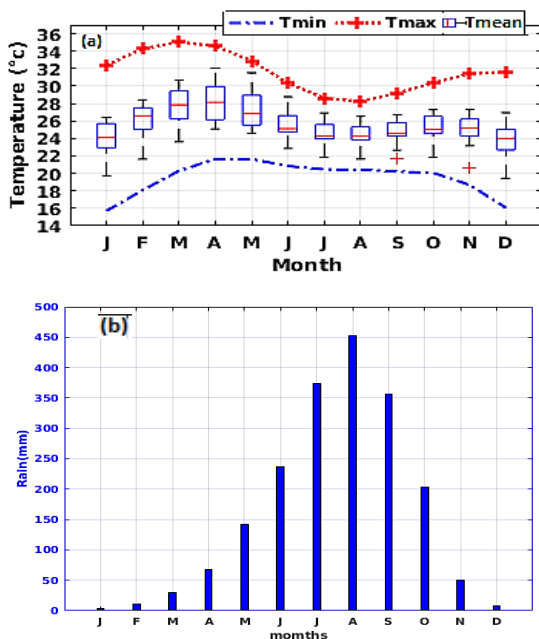


Figure 4: Overall distribution of temperature (a) and rainfall (b).

Latitudinal variation of temperature and rainfall

Figures 5(a) and 5(b) show the temperature and rainfall variation according to the increasing latitudinal positions of each station. It is evident that an increase in temperature with latitude is significant except for the Labe site and Macenta site. It is also notice that there is a significant decrease in temperature for the station of Labe in spite of its position which is further north compared to Boke site. We also noticed such decrease in temperature at the station of Macenta which is further north compared with that of N’zerekore. The observed decrease in temperature at both stations Labe (the highest meteorological station above the sea level in Guinea) and Macenta (a very rainy and great forest area in Guinea), may result from the influence of the massif of Fouta Djallon (which arises up to 1025 m above the sea level) for Labe site and the forest of Ziama (112.300 hectares of woodland) for Macenta site.

The variation of the pluviometry is characterized by a northward decreasing. It is also observed that there is an exception at the station of Conakry and Macenta. The rise of the pluviometry at Conakry is understandable by the coastal effect. The presence of the forest of Ziama explains the rise of the pluviometry compared to the neighbouring stations.

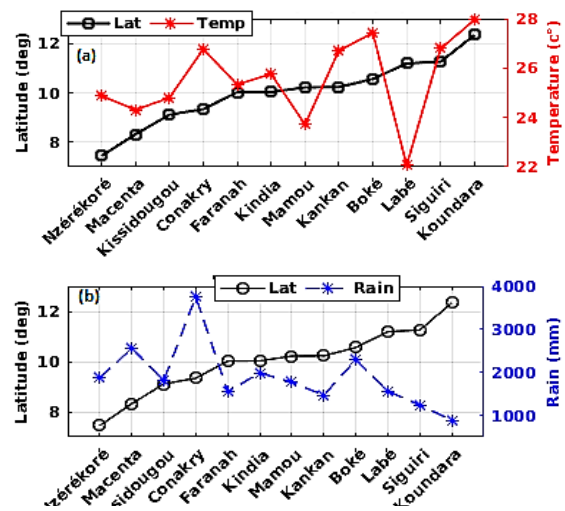


Figure 5: Latitudinal variation of temperature (a) and rainfall (b).

Summary

This climatological analysis allowed us to improve our understanding of the variability of temperature and pluviometry during 57 year in Guinea. An upward trend of the temperature is observed in all Guinea meteorological sites used in this study. A decrease in pluviometry since the end of 1960s characterized by a disturbance in rainfall patterns modifies gradually the climate.

The extension of this analysis over the whole western Africa by using Era-Interim data coupled with satellite data would allow to describe more on the climate variability and to improve the knowledge in this zone which is besides the political conflicts, the victim of the consequences of climate risks.

Acknowledgements

This work is undertaken in the framework of the International Research Group GDRI ARSAIO (Atmospheric Research in Southern Africa and Indian Ocean) supported by the NRF and CNRS and by the SA-France Protea programme. We are grateful to the Guinean Meteorological Service (GWS) for providing the temperature and rainfall data series used in this study.

References

Cleave, K.V., Lenters, J.D., Wang, J., Verhamme, E.M., 2017. A regime shift in Lake Superior ice cover, evaporation, and water temperature following the warm El Niñ winter of 1997–1998. *Limnology and Oceanography* 59, 1889–1898. <https://doi.org/10.4319/lo.2014.59.6.1889>

CLIVAR, 2017. African Monsoon | [www.clivar.org](http://www.clivar.org) [WWW Document]. URL /african-monsoon (accessed 12.27.17).

Conway, D., 2011. Adapting climate research for development in Africa. *WIREs Clim Change* 2, 428–450. <https://doi.org/10.1002/wcc.115>

Cook, K.H., 2015. Role of inertial instability in the West African monsoon jump. *J. Geophys. Res. Atmos.* 120, 2014JD022579. <https://doi.org/10.1002/2014JD022579>

Descroix, L., Diongue Niang, A., Panthou, G., Bodian, A., Sane, Y., Dacosta, H., Malam Abdou, M., Vandervaere, J.-P., Quantin, G., 2015. Évolution récente de la pluviométrie en Afrique de l’ouest à travers deux régions: la Sénégalie et le Bassin du Niger Moyen. Recent trend on rainfall in West Africa through two regions: Senegambia

- and the Middle Niger River Basin 25–43. <https://doi.org/10.4267/climatologie.1105>
- Espinoza Villar, J.C., Ronchail, J., Guyot, J.L., Cochonneau, G., Naziano, F., Lavado, W., De Oliveira, E., Pombosa, R., Vauchel, P., 2009. Spatio-temporal rainfall variability in the Amazon basin countries (Brazil, Peru, Bolivia, Colombia, and Ecuador). *Int. J. Climatol.* 29, 1574–1594. <https://doi.org/10.1002/joc.1791>
- Gbobaniyi, E., Sarr, A., Sylla, M.B., Diallo, I., Lennard, C., Dosio, A., Dhiédiou, A., Kamga, A., Klutse, N.A.B., Hewitson, B., Nikulin, G., Lamptey, B., 2014. Climatology, annual cycle and interannual variability of precipitation and temperature in CORDEX simulations over West Africa. *Int. J. Climatol.* 34, 2241–2257. <https://doi.org/10.1002/joc.3834>
- Hope, P., Timbal, B., Fawcett, R., 2010. Associations between rainfall variability in the southwest and southeast of Australia and their evolution through time. *Int. J. Climatol.* 30, 1360–1371. <https://doi.org/10.1002/joc.1964>
- Loua, R.T., Beavogui, M., Bencherif, H., Barry, A.B., BAMBA, Z., Amory-Mazaudier, C., 2017. Climatology of Guinea: Study of Climate Variability in N'zerekore. *Journal of Agricultural Science and Technology (JAST)* 7. <https://doi.org/10.17265/2161-6256/2017.04.001>
- Nicholson, S.E., 1981. Rainfall and Atmospheric Circulation during Drought Periods and Wetter Years in West Africa. *Mon. Wea. Rev.* 109, 2191–2208. [https://doi.org/10.1175/1520-0493\(1981\)109<2191:RAACDD>2.0.CO;2](https://doi.org/10.1175/1520-0493(1981)109<2191:RAACDD>2.0.CO;2)
- Simmons, A.J., Berrisford, P., Dee, D.P., Hersbach, H., Hirahara, S., Thépaut, J.-N., 2008. A reassessment of temperature variations and trends from global reanalyses and monthly surface climatological datasets. *Quarterly Journal of the Royal Meteorological Society* 134, 101–119. <https://doi.org/10.1002/qj.2949>
- Wang, S., Gong, D., 2000. Enhancement of the warming trend in China. *Geophysical Research Letters* 27, 2581–2584.
- WMO, 2017. Directives de l'OMM pour le calcul des normales climatiques, Édition 2017. ed, OMM. OMM, Genève.

# **An assessment of the importance of combining wind, ocean currents and stochastic motions in a particle trajectory model for search and rescue applications**

Michael G. Hart-Davis<sup>1,a,c,d</sup>, Björn C. Backeberg<sup>b,c,e</sup> and Mostafa Bakhoday-Paskyabi<sup>e</sup>

<sup>a</sup> Institute for Coastal and Marine Research, Nelson Mandela University, Port Elizabeth, South Africa

<sup>b</sup> Council for Scientific and Industrial Research, Natural Resources and the Environment, Cape Town, South Africa

<sup>c</sup> Nansen-Tutu Centre for Marine Environmental Research, University of Cape Town, Cape Town, South Africa

<sup>d</sup> Egagasini Node, South African Environmental Observation Network, Cape Town, South Africa

<sup>e</sup> Nansen Environmental and Remote Sensing Center, Bergen, Norway

## ***Abstract***

A Lagrangian numerical model for at sea search and rescue applications is presented. The model incorporates the effects from wind, surface currents, as well as stochastic diffusivity in order to determine the horizontal trajectory of each virtual particle released. The importance of including each of these two parameters as well as stochastic motions when predicting the path of an object lost at sea were determined through a number of model simulations. The preliminary results suggest that the drift of an object depends on the variability of the wind field, surface currents and characteristics of sub-grid scale effects of unresolved motions.

## ***Keywords***

Particle tracking, Capsized Vessel, Agulhas Current, Surface Currents, Windage

## ***Introduction***

Lagrangian analyses of oceanic fluid by virtual particles, advected with the background flow information of ocean models, have been increasingly used to study physical and biogeochemical oceanographic processes (van Sebille et al. 2018), and are used extensively to investigate the ocean dynamics simulated by ocean models (Xu et al. 2016; Biastoch et al. 2015). Additionally, synthetic particle tracking tools have been developed for a variety of applications (Fredj et al. 2016) including larval dispersion (Thorpe et al. 2004), oil spills (Sayol et al. 2014), hydrodynamic connectivity (van Sebille et al. 2010) and search and rescue (Hart-Davis et al. 2018). In Hart-Davis et al (2018) particle trajectory modelling was used in a search and rescue application using a satellite-derived ocean product. This case study identified the shortcomings of using only passive particles and surface current velocities in predicting the path of a capsized vessel.

On the 18th of January 2016, the upturned hull of a catamaran was spotted approximately 113 Nautical Miles off Cape Recife, near Port Elizabeth (South Africa), which was first reported missing a year earlier, in January of 2015. 5 days after being spotted off Cape Recife, on the 22nd of January 2016, the National Sea Rescue Institute (NSRI) found the capsized catamaran south of Cape Agulhas. The approximate locations, the last known position (25° 41' 59.46"E and 34° 24' 11.08"S) and

the recovery site (20° 07' 32.58"E and 35° 01' 31.94"S), of the capsized vessel provides valuable information that can be used to address the shortcomings of the particle trajectory model developed in Hart-Davis et al (2018). An approach is presented here to assess the accuracy of using a particle trajectory model that combines predicted surface current velocities, 10-meter winds and stochastic motion to estimate the path of the capsized vessel. The analyses in this paper are restricted to the conditions when there is no interactions between wind and current, in the absence of spatial variability of turbulent forcing.

## ***Data and Methods***

### ***Mercator global ocean and ECMWF global wind forecasts***

The operational Mercator global ocean analysis and forecast system provides 10-day, 3D global ocean forecasts on a daily basis (available at <http://marine.copernicus.eu>). This product includes daily data of temperature, salinity, currents, sea level, mixed layer depth and ice parameters throughout the full depth of the global ocean. Output files are available at a 1/12° horizontal resolution with regular longitude/latitude equirectangular projection and 50 vertical levels ranging from 0 to 5500 meters. The ocean model is forced using winds from the ECMWF (European Centre for Medium-Range Weather Forecasts), which contains the wind-induced drift used to account for the wind drift of the virtual particles.

<sup>1</sup>Corresponding author at: Department of Oceanography, Nelson Mandela University, South Africa.  
E-mail Address: mhartd@gmail.com

Table 1. Summary of the results of the simulations using four different fixed values of horizontal eddy diffusivity. The mean Lagrangian displacement was calculated by the formula adapted from LaCasce (2000) :  $M_x(t) = \frac{1}{N}(x_t - x_o)$ .

Fixed Horizontal Eddy Diffusivity ( $m^2/s$ )	Percentage of particles that hit the coast	Furthest particle from recovery point of vessel (in km)	Percentage of particles that passed through the bin of the capsized catamaran on the final day of the simulation	Mean Lagrangian displacement (in m)	Standard deviation of mean Lagrangian displacement (in m)
200	87.51	135.28	9.99	0.02	0.01
500	91.16	186.40	25.49	0.02	0.02
1000	85.74	329.08	22.48	0.07	0.04
2000	76.69	357.94	26.74	0.06	0.04

Here, the 3-hourly  $1/10^\circ$  wind forecasts 10 m above the ocean surface are averaged to daily mean winds and interpolated to the  $1/12^\circ$  Mercator ocean forecast grid to obtain consistent spatio-temporal resolution between the ocean and wind forecasts products used.

### Virtual Particle Tracking

Particle tracking is the observation of the motion of an individual particle within a fluid (Hart-Davis et al 2018). A Lagrangian particle tracking tool known as Parcels (Lange and van Sebille 2017) was used within this study. The governing equation of two-dimensional particle motion (Bakhoday-Paskyabi 2016) is represented as follows:

$$\delta X_p(t) = \mathbf{u}_p(X_p(t), t) + \sqrt{2A_h \cdot \delta t} \cdot \delta W_t, \quad (1)$$

where  $X_p$  denotes the horizontal position of a particle at time  $t$ ,  $\mathbf{u}_p$  is the space-time dependent velocity field and  $\delta t$  is the model time step.  $A_h$  and  $\delta W_t$  are the horizontal eddy diffusivity (magnitude of stochastic forcing) to parameterise sub-grid scale processes or unresolved physical processes (van Sebille et al. 2018) and a zero-mean white noise random number (Bakhoday-Paskyabi 2016). Here, the velocity field is composed as  $\mathbf{u}_p = \mathbf{u}_o + \mathbf{u}_a$ , where  $\mathbf{u}_o$  is the surface current and  $\mathbf{u}_a$  is related to the wind speed at 10 m ( $\mathbf{u}_{10}$ ) through the formulation  $\mathbf{u}_a = \mathbf{u}_{10} * 4 \times 10^{-2}$  to account for the effects of a capsized vessel in the ocean (pers. comms. NSRI).

### Results and Discussion

For all of the following experiments, 1000 virtual particles were deployed for five days starting on the 18th of January 2016 at the last known position of the capsized vessel ( $25^\circ 41' 59.46''E$  and  $34^\circ 24' 11.08''S$ ). In the horizontal eddy diffusivity experiments, we investigated the use of four different fixed horizontal eddy diffusivities in calculating the stochastic motion (Brownian Motion, Hida 1980). In the virtual particle forcing section, we conduct a series of virtual particle experiments to investigate the importance of

combining wind and surface currents in an example of a capsized vessel. For all experiments the ECMWF  $1/10^\circ$  daily mean winds and/or the  $1/12^\circ$  Mercator ocean surface velocity data was used. The information of wind and surface currents were calculated along the particle trajectories using bilinear interpolation for all the experiments done in this study.

### Horizontal Eddy Diffusivity

In order to assess the impacts of stochastic motion on virtual particle trajectories along the southern coast of South Africa, experiments were derived based on the research carried out by Abernathey and Marshall (2013) and Ruhs et al. (2018) who found an estimated range of surface horizontal eddy diffusivity for the Agulhas Bank of between 200 and 2000  $m^2/s$ . Therefore, four fixed values of horizontal eddy diffusivity were chosen, 200, 500, 1000 and 2000  $m^2/s$ , and compared in the following analysis (Table 1).

The percentage of virtual particles that hit the coast of South Africa were calculated to assess how different horizontal eddy diffusivities impacted the outcomes of the virtual particles. The experiment with the highest amount of diffusivity (2000  $m^2/s$ ) had the lowest number of virtual particles hitting the coastline (76.69%). Furthermore, this experiment also resulted in the highest maximum distance from the recovery site of the capsized vessel (357.94 km). This is expected due to the higher value of horizontal eddy diffusivity resulting in higher turbulence and, therefore, it is less likely that particles will travel in similar directions.

This is confirmed in the lower horizontal eddy diffusivity values (200 and 500  $m^2/s$ ), where there is a greater percentage of virtual particles that reach the coast (87.51% and 91.16%) and a lower maximum distance from the recovery site (135.28 and 186.40 km respectively).

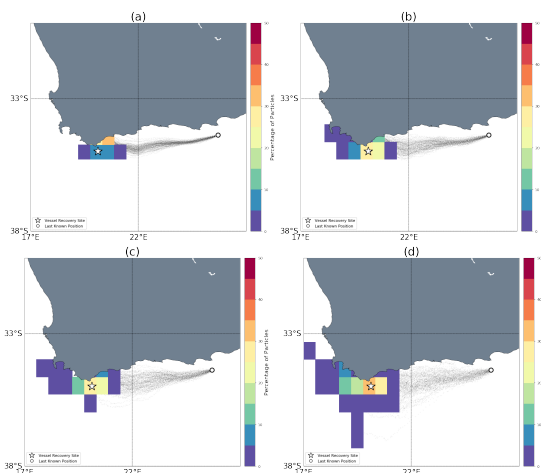


Figure 1. Illustration of the impact of the four different fixed horizontal eddy diffusivities on the outcome and pathways of the virtual particles. The fixed values of horizontal eddy diffusivity for each experiment is (a) 200, (b) 500, (c) 1000 and (d) 2000  $m^2/s$ . The  $0.5^\circ \times 0.5^\circ$  bins represent the percentage of particles that fall within each bin between the final day of simulations (day 4 – 5). The grey lines indicate the trajectories of all 1000 particles for the duration of the experiment. The black and white circle represent the last known position of the capsized vessel and the black and white star represent the recovery site of the capsized vessel.

The relatively high values of particles reaching the coast in all of the experiments ( $> 75\%$ ) suggests that the dominant flow of this region as a result of the surface currents and windage is in a north-westerly direction which is pushing the virtual particles towards the coast. Despite experimenting with different values of horizontal eddy diffusivity, the results still represent a similar pattern for the particle trajectories. This spatial feature, in accord with the non-turbulent pathways of particles, may be partly explained due to the lack of information associated with the statistical properties of fluctuating components of motion. The tentative results of diffusion analysis suggest that the experiment with the lowest value of mean Lagrangian displacement ( $M_x$ ) of  $0.02 \pm 0.01$  was the experiment with the lowest horizontal eddy diffusivity, while the highest was 1000  $m^2/s$  experiment with an  $M_x$  of  $0.07 \pm 0.04$ .

The influence of the horizontal eddy diffusivity on the trajectory and final location of the virtual particles is presented in Fig. 1. The overall direction of the virtual particles for all the experiments tends to be in a westward direction regardless of the value of horizontal eddy diffusivity. It is evident that the horizontal eddy diffusivity influences the directional spread of the virtual particles, with higher horizontal eddy diffusivity resulting in greater variability and vice versa. In order to better quantify this variability, the percentage of total virtual particles in the ocean per  $0.5^\circ \times 0.5^\circ$  grid at the end of day 5 is calculated. This provides an estimate of the maximum likelihood for a virtual particle to be found in a  $0.5^\circ \times 0.5^\circ$  geographical grid on the last day of the simulation experiment.

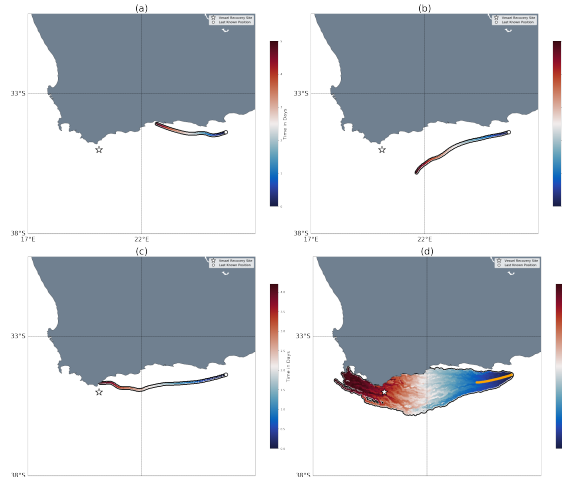


Figure 2. A simulation of 1000 virtual particles deployed at the location where the capsized vessel was last seen (white circle) forced (a) wind only, (b) current only, (c) wind and current only and (d) wind, current and Brownian motion. The colorbar represents the time in days since deployment, reaching a maximum of five days. The orange line on (d) represents the mean trajectory of the 1000 particles. It should be noted that (c) hits the coast after 4.1 days of the simulation.

As shown in Fig. 1 the highest percentage of virtual particles on the day when the capsized vessel was recovered (day 4 – 5) are found in the  $0.5^\circ$  grid cell that contains the location where the capsized catamaran was recovered in three of the simulation experiments (Figs. 1b, c, d).

The results suggest that the lowest fixed horizontal eddy diffusivity ( $200 m^2/s$ ) based on the studies by Abernathy and Marshall 2013 and Rühls et al. 2018, may be too low for this highly dynamic region. That being said, almost 10% of virtual particles that were deployed in this experiment made it to the bin where the capsized vessel was located. In the other three experiments, however, this percentage encouragingly exceeded 20%. The experiments have used a fixed diffusivity and have not accounted for the spatial variability of diffusivity fields, which will have an impact on the results and will be addressed in a future study.

### Virtual Particle Forcing

In order to assess the importance of including both wind and surface current data when conducting simulations on capsized vessels in the ocean, experiments were conducted to assess the contribution of each forcing field (Fig. 2). The virtual particles in simulations forced with only surface currents (Fig. 2b) are in agreement with Hart-Davis et al (2018) who suggest that using only ocean surface currents to force the synthetic particles is inadequate in terms of simulating the pathway of the capsized vessel. Although surface current velocity data plays a key role, this result suggests that other parameters play important roles in determining the accuracy of the

trajectory of a capsized catamaran. Wind forcing only was also not sufficient (Fig. 2a) and although, combining wind and surface currents (Fig. 2c) improved the result drastically, the results remained insufficient in estimating the path of the capsized vessel.

This could be due to the spatial resolutions of the surface current velocity data ( $1/12^\circ$ ) and the wind data ( $1/10^\circ$ ) which are not able to represent the correct effects of sub-grid scale processes of the region. In an attempt to resolve the sub-grid scale processes in the particle trajectory model, Brownian motion (Hida 1980) was applied to account for the turbulent features not resolved in the velocity field (Fig. 2d). The results show a strong number of virtual particles that pass through the point where the capsized vessel was recovered. When combining this result with the results show in Fig. 1, it can be implied that the particle trajectory model performs the best when the wind, surface currents and stochastic motion are incorporated as a high percentage of particles end up in the region where the capsized vessel was recovered at the end of the simulation.

### Conclusions

A particle trajectory model combining ocean surface currents, winds and stochastic motions is assessed for potential application in a search and rescue scenario for a capsized catamaran drifting past Cape Recife, South Africa. It is shown that, by incorporating wind and surface current data into the particle trajectory model, the model more accurately predicts the drift of the capsized vessel over a five day period. Furthermore, by incorporating the impacts of stochastic motion into the model, the model provides a better probabilistic forecast of the final outcome of the capsized vessel. It is anticipated that with some refinement (such as using spatially varying horizontal eddy diffusivity and different boundary conditions) and the incorporation of other parameters (e.g. interactions between wind, current, wave and turbulence), that the accuracy of the particle trajectory model will continue to improve and result in the increased use of this model in scientific and operational applications.

### Acknowledgements

Mr Michael G. Hart-Davis acknowledges financial support from the Nansen-Tutu Centre for Marine Environmental Research and the South African Environmental Observation Network Egagasini Node. Mr Hart-Davis would also like to thank Prof Juliet Hermes for her contributions to this research. The Lagrangian particle tracker, Parcels is licensed under an open source MIT license and can be downloaded from <https://oceanparcels.org/>.

### References

- Abernathey, R. P., and Marshall, J. 2013. Global Surface Eddy Diffusivities Derived from Satellite Altimetry. *Journal of Geophysical Research, C: Oceans* 118 (2): 901–16.
- Bakhoday-Paskyabi, M., 2016. Turbulence-particle interactions under surface gravity waves. *Ocean Dynamics*, 66(11), pp.1429–1448.
- Biastoch, A., Durgadoo, J.V., Morrison, A.K, van Sebille, E., Weijer, W. and Griffies, S.M. 2015. Atlantic Multi-Decadal Oscillation Covaries with Agulhas Leakage. *Nature Communications* 6 (December): 10082.
- Fredj, E, Carlson, D.F., Amitai, Y., Gozolchiani, A. and Gildor, H. 2016. The Particle Tracking and Analysis Toolbox (PaTATO) for Matlab. *Limnology and Oceanography, Methods / ASLO* 14 (9): 586–99.
- Hart-Davis, M.G., Backeberg, B.C., Halo, I., van Sebille, E. and Johannessen, J.A. 2018. Assessing the accuracy of satellite derived ocean currents by comparing observed and virtual buoys in the Greater Agulhas Region. *Remote Sensing of Environment*. <https://doi.org/10.1016/j.rse.2018.03.040>.
- Hida, T. 1980. Brownian Motion. In *Brownian Motion*, edited by T. Hida, 44–113. New York, NY: Springer US.
- Kloeden, P. and Platen, E. 1991. Numerical Methods for Stochastic Differential Equations. *Stochastic Hydrology and Hydraulics* 5 (2): 172–172.
- Lacasse, J. H. 2000. Floats and f/H. *Journal of Marine Research* 58 (1): 61–95.
- Lange, M. and van Sebille, E. 2017. Parcels v0.9: prototyping a Lagrangian ocean analysis framework for the petascale age. *Geoscientific Model Development*, 10(11), pp.4175–4186.
- Rühs, S., Zhurbas, V., Koszalka, I. M., Durgadoo, J.V. and Biastoch, A. 2018. Eddy Diffusivity Estimates from Lagrangian Trajectories Simulated with Ocean Models and Surface Drifter Data—A Case Study for the Greater Agulhas System. *Journal of Physical Oceanography*, 48(1), pp.175–196.
- Sayol, J.M., Orfila, A., Simarro, G., Conti, D., Renault, L. and Molcard, A. 2013. A Lagrangian model for tracking surface spills and SaR operations in the ocean. *Environ. Model. Softw.* 52, 74–82.
- Straton, A. 2016. Tragic capsized catamaran drifts past Port Elizabeth. *MyPE News*. (Available). [www.mype.co.za/new/tragic-capsized-catamaran-drifts-past-portelizabeth/59957/2016/01](http://www.mype.co.za/new/tragic-capsized-catamaran-drifts-past-portelizabeth/59957/2016/01), Accessed date: 20 January 2018.
- Thorpe, S.E., Heywood, K.J., Stevens, D.P. and Brandon, M.A. 2004. Tracking passive drifters in a high-resolution ocean model: implications for interannual variability of larval krill transport to South Georgia. *Deep-Sea Res. I Oceanogr. Res. Pap.* 51, 909–920.
- van Sebille, E., Biastoch, A., van Leeuwen, P.J. and de Ruijter, W.P.M. 2009. A weaker Agulhas Current leads to more Agulhas leakage. *Geophysical Research Letters*, 36(3). Available at: <http://dx.doi.org/10.1029/2008gl036614>.
- van Sebille, E., Griffies, S.M., Abernathey, R., Adams, T.P., Berloff, P., Biastoch, A., Blanke, B., Chassignet, E.P., Cheng, Y., Cotter, C.J., Deleersnijder, E., Döös, K., Drake, H.F., Drijfhout, S., Gary, S.F., Heemink, A.W., Kjellsson, J., Koszalka, I.M., Lange, M., Lique, C., MacGilchrist, G.A., Marsh, R., Adame, C.G.M., McAdam, R., Nencioli, F., Paris, C.B., Piggott, M.D., Polton, J.A., Rühs, S., Shah, S.H.A.M., Thomas, M.D., Wang, J., Wolfram, P.J., Zanna, L. and Zika, J.D. 2018. Lagrangian ocean analysis: Fundamentals and practices. *Ocean Modelling*, 121, pp.49–75.
- Xu, J., Lowe, R.J., Ivey, G.N., Jones, N.L. and Zhang, Z. 2016. Ocean transport pathways to a world heritage fringing coral reef: Ningaloo reef, western Australia. *PLoS* 11 (1), 1–26.

## Delegates contact email details

FULL NAME	INSTITUTION/ORGANIZATION	EMAIL ADDRESS
Sivakumar Venkataraman	University of KwaZulu Natal	venkataramans@ukzn.ac.za
Paulene Govender	University of KwaZulu-Natal	paulenegovender@gmail.com
Yegeshni Moodley	University of KwaZulu-Natal	yegeshnin@gmail.com
Lerato Shikwambana	South African National Space Agency	lshikwambana@gmail.com
Perfect P Chifoto	University of Kwazulu-Natal	perfectpeechifoto@gmail.com
BENCHERIF Hassan	Reunion University	hassan.bencherif@univ-reunion.fr
Nelson Begue	Reunion University	nelson.begue@univ-reunion.fr
Chris Reason	University of Cape Town	chris.reason@uct.ac.za
Mathieu Rouault	University of Cape Town	Mathieu.Rouault@uct.ac.za
Arielle Stella Nkwinkwa Njouodo	University of Cape Town	a.nkwinkwa@yahoo.fr
Folly Serge Tomety	University of Cape Town	sertom1@hotmail.fr
Georges-Noel T. Longandjo	University of Cape Town	gntiers@gmail.com
Mare-Lou Bachelery	University of Cape Town	bachelery.marielou@gmail.com
Bellinda Monyela	University of Cape Town	mnybel003@myuct.ac.za
Ross Blamey	University of Cape Town	ross.blamey@uct.ac.za
Naomi Kumi	University of Cape Town	naomi.kumi@uct.ac.za
Rakhee Lakhraj-Govender	Tshwane University of Technology	lakhrajgovenderr@tut.ac.za
Lisa Gaustella	University of Cape Town	lisa.guastella@alumni.uct.ac.za
Nisa Ayob	North West University	nisa.ayob@hotmail.com
Izidine Pinto	University of Cape Town	izidinep@csag.uct.ac.za
Temitope Egbebiyi	University of Cape Town, South Africa	EGBTEM001@myuct.ac.za
Kwesi Quagraine	University of Cape Town	kwesi@csag.uct.ac.za
Luleka Dlamini	University of Cape Town	lulehdlamini@gmail.com
Siyabusa Mkuhlani	Climate Systems Analysis Group	siyabusa@gmail.com
Willem Stefaan Conradie	Climate System Analysis Group	stefaan@csag.uct.ac.za
Sibusiso Mthembu	University of KwaZulu-Natal	mthembus3@ukzn.ac.za
Neil Hart	University of Oxford	neil.hart@ouce.ox.ac.uk
Liesl Dyson	University of Pretoria	liesl.dyson@up.ac.za
Thando Ndarana	University of Pretoria	thando.ndarana@weathersa.co.za
Anzel de Lange	University of Pretoria	u11077396@up.ac.za
Aimee Serafini	University of Pretoria	aimeeserafini@gmail.com
Surprise Mhlongo	University of Pretoria	surpmhlongo@gmail.com
Mzimkhulu Msimanga	University of Pretoria	u12012922@tuks.co.za+
Henno Havenga	North West University	22743529@nwu.ac.za
David Jean du Preez	South African Weather Service	jean.dupreez@weathersa.co.za
Nosipho Zwane	South African Weather Service	Nosipho.Zwane@weathersa.co.za
Siphesihle Fortunate Sithole	South African Weather Service	Siphesihle.Sithole@weathersa.co.za
Thabo Elias Makgoale	South African Weather Service	thabo.makgoale@weathersa.co.za
Thato Caroline	South African Weather Service	Thato.Masithela@weathersa.co.za
Brighton Mabasa	South African Weather Service	brighton.mabasa@weathersa.co.za

Tshidi Machinini	South African Weather Service	tshidi.machinini@weathersa.co.za
Lucky Ntsangwane	South African Weather Service	lucky.ntsangwane@weathersa.co.za
Siphamandla Daniel	South African Weather Service	siphamandla.daniel@weathersa.co.za
Mary-Jane Bopape	South African Weather Service	mary-jane.bopape@weathersa.co.za
Kabelo Mathibela	South African Weather Service	kablo.mathibela@gmail.com
Njabulo Mchunu	South African Weather Service	Njabulo.Mchunu@weathersa.co.za
Stephanie Landman	South African Weather Service	stephanie.landman@weathersa.co.za
Gift Rambuwani	South African Weather Service	gift.rambuwani@weathersa.co.za
Jaco de Wit	South African Weather Service	jaco.dewit@weathersa.co.za
Morwakoma Matabane	South African Weather Service	morwakoma.matabane@weathersa.co.za
Patience Tlangelani Mulovhedzi	South African Weather Service	patience.mulovhedzi@weathersa.co.za
Ngwako Mohale	South African Weather Service	ngwakomohale@yahoo.com
Christo Rautenbach	South African Weather Service	christo.rautenbach@weathersa.co.za
Marc De Vos	South African Weather Service	Marc.DeVos@weathersa.co.za
Tania Williams	South African Weather Service	Tania.Williams@weathersa.co.za
Nkanyiso Mbatha	University of Zululand	nkanyisombatha5@gmail.com
Willard Zvarevashe	University of Zululand	wzvarevashe@gmail.com
Deon VanderMescht	South African Weather Service	deon.vandermescht@weathersa.co.za
Lehlohonolo Thobela	University of Pretoria/SAWS	Hlonithobela@gmail.com
Hector Chikoore	University of Venda	hector.chikoore@univen.ac.za
Johan Malherbe	CSIR	JMalherbe@csir.co.za
Thulebona Mbhamali	University of Zululand	twmbhamali@gmail.com
Jan Vermeulen	South African Weather Service	jan.vermeulen@weathersa.co.za
Samkelisiwe Thwala	University of Pretoria	u13341309@tuks.co.za